

ELECTRICAL AND CONTROL TECHNOLOGIES

PROCEEDINGS
OF THE 8TH INTERNATIONAL CONFERENCE ON
ELECTRICAL AND CONTROL TECHNOLOGIES ECT-2013



KAUNAS
UNIVERSITY OF
TECHNOLOGY



FACULTY OF ELECTRICAL
AND CONTROL
ENGINEERING

ISSN 1822-5934

ELECTRICAL AND CONTROL TECHNOLOGIES

**PROCEEDINGS
OF THE 8TH INTERNATIONAL CONFERENCE ON
ELECTRICAL AND CONTROL TECHNOLOGIES**



**Sponsored by:
Research Council of Lithuania
Siemens Osakeyhtio Lietuvos filialas**

SIEMENS

KAUNAS, TECHNOLOGIJA, 2013

UDK 621.3(474.5)(06); 681.5(474.5)(06)

**The :th International Conference on Electrical and Control Technologies
ECT-2015.**

Selected papers of the International Conference, May 4-5, 2015, Kaunas, Lithuania (Kaunas University of Technology), edited: A. Navickas (general editor), A. Sauhats, A. Virbalis, M. Ažubalis, V. Galvanauskas, K. Brazauskas, A. Jonaitis

The :th International Conference on Electrical and Control Technologies ECT-2015 is the continuation of series of annual conferences on electrical, power engineering, electrical drives and control technologies held earlier in Kaunas Polytechnic Institute and from 1990 in Kaunas University of Technology.

The aim of the Conference is to create the forum for presentations and discussions to consider the newest research and application results of investigations on electrical and power engineering, electric drives, power converters, automation and control technologies.

All papers were reviewed by Conference Editorial Committee and Conference Program Advisory Committee and independent peer reviewers.

For information write to:

Kaunas University of Technology
Department of Electric Power Systems
Studentų g. 48, LT-51367 Kaunas
Lithuania

Conference organizers

Kaunas University of Technology, Lithuania
IFAC Committee of National Lithuanian Organisation
Lithuanian Electricity Association, Full Member of EURELECTRIC

Conference Chairman

Prof. **J. Daunoras**, Dean of Kaunas University of Technology,
Faculty of Electrical and Control Engineering, Lithuania

Honorary Chairman

Prof. **A. Pundzienė**, Vice Rector of Kaunas University of Technology, Lithuania

Conference Program Advisory Committee:

Prof. R. Deksnys, Kaunas University of Technology, Lithuania
Prof. L. Fara, Polytechnic University of Bucharest, Romania
Prof. J. Gerhards, Riga Technical University, Latvia
Prof. E. Heinemann, Schmalkalden University, Germany
Dr. B. Jaekel, Siemens AG, Germany
Prof. T. Jokinen, Helsinki Technical University, Finland
Prof. V. Kaminskas, Vytautas Magnus University, Lithuania
Prof. S. Kaušinis, Kaunas University of Technology, Lithuania
Assoc. Prof. V. Mačerauskas, Kaunas University of Technology, Lithuania
Prof. L. Markevičius, Kaunas University of Technology, Lithuania
Prof. V. Miškinis, Lithuanian Energy Institute, Lithuania
Prof. A. Morkvėnas, Kaunas University of Technology, Lithuania
Prof. A. Nargėlas, Kaunas University of Technology, Lithuania
V. Paškevičius, President of Lithuanian Electricity Association, Lithuania
Prof. L. Ribickis, Riga Technical University, Latvia
Assoc. Prof. J. Sa da Costa, Technical University of Lisbon, Portugal
Prof. A. Sauhats, Riga Technical University, Latvia
Prof. R. Simutis, Kaunas University of Technology, Lithuania
Prof. A. W. Sowa, Bialystok Technical University, Poland
Prof. R. Strzelecki, Gdynia Maritime University, Poland
Prof. M. Valdma, Tallinn University of Technology, Estonia

Conference Editorial Committee:

General Editor: Prof. A. Navickas, Kaunas University of Technology, Lithuania
Prof. A. Sauhats, Riga Technical University, Latvia
Prof. A. Virbalis, Kaunas University of Technology, Lithuania
Assoc. Prof. V. Ažubalis, Kaunas University of Technology, Lithuania
Prof. V. Galvanauskas, Kaunas University of Technology, Lithuania
Assoc. Prof. A. Jonaitis, Kaunas University of Technology, Lithuania

Organizing committee:

Prof. V. Galvanauskas, Kaunas University of Technology, Lithuania
Assoc. Prof. M. Ažubalis, Kaunas University of Technology, Lithuania
Prof. K. Brazauskas, Kaunas University of Technology, Lithuania
Assoc. Prof. A. Jonaitis, Kaunas University of Technology, Lithuania

CONTENTS

Investigation of Lithuanian Digit Names Recognition Accuracy.....	9
Gintarė Bartišiūtė, Kastytis Ratkevičius <i>Kaunas University of Technology, Lithuania</i>	
Automation Control for Sorting Station Based on IEC 61499 Function Blocks	13
Georgi Popov, Kostadin Stoyanov, Grigor Stambolov <i>Technical University – Sofia, Bulgaria</i>	
Development of Reconfigurable Control System for Milling Machines Based on IEC 61499 Reusable Function Blocks.....	19
Grigor Stambolov <i>Technical University – Sofia, Bulgaria</i>	
Hexapod Walking Robot Energy Consumption Dependence on the Number of Legs Set on the Surface.....	25
Mindaugas Luneckas, Tomas Luneckas, Dainius Udris <i>Automation Department, Electronics Faculty, Vilnius Gediminas Technical University, Vilnius, Lithuania</i>	
Performance Evaluation of Wireless Network for Vehicular Environment.....	29
Nikolajs Bogdanovs, Ernests Petersons, Janis Jansons <i>Department of Transport Electronics and Telematics, Riga Technical University, Latvia</i>	
Synthesis and Investigation of the Control Algorithms of New Generation Controllers	33
Dinas Šulskis <i>Faculty of Electrical and Control Engineering, Kaunas University of Technology, Lithuania</i>	
Control of Computer Programs by Voice Commands	37
Vytautas Slivinskas*, Gražina Pyž***, Virginija Šimonytė* *Lithuanian University of Educational Sciences, Lithuania **Vilnius University Institute of Mathematics and Informatics, Lithuania	
Seabed Image Segmentation Using Random Forests and Support Vector Machines.....	41
Tadas Rimavičius*, Adas Gelžinis*, Evaldas Vaičiukynas*, Sergej Olenin**, Aleksej Šaškov** *Department of Electrical and Control Instrumentation, Kaunas University of Technology, Lithuania **Klaipėda University Coastal Research and Planning Institute, Lithuania	
The Method for Human-Computer Interaction Based on Hand Gesture Recognition	45
Vidas Raudonis, Domas Jonaitis <i>Kaunas University of Technology, Lithuania</i>	
Real-Time Vibration Reduction in UAV's Image Sensors Using Efficient Hough Transform.....	50
David Afolabi ¹ , Zhun Shen ² , Tomas Krilavičius ^{3,5} , Vladimir Hahanov ⁵ , Eugenia Litvinova ⁵ , Svetlana Chumachenko ⁵ , Ka Lok Man ^{1,4,5} , Hai-Ning Liang ¹ , Nan Zhang ¹ , Tomas Žalandauskas ⁵ ¹ <i>Xi'an Jiaotong-Liverpool University, Suzhou, China</i> ² <i>IBM China, Suzhou, China</i> ³ <i>Vytautas Magnus University, Kaunas, Lithuania</i> ⁴ <i>Kharkov National University of Radioelectronics, Kharkov, Ukraine</i> ⁵ <i>Baltic Institute of Advanced Technologies, Lithuania</i>	
The Application of Stable and Skew T-Distributions in Predicting the Change in Accounting and Governance Risk Ratings	53
Leonidas Sakalauskas*, Zivile Kalsyte**, Ingrida Vaiciulyte*, Irmantas Kupciunas** *Vilnius University, Institute of Mathematics and Informatics, Lithuania; **Kaunas University of Technology, Department of Electrical & Control Equipment, Lithuania	
Application of Uppaal for Heating Systems Temporal Behavior Analysis.....	59
Paulius Stankevičius*, Gintarė Sukarevičienė*, Tomas Krilavičius*, Henrikas Pranevičius** * Vytautas Magnus University, Lithuania; ** Kaunas University of Technology, Lithuania	
Investigation of Dependencies between Virtual 3D Face Stimuli and Emotion-Based Human Responses	64
Egidijus Vaškevičius, Aušra Vidugirienė, Vytautas Kaminskas <i>Vytautas Magnus University, Faculty of Informatics, Lithuania</i>	

Comparison of State Estimation Techniques for Biotechnological Processes	70
Vytautas Galvanauskas*, Rimvydas Simutis*, Donatas Levišauskas*, Jolanta Repšytė*, Andreas Lübbert**	
<i>*Process Control Department, Kaunas University of Technology, Lithuania</i>	
<i>**Martin Luther University Halle-Wittenberg, Halle/S., Germany</i>	
Forecasting of Device Component Failures by Advanced Algorithms.....	76
Saulius Žiūkas, Vygandas Vaitkus	
<i>Kaunas University of Technology, Lithuania</i>	
Embedded Platform Hardware Implementation for Object Counting Using Video Data Processing.....	82
Paulius Lengvenis, Audrius Bukis, Rimvydas Simutis	
<i>Process Control Department, Kaunas University of Technology, Lithuania</i>	
Calculation of Low Voltage Electric Cables Zero Sequence Parameters	86
Gytis Svinkunas	
<i>Kaunas University of Technology, Lithuania</i>	
Investigation of Compatibility of the Variable Speed Pumped Storage Unit and Wind Power Plants in the Power System.....	90
Rimantas Pranas Deksnys, Darius Ališauskas	
<i>Kaunas University of Technology, Lithuania</i>	
Electrostatic Field of Axially Symmetrical Electrode System “Needle near the Plate”.....	94
Povilas Marčiulionis, Stasys Žebrauskas	
<i>Department of Electrical Engineering, Kaunas University of Technology, Lithuania</i>	
Investigation of Electric Field under Three-Phase Line	98
Ramūnas Deltuva, Gabija Nedzinskaitė, Juozapas Arvydas Virbalis	
<i>Department of Electronics Engineering, Kaunas University of Technology, Lithuania</i>	
Drying of Plants and their Seeds in the Corona Field	102
Stasys Žebrauskas*, Ernestas Kalinskas**	
<i>*Kaunas University of Technology, Lithuania; **Aleksandras Stulginskis University, Lithuania</i>	
The Need to Consider the Skin Effect in the Study of Direct Start-Up of a Squirrel-Cage Induction Motor	106
Julija Maksimkina	
<i>Institute of Industrial Electronics and Electrotechnics, Riga Technical University, Latvia</i>	
Smart System for Condition Monitoring of the Power System Equipments Insulation	111
Alfonsas Morkvėnas, Povilas Valatka	
<i>Department of Electric Power System, Kaunas University of Technology, Lithuania</i>	
Analysis of an Electrostatic Field in Electrode System of Devices for Drying of Powdery Materials.....	117
Ignas Andrijauskas, Stasys Žebrauskas	
<i>Kaunas University of Technology, Lithuania</i>	
Optimization of Transmission Line Parameters	121
Svetlana Berjozkina* **, Viktoria Neimane***, Antans Sauhats* **	
<i>* Riga Technical University, Institute of Power Engineering, Latvia;</i>	
<i>** JSC “Siltumelektroprojekts”, Latvia;</i>	
<i>*** Vattenfall Research and Development, Sweden</i>	
Modelling and Analysis the Compensation of Power Fluctuation of Wind Power Farm.....	126
Rimantas Pranas Deksnys, Aldas Stankevičius	
<i>Kaunas University of Technology, Department of Electric Power Systems, Lithuania</i>	
Sizing of the DC Chopper Parameters for the Grid-Tied Converter Efficient Operation	130
Česlovas Ramonas, Vytautas Adomavičius	
<i>Renewable Energy Centre at Kaunas University of Technology, Lithuania</i>	
Computer Modeling of the Field in Multi-Electrode Corona System with Ionized and Non-Ionized Areas.....	136
Ričardas Barčiauskas, Stasys Žebrauskas	
<i>Kaunas University of Technology, Lithuania</i>	
Parameter Estimation of DC Motor.....	140
Aurelijus Pitrenas, Andrius Petrovas	
<i>Vilnius Gediminas Technical University, Lithuania</i>	

The Investigation of Solar Energy Conversion and Storage Processes in Biomass	144
Povilas Algimantas Sirvydas*, Vidmantas Kučinskas**	
<i>*Aleksandras Stulginskis University, Lithuania; **UAB "ARVI" ir ko, Lithuania</i>	
Synchronous Interconnection of Baltic Power System to the Grid of Continental Europe: Realities and Views.....	148
Sigitas Kadiša, Virginijus Radziukynas, Arturas Klementavičius, Neringa Radziukynienė, Algimantas Leonavičius	
<i>Lithuanian Energy Institute, Lithuania</i>	
Transformer Model Based on Admittance Inverter	154
Adam Abramowicz	
<i>Warsaw University of Technology, Institute of Electronic Systems, Poland</i>	
Dispatch Training for TSO from Power Flow Calculations	158
T. Kuzņecovs*, A. Mahnitko*, T. Loman*, V. Rimarevs**, A. Dambis**	
<i>*Rīgas Tehniskā Universitāte, Latvia; **Augstsprieguma tīkls, Latvia</i>	
A Review of the Effects of Electric Vehicle Charging on Distribution Network Operation and Power Quality .	162
Lauri Kütt*, Eero Saarijärvi*, Matti Lehtonen*, Heigo Mölder**, Jaan Niitsoo***	
<i>*Aalto University, Dept. of Electrical Engineering, Finland</i>	
<i>**Tallinn University of Technology, Dept. of Electrical Engineering, Estonia</i>	
<i>***Tallinn University of Technology, Dept. of Electrical Power Engineering, Estonia</i>	
Influence of Electric Railway System on Voltage Unbalance Distribution between High Voltage and Low Voltage Electrical Networks.....	168
Tanel Sarnet, Jako Kilter, Ivo Palu	
<i>Department of Electrical Power Engineering, Tallinn University of Technology, Estonia</i>	
Modelling Possibilities for the Assessment of Wind Rotor Blades' Aeroelasticity and Strength.....	172
Tomas Narbutas, Jonas Valickas	
<i>Faculty of Technologies of Panevėžys Institute at Kaunas University of Technology, Lithuania</i>	
Static Electricity as Disburbance in High Voltage Substations	178
Nerijus Baršiukaitis*, Vitalijus Gvozdas**	
<i>* Kaunas University of Applied Engineering Sciences, Lithuania</i>	
<i>** Kaunas University of Technology, Lithuania</i>	
The Asymmetry Evaluation in the Distribution Network.....	182
Gintvilė Maslauskaitė, Ugnė Ilioitienė	
<i>Kaunas University of Technology, Lithuania</i>	

INVESTIGATION OF LITHUANIAN DIGIT NAMES RECOGNITION ACCURACY

Gintarė BARTIŠIŪTĖ, Kastytis RATKEVIČIUS
Kaunas University of Technology, Lithuania

Abstract: Paper deals with the recognition accuracy of Lithuanian ten digit names. The recognition of the digit names is of the essential importance for the successful implementation of various voice-based internet and telephony applications. Three types of recognizers are investigated for above mentioned purpose: a) the adapted foreign language recognizer used in Windows'7 or Windows'8 operation systems; b) the adapted foreign language recognizer used in Microsoft Speech Server'2007; c) purely Lithuanian speech recognizer based on HMM (Hidden Markov Models) modeling. The efficiency of all recognizers was evaluated using speech corpora. The results of investigation will be used for the development of hybrid Lithuanian recognizer.

Keywords: speech recognition, hybrid recognizer, recognition accuracy.

1. Introduction

Speech processing provides a natural and intuitive interface for the user. People communicate with one another through conversation, so it is comfortable and efficient to use the same method for communication with computers. The use of speech technologies lets us to create more natural, intuitive, more reasonable information service for much lower operational cost. The use of speech interface means that information will be available to the user independent from live operator.

A speech input interface based on speech recognition technology has already been applied to many applications, but it is in particular important to people with physical disabilities [1].

The project "Hybrid recognition technology for voice interface" was started in Lithuania in 2012. The main goal of the project is to develop hybrid voice commands recognition technology and implement it in the first practical informative service using recognition of Lithuanian voice commands. The informative service is oriented to the workplace of physician/ pharmacist and seeks to support/ to speed up the search of the necessary

information in pharmaceutical data base. The possibilities to fill the internet forms by voice will be investigated during the project too.

The careful investigation of the vocabulary used in such task showed that most of the commands could be constructed from the digit names or digit strings, e.g. the person could be identified from the personal code, the disease name is coded using letter name and several digit names, other important information for the successful filling of the form is the date when patient went sick and the duration of the leave. All these considerations leave to the conclusion that the recognition of the digit names is of the essential importance for the successful implementation of such service.

2. Hybrid recognition technology

This hybrid approach to speech recognition is based on the idea that some foreign language (non-Lithuanian) HMM-based speech recognizer (referred to as basic recognizer) can be adapted to recognize a large set of Lithuanian voice commands. This approach also states that this basic recognizer can be combined and extended with supplementary alternative speech recognition techniques that are invoked to process voice commands for which the recognition performance of the basic engine is less than satisfactory.

The idea of hybrid approach to speech recognition is not new: multiple engines are used in MASTOR system [2]. During speech recognition in this system, the input speech is sent to the multiple engines simultaneously. The speech utterance is then recognized by these ASR engines in parallel. Each engine then returns its own best recognition hypothesis. The ASR hypothesis from these multiple engines are further unified, sorted and displayed as N-best ASR hypothesis to the users. A special algorithm is designed and implemented to generate the best ASR result based on these N-best ASR hypothesis.

The hybrid approach of recognizer could be implemented using some modifications of the same

recognizer, for example, a system might recognize speech based on both Mel cepstral coefficients and perceptual linear prediction cepstrum, and combine the result. Very popular decision of the hybrid recognizer – the combination of HMM and neural network based recognizers: using MLP (Multi Layer Perceptron) as a post processor for HMM, it is possible to improve the recognizer performance. The increase in computational cost during recognition procedure is negligible, but it requires a more sophisticated and longer training procedure [3]. Similar hybrid recognition system uses a multilayer perceptron to estimate the observation likelihoods associated with the states of a HMM [4].

The combination of multiple speech recognizers based on different signal representations is increasingly attracting interest in the speech community – the example of such hybrid approach is hybrid speech recognition system based on the combination of acoustic and articulatory information [5]. It achieved significant word error rate reductions under highly noisy conditions on a small-vocabulary numbers recognition task.

In other words all state-of-the-art speech recognition systems are using hybrid recognition approach: implementing several recognizers operating in parallel and combining the results of several recognizers to get the final integral decision. So it is hard to expect achieve the appropriate recognition results using single recognizer as experience of various researchers in the field suggests.

The main point of a hybrid recognizer is a parallel usage of two different recognizers expecting that at least one of the recognizers will give the right result.

Another important factor – quite good voice commands endpointing using Windows'7 OS recognizer. A usage only of a Lithuanian recognizer would lead to additional solving of this problem.

Additional factor – the HTK-based realization of Lithuanian recognizer requires a high performance computer (in the project it is foreseen a recognition of 1000 commands). Therefore the structure “client-server” of hybrid recognizer was chosen (Fig.1): signal is applied to the basic recognizer (it should be Windows'7 OS Spanish language recognizer). If the confidence measure of recognized command is less than fixed threshold or there are some similar hypotheses of voice command, then the input signal is transmitted to the web server running the Lithuanian recognizer (or speech server MSS'2007). It returns recognition result to the client computer decision-making unit, forming the final recognition result.

3. Speech corpora

The first step in the development of the above mentioned informative service is the collection of the drug and medicines speech corpora. These corpora will be used to adapt foreign language speech recognizer and to train proprietary recognizer. This is costly and time consuming process and it should be ended in 2013. Trying to evaluate the possibilities and the efficiency of some recognizers we carried on several experiments

using earlier prepared corpora of Lithuanian digit names.

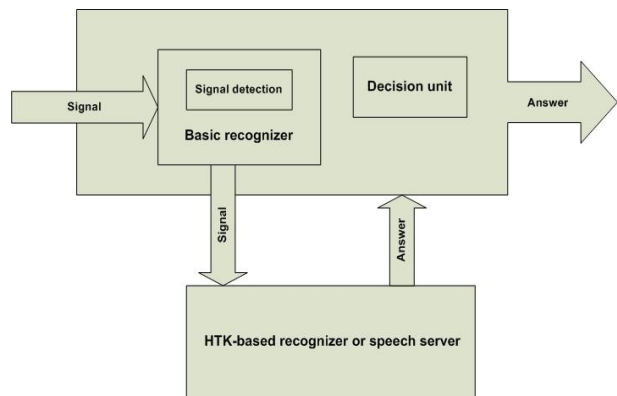


Fig. 1. Bloc-diagram of hybrid recognizer

For our experiments with Lithuanian digit names, speech corpus HKL7 was collected, which contain utterances from 20 different speakers (5 speaker-men, 15 speaker-women). Each speaker pronounced 10 digit names 20 times at sampling rate 16 kHz. This corpus was used for selecting the transcriptions of Lithuanian digit names, suitable for the Microsoft Speech Server'2007 (MSS'2007).

The additional speech corpus HKL8 was prepared from 10 new speakers (2 speaker-men, 8 speaker-women) for the testing procedure of MSS'2007.

Speech server needs telephony format of speech input, so speech corpora were adopted by down-sampling the speech corpora from the original 16 kHz to 8 kHz sampling rate.

HTK-based recognizer [6] requires separate speech files of WAV format, so speech corpora HKL7 and HKL8 should be segmented before investigations. We used earlier collected speech corpus SKAIC (50 speaker-men, 50 speaker-women). Each speaker pronounced 10 digit names 20 times at sampling rate 16 kHz. The shortcoming of this speech corpus is that some recordings are damaged, so the manual verification of speech corpus is needful.

4. Investigation of MSS'2007 speech recognizer

Microsoft Office Communications Server Speech Server (MSS'2007) [7] was chosen as the pretender to be used in the hybrid recognizer. It performs speech recognition, speech synthesis and telephony control operations. MSS'2007 has some language recognizers to choose from, but our earlier experiments showed, that *Microsoft Speech Recognizer 9.0 for MSS (Spanish-US)* provides significantly better results of Lithuanian digit names recognition comparing with English, German or French speech recognizers [8].

First of all Lithuanian digit names were rewritten to Spanish language transcriptions using “synthesis”, i.e., each Lithuanian digit name was synthesized with Spanish language synthesizer and the most similar to Lithuanian pronunciation Spanish transcriptions of digit names were selected. The number of found transcriptions for each digit was unequal: for a short

number, as “du”, 7 transcriptions were enough, but for longer digits (“septyni”, “aštuoni”) - 10 transcriptions were selected.

At the initial transcription selection stage, a separate grammar and test were prepared for each digit. Two speakers (man and woman) took part in the experiments. Each digit was spoken 100 times through the microphone: the recognized transcriptions were selected as the winners. If the same digit had more than one recognized transcription, all those transcriptions were used for further research and testing.

The averaged recognition accuracy of ten Lithuanian digit names using Spanish MSS’2007 engine and HKL7 speech corpus was equal to 97.0%.

After that new transcriptions were added for the worst recognized digit names and the testing experiments with HKL7 and HKL8 speech corpora were done.

The averaged recognition accuracy of ten Lithuanian digit names is shown in the table 1.

Table 1. Accuracy of digit names recognition by MSS’2007 Spanish recognizer

Digit name	Accuracy, %
Nulis	99.67
Vienas	100
Du	98.8
Trys	99.5
Keturi	95.5
Penki	100
Šeši	99
Septyni	99.8
Aštuoni	100
Devyni	100
Average	99.23

The average accuracy of digit names recognition by MSS’2007 Spanish recognizer is 99.33%. The worst recognized digit is “keturi”. The average recognition accuracies of females (23 speakers) and males (7 speakers) are 99.3% and 98.6%.

5. Investigation of the adapted foreign language recognizer

Our earlier experiments showed, that *Microsoft Speech Recognizer 8.0 (Spanish-US)* provides significantly better results of Lithuanian digit names recognition comparing with English and other recognizers, implemented in Windows’7 operation system [9]. So the above mentioned recognizer was selected as the basic recognizer.

The testing experiments with HKL7 and HKL8 speech corpora were done using Spanish recognizer 8.0 and the same Lithuanian digit names transcriptions as in the MSS’2007 speech server case. The averaged recognition accuracy of ten Lithuanian digit names is shown in the table 2.

The average accuracy of digit names recognition by Spanish recognizer 8.0 is 96.08%. The worst recognized digit is “du”. The average recognition accuracies of

females (23 speakers) and males (7 speakers) are 97% and 93%.

Table 2. Accuracy of digit names recognition by Spanish recognizer 8.0

Digit name	Accuracy, %
Nulis	95
Vienas	94.5
Du	84.5
Trys	99.33
Keturi	92.17
Penki	98.5
Šeši	99.67
Septyni	99.17
Aštuoni	99.67
Devyni	98.33
Average	96.08

6. Investigation of Lithuanian speech recognizer

For the development of Lithuanian speech recognizer well known continuous density hidden Markov models (CD-HMM) approach has been used. The core of the Lithuanian recognizer is HMM models of Lithuanian phonetic units which are trained in offline mode. Experiment described in this section is based on the acoustic models that were obtained/trained on a previously collected general purpose corpus of read speech (about 50 hour recordings) [10].

Speech recordings were transformed to the feature vectors. The recordings were sampled at 16 kHz, split into 20 ms duration frames using 10 ms displacement. Then 12 mel-frequency cepstrum coefficients (MFCC) were obtained out of 26 outputs of triangular filters linearly spaced in the nonlinear mel-frequency scale using discrete cosine transform. In addition to 12 cepstral coefficients 12 first and second order cepstrum change rate coefficients (derivatives) were calculated. These coefficients together with energy, first and second order energy derivatives were packed to make a single vector of 39 coefficients for each 20 ms signal frame. For the description of acoustic units the set of 141 monophones were used [11]. Lithuanian HMM speech recognizer was trained following the sequence of processing steps described in [6] and [10].

The averaged recognition accuracy of ten Lithuanian digit names is shown in the table 3.

The average accuracy of digit names recognition by HTK-based Lithuanian recognizer is 98.76%. The worst recognized digit is “trys”.

7. Comparison of three recognizers

The accuracy of digit names recognition by three recognizers is presented in Fig. 2. It could be seen that the accuracy achieved with Microsoft Speech server Spanish recognizer 9.0 wasn’t achieved with the computers using Microsoft Windows with Spanish speech recognizer 8.0, but the hybrid approach of these recognizers should be useful for the recognition of digit

“du”. Both recognizers have problems with the recognition of digit “keturi”.

Table 3. Accuracy of digit names recognition by Lithuanian HTK-based recognizer

Digit name	Accuracy, %
Nulis	99.78
Vienas	99.84
Du	98.13
Trys	94.65
Keturi	99.18
Penki	99.23
Šeši	99.85
Septyni	99.24
Aštuoni	98.8
Devyni	98.94
Average	98.76

Lithuanian HTK-based recognizer outperforms Spanish speech recognizer 8.0, but lightly loses to MSS'2007 speech recognizer. The hybrid approach of Lithuanian and Spanish recognizers should be useful for the recognition of digits “du”, “trys” and “keturi”.

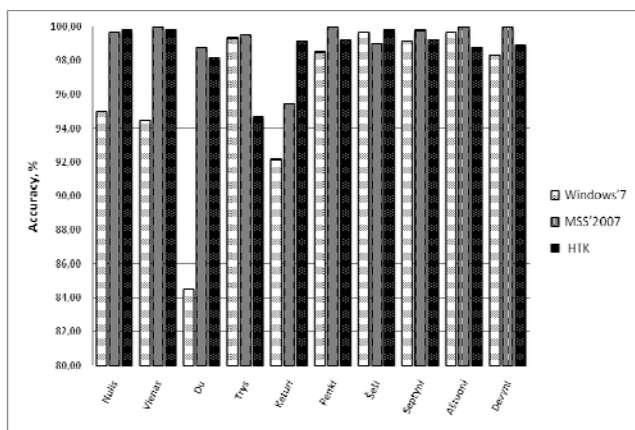


Fig. 2. Accuracy of digit names recognition by three recognizers

8. Conclusions

The experiments showed that Lithuanian recognizer outperformed an adapted Spanish language recognizer implemented in Windows'7 operation system and operated similarly well as MSS'2007 speech server Spanish recognizer, even if it was trained on a general purpose speech corpus.

The error analysis showed that errors made by different recognizers aren't exactly correlated and the performance of one recognizer may be used for the improvement of performance of the other recognizer.

9. References

1. Hawley M.S., Green P., Enderby P., Cunningham S., Moore R.K. Speech Technology for e-Inclusion of People with Physical Disabilities and Disordered Speech. Proc. Interspeech, Lisbon, 2005, p. 445-448.
2. Gao Y., Zhou B., Gu L., Sarikaya R., Kuo H.K., Rosti A., Afify M., Zhu W. IBM MASTOR: Multilingual automatic speech-to-speech translator. Proc. of ICASSP, p. 1205-1208, 2006.
3. Martins J. A., Violaro F. Hybrid recognizers combining Hidden Markov Models and multilayer perceptron. Proceedings of Telecommunications Symposium, 1998, vol. 1, p.146-150.
4. Abrash V., Cohen M., Franco H., Arima I. Incorporating linguistic features in a hybrid HMM/MLP speech recognizer. Proceedings of International Conference on Acoustic, Speech and Signal Processing, 1994, vol.2, p.673-676.
5. Kirchhoff K., Fink G.A., Sagerer G. Conversational speech recognition using acoustic and articulatory input. Proceedings of International Conference on Acoustic, Speech and Signal Processing, 2000, vol. 3, p. 1435-1438.
6. Young, S., Kershaw, D., Odell, J., Ollason, D., Valtchev, V., Woodland, P. The HTK book – version 2.2, Entropic, 1999.
7. Dunn M. Pro Microsoft Speech Server 2007: Developing Speech Enabled Applications with .NET. ISBN10: 1-59059-902-0. ISBN13: 978-1-59059-902-0, 2007. 275 p.
8. Maskeliunas R., Rudzionis A., Ratkevicius K., Rudzionis V. Investigation of Foreign Languages Models for Lithuanian Speech Recognition. Electronics and Electrical Engineering, No. 3(91), Kaunas, Technologija, 2009. p. 37-42.
9. Maskeliunas R., Rudzionis A., Ratkevicius K., Rudzionis V. User Identification Based on Lithuanian Digits Recognition. Proceedings of IT'2009, Kaunas University of Technology, Kaunas: Technologija, 2009, p. 256-261.
10. Raškinis G., Raškinienė D. Development of Medium-Vocabulary Isolated-Word Lithuanian HMM Speech Recognition System, Informatica, Vilnius: Institute of Mathematics and Informatics, No. 14(1), 2003, p. 75-84.
11. Raškinis A., Raškinis G., Kazlauskienė A., SAMPA (Speech Assessment Methods Phonetic Alphabet) for Encoding Transcriptions of Lithuanian Speech Corpora, Information Technology and Control, Kaunas: Kaunas University of Technology, No. 29(4), 2003, p. 50-56.

AUTOMATION CONTROL FOR SORTING STATION BASED ON IEC 61499 FUNCTION BLOCKS

Georgi POPOV, Kostadin STOYANOV, Grigor STAMBOLOV
Technical University – Sofia, Bulgaria

Abstract: One of the modern approaches, which are used in the last years, is the development of control systems for automation manufacturing systems based on IEC 61499 function blocks. Function blocks (FBs) are defined as IEC 61499 standard for distributed industrial processes, measurement and control systems for PLC control. This paper presents an approach for developing a control system for sorting station based on IEC 61499 function blocks. Function Block Development Kit (FBDK) is the software tool used for the development of the FBs. The developed control system is simulated with FBDK and implemented in sorting station FESTO.

Keywords: IEC 61499, PLC, automation control.

1. Introduction

The development in the field of mechanical processing is strongly associated with the development and application of distributed control systems to achieve high-quality products according to the fast changing demands of users. In order to achieve an automated manufacturing the modern production systems need to have decentralized architecture which includes module based hardware and software enabling distributed control, monitoring and diagnostic of processes in real time and dynamic planning of processes and resources in the system. One of the ways to implement the automated control is the implementation of the international standard IEC 61499, which is based on function blocks for control of programmable logic controllers (PLC). Most of the researches in the field from the last years are presenting many different approaches to solve the problems of this area – some of them are utilizing function blocks, including a multi-agent control using UML [1,2], reconfiguration of real-time distributed systems [3], function block-oriented engineering support systems [4], motion control design in reconfigurable machine tools [5], and implementation of a real-time distributed control model using a Java-based platform [6,7]. This paper is focused on the development of automated control for sorting station FESTO based on the IEC 61499 standard as a first step

of conception for the development of planning structure with reusable IEC 61499 function blocks.

2. Overview of the IEC 61499 standard

The standard defines several basic functional and structural entities. They can be used for specification, modelling and implementation of distributed control applications. Some of them stand for pure software components. Others represent logical abstractions of a mixed software/hardware nature. The main functional entities are function block types, resource types, device types, and applications that are built of function block instances [8].

The standard defines several types of blocks: basic function blocks, service interface function blocks, and composite function blocks. Although the term function block is known from IEC 61131, a function block of IEC 61499 is different from IEC 61131 function blocks. Fig. 1 shows a function block interface. The upper part is often referred to as the “head” and the lower as the

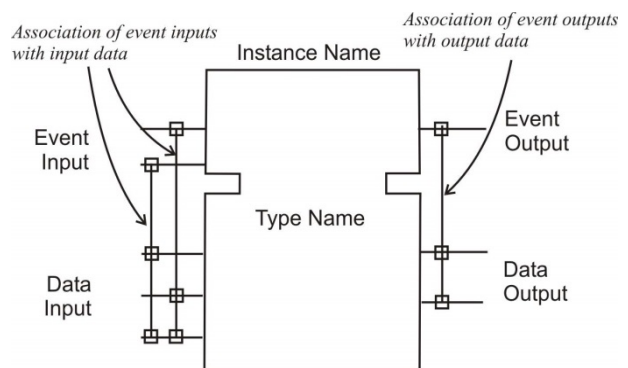


Fig. 1. Function block interface according the IEC 61499 standard [8]

“body” of the function block. A block may have inputs and outputs. There is a clear distinction between data and event input/output signals. Events serve for synchronization and interactions among the execution control mechanisms. In the graphical representation in Fig. 1, the event inputs and outputs are associated with

the head of the function block, and the data inputs and outputs are associated with the body [8].

2.1. Basic Function Blocks

Basic function blocks (BFB) are software structures intended to implement basic functions of distributed control applications.

The standard says that in addition to inputs and outputs, the internal structure of a basic function block may include internal variables, one or more several algorithms and an Execution Control Chart (ECC).

The algorithm represents a piece of software code operating on the common input, output and internal data of the function block.

An ECC (Fig. 2) consists of states with associated actions (designated by ovals) and of state transitions (designated by arrows). The actions contain algorithms to invoke and output events to issue upon the completion of the algorithms' execution [8].

Each state transition is labelled with a BOOLEAN condition that is a logic expression utilizing one or more event input variables, input variables, output variables, or internal variables of the function block.

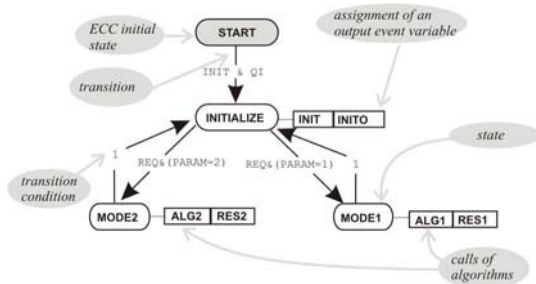


Fig. 2. Execution Control Chart of a basic function block [8]

2.2. Composite Function Blocks

In sharp contrast to the BFBs, the Composite function blocks (CFBs) are defined by a network of interconnected function blocks which are situated in the CFB (Fig. 3).

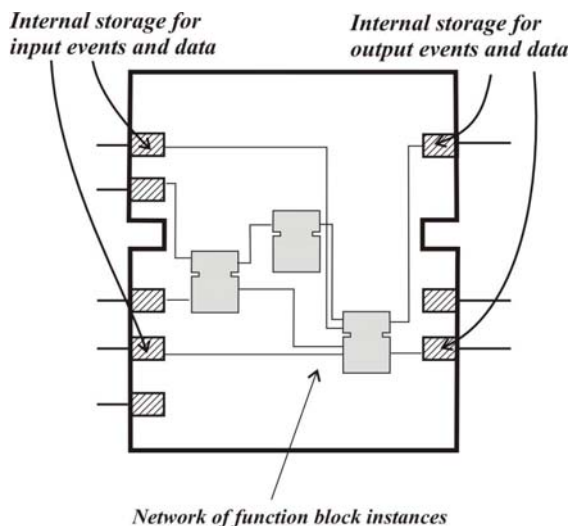


Fig. 3. An example of Composite function block [8]

More precisely, members of the network are instances of function block types which can be either BFBs, or other CFBs. Therefore, hierarchical applications can be built.

It is important to note that CFBs have no internal variables, except for those storing the values of input and output events and data. Thus, the functionality of CFBs completely depends on the state and behaviour of the constituent function blocks and their interconnections by events and data. Along with BFBs, the CFBs are intended to be main instruments of an application developer [9].

2.3. Service Interface Function Blocks

In contrast to BFBs and CFBs, Service Interface Function Blocks (SIFB) are not intended to be developed by an application developer. These have to be provided by vendors of the corresponding equipment, e.g. controllers, field buses, remote input/output modules, intelligent sensors and so on.

To hide the implementation-specific details of the system from the application, the IEC 61499 defines the concept of services the system provides to an application. A service is a functional capability of a resource that is made available to an application. A service is specified by a sequence of service primitives which define properties of the interaction between an application and a resource during the service. The service primitives are specified in a graphical form of the time-sequence diagrams [9].

3. Sorting Station - overview of the station, actuators and sensors

The sorting station FESTO is used for distributing cylindrical objects based on detection by optical and inductive sensors. The received parts are distributed through classification of material (metal) and colour (red and black). The control is performed by a programmable logic controller (PLC) Netmaster which is not a component of the station but has a Java Virtual Machine (JVM) installed on it. The availability of JVM enables the integration of pre-designed function blocks according to the IEC 61499 standard. The station consists of the following modules: sorting conveyor module, slide module, profile plate. Fig. 4 shows the sorting station.



Fig. 4. Sorting station FESTO

On the sorting conveyor module are situated most of the sensors and all of the actuators. Fig. 5 shows these sensors.

The optic sensor (PART_AV) detects if there is a work piece at the beginning of the sorting conveyor module. If there is one the program for distribution of the parts is started and executed in the following sequence: the conveyor DC gear motor is started and the pneumatic stopper is off. Then another optic sensor (B3) identifies the colour of the work piece (red or black). In close proximity there is another inductive sensor (B2) which detects if the passing part is metallic or not.

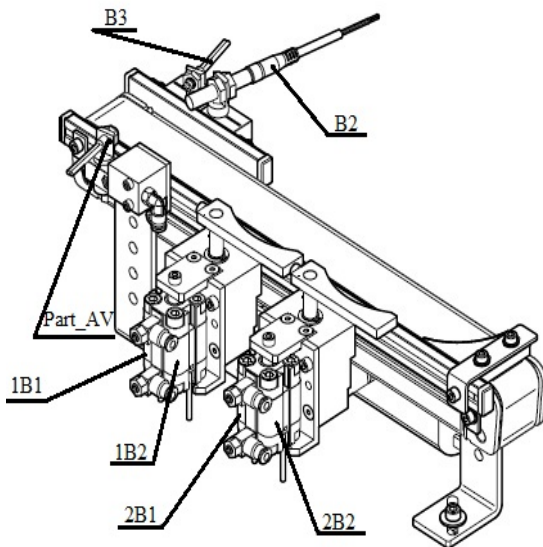


Fig. 5. Sorting conveyor module [10]

Depending from the information that comes from three the sensors the two branches are turned on or off so that the parts are distributed on the right place.

The two branches are switched by the short-stroke cylinders which are attached to them (1B2 is to switch on the first branch and 2B2 is for the second one).

The executed program is stopped when a work piece pass through the retro-reflective sensor (B4) which is not shown on Fig. 5.

4. Development of IEC 61499 function blocks for control of the Sorting station

Distributed control architecture based on the IEC 61499 standard is built on the following key components - application, resource, device and system.

The application is composed by a network of function blocks whose data outputs and inputs and event inputs and outputs are interconnected.

The resource is considered to be a functional unit, contained in a device that has independent control of its operation. It may be created, configured, parameterized, and started up, deleted without affecting other resources within a device. The functions of a resource are to accept data and/or events from the process and/or communication interfaces, process the data and/or events, and to return data and/or events to the process and/or communication interfaces, as specified by the

applications utilizing the resource [8]. Fig. 6 shows a model of a resource.

The device in the IEC 61499 standard is the basic element of a system configuration. The standard provides architectural frames for creating models of devices, including their subdivision in computationally independent resources. A device type is specified by its process interface and communication interfaces. A device can contain zero or more resources and function blocks networks (this option is reserved for the devices having no resources) [8]. Fig. 7 presents a model of a device.

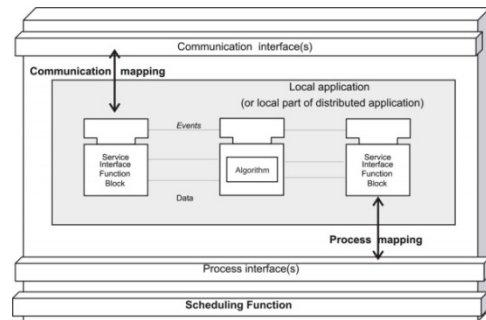


Fig. 6. A model of resource [9]

The system is built by one or more devices. The devices communicate with each other over communication networks. The devices are linked with the controlled process via sensor and actor signals.

When the applications are mapped to the device function blocks are assigned to the resources of the corresponding devices. In this way a system, configuration is formed. A system configuration is viable if each device in it supports the function block types that are mapped on it. Otherwise the system will not run.

An important stage in the development of applications is the configuration of the function blocks. The information flows that pass through the function blocks are divided in into two main types - flows describing the events that occur during the implementation of a production process and flows of information containing data (different technological parameters) needed to implement production processes.

The control of the sorting station in the presented paper is realized by a system configuration which includes a device with two resources and an application which is designed in the free software Function Block Development Kit (FBDK) [11] for the main resource with seven BFBs and two SIFBs.

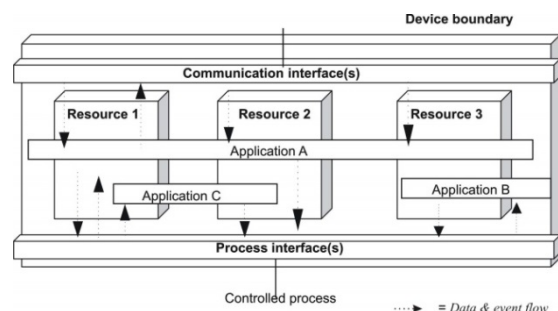


Fig. 7. A model of device [8]

For the same resource was developed another application with Composite function blocks. The application is arranged hierarchically in three levels. To position the work pieces in different order in the three channels were designed another five similar in structure control systems.

4.1. Development of Basic function blocks control system

The sorting station is distributing the work pieces in the following order (Fig. 8): on the first position is sorted the metallic part, on the second position is sorted the red part and on the third position is sorted the black part. Once the system is started it generates an event to the SIFB "Input" from the function block (FB) "E_RESTART" (this block is generated automatically when a new resource is created). After receiving this event the function block "Input" sends it as initiating event (INITO) to the FB "Splitter" and this FB separates the event and generates initiating events (INITO_M, INITO_B1, INITO_B2, INITO_S) to the following blocks: "Motor", "Branch_1", "Branch_2" and "Stopper", for whose this is an input event (INIT). Finally the FBs generate initiating event (INITO) to the FB "Merger", which combines the events (INITO_Motor, INITO_Branch_1, INITO_Branch_2, INITO_Stopper) and generate initiating event (INITO_Output) to the SIFB "Output". Thus, all function blocks are activated.

Receiving a signal from the sensor Part_AV, the service interface function block "Input" generate initiating event (IO_Part_AV) to the block "Splitter", which divides the event and generates output events (Part_AVM and Part_AVS) to the function blocks "Motor" and "Stopper". The function blocks generate output events (Motor_on and Stopper_off) to the service interface function block "Output" to start the DC gear motor and

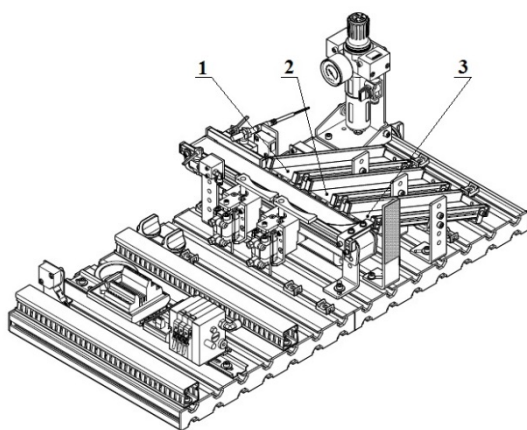


Fig. 8. Positions for distribution of the work pieces

turn off the stopper. The function block Motor is shown on Fig. 9 along with its execution control chart. The interfaces and execution control charts of the other function blocks from which the IEC 61499 control application is consisted are similar and shown in Fig. 10 - 15. The service interface function blocks "Input" and "Output" are presented in Fig. 17 – 18.

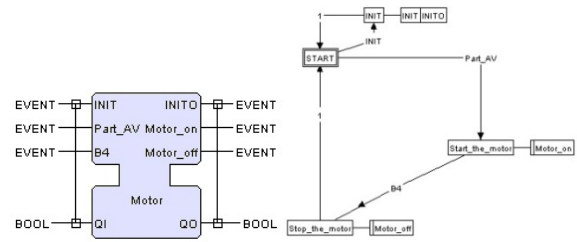


Fig. 9. Interface of the FB Motor and its ECC

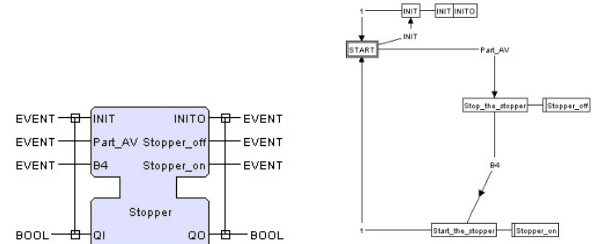


Fig. 10. Interface of the FB Stopper and its ECC

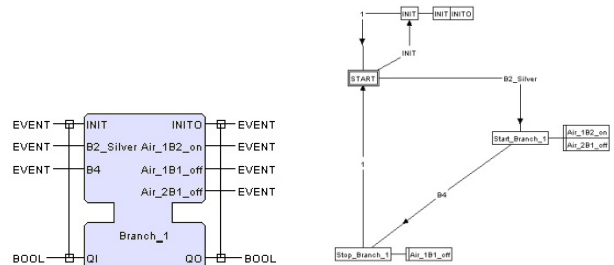


Fig. 11. Interface of the FB Branch 1 and its ECC

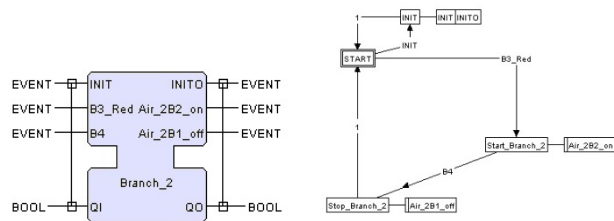


Fig. 12. Interface of the FB Branch 2 and its ECC

Receiving a signal from the sensor B2, the SIFB "Input" generate initiating event (I1_B2_Silver) to the FB "Branch_1", which generates output events (Air_1B2_on and Air_2B1_off) to the SIFB "Output" and the FB "Merge_Air_2B1_off" to turn on branch 1 and turn off branch 2.

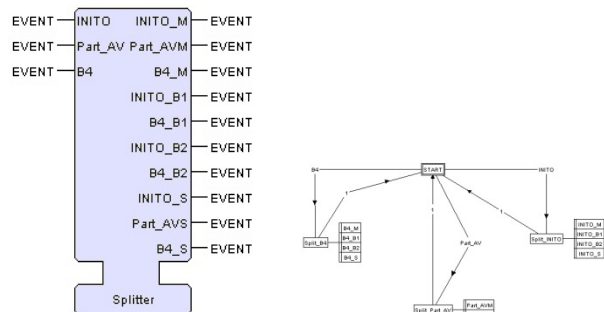


Fig. 13. Interface of the FB Splitter and its ECC

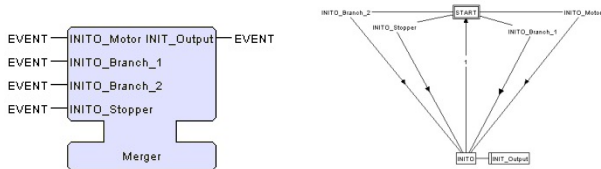


Fig. 14. Interface of the FB Merger and its ECC

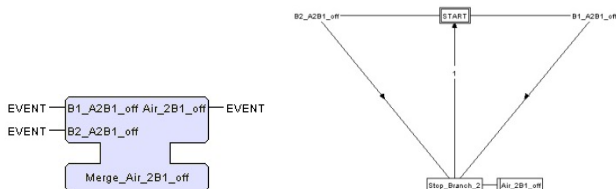


Fig. 15. Interface of the FB Merger Air 2B1 off and its ECC

Receiving a signal from the sensor B3, SIFB "Input" generate initiating event (I2_B3_Red) to the block "Branch_2", which generates initiating event (Air_2B2_on) to the SIFB "Output" to turn on branch 2. Receiving the signal from the sensor B4, SIFB "Input" generate initiating event (I3_B4) to the block "Splitter", which divides the event and generates output events (B4_M, B4_B1, B4_B2 and B4_S) to the FBs "Motor", "Branch_1", "Branch_2" and "Stopper". The FBs generated output events (Motor_off, Air_1B1_off, Air_2B1_off and Stopper_on) to the SIFB "Output" to turn off the DC gear motor, to turn on the stopper and to return to the initial state branch 1 and branch 2 (if some of these were turned on).

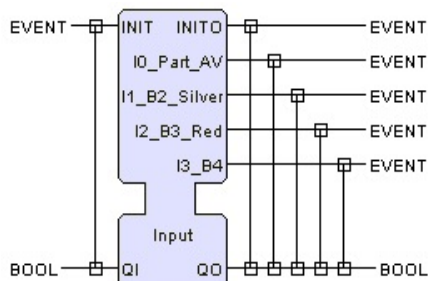


Fig. 16. Interface of the SIFB Input and its ECC

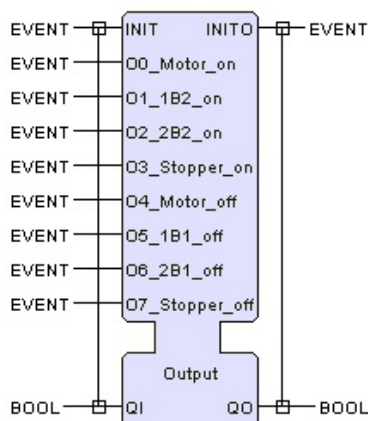


Fig. 17. Interface of the SIFB Output and its ECC

The application of the system is shown on Fig. 18.

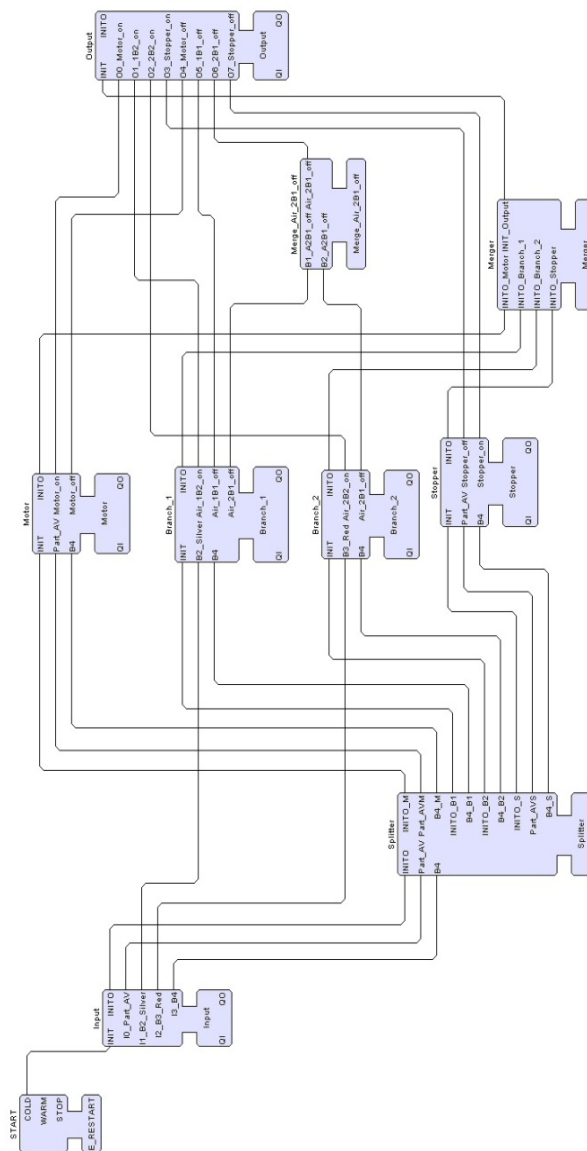


Fig. 18. Application of the IEC 61499 control system

The software environment for the development of function blocks FBDK allows the simulation of the basic functional blocks functions. Each function block of the presented control application is simulated before the implementation on the PLC of the sorting station. The simulation of the basic FB Splitter is shown on Fig. 19. For the other BFBs the simulation framework is similar.

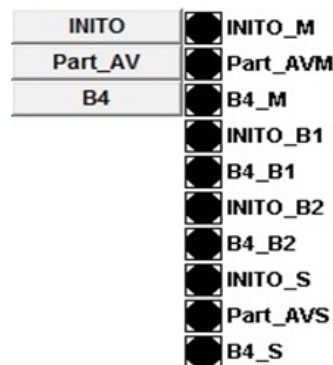


Fig. 19. Simulation frame for FB Splitter

4.2. Implementation of developed IEC 61499 models in control system of sorting station

To bring the sorting station FESTO in operation it is necessary to build a communication network between the different hardware components that are involved in the control system. In order to achieve implementation of the communication network which is of local character the required components are as follow – personal computer (PC), switch, PLC “Netmaster” and sorting station.

The PLC is connected to the PC on which the necessary software for the control of the sorting station is loaded. The availability of JVM in the PLC “Netmaster” enables the integration of pre-designed FB according to the IEC 61499 standard, realized with the help of the development software FBDK.

If there is more than one controlled device and that device is connected to another PLC, for the communication network is required a signal distribution device (Switch), through which it is possible to achieve distributed control. In this case (for the control of only one workstation) it is not necessary to have a switch but, thus increasing the possibilities for operation with more than one workstation with only one PC.

The general appearance of the communication control network for the sorting station FESTO is shown in Fig. 20.

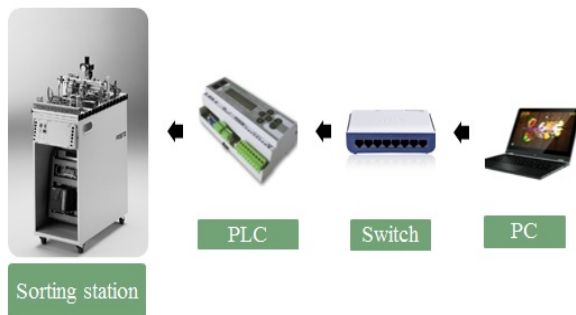


Fig. 20. Communication control network for the sorting station FESTO

5. Acknowledgments

This piece of work was possible to be realized thanks to the purchased material base under the Project WU-TN 208/06.

6. Conclusions

The paper presents an approach for the development of automation control for FESTO sorting station based on IEC 61499 function blocks. The main benefits of the proposed approach may be summarized as follows:

- There are realized six fully developed systems for automation control for the sorting station based on the IEC 61499 function blocks standard. The developed control systems are covering all possible scenarios for the distribution of the three work pieces (red, silver and black);

- The developed control system is simulated on low (application) and high (system) level;
- The developed models of the basic function blocks (thirty-six) are structured in library and can be used for the realization of each sorting scenario for the FESTO station;
- For the implementation of the developed IEC 61499 models a Java based PLC Netmaster is used;
- The developed control system for sorting station can be used like a part of every distribution control system, based on the IEC 61499 standard.

7. References

1. Antonova I., Batchkova I., Development of Multi-Agent Control Systems using UML/SysML, book capter, pp.67-90, InTech, ISBN: 978-953-307-174-9, 2010.
2. Antonova I., Application of UML and SysML for Modeling of IEC-61499 based Control Systems, Proceeding of the International Conference „Automatics and Informatics”, Sofia, pp. III-13 – III-16, 2009.
3. Karamishev H., IEC 61499 Based Control of Feed Motions in Machine Tools, International Conference “Automatics and Informatics”, Sofia, pp. III-427 – III-430, 2010.
4. Brennan R.W., Zhang X., Xu Y., Norrie D.H., A reconfigurable concurrent function block model and its implementation in real-time Java, Integrated Computed –Aided Engineering, Vol. 9, pp. 263-279, 2002.
5. Thramboulidis K., Tranoris C, An architecture for the development of function block-oriented engineering support systems, IEEE International Conference on Computational Intelligence in Robotics and Automation, pp.536-542, Canada, 2001.
6. Strasser T., Auinger F., Zoitl A., Development, implementation and use of an IEC 61499 function block library for embedded close loop control, The Second IEEE International Conference on Industrial Informatics, pp. 594-599, 2004.
7. Hussain T., Frey G., Developing IEC 61499 compliant distributed systems with network-enabled controllers, Proceedings of the 2004 IEEE Conference on Robotics, pp. 613-618, 2004.
8. Hanisch H.-M., Vyatkin V. Achieving Reconfigurability of Automation Systems by Using the New International Standard IEC 61499: A Developer’s View, In: Richard Zurawski(ed.), The Industrial Information Technology Handbook., USA, CRC Press, p.661-680, 2005.
9. Vyatkin, V., IEC 61499 Function Blocks for Embedded and Distributed Control Systems Design, 297 pp., Instrumentation Society of America, USA, October, 2011 – Second Edition.
10. FESTO Sorting station Manual.
11. Holobloc Inc., Function Block Development Kit (FBDK), <http://www.holobloc.org>.

DEVELOPMENT OF RECONFIGURABLE CONTROL SYSTEM FOR MILLING MACHINES BASED ON IEC 61499 REUSABLE FUNCTION BLOCKS

Grigor STAMBOLOV
Technical University – Sofia, Bulgaria

Abstract: Production methods and systems currently used can't satisfy the new market demands, which is leading to the development of new concepts such as agile production, reconfigurable manufacturing systems etc. The reconfiguration provides the ability to add, remove and modify specific work processes as control units, software and machine structures. One of the most important tasks in the design of reconfigurable manufacturing systems (RMSs) is the achievement of reconfigurable control systems integrated in different functions as control, diagnostic and planning. This paper presents an approach for development of reconfigurable control system for milling machines based on IEC 61499 standard.

Keywords: Reconfigurable Manufacturing Systems (RMS), control, IEC 61499 Function Blocks.

1. Introduction

The advances in the field of mechanical processing are highly connected with the development and application of reconfigurable distributed motion control systems supporting the achievement of high product quality and rapidly response to the customer needs. The main features of mechanical processing systems may be summarized as follows: they are composed of a large number of tools, their working positions and velocities are digitally controlled; for separated technological operations only part of the available tools is used; the reconfiguration processes concern not only the software, but the hardware parts too (changes of tools, fixing of mechanical parts etc.); the reconfiguration itself is performed during time periods of varying length (from hours to days and weeks) etc. The RMSs have an open structure that makes possible the integration of new technologies and the modification of the systems for a new type of manufacture on the basis of adding, removing or updating of elements and units in their structure. The manufacturing processes involved in an RMSs are very complicated, including a large variety of products with their geometry and features. The RMSs must be responsive to unpredictable (infernal and

eternal) changes of production capacity and functionality with goal to realize both the flexibility and dynamism of shop floor operations. For realization of automation processes the RMS requires a decentralized system architecture, building of reconfigurable hardware (developing of module principles) and software, including distributed control with real-time monitoring and diagnostic, distributed process planning and dynamic resource scheduling. One of the way for realization of control architecture of RMS is used a concept of international standard IEC 61499, which developed distributed control structure on the base of function blocks.

The main goal of this paper is to develop a framework for control of milling reconfigurable machines using IEC 61499 function blocks and its implementation on the distributed control system of RMS..

2. Requirements for reconfigurable machine tools

During the design of the production parts, there are several phases that are carried in the following sequence:

- Design of the parts;
- Planning of the technological process;
- Design of production system;
- Process management.

In the all these phases are using computers, which make the process quick and easy for designing. As a result, there are many software packages available service, which is perform processes such as computer aided design (CAD), process planning, automated manufacturing (CAM) and others.

RMS required dynamic configuration, where each of the components that make up the system has its own characteristics, which determine the overall cost, quality and reliability of the system.

The modular principle of construction and dynamic structure of the RMS consider the design of its components as a highly complex task. In conventional design of specific machines and machine tools, their features are optimized based on unique and strictly defined architecture.

The modular principle of machine tools was designed for processing subsystems (mechanical units), for components of the translation (use when moving the axes of the machine, for replacing the components of the transport system) and to support specific configuration. One of the main advantages of modular design [1] is the ability to reuse the modules. Single modules of the modular production system, that not used anymore, can be removed and integrated into other production systems, reducing investments for new equipment.

One of the key factors involved in evaluating the quality of a product is the accuracy machining. To achieve a high accuracy of manufacturing operations, it is necessary to correlate the data for the process measured in real time by sensors, positioned in the work area with predefined characteristics of the production process that are stored in a database. Thereby aims to prevent production accidents that may lead to suspension of the machine and to the quality of manufactured parts. Sensor data measured in real time can be used to evaluate:

- Errors dimensional (geometric accuracy);
- Quality of the processed surface;
- Thermal deformation during the process;
- Geometric deformation of the machine and workpiece;
- Vibrations;
- Cutting forces etc.

Regardless of the type of process in modern machine tools with intelligent control, there is a set of key components to be checked by the system and that is divided into data processing, consisting of

- Sensor system for collecting data;
- Program for processing signals received from the sensor system;
- Program data analysis and classification of the results.

An essential part of the reconfigurable machine tool (RMT) is software, whereby tasks is performed at different levels, such as: control, monitoring and communication of mechanical, electrical and electronic nodes (low-level), as well as tasks at a higher level such as planning and control of the technological processes, user interfaces, collection and generalization of data from the processes, etc. Therefore the structure and functionality of the communication and control software are exceptionally important and directly affect to the work quality of the whole processing system.

3. Reconfigurable machine tools control with IEC 61499 function blocks

The core of cutting processes control in RMT are the motion control systems, which are highly incompatible in respect to their engineering, implementation and reusability. With the advent of machines program control and their further development (CNC machine tools) leads to a radical transformation of existing production. CNC machine tools allow for increasing the quality of products and reduce their cost. CNC machines are equipped with their own control

systems so that users can not access the controller and further modification of the system is either impossible or too long [2, 3]. This type of management is not able to guarantee the basic characteristics of RMS. To achieve this, the system controls to be an open architecture, ie to allow continuous modification. The current commercially available controllers offer very limited users access options for modification and reprogramming (e.g. controllers for motion control of axes) as a fixed control structure (e.g. traditional PID-controllers).

The standardization process initiated from the worldwide association PLCopen aims to reduce these negative factors through supporting the development of reusable, scalable and hardware independent motion control applications based on IEC61131-3 standard [4] and defining function block library for motion control [5]. The main drawback in using the proposed library but is that it can not be used for design of reconfigurable and distributed motion control application.

The analysis of the function block library developed by the organization shows that it is a powerful tool in the development of control system for the variety of cutting operations (drilling, reaming, core drilling etc.). The main problem is but their usage for designing of distributed control systems, which more fully reply to the requirements for dynamical reconfigurability of the control system. The architecture of such control projects is underlined in the IEC61499 that is the new standard supporting the development of distributed process measurements and control systems through proposed set of reference models and reference architecture based on the Function Block (FB) concept and that can be seen as a logical continuation of the IEC61131 standard [6].

IEC 61499 standard defines the basic concepts, models and reference architecture for design of modular, reusable, open and vendor independent distributed control applications, characterized through the three main features: interoperability, portability and configurability. This standard uses the function block concept as a main building block of a control system, represented at the different level of integration – device, resource and application. One of the most widely used tool for development of IEC61499 based FB and applications is the Function Block Development Kit (FBDK) of Rockwell Automation, consisting of two basic parts: FB Editor as a development environment and FBRT as a run time platform [7].

In each machine tool the cutting process is realized in one or more transitions characterized by two different motions:

- Primary motion – it is characterized with two components – velocity and direction (primary and reverse turning motion);
- Feed motion – characterized again with two components – velocity, fast and cutting feed motion, and direction (primary and reverse straightforward motion). The feed motion can be realized for one or more axis – it's depends on the type of technological operation.

IEC 61499 Standard defines the basic concepts, models and reference architecture for design of modular, reusable, open and vendor independent distributed control

applications, characterized through the three main features: interoperability, portability and configurability. This standard uses the function block concept as a main building block of a control system, represented at the different level of integration – device, resource and application.

The basic elements for realization of functional block concept are Basic Function Block (BFB), Composite Function Block (CFB) and Service Interface Function Block (SIFB). An application model is a network of FBs and may be executed by one or more devices, including one or more resources. On the base of these building components are developing different applications, resources and devices, which consists in the control system of the manufacturing station. The basic function block is presented by an input and an output interface composed of input and output events and data. The internal view of a basic function block includes an Execution Control Chart (ECC), internal data and internal algorithms. The ECC is a state machine used to control the execution of algorithms associated to the function block. A function block is characterized by its type name and instance name, which are used to identify a function block, the event and data inputs and outputs are required for the interconnection of different function blocks to function block systems, while the ECC, internal data and internal algorithm describe the internal behaviour of the function block.

The kernel of the function block is its Execution Control Chart. An ECC consist of states, transitions and actions, which invokes the execution of the algorithms, which are associated to the ECC states, in response to event inputs. One of the states is initial state and other execution control states may have one or more execution control actions associated. Each execution control actions may have one algorithm or one output event associated. The evaluation of the ECC state machine from an execution control state to other is realized by the execution control transitions. In general the ECC is the relationships between events and algorithm executions, which are specified by the special kind of even-driven state machines.

The main cutting processes for reconfigurable milling station are milling operations (slab milling, face milling, end milling, form milling, slot milling, slitting and contour milling) and drilling operations (drilling, core drilling, reaming, thread cutting and boring with boring bar). The implementation of one or another process or all of them in some sequence depends on the requirements of accuracy and surface roughness of processed surfaces. The cutting operations are executed on milling, drilling and drilling-boring tools, but lathes and aggregate machining tools also may be used.

The considered milling reconfigurable workstation consists of the following basic axes – one for primary motion (in this case vertical milling cutting head by Z axe) and three for feed motions – by X, Y and Z axes. The motion by each of these axes is realized from separate motor (Fig.1)

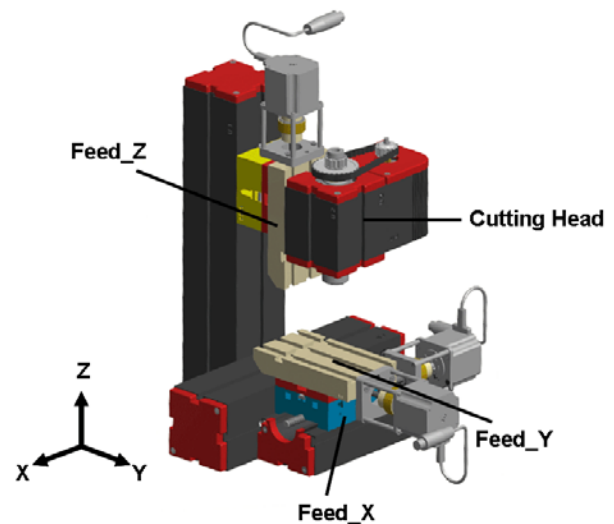


Fig. 1. Reconfigurable milling workstation (RMW) with three axes (X, Y, Z) and vertical cutting head

The combination of different cutting processes (milling, drilling and etc.) puts special requirements towards the processing parts, the additions and properties of billets, the methods for grounding, fixing and tightening of cutting processes parts and special attention towards the differentiation of technological operations and the sequence of their execution. The workstation allows the performance of different cutting operations which are built concerning the specific requirements and technological specifications. The technology of cutting processes requires different precedence and obligatory constraints.

For designing of control system with IEC 61499 function blocks the first step is to develop in software package FBDK system model (Fig. 2)

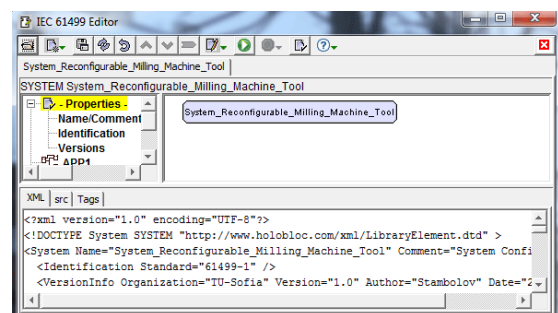


Fig. 2. IEC 61499 system model of RMW with three axes

The next step is to build the models of devices, which consists in the control system – in this case that will be one device for primary motion and three devices for feed motions (by one device for each of the translation axes – X, Y and Z). The device level is shown in Fig. 3. Every device from the control system consist one resource with one application with several functional blocks.

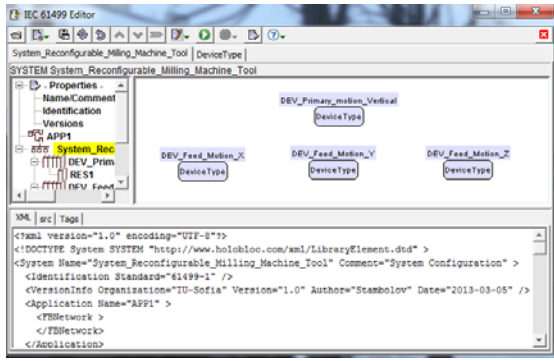


Fig. 3. IEC 61499 device model of RMW with three axes

Conditionally applications can be divided into two main types – the primary and the feed motions. The internal network of the primary motion consists of instances of the following basic function blocks: “Primary_Motion_Z_Vertical” (Fig. 4) and “E_Ton” (Fig. 5). The basic FB “Primary_Motion_Z_Vertical” performs the primary spindle motion by technologically determined revolution. FB “E_Ton” is use in the case when is need reverse of the direction of the motion. When “E_Ton” is started the primary motor is stopped. After 500 ms, the primary motor is reversed by direction and is turned on.

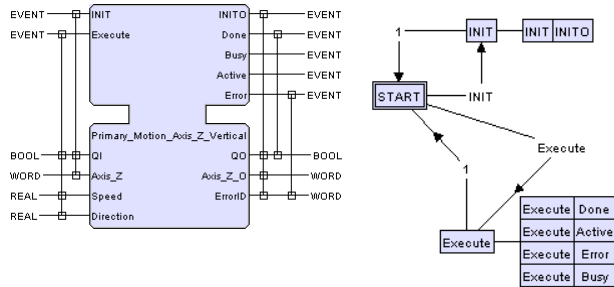


Fig. 4. Basic FB for primary motion with ECC

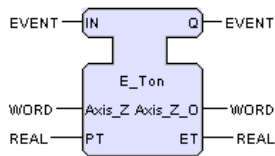


Fig. 5. Basic FB for primary and feed motions

The application in resource level for primary motion is shown in the Fig. 6.

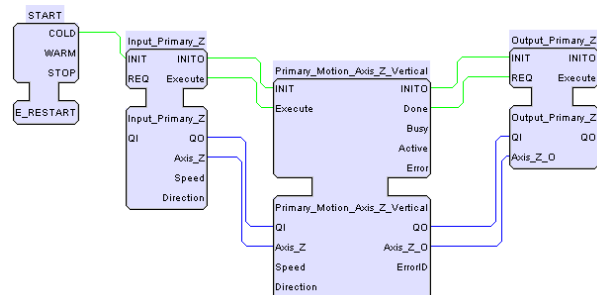


Fig. 6. The IEC 61499 application for primary motion

The IEC 61499 application for primary motion include basic FB “Start” (generating on application in FBDK), FB “Primary_Motion_Axis_Z_Vertical” and two Service Interface Function Blocks – “Input_Primary_Z” and “Output_Primary_Z” (Fig. 7).

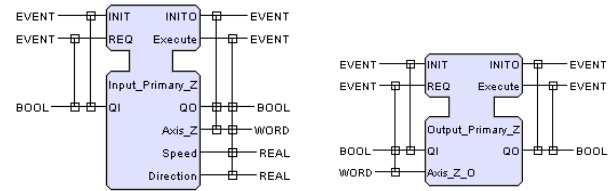


Fig. 7. SIFB for primary motion – “Input_Primary_Z” and “Output_Primary_Z”

When is need reverse of the primary motion (for example when is realize technological operation thread cutting) is necessary to add FB “E_Ton” and second FB “Primary_Motion_Axis_Z_Vertical” (Fig. 8)

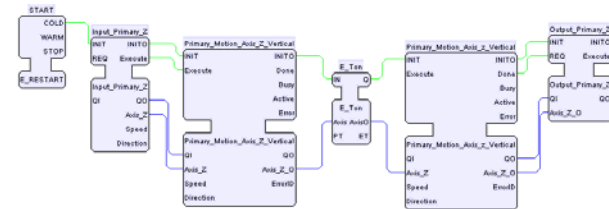


Fig. 8. The IEC 61499 application for primary motion with reverse

The internal network of the feed motion is separate for each axis and consists of instances of the following basic function blocks:

- “Feed_Motion_X_Absolute” (Fig. 9), “Feed_Motion_X_Relative” (Fig. 10) and “E_Ton” (Fig. 5);
- “Feed_Motion_Y_Absolute”, “Feed_Motion_Y_Relative” and “E_Ton”;
- “Feed_Motion_Z_Absolute”, “Feed_Motion_Z_Relative” and “E_Ton”.

The FB “Feed_Motion_X_Absolute” is using when the cutting instrument going from start point of the workstation to point, when will be start cutting operation.

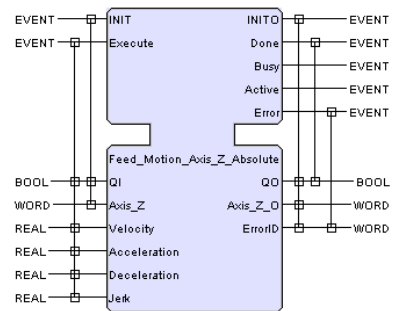


Fig. 9. Basic FB for feed motion in axis Z (fast motion)

The FB “Feed_Motion_X_Relative” (Fig. 10) is using when the cutting tool starting the cutting operation (from point to point).

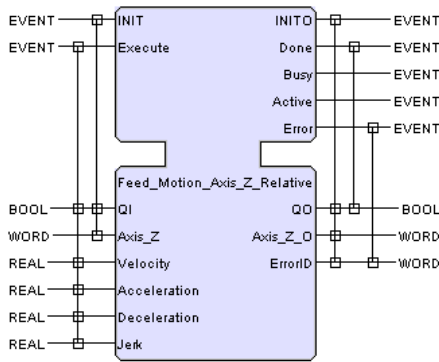


Fig. 10. Basic FB for feed motion in axis Z (cutting motion)

To reverse the direction of feed motion again is using the FB “E_Ton”. For example, when is realizing reaming operation (for this workstation will be used primary motion by axis Z and feed motion by axis Z), the IEC 61499 application for feed motion will be build like a sequence of the next FBs - “Feed Motion Z Absolute”, “Feed Motion Z Relative”, “E Ton”, “Feed Motion Z Relative” and “Feed Motion Z Absolute”. In the Fig. 11 is shown the technological scheme of reaming operation, as long as in Fig. 12 is present the application for feed motion of this operation.

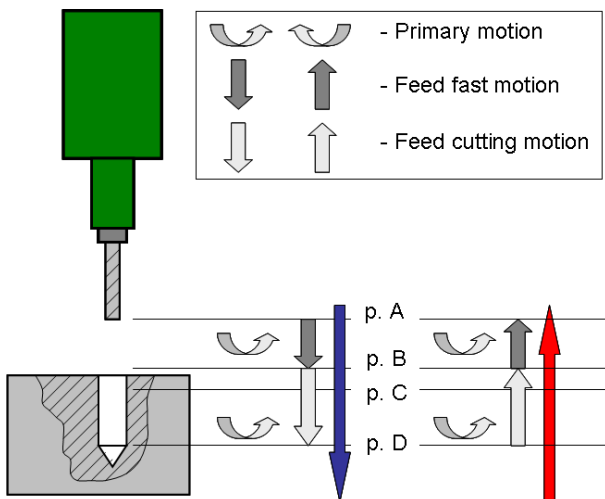


Fig. 11. Technological scheme of reaming

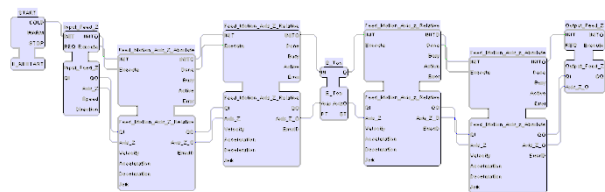


Fig. 12. The IEC 61499 application for feed motion of reaming

For other axes (X and Y) the function blocks such as similar instances, when the difference is in the use of various technological data processed by control algorithms in the body of the function block.

For the processing of complex shapes by milling is necessary to realized coordination of feed motions in the three axes. The trajectory of the tool is performed by setting points in the coordinate system (X, Y, Z), and

for this purpose the application of FBs are designed in the required sequence.

4. Reconfiguration of the control system for milling and drilling technological operations

The cutting sequence is determined through solving of optimal scheduling task by previously defined precedence and technological constraints. The workstation with vertical milling head, shown in Fig.1, performs four motions – one primary motion and three feed motion (by X, Y and Z axes). In the case of changes due to internal or external disturbances, the presented workstation must adapt to the new requirements through reconfiguration on hardware and/or software levels.

The hardware reconfiguration is realized through adding, modifying or removing of axis in the workstation configuration. The workstation components are designed on modular principle, which allows the accomplishment of modifications at machine level. Hardware reconfiguration through adding axes (A and C) is presented on Fig. 13. The new configuration has additional axes whose control should be added to the control system of workstation.

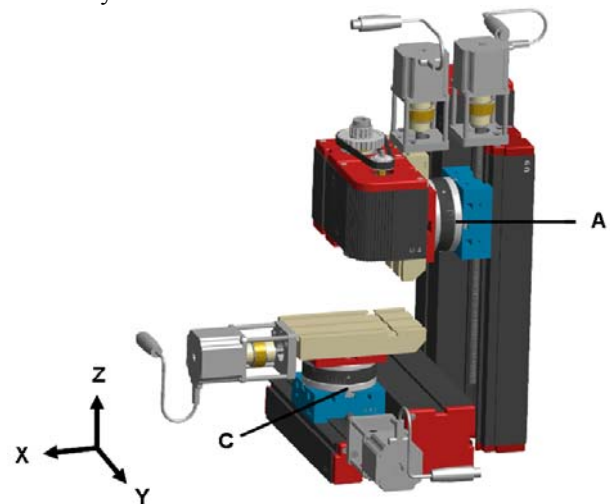


Fig. 13. Reconfigurable milling workstation with five axes (X, Y, Z, A, C) and vertical cutting head

This configuration (Fig. 13) of the workstation provides one primary and five feed motion (three translation and two rotary motions). The control of “new” axes should be “added” to IEC-61499 based control model of the workstation. It can be realized at the application level, when a new resources, for the additional feed motions are inserted to the control model. From the structural point of view, the added feed motion models consists of similar basic function blocks as the existing one Feed Motion Absolute”, “Feed Motion Relative”, and “E Ton”), but with different technological parameters for the required cutting operation. Inserted FBs at the application level changes the IEC-61499 based control model at the device level of considered workstation too – added new two devices (“DEV Feed Motion A” and “DEV Feed Motion C”). The hardware reconfiguration will be change the vertical spindle with horizontal, but for control system this change would not lead to

significant changes. In the same way the motion on one or more axis may be removed and the reconfiguration of control system will be expressed in removing the corresponding IEC-61499 based FBs for the removed feed motion. And again alterations of control structure on the application and device level are needed. So, the distributed control structure facilitates the reconfigurability of the system through inserting, deleting and replacing IEC-61499 based functional components. Another case of control system reconfiguration is when only changing the type of processing part, without changes in the axes. In this situation reconfiguration will be realized through adding, and deleting of FBs, or change the sequence of execution of control algorithms. Generally, the developed FBs can be structured in library and reused for different technological operations. For designing of control system for each configuration of machine tool can use the next FBs (Table 1).

Table 1. Library of reusable basic function blocks

IEC 61499 control motion basic FBs		
Cutting operation	Primary Motion	Feed Motion
Milling Operations		
Slab Milling, Face Milling, End Milling, Form Milling, Slotting, Slitting, Contour Milling	Primary Motion Axis Z	Feed Motion X Absolute, Feed Motion X Relative, Feed Motion Y Absolute, Feed Motion Y Relative, Feed Motion Z Absolute, Feed Motion Z Relative, Feed Motion A Absolute, Feed Motion A Relative, Feed Motion C Absolute, Feed Motion C Relative, E Ton
Drilling Operations		
Drilling, Core Drilling, Reaming, Boring, Thread Cutting	Primary Motion Axis Z, E Ton	Feed Motion Z Absolute, Feed Motion Z Relative, E Ton

In the presented reconfigurable milling machine tool can be added not only feed motion axes but also second spindle. In this case to the library of IEC control basic motion FBs will be added new instances of basic FB – Primary Motion Axis (X or Y) and to the system level –

new device, which will be analogical like structure of the device of primary motion by axis Z.

5. Conclusions

The paper briefly introduces the concept for reconfiguration of the milling machine tools with reusable function blocks on the base of IEC-61499 standard. The reconfiguration is presented like a function of the consumer requirements change and can be realized in the hardware level – adding and removing of the axes of motion and in the software level – changing or modifying the control functions and algorithms. The main benefits of the proposed approach may be summarized as follows:

- The proposed approach supports the reusability of developed motion control models for milling and drilling cutting operations in the reconfigurable milling machine tool through the applied IEC61499 based reusable models;
- The presented distributed control system is designed from devices for each motion axis, resources and applications;
- For realizing the control functions of the milling and drilling operations are developed library of basic function blocks for primary and feed motions.

6. References

1. Toenshoff, H. K., Schnuelle A. - High Productive And Reconfigurable Manufacturing Systems (HIRARMS), Institute for Production Engineering and Machine Tools (IFW), University of Hanover, 2001.
2. Gopalakrishnan V., Fedewa D., Mehrabi M.G., Kota S., Orlandea N., "Parallel Structures and their applications in reconfigurable machining systems", J. of Manufacturing Science and Engineering, May, Vol.124, pp.483., 2002.
3. Park E., D. M. Tilbury, P. P. Khargonekar, "A Modeling and Analysis Methodology for Modular Logic Controllers of Machining Systems with Auto, Hand and Manual Modes", Proceedings of the American Control Conference, Chicago, 2000, pp. 3158-3164.
4. IEC65B/WG7/TF3, IEC61131-3, Programmable controllers – programming languages, 1998.
5. PLCopen TC2, Function Blocks for Motion Control, 2005. <http://www.plcopen.org/forms/motioncontrol.htm>.
6. IEC TC65/WG6, International Standard IEC61499, Function Blocks, Part 1 - Part 4, International Electrotechnical Commission (IEC), IEC Press, January, 2005.
7. Holobloc Inc., Function Block Development Kit (FBDK), <http://www.holobloc.org>.

HEXAPOD WALKING ROBOT ENERGY CONSUMPTION DEPENDENCE ON THE NUMBER OF LEGS SET ON THE SURFACE

Mindaugas LUNECKAS, Tomas LUNECKAS, Dainius UDRIS
Automation Department, Electronics Faculty, Vilnius Gediminas Technical University, Vilnius, Lithuania

Abstract: Energy consumption is one of the biggest issues for walking robots. Due to the problem in selecting gaits for different tasks, the calculation of power consumption becomes important. Energy consumption dependence on the number of legs set on the surface of a hexapod walking robot is investigated in this paper. Cases with six, three and zero legs set on the surface are evaluated. Experiments were carried out only on even terrain. In addition, the force distribution between feet of a hexapod robot is taken into account. Results clearly show that the energy consumption of a walking robot increases as the number of legs set on the surface decreases. The paper also discusses possible energy consumption of different gaits, future plans and experiments.

Keywords: hexapod robot, energy consumption, foot force distribution, legged locomotion.

1. Introduction

Autonomous walking robots are far more superior to those of wheeled machines due to the ability to overcome very rough terrain [1]. Hexapod type robots, as compared to those with fewer legs, have the advantage of walking, when one or two legs brake or stop functioning [2]. They are considered being one of the most stable and flexible. Also, hexapod robots offer a great number of different gaits and require the least complex control methods [3]. However, legged locomotion has a disadvantage of having to carry its own frame and driving parts which indicates poor energy efficiency [2]. Therefore, a great number of various hexapod robots have been created and a series of different experiments carried out to test legged locomotion and power consumption in various tasks. While having the problems like leg movement and planning [4], robot navigation [5] or surface analysis [6, 7] solved with various methods, energy consumption of walking robots remain of much bigger complexity. The problems arise from attempts to simulate real biological organisms. As paper [8] suggests, animals tend to

evolve the best possible structures and behaviours, which means that robotic machines should be programmed to act the same. In addition to simulation problems, there is also a great number of possible tests. Changing different parameters require a completely new observation of energy consumption.

In paper [2], only a power consumption dependence on different gaits while robot is turning is observed. Mainly, because observing power consumption of straight motion is quite unnecessary. Experimental results showed that hexapod robot uses least power when moving by wave gait. Higher movement speeds and gaits with a smaller number of supporting legs require higher power consumption.

Another method used to lower energy consumption of a hexapod is to observe torque changes of each joint while robot is moving. This method is discussed in paper [3]. The main goal of this method is to calculate torques for each leg correctly, so when moving, energy consumption is the lowest. Unfortunately, hexapod model used during experiment had no similarities to any of the real animals or insects, and comparing to some of quadruped or biped machines, energy consumption is still far away from any real numbers.

2. Problem formulation

As mentioned before, energy consumption remains of great importance for six-legged locomotion. Still a great number of experiments have to be carried out before hexapod robots can finally be used in various tasks, such as planetary exploration [9], underground mining and deactivation of bombs [3], moving through catastrophic and hazardous environments [10] or carrying cargo [11].

Despite the fact that some experiments mentioned in section 1 showed great results, none of them particularly tested energy consumption dependence on the number of legs set on the surface while hexapod machine is not moving. The problem is in difficulty to understand energy consumption dynamics without having the information about the static characteristics.

The static characteristics of hexapod robots energy consumption are investigated in this paper. First, the force distribution between feet is calculated to understand the possible outcome. It is widely discussed in section 3. In order to see whether energy consumption dependence on the number of legs set on the surface and different force distribution cases are proportional, experiments are made.

3. Force distribution

Calculating force distribution between all hexapod robots feet is very important. Knowing the forces in each leg in different robot states would help understand the possible results of experiment.

Force distribution for three different cases is calculated. Each case differs from other by the number of legs set on the surface. In first case, force distribution for six legs set on the surface is calculated. In second case, force distribution for three legs set on the surface is calculated. In third case – force distribution for none legs set on the surface is calculated.

The first and the third cases are similar because force between feet is distributed equally. The second case is a bit more complex than the other two due to the different force distribution on the left and the right sides.

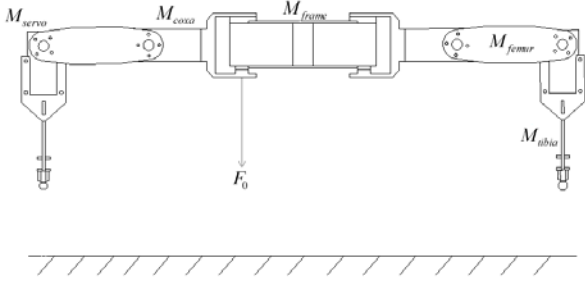


Fig. 1. Hexapod robot model with no legs set on the surface

Having no legs set on the surface, makes it easy to calculate force for each individual actuator, because each of them has to carry the weight of only the lower part of the leg. Having that said, we only need to calculate force for one leg, or more precisely, one servo actuator (Fig. 1). With that in mind, normal force F_0 for one actuator, while no legs are set on the surface, can be calculated by:

$$F_0 = M_{femur} + M_{tibia} + M_{servo}; \quad (1)$$

where M_{femur} and M_{tibia} – weight of the femur and tibia parts of the leg as shown in Fig. 1.

Hexapod robot model, while all six legs are positioned on the surface, is shown in Fig. 2.

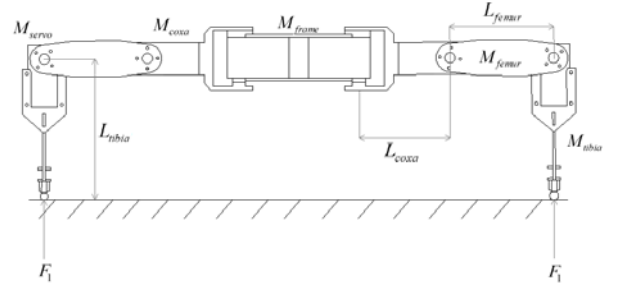


Fig. 2. Hexapod robot model with six legs set on the surface

In this case, all six legs have to carry the weight of the robot, which includes the weight of the robots main body M_{frame} , weight of all actuators M_{servo} , weight of the battery $M_{battery}$, and the weight of all legs. Also, as mentioned before, force is equal for each foot, so, the normal force F_1 can now be found by:

$$F_1 = \frac{M_{frame} + 18 \cdot M_{servo} + M_{battery}}{6} + (M_{coxa} + M_{femur} + M_{tibia}) \quad (2)$$

Now, in the last case, comparing to the second, only three legs are supporting all the weight: two on the right side and one on the left. As it is known, weight between the two sides is not distributed equally, which states that force between all supporting legs is also not the same. However, force between two feet on the right side is said to be equal. With that in mind, force distribution between three feet can be found by:

$$F_2 + 2 \cdot F_3 = M_{frame} + 18 \cdot M_{servo} + M_{battery} + 6 \cdot (M_{coxa} + M_{femur} + M_{tibia}) \quad (3)$$

The value of the normal force F_3 can be found by doing a torque balance about F_2 :

$$\begin{aligned} \sum T_{LeftFoot} = & -M_{servo} \cdot L_{tibia} \cdot \cos \theta_1 - \\ & -2 \cdot M_{servo} \cdot (L_{tibia} \cdot \cos \theta_1 + L_{femur} \cdot \cos \theta_2) - \\ & -M_1 (L_{tibia} \cdot \cos \theta_1 + L_{femur} \cdot \cos \theta_2 + L_{coxa}) - \\ & -2 \cdot M_{servo} \cdot (L_{tibia} \cdot \cos \theta_1 + L_{femur} \cdot \cos \theta_2 + 2 \cdot L_{coxa}) - \\ & -2 \cdot M_{servo} \cdot (L_{tibia} \cdot \cos \theta_1 + 2 \cdot L_{femur} \cdot \cos \theta_2 + 2 \cdot L_{coxa}) + \\ & + 2 \cdot F_3 (2 \cdot L_{tibia} \cdot \cos \theta_1 + 2 \cdot L_{femur} \cdot \cos \theta_2 + 2 \cdot L_{coxa}), \end{aligned} \quad (4)$$

where L_{tibia} , L_{femur} , L_{coxa} – lengths of the parts of the leg as shown in Fig. 3.

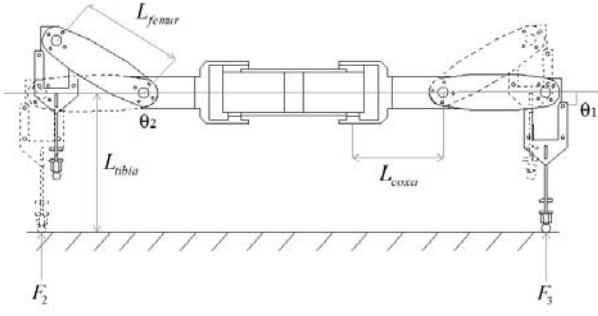


Fig. 3. Hexapod robot model with three legs set on the surface

By determining the angles from Fig. 3, it is possible to simplify equation (4). The angle values are $\theta_1 = 90^\circ$ and $\theta_2 = 0^\circ$, so the final expression is:

$$\begin{aligned} \sum T_{LeftFoot} = & -2 \cdot M_{servo} \cdot L_{femur} \cdot \cos \theta_2 - \\ & -M_1 \cdot (L_{femur} + L_{coxa}) - \\ & -2 \cdot M_{servo} \cdot (L_{femur} + 2 \cdot L_{coxa}) - \\ & -4 \cdot M_{servo} \cdot (L_{femur} + L_{coxa}) + \\ & +2 \cdot F_3 \cdot (L_{femur} + L_{coxa}) \end{aligned} \quad (5)$$

where

$$\begin{aligned} M_1 = & M_{frame} + 18 \cdot M_{servo} + M_{battery} \\ & +6 \cdot (M_{coxa} + M_{femur} + M_{tibia}) \end{aligned} \quad (6)$$

Although long, the equation (5) uses only known variables, and since the combined torque about the left foot is zero, this equation allows solving it for F_3 :

$$\begin{aligned} F_3 = & \frac{2 \cdot M_{servo} \cdot L_{femur} + M_1 \cdot (L_{femur} + L_{coxa})}{4 \cdot (L_{femur} + L_{coxa})} + \\ & + \frac{M_{servo} \cdot (L_{femur} + 2 \cdot L_{coxa})}{2 \cdot (L_{femur} + L_{coxa})} + M_{servo}. \end{aligned} \quad (7)$$

This value is inserted into the equation (3), to solve for F_2 :

$$F_2 = M_1 - 2 \cdot F_3. \quad (8)$$

4. Experimental results

In this experiment a model of a hexapod walking robot with such parameters was used:

$$\begin{aligned} M_{frame} = & 0.06 \text{ kg}; M_{battery} = 0.092 \text{ kg}; M_{servo} = 0.055 \text{ kg}; \\ M_{tibia} = & 0.01 \text{ kg}; M_{femur} = 0.012 \text{ kg}; M_{coxa} = 0.012 \text{ kg}; \quad (9) \\ L_{tibia} = & 0.105 \text{ m}; L_{femur} = 0.08 \text{ m}; L_{coxa} = 0.068 \text{ m}. \end{aligned}$$

Using (1), (2), (7) and (8), the normal forces for each leg were calculated:

$$\begin{aligned} F_0 = & 0.077 \text{ kg}; F_1 = 0.224 \text{ kg}; \\ F_2 = & 0.452 \text{ kg}; F_3 = 0.447 \text{ kg}. \end{aligned} \quad (10)$$

Obviously, the normal force increases as the number of legs supporting the weight decreases. The same should apply for energy consumption because the normal force, needed to hold the weight, is somewhat proportional to energy consumption.

Despite having calculated forces for each individual leg, forces that affect the whole robot for each of three cases should be taken into account. The calculated values are:

$$\begin{aligned} 6 \cdot F_0 = & 0.462 \text{ kg}; 6 \cdot F_1 = 1.344 \text{ kg}; \\ F_2 + 2 \cdot F_3 = & 1.346 \text{ kg} \end{aligned} \quad (11)$$

Even though $6 \cdot F_1 = F_2 + 2 \cdot F_3$, while the weight is the same, the number of legs supporting that weight is not. This result states that the parameter which matters the most in this case is the number of legs set on the surface.

Having the force distribution between feet, the graph below can be used to compare energy consumption for all different cases (Fig. 4).

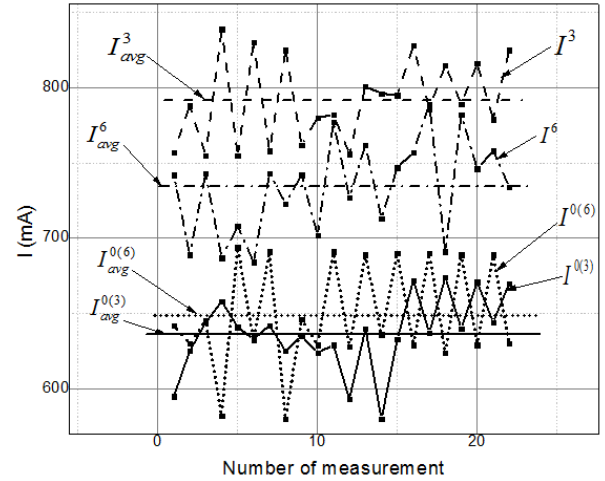


Fig. 4. Energy consumption for different cases

The average energy consumption for each individual case can be calculated using data from Fig. 4: $I_{avg}^{0(6)} = 649 \text{ mA}$; $I_{avg}^6 = 734 \text{ mA}$; $I_{avg}^{0(3)} = 637 \text{ mA}$; $I_{avg}^3 = 792 \text{ mA}$, where $I_{avg}^{0(6)}$ – energy consumption while no legs are positioned on the surface with three legs slightly raised, I_{avg}^6 and I_{avg}^3 – energy consumption while six and three legs are positioned on the surface. It is noticeable, that energy consumption while no legs are set on the surface is observed. The reason was to test whether or not each actuator, holding only the weight of the leg, consumes more energy rather than two or three actuators, holding the whole weight of the robot.

Results show that $I_{avg}^{(6)} > I_{avg}^{(3)}$. This is due to three legs being slightly raised. Energy needed to hold the leg in the air is at the highest peak at the angle of 90°.

It is clearly seen from Fig. 4 that energy consumption increases while the number of legs positioned on the surface decreases. The same tendency also applies to force distribution. This is logical because the more legs are raised, the more weight remaining legs have to hold, thus the more energy actuators consume.

Although, the difference between power consumption in each case is small (~12 – 58 mA), it is enough to see that energy consumption strongly depends on weight. In addition, observing how energy consumption depends on different parameters (different gates, step height, body raise, different roughness terrain, movement speed) might give a better understanding of robotic energetic.

5. Conclusions and future work

Energy dependence on the number of legs set on the surface for a hexapod walking robot was investigated in this paper. First, normal force distribution between the feet was calculated. Inspiration to do so came from the fact that energy consumption should be proportional to the normal force distribution. Calculations showed that the normal force increases as the number of legs supporting the weight decreases. Experiments, carried out only on even terrain for six, three and zero legs on the surface, showed that the same tendency also applies for energy consumption. The result is logical because actuators consume more energy when fewer legs have to carry the same weight. Experiments carried out in this paper clearly show that the robotic energetics strongly depends on the number of legs positioned on the surface.

However, in this paper we observed only static energy consumption characteristics depending only on the number of legs set on the surface, which is one parameter. Future aim is to observe energy consumption of a six-legged locomotion and the dependence on different gaits. Furthermore, adding more parameters, such as movement speed, step height, body pose, additional weight, should help in future experiments, that would involve rough terrain and observation of energy consumption levels in real-time. Also, having the information above should give more assistance in selecting suitable gaits for different roughness terrain in order to lower energy consumption. The importance is

clear, as it is the only way to improve the efficiency of a hexapod robot.

6. References

1. Pongas D., Mistry M., Schaal S. A Robust Quadruped Walking Gait for Traversing Rough Terrain. IEEE International Conference on Robotics and Automation, 2007. p. 1474 – 1479.
2. Shekhar S. R., Pratihari D. K. Effects of turning gait parameters on energy consumption and stability of a six-legged walking robot. Robotics and Autonomous Systems 60, 2011. p. 72 – 78.
3. Jin B., Chen C., Li W. Power Consumption Optimization for a Hexapod Walking Robot. Journal of Intelligent & Robotic Systems, 2011. p. 1 – 15.
4. McGhee R. B., Iswandhi G. I. Adaptive Locomotion of a Multilegged Robot over Rough Terrain. IEEE Transactions on Systems, Man, and Cybernetics, Vol. smc-9, no. 4, 1979. p. 176 – 182.
5. Homayoun S., Ayanna H., Tunstel E. Terrain-Based Navigation of Planetary Rovers: A Fuzzy Logic Approach. Proceeding of the 6th Intl. Symposium on Artificial Intelligence and Robotics and Automation in Space: i-SAIRAS 2001, 2001. p. 1 – 8.
6. Chow Y. H., Chung R. VisionBug – A Hexapod Robot Controlled by Stereo Cameras. Autonomous Robots 13, Kluwer Academic Publishers, 2002. p. 259 – 276.
7. Kimura H., Kitano H. Vision-Based Motion Recognition of the Hexapod for Autonomous Assistance. Proceedings of 1998 IEEE/RSJ Intl., 1998. p. 1 – 6.
8. Kar D. C., Kurien K. I., Jayarajan K. Gaits and energetics in terrestrial legged locomotion. Mechanism and Machine Theory 38, 2003. p. 355 – 366.
9. Hoffman R., Krotkov E. Terrain Roughness Measurement from Elevation Maps. SPIE Vol. 1195 Mobile Robots IV, 1989. p. 104 – 114.
10. Belter D., Labecki P., Skrzypczynski P. Map-based Adaptive Foothold Planning for Unstructured Terrain Walking. Proceedings of 2010 IEEE Intl., 2010. p. 5256 – 5261.
11. Buchli J., Kalakrishnan M., Mistry M., Pastor P., Schaal S. Compliant Quadruped Locomotion Over Rough Terrain. IEEE/RSJ International Conference on Intelligent Robots and Systems, 2009. p. 814 – 820.

PERFORMANCE EVALUATION OF WIRELESS NETWORK FOR VEHICULAR ENVIRONMENT

Nikolajs BOGDANOVŠ, Ernests PETERSONS, Janis JANSONŠ
 Department of Transport Electronics and Telematics, Riga Technical University, Latvia

Abstract: In this paper, the main aim is to determine the number of the vehicles, depending on the remoteness to the base station. On the basis of this, the objective is resolved with the determination of the actual speed of data transmission from the moving objects. In this article, a goodput of standards IEEE802.11n and IEEE802.16e for open network systems was calculated. As a result, the proposed mathematical models for two layer wireless networks have been used for choosing goodput evaluation of Vehicular network. In this research, the usage possibility of the two level wireless networks for the vehicles on highways is demonstrated.

Keywords: Two layer network, IEEE 802.11n, IEEE 802.16e, goodput.

1. Distribution of the vehicles

The main goal of the paper is the rate calculation of the data transmission, depending on the remoteness of the mobile object from the base station and its moving speed. For the calculation of the goodput we have 200 meters long base station operational zone of is divided into 5 zones, as show Fig. 1:

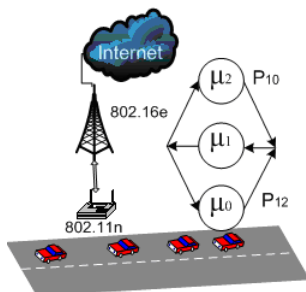


Fig. 1. Two layer network with three access points

Out of the experimental data, it follows that vehicle speed is growing exponentially, as shown in Fig. 2.

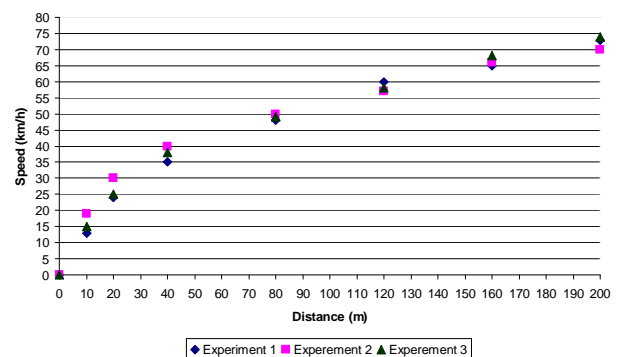


Fig. 2. Speed of vehicle \mathcal{G}_0

Distribution is exponential with the parameter μ_i . According to this research, the speed of vehicle movement on a highway is characterized by density. The placement of vehicles per meter:

$$\mathcal{G} = \mathcal{G}_0 \left(1 - \frac{k}{k_c} \right), \quad (1)$$

where, k_c - is the maximum allowable flux density, \mathcal{G}_0 - the speed of the free movement of the flow (the maximum allowable) Fig. 2, k - the number of vehicles.

Let's assume that the area of interaction between vehicles and base station can be divided into M intervals. Let's provide a number of trespassing vehicles per second for each interval according to query intensity and processing. If the interval length equals S_i , and vehicle movement speed equals \mathcal{G}_i , then the intensity of vehicle service by road interval equals:

$$\varpi_i = \frac{\mathcal{G}_i}{S_i} \quad (2)$$

According to (2) the intensity of vehicle service will be depending as from initial vehicle flow rate into the road interval as from density of vehicle location on the road interval [1].

The experiment results show that the possibility of using a wireless distribution system (WDS) to connect APs wirelessly extending the transmission range area of network architecture and the connectivity time of the data transmission [2], as shown in Fig. 3. It is important to note that speed measurement of the data transmission was carried out only for the single mobile object without the competition from the possible other moving vehicles.

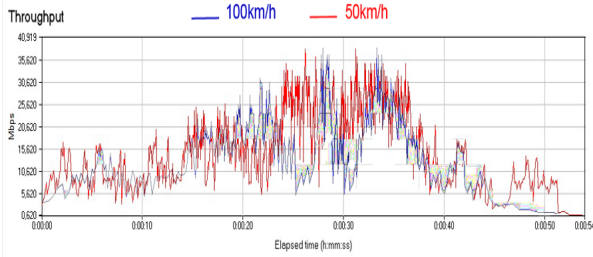


Fig. 3. The goodput over the distance for IEEE 802.11n

The model (Fig. 4) was created in the graphical Simulink environment of MATLAB package. As the source of source blocks was used the blokset SimEvents. The scheme consists of 5 nodes (Node k, where k = 1...5), offered in which contain more convenient interface for the introduction of parameters as well as more pictorial. Nodes consist of block of waiting line and server unit with a random-number generator. The last one generates the random-number sequence for the organization of service time in the server, as shown in Fig. 4. If at the entrance of the node there is a Poisson flow then the given node can be presented as the model of MMNK system as the service time is distributed in accordance with the exponential law.

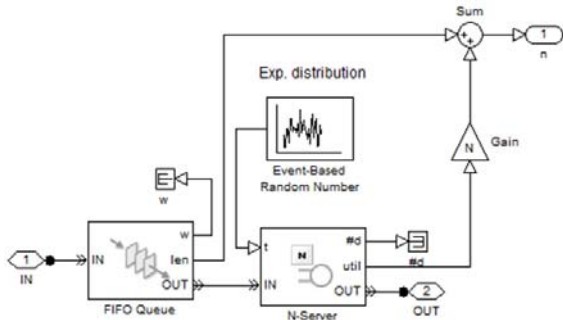


Fig. 4. The scheme of node

On the basis of the previous calculation in the model for each Node k has chosen the following parameters:

- Queue length $K=\infty$;
- The number of servers $N=1$;

- The service rate for each node: $\varpi_1=0.277$, $\varpi_2=0.444$, $\varpi_3=0.544$, $\varpi_4=0.604$ and $\varpi_5=0.642$.

Here x_i is estimated by the system of equations:

$$\varpi_i x_i = \sum_{i=1}^M \varpi_i x_i p_{ij} \quad (3)$$

Due to the periodic nature of this model $x_1 = 1$ and the next step is calculated as follows:

$$x_2 = \frac{\varpi_1}{\varpi_2}, x_3 = \frac{\varpi_1}{\varpi_3}, \dots, x_M = \frac{\varpi_1}{\varpi_M} \quad (4)$$

Buzen's algorithm is among the most effective methods for closed network analysis. Buzen's matrix (Table 1), at the row i and column j can be calculated using the formula: x_1

$$g(i, j) = g(i, j-1) + g(i-1, j)x_j \quad (5)$$

Table 1. Buzen's matrix

Nr.	$x_1=1$	x_2	x_3	x_4	x_5
0	1	1	1	1	1
...
9	1	4,11	10,63	22,53	42,28
10	1	4,19	11,03	23,83	45,56
...
19	1	4,43	12,37	28,43	57,99
20	1	4,44	12,41	28,56	58,37

Probability that i – zone is occupied:

$$P\{n_i \geq 1\} = x_i \frac{g(i-1, j)}{g(i, j)} \quad (6)$$

Then probability of query (vehicle) distribution among service devices (road intervals):

$$P_{n_1, \dots, n_M} = \frac{1}{G(N)} \cdot \frac{\varpi_1^{N-n_1}}{\varpi_2^{n_2} \cdot \varpi_3^{n_3} \dots \varpi_M^{n_M}} \quad (7)$$

where $G(N)$ – normalizing constant, resulted either from adding up and equating to one all probabilities either by Buzen's method. Naturally, there are no limitations for the number of vehicles (queries) in the i -th interval [3].

Average number of queries (vehicles) in i -th interval (Table 2):

$$E[n_i] = \sum_{K=1}^M (x_i)^K \cdot \frac{G(N-K)}{G(N)} \quad (8)$$

Table 2. Average number of vehicular

Vehicle (N)	Zone 1	Zone 2	Zone 3	Zone 4	Zone 5
10	6	1	1	1	1
20	15	2	1	1	1

2. Mathematical equations Two Layer Vehicular Network modeling

Evaluating the performance of these schemes in various conditions can help researchers discover their performance. On the experimental data there was developed a mathematical model, connecting the number of transport and data transmission feature. In this paper there was developed the model to determine the actual speed of data transmission, depending on the number of mobile objects.

The object of the research is wireless network with three Access Points and one base station for data transmission between mobile objects and the remote server. Further from the Access Points the data is transmitted to the remote base station on the protocol IEEE 802.16e [4]. This variant provides the data transmission at the distance up to the several kilometers. The two-level vehicular network model with one Access Points is present in Fig. 1.

In our model, wireless clients (vehicles) will null node generate the data transmission from a movable object with the intensity of the data transmission μ_0 (Fig. 1).

For our model we will consider that on 99 passed packages a 1 package and that on 999 passed packages a 1 package is used a client for confirmation of ACK. ACK is a signal passed between communicating processes to signify acknowledgement, or receipt of response, as part of a communications protocol [5].

The second node stimulates the Access Points wireless network providing the data reception and transmission from the mobile objects of the null node. The intensity of the data processing is equal to μ_1 .

$$\mu_1 = \beta_i \quad (9)$$

where β_i - goodput from Fig. 3.

In its turn AP connects with the remote base station along the wireless network with the IEEE 802.16e standard. The intensity of the data transmission of the second node is to be taken to be equal to μ_2 .

The route of the data transmission keeps the track from the null node to the first node and then to the second, if the file transfer is considered from the car to the BS. From the BS is transmitted the ACK confirmations on the packet's transmission. In this case the average time for the transmission will be varying: more time is spending on the transmission of the data packets, which we denote as $E(t_i)$. The ACK transmission takes less time denotes it as $E(t_0)$. Then the average time of the data processing in the first node will be:

$$E(t_1) = E(t_i) + E(t_0) / 2 \quad (10)$$

If on the top of each transmitted packet we receive the ACK confirmations. In this case the intensity of the processing in the first node will be:

$$\mu_0 = 1 / E(t_1) \quad (11)$$

In fact, the model participates in the parameter N determining the number of data transmission initiators, which compete for the resource sharing of the 1 and 2 nodes. In our case this is the number of automobiles in the AP coverage area [3][6]. Then three-node and two-level model of the goodput can be expressed by the (19) formula. In this formula the parameters α and x determine by the value from (12). The valuation problem of the goodput provided by the model consists of the determination of the value N – the number of cars in the AP coverage area. Moreover, in the wireless network standard IEEE 802.11n the speed of data transmission depends on the remoteness of the vehicles from AP. The terminal count in each vehicular wireless network is usually high. Bandwidth equation for a two layer network:

$$X_1 = \frac{\mu_0}{\mu_1 P_{10}}; X_2 = a X_1; a = \frac{\mu_1}{\mu_2} P_{12}. \quad (12)$$

Symbols in your equation should be defined before the equation appears The intensity for the μ_2 :

$$\mu_1 = \beta_i \quad (13)$$

$$t = l_p / V_f \quad (14)$$

where V_f - effective data transfer rate for the IEEE 802.16e protocol. For the data transmission between the Access Points and the base station is used IEEE 802.16e protocol, this protocol will have the peak transfer rate $V_n = 50\text{Mbps}$. The packet length will be $l_p = 1500\text{bytes}$, but the actual speed is determined in the following way:

$$V_f = V_n / 2 \quad (15)$$

Starting point for the calculation is the normalizing function $G(N)$, that is chosen from the principle of the sum of probabilities being one. $p(n_0, n_1, n_2)$, where n_i in vector $\bar{n} = (n_1, n_2, n_3)$ is the inquiry count in i -th node. The resulting equation for $G(N)$ calculation looks like this:

$$G(N) = \sum_{\bar{n}} \prod_{i=1}^3 (X_i)^{n_i} \quad (16)$$

where N - number of vehicles. Function for the studied two layer vehicular network looks like this:

$$G(N) = \frac{1}{1-a} \sum_{j=0}^N X_1^j (1-a^{j+1}) \quad (17)$$

Goodput η of the two layered network is defined as the count of processed inquiries in a unit of time. The finished task is put out trough the subsystem of input/output, and instantly trough it a new task is loaded. Probability of a lack of inquiries in i-th node:

$$p\{n_i = 0\} = \frac{G(N) - X_i G(N-1)}{G(N)} \quad (18)$$

The output flow is equal to input flow and from this rule of flow balance it is possible to write:

$$\eta = P_{10} \mu_1 (1 - p\{n_i = 0\}) \quad (19)$$

On the network performance influences the probability of transmission of the confirmation ACK, as increases ACK, increases the number of packages per unit time. If the probability will be P10=0.999 P12=0.001 then the goodput with N=10 and N=20 will be (Fig. 5):

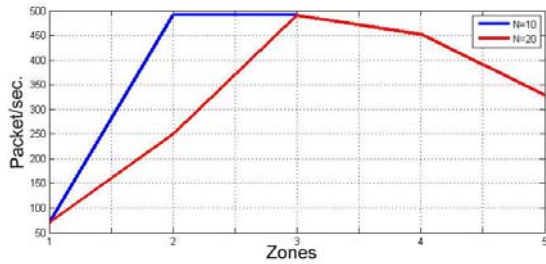


Fig. 5. Goodput for a Two layer Network model with P10=0.999 P12=0.001 for IEEE 802.11g and IEEE 802.16e

Goodput with the probability P10=0.99 P12=0.01 for N=10 and N=20 will be (Fig. 6):

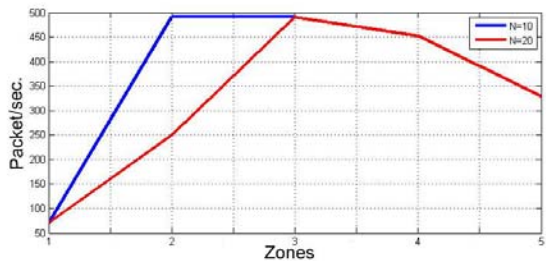


Fig. 6. Goodput for a Two layer Network model with P10=0.99 P12=0.01 for IEEE 802.11g and IEEE 802.16e

3. Conclusions

In the paper were considered the modelling and the calculation of performance of two layer wireless networks for transport, using graphical Simulink environment of MATLAB package and experimentally obtained date of protocol IEEE 802.11n.

On the basis of the experimental data was developed a mathematical model, connecting the number of transport and data transmission feature. In this paper was developed the model to determine the actual speed of date transmission, depending on the number of mobile objects which are in the coverage area of the base station of the wireless network. On the basis of the given paper the actual speed of date transmission will be depend on the number of objects, interacting with the base station and their remoteness from it as well as from the transmission type of traffic.

4. References

1. Shortle G. J., Thompson J., Harris C., "Fundamentals of Queuing Theory." Willy, 2008, pp. 500.
2. Kleinrock, "Queuing Systems." John Wiley & Sons Ltd. 1975, 600p.
3. Wee Lum Tan, Member, IEEE, Wing Cheong Lau, Senior Member, IEEE, OnChing Yue, Senior Member, IEEE, and Tan Hing Hui, "Analytical Models and Performance Evaluation of Drive-thru Internet Systems." IEEE Journal on selected areas in Communications. Vol. 29, 2011, pp. 207-222.
4. Ipatovs A., Petersons E., "Performance Evaluation of WLAN depending on number of Workstations and Protocols", Proceedings of International Conference Electrical and Control Technologies, ISSN 9955-25054-2, 2006, pp. 266-270.
5. Wellens M., Westphal B., and Mähönen P., "Performance Evaluation of IEEE 802.11-based WLANs in Vehicular Scenarios", in Proc. VTC Spring, 2007, pp.1167-1171
6. Czajkowski K., Fitzgerald S., Foster I., Kesselman C., Grid Information Services for Distributed Resource Sharing. In: 10th IEEE International Symposium on High Performance Distributed Computing, pp. 181-184. IEEE Press, New York, 2001.

SYNTHESIS AND INVESTIGATION OF THE CONTROL ALGORITHMS OF NEW GENERATION CONTROLLERS

Dinas ŠULSKIS

Faculty of Electrical and Control Engineering, Kaunas University of Technology, Lithuania

Abstract: In new generation controllers, simplicity of PID controllers' tuning and effectiveness of MPC based control strategy is combined. The tuning parameters are normalized to lie between 0 and 1, they are simple to choose and adjust and directly influence the robustness, set-point tracking, disturbance rejection and overall aggressiveness of the system.

In this work, a novel method of automatic control systems synthesis is presented. When using this method, it is possible to obtain control law of the system when mathematical model is complex, i. e. when explicit analytical solution of the problem of control law calculation is impossible.

Keywords: Model predictive control, PID control, control action computation, optimizer, controller tuning, search optimization.

1. Introduction

There are known many methods for adjusting parameters of proportional, derivative and integral part of the controller. However it is well known that using classical PID controller it is impossible to directly regulate robustness, disturbance rejection, tracking and aggressiveness of the system. That is, it is impossible to tune PID controller to achieve best performance in all cases independently [1, 4].

When the process dynamics becomes more complicated PID controller often is not sufficient and more sophisticated controller structure with more control performance is necessary. The benefits of using more sophisticated controller are for example for systems of higher order than two, for systems with long dead times as well as systems with long time delays etc. [4].

In [1] an alternative control scheme is presented. Using this approach named RTD-A (short of Robustness, setpoint Tracking, Disturbance rejection and overall Aggressiveness) it is possible to combine the simplicity of the PID controller and the versatility of model. The main sequence of steps of MPC control strategy may be described as follows [3]:

predictive control (MPC). Also avoiding the tuning problems associated with both.

The tuning parameters of this control scheme are directly related to the controller performance attributes; they are normalized to lie between 0 and 1; and they arise naturally from the formulation in a manner that makes it possible to tune the controller directly for each performance attribute independently. The result is a controller that can be designed and implemented much more directly and transparently, and one that outperforms the classical PID controller both in set-point tracking and disturbance rejection while using precisely the same process reaction curve information required to tune PID controllers [1].

Parameters θ_R , θ_T , θ_D and θ_A directly influence robustness, setpoint tracking, disturbance rejection and overall aggressiveness of the system [1].

In this case, if tuning parameter is changed, the corresponding characteristic changes accordingly. For instance, response of the system becomes closer to defined setpoint if setpoint tracking parameter θ_T is decreased or controller becomes more prone to external disturbances if disturbance rejection parameter θ_D is decreased.

Investigated RTD-A scheme is based on popular in modern industry model predictive control (MPC) strategy. Similar to MPC, this strategy has such common elements as prediction model, objective function, control law computation. A disturbance model can also be used in order to describe the behaviour of the system which is not reflected by the process model.

In this work novel method [2] of automatic control systems synthesis is presented. When using this method it is possible to obtain control law of the system when mathematical model is complex and explicit analytical solution of the control law calculation is impossible.

2. RTD-A control concept

1. The future output values for a determined horizon N are predicted at each instant using the process model. These predicted outputs $y(k+m+1)$ for $m=1..N$

depend on the known values up to instant k (past inputs and outputs) and on the future control signals $u(k+m|k)$, $k=0..N-1$ which are then to be sent to the system and to be calculated.

2. The set of future control signals is calculated by optimizing a determined criterion in order to keep the process as close as possible to the reference trajectory $y^*(k+j)$, $j=1..∞$ (which can be the setpoint itself or a close approximation of it). This criterion usually takes the form of a quadratic function of the errors between the predicted output signal and the predicted reference trajectory. The control effort is included into objective function in most cases. An explicit solution can be obtained if the criterion is quadratic, otherwise an iterative optimization method has to be used

3. The control signal $u(k|k)$ is sent to the plant, whilst the next control signals calculated are rejected, because at the next sampling instant $y(k+1)$ is already known and step 1 is repeated with this new value and all the sequences are brought up to date. Thus the $u(k+1|k+1)$ is calculated. Prediction horizon is displaced towards the future, which involves the application of the first control signal of the sequence calculated at each step.

In RTD-A controller additionally are included 4 parameters which affect the system in the following way [1]:

$$y^*(k) = \theta_T y^*(k-1) + (1-\theta_T) y_d(k). \quad (1)$$

Here $y^*(k)$ - the desired trajectory for response of the plant to follow, $y_d(k)$ - desired setpoint.

Obviously when tuning parameter $\theta_T \approx 0$, desired trajectory becomes close to setpoint trajectory: $y^*(k) \approx y_d(k)$. Near the other extreme when $\theta_T \approx 1$, (1)

becomes $y^*(k) \approx y^*(k-1)$. It means that system becomes almost uninfluenced by the setpoint function. Here θ_T directly influences the setpoint tracking of the system.

Current disturbance effect estimation from $e(k)$ as the current disturbance effect is done as follows:

$$\hat{e}_D(k) = \theta_R \hat{e}_D(k-1) + (1-\theta_R) e(k). \quad (2)$$

Here θ_R is robustness tuning parameter. Since if $\theta_R \approx 0$, (2) becomes $\hat{e}_D(k) \approx e(k)$, so current disturbance effect equals to model error. When $\theta_R \approx 1$, $\hat{e}_D(k) \approx \theta_R \hat{e}_D(k-1)$. It means increased indifference of the system to model-plant mismatch.

Similar influence on future disturbance effect prediction has third tuning parameter θ_D , which is also requires to lie between 0 and 1. In case when $\theta_D \approx 1$, future disturbance effect is predicted to be close to constant into the future at the current estimated value (2). Conversely when $\theta_D \rightarrow 0$, future disturbance effect is predicted to evolve into the future as an indefinitely increasing ramp [1].

The fourth parameter θ_A , characterizing overall aggressiveness of the controller directly influences the prediction horizon of the system i.e.:

$$N = 1 - \frac{\tau}{\Delta t} \ln(1-\theta_A) \quad (3)$$

here τ is time constant, Δt - sampling period.

RTD-A control strategy may be represented by the control diagram (Fig.1)

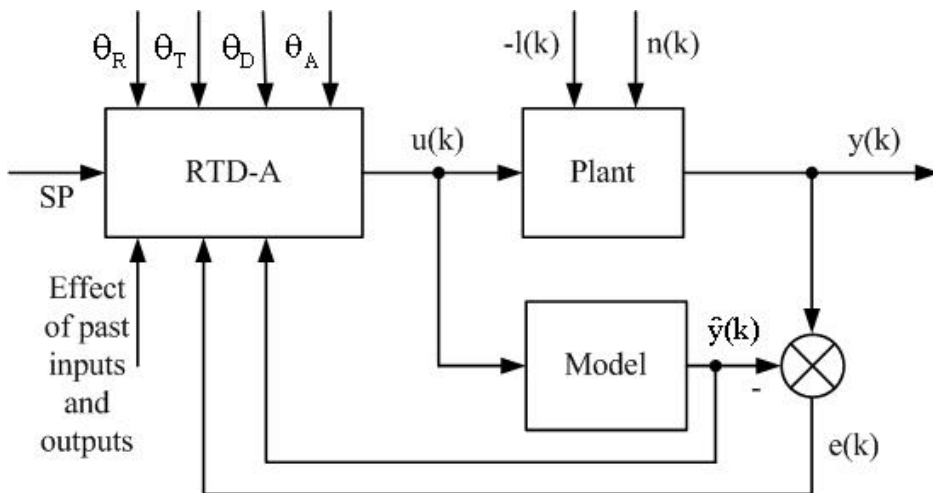


Fig. 1. The RTD-A control diagram

here SP - desired setpoint; $u(k)$ - calculated control signal; $l(k)$ - load disturbance; $n(k)$ - zero mean white noise; θ_R , θ_T , θ_D and θ_A - parameters which sets robustness, tracking, disturbance rejection and

aggressiveness of the RTD-A controller respectively; $y(k)$ - response of the plant; $\hat{y}(k)$ - prediction of the plant output, calculated by the model of the process $e(k)$ - error (difference between the model output and the

plant output). The control action $u(k)$ may be computed solving minimization problem over the N step horizon beyond the delay period m . Minimization problem is given by [1]:

$$\min_{u(k)} \sum_{i=1}^N (y^*(k+i) - \hat{y}(k+m+i))^2. \quad (4)$$

3. Formulation and ways of synthesis of the system

Optimal solution to the minimization problem (4) is easily obtained analytically in cases when mathematical model of the control object is simple. Otherwise more complex numerical optimization methods should be used. By using proposed technique it is possible to obtain close to optimal (quasi-optimal) solution to control system synthesis.

It is required to determine the vector \mathbf{x}^* , which ensures the minimum of the functional:

$$J(x) = J[\mathbf{y}, \mathbf{u}(\mathbf{x}, t)], \quad 0 \leq t \leq t_f, \quad (5)$$

while obeying the constraints:

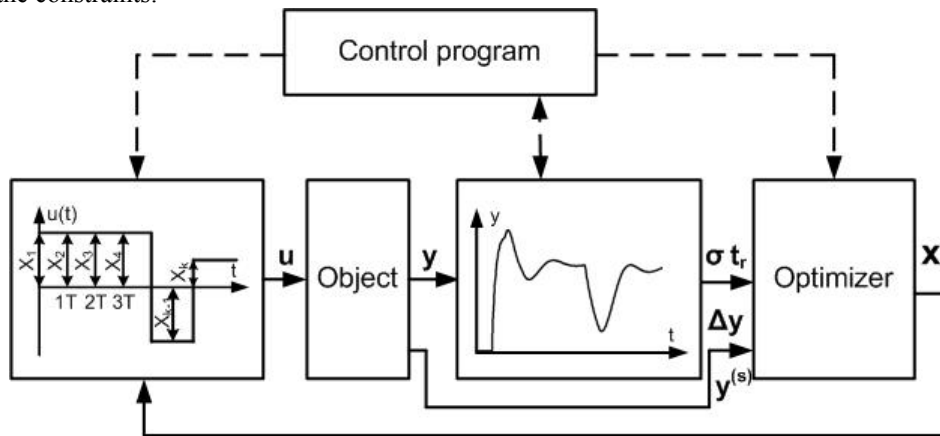


Fig. 2. The optimization diagram of the control action calculation for open quasi-optimal control system with coordinate constraints

Control effort $u(t)$ is calculated according to vector \mathbf{x} and then supplied to input of the control object. Vector \mathbf{x} is formed by optimizer as a result of cost function which involves data from past control actions.

This method may be used to solve quasi-optimal systems synthesis problems, which can't be solved by means of methods of classical optimal control and variation calculation. The main precondition for solving the problem is experimental determining of the functional (5), the functions of constraints (6) and finding the values of the limited coordinate (7) for the given components of vector \mathbf{x} .

Control action was calculated under following conditions. System with process model (8)

$$g(s) = \frac{e^{-s}}{2s+1} \quad (8)$$

was subjected to step disturbance of -1 at $t=10$. Sampling time dt is 0.1 and noise level is set to zero. In order to simulate model uncertainty 10 percent

$$g_j[\mathbf{y}, \mathbf{u}(\mathbf{x}, t)] \geq 0, \quad j = 1, \dots, q, \quad (6)$$

$$|y^{(s)}| \leq y_m^{(s)}, \quad (7)$$

where J , g_j - are the control quality indicators (regulation time t_r , maximum dynamic deflection σ , error of control Δy etc.).

The determined constraints concerning one or the other vector y coordinates form certain allowable areas inside which there has to be an optimal trajectory, e.g. during the process of control the object velocity y is not allowed to exceed the indicated boundary, namely $y \leq |y_m|$.

The synthesis problem of open quasi-optimal control system with coordinate constraints is solved by using the software package Kvazio 1 which was created by author. Fig 2 presents the diagram of problem solution using the improved simplex search algorithm.

plant/model mismatch was applied. Tuning parameters are set to fixed values and are not changed during the simulation process. Obtained control law is shown in Fig 3. Corresponding response of the system is shown in Fig. 4.

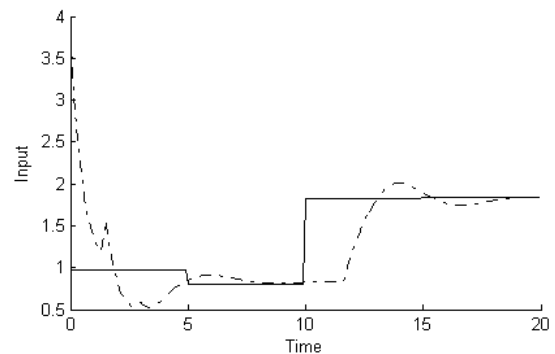


Fig. 3. Computed control action (Solid line) and original control action (dashed line)

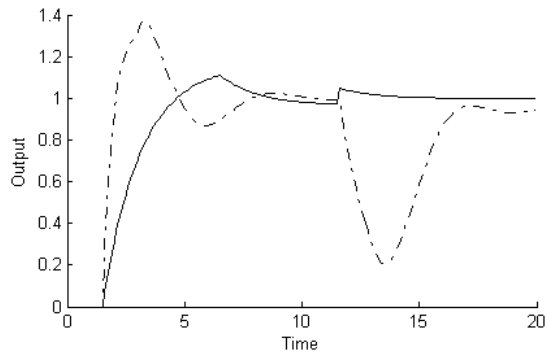


Fig. 4. Resulting system response (solid line) and original response (dashed line)

The resulting process is significantly better if compared with original response. The effect of step disturbance and overshoot created by setpoint change were eliminated. The main advantages of the proposed method is that there is no need for explicit analytical solution of the control law calculation, which is often impossible to obtain when model is not linear or defined by complex differential equations.

4. Conclusions

1. Novel control technology RTD-A was investigated, which combines simplicity of the PID controller with effectiveness of model predictive control (MPC) technology while avoiding the tuning problems associated with both.

2. Using classical PID controller parameter tuning methods it is impossible to directly regulate robustness, disturbance rejection, tracking and aggressiveness of the system. As shown by the simulation, parameters θ_R , θ_I , θ_D and θ_A directly influence robustness, setpoint tracking, disturbance rejection and overall aggressiveness of the system.

3. In this work novel method of automatic control systems synthesis is presented. When using this method it is possible to obtain control law of the system when mathematical model is complex. Also there is no need for explicit analytical solution of the problem of control law calculation, which is often impossible to obtain when model is not linear or complex.

5. References

1. Mukati K., Ogunnaike B., "An alternative structure for next generation regulatory controllers. Part I: Basic theory for design, development and implementation", *Journal of Process Control*, p. 499-509, 2006.
2. Dambrasuskas A., Karaliūnas B., Šulskis D., "Synthesis of the Control System with Variable Structure and Limitations of coordinates", *Electronics and Electrical Engineering. – Kaunas: Technologija*, No. 4(84), p. 31-34, 2008.
3. Camacho E. F. and Bordons C., *Model Predictive Control*, Springer-Verlag, London, 1999.
4. Astrom K. J. and Haagglund T., *PID controllers: theory, design, and tuning*, Instrument Society of America, NC, 1995.

CONTROL OF COMPUTER PROGRAMS BY VOICE COMMANDS

Vytautas SLIVINSKAS*, Gražina PYŽ***, Virginija ŠIMONYTĖ*

*Lithuanian University of Educational Sciences, Lithuania

**Vilnius University Institute of Mathematics and Informatics, Lithuania

Abstract: The paper deals with the computer program control using voice commands. The problem of the voice command recognition is discussed and the results of investigation of the voice command recognition are presented. The use of voice commands is illustrated by an example.

Keywords: Speech recognition, voice commands, computer program control.

1. Introduction

Speech recognition is a process that converts spoken words and phrases to a computer-readable format. Speech recognition is mostly developed for the languages of big countries especially for English language. There exists a number of programs (Dragon Naturally Speaking, Speech Recognition in Windows 7, Dragon Dictate for iPhone/iPad, etc.) that are intended for the use with English language. The languages of small countries cannot boast of such a great attention, nevertheless the local researchers give much effort to developing recognizers of the local languages. Lithuanian speech engineering is a popular field of engineering in Lithuania. Lithuanian speech recognition is one of the Lithuanian speech processing problems taking considerable attention of Lithuanian researchers. One of the best known group works at Vilnius University Institute of Mathematics and Informatics. This group solves such problems as: quality estimation of speech recognition features [1], speaker recognition by voice [2], development of isolated word recognition systems [3], acoustic modelling of Lithuanian speech recognition [4], etc. Scientists from Vilnius University Faculty of Mathematics and Informatics and Forensic Science Centre of Lithuania investigate speaker recognition problems [5]. Researchers from Vilnius Gediminas Technical University deal with control of robots by voice [6], development of biometric systems for person recognition [7], development and implementation of means for word duration signal processing [8], [9]. A group of scientists from Kaunas

University of Technology, Vytautas Magnus University and Vilnius University Kaunas Faculty of Humanities carries out investigation of foreign languages models for Lithuanian speech recognition [10], analyse control of electric devices by voice [11], deal with hierarchical phoneme classification approach [12], develop isolated-word Lithuanian HMM speech recognition system [13], investigate HMM for large vocabulary continuous speech recognition [14].

Speech recognition allows one to give input to a computer program using voice. A program that is called the speech recognition engine carries out the speech recognition task.

There exist two cases of the computer program control by voice:

- 1) the speech recognizer depends on the speaker (speaker-dependent recognition),
- 2) the speech recognizer does not depend on the speaker (speaker-independent recognition).

Implementation of the second case is much harder although the result is more attractive to the user. The first case only is considered in this work. The results of automatic Lithuanian speech recognition performed by a system that was developed for a construction estimate program are presented in this paper. Section 2 deals with voice command recognition using cepstral approach. The requirements for the recognition system software and hardware are presented in Section 3. Section 4 contains a description of an example of practical application of computer program control by voice commands.

2. Voice command recognition using cepstral approach

The system consists of two parts: the training part and recognition part. The system performs in the following way:

- 1) A list of commands is compiled;
- 2) The commands are recorded to a .wav format file (11.025 kHz, 16-bit mono);

- 3) The extraction of features of each command is carried out;
- 4) These features are stored in a database;
- 5) The process of command recognition is performed.

2.1. Voice commands

The voice commands can be divided into a few categories:

- 1) the commands specified by words (e. g., “atidaryti” (*open*), “uždaryti” (*close*), “spausdinti” (*print*));
- 2) the commands described by a numerical code – they are pronounced by uttering each digit separately (e. g., the code “999” is uttered as “nine, nine, nine” and means *to open*);
- 3) the commands specified by words and a numerical code (e. g., “samata 45” (*estimate four five*), “laiškas 52” (*letter five two*)); in this case an object (*estimate, letter*) and the action to be taken with that object are specified.

The number of commands can be large. In this case the command coding has a drawback – the user can encounter difficulty to memorize the command code. In order to avoid this difficulty, the system can return the command name after recognizing it. When the user confirms the command, the system runs it.

If the number of commands is large, then it is useful to divide them into groups. The names of such groups can be as follows: editing, saving, printing, etc.

The system should recognize the commands and their codes without mistakes.

2.2. Feature extraction

The cepstral method is used for speech recognition [15]. The features that specify the spectrum of the uttered word are selected. The main feature selection algorithm steps are shown in Fig. 1.

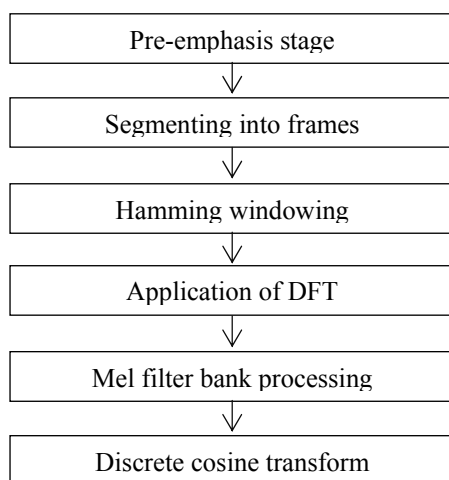


Fig. 1. The feature selection steps

The result of this algorithm is a feature row-vector for each frame. We then make a matrix whose rows are the obtained vectors. This matrix is called a feature matrix.

2.3. Speech command interpreting and running

After the voice command is given, the program controlled by voice starts to compute the command cepstrum parameters if the microphone sound signal amplitude is higher than a certain level. The command utterance is considered to be finished if the pause following it is longer than a certain prespecified value, e. g. 0.2 s.

A feature vector is obtained for each command that is compared with the feature vectors of the etalon commands. The program selects that etalon whose parameter correlation with the uttered word parameters is the highest.

How to pass the result to the controlled program? The simplest way is to use a text file as an inbox that is regularly checked by the controlled program with the help of a small agent procedure. For example, if a command identifier is stored in this text file then this procedure cleans the inbox and runs the command. Such a connection is sufficiently flexible and universal.

3. Requirements for the voice command software and hardware

In order to control successfully a computer by voice, the computer software and hardware has to meet certain requirements. The main requirement for the software is the following: the processing of the uttered word has to be done in a sufficiently small time less than 0.5 s.

A proper selection of the computer microphone and sound card is very important.

All current sound cards support signal audio playback at 44.1, 22.05, 11.025, and 8 kHz. The sampling frequency is selected to be equal to 11.025 kHz, the dynamic range is of 16 bit, and quality is MONO. This is a good compromise between the processing rate and quality. The sound card should not have an inner noise.

It is important to have a good microphone for speech recognition. The microphone should be resistant to environment noise. The microphones used in speech recognition usually do not pass frequencies lower than 100 Hz.

4. The experiment results

In this section, an example of application of the computer program control by voice is presented. In order to control the program by voice, it is necessary to run the recognition program at the same time. The window of the recognition program is given in Fig. 2.

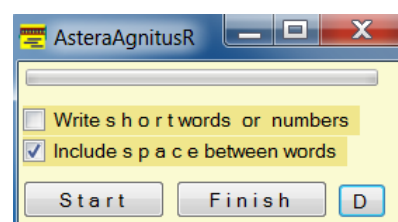


Fig. 2. The window of the recognition program

The recognition program stores the uttered command in a text file. The program controlled by voice uses this text file as an inbox. Before running the recognition program it has to be trained, i. e. the etalon parameter database has to be

created. In order to create the etalons and track the recognition process, a specialized user-program interface has been developed. This window is presented in Fig. 3.

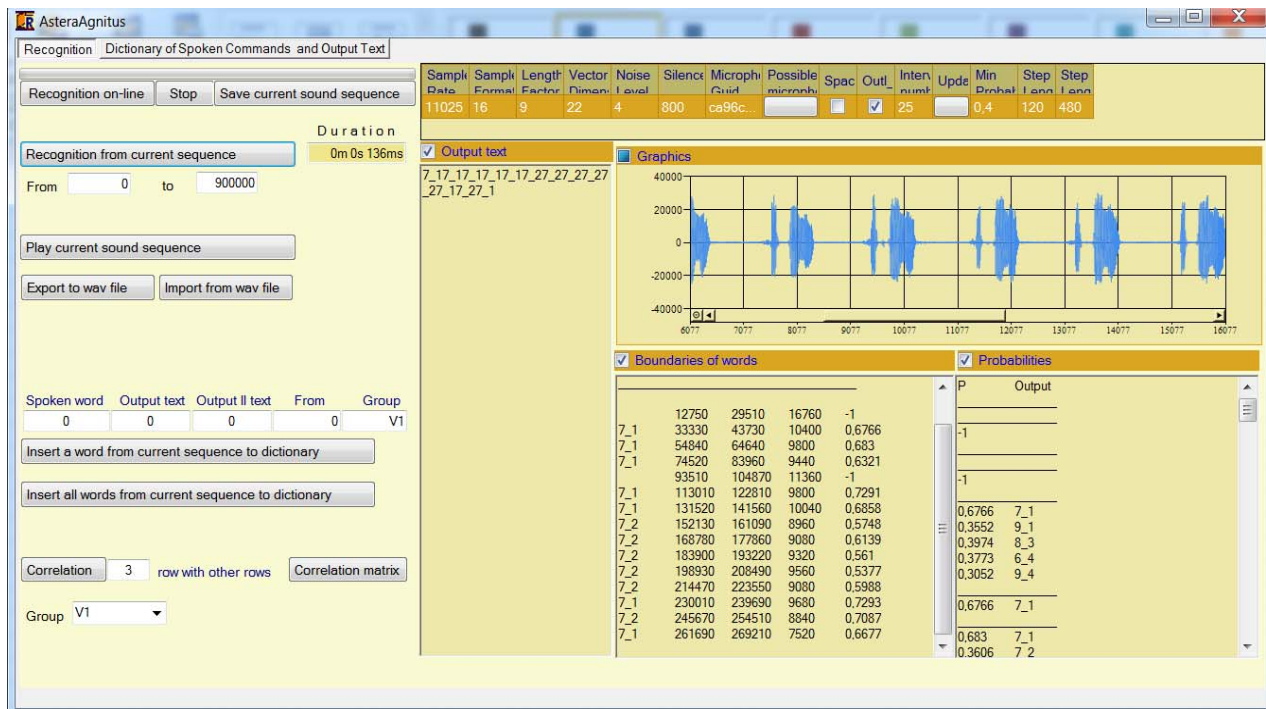


Fig. 3. The recognition process tracking window

The program user records the program control voice commands into a database. He/she records these commands uttered in his/her own voice. These commands are called the etalons. Each command can be uttered several times therefore a single command can have many etalons. In the experiment, a list of commands described by integer numbers from one to nine has been made. Each command is pronounced two times and the obtained speech signals are stored into the etalon database. The feature matrix is determined for each etalon using the algorithm described in Section 2. 2.

The user gives a voice command to the program. Then the features for this command are computed analogously as in the etalon case. An example of the feature matrix of the word “septyni” (*seven*) is shown in Fig. 4 (each row of the matrix is depicted by a single sequence).

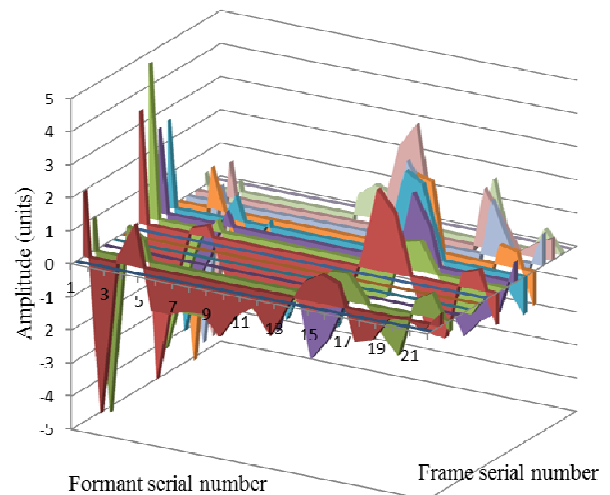


Fig. 4. The feature matrix of the word “septyni” (*seven*)

These features are compared with the etalon features and the correlation between them is determined. The etalon is ascribed to the command whose correlation with that command is the largest. The largest ten values of the correlation coefficients between the feature matrix of the speech signal of the word “septyni” and the feature matrices of etalons are shown in Fig. 5.

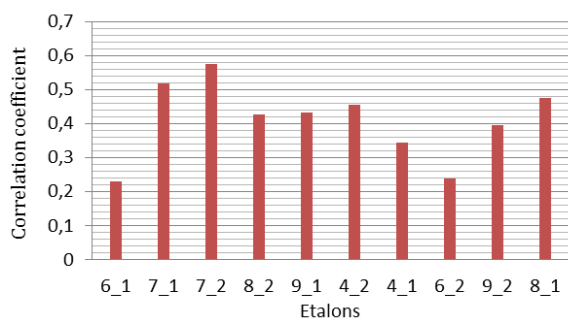


Fig. 5. The values of the correlation coefficient between the feature matrix of the speech signal of the word “septyni” and the feature matrices of etalons

As can be seen from Fig. 5, the highest correlation coefficient corresponds to the etalon 7_2 (the second speech signal of the word “septyni”). Therefore one can state that the system recognized the command “septyni”. In order to evaluate the recognition accuracy, each command was pronounced 20 times. The number of the cases with the correct recognition was then calculated. The result of investigation of the recognition accuracy is presented in Table 1.

Table 1. The recognition accuracy

Command	Accuracy
vienas (<i>one</i>)	100 %
du (<i>two</i>)	95 %
trys (<i>three</i>)	95 %
keturi (<i>four</i>)	80 %
penki (<i>five</i>)	90 %
šeši (<i>six</i>)	85 %
septyni (<i>seven</i>)	95 %
aštuoni (<i>eight</i>)	90 %
devyni (<i>nine</i>)	95 %

5. Conclusions

1. In this paper a speaker-dependent Lithuanian speech recognizer is used.
2. The speech recognition process comprises of two parts: the training part and recognition part.
3. The cepstral approach is used for speech parameter estimation.
4. If several etalons are created for the same command then the recognition result is better.
5. The experiment results show that the recognition process is sufficiently accurate what is important for successful control by voice.
6. In order the recognition process is successful, the computer sound card and microphone have to be of good quality.

6. References

1. Lileikytė, R., Telksnys, L. (2011). Quality estimation methodology of speech recognition features. *Electronics and Electrical Engineering*, 4(110), 113–116.
2. Kamarauskas, J. (2009). *Speaker recognition by voice* (doctoral dissertation), Vilnius: Technika, 124 p. [in Lithuanian].
3. Tamulevičius, G. (2008). *Development of isolated word recognition systems* (doctoral dissertation), Vilnius: Technika, 124 p. [in Lithuanian].
4. Laurinčiukaitė, S., Lipeika, A. (2007). Framework for choosing a set of syllables and phonemes for Lithuanian speech recognition, *Informatica* 18(3): 395–406.
5. Bastys, A., Kisel, A., Šalna, B. (2010). The use of group delay features of linear prediction model for speaker recognition. *Informatica*, 1(21), 1-12.
6. Navakauskas, D., Paulikas, Š. (2006). Autonomous robot in the adverse environment: Intelligent control by voice. *Solid State Phenomena*, vol. 113 Mechatronic Systems and Materials, 325-329.
7. Ivanovas E., Navakauskas D. (2010). Development of biometric systems for person recognition: Biometric feature systems, traits and acquisition. *Electronics and Electrical Engineering*, 5(101), 87-90.
8. Ivanovas E., (2012). *Development and implementation of means for word duration signal processing* (doctoral dissertation), Vilnius: Technika, 128 p. [in Lithuanian].
9. Tamulevičius, G., Arminas, V., Ivanovas, E., Navakauskas, D. (2010). Hardware accelerated FPGA implementation of Lithuanian isolated word recognition system. *Elektronika ir elektrotechnika*, 3(99), 57-62.
10. Maskeliūnas, R., Rudžionis, A., Ratkevičius, K., Rudžionis, V. (2009). Investigation of foreign languages models for Lithuanian speech recognition. *Elektronika ir elektrotechnika*, 3(91), 15-20.
11. Driaunys, K., Rudžionis, V. E., Žvinys, P. (2009). Implementation of hierarchical phoneme classification approach on LTDIGITS corpora. *Information Technology and Control*, 4(38), 303-310.
12. Rudžionis, A., Ratkevičius, K., Dumbliauskas, T., Rudžionis, V. (2008). Control of computer and electric devices by voice. *Elektronika ir elektrotechnika*, No. 6, 11-16.
13. Raškinis, G., Raškinienė, D. (2003). Building medium-vocabulary isolated-word Lithuanian HMM speech recognition system. *Informatica*, 14(1), 75–84.
14. Šilingas, D., Telksnys, L. (2004). Specifics of hidden Markov model modifications for large vocabulary continuous speech recognition. *Informatica*, 1(15), 93–110.
15. Sigmund, M. (2003) *Voice Recognition by Computer*. Tectum Verlag, Marburg, 110 p.

SEABED IMAGE SEGMENTATION USING RANDOM FORESTS AND SUPPORT VECTOR MACHINES

Tadas RIMAVIČIUS*, Adas GELŽINIS*, Evaldas VAIČIUKYNAS*, Sergej OLENIN**, Aleksej ŠAŠKOV**

*Department of Electrical and Control Instrumentation, Kaunas University of Technology, Lithuania

**Klaipėda University Coastal Research and Planning Institute, Lithuania

Abstract: Segmentation of the seabed views is particularly important for ecologists for several reasons e.g. creation of seabed maps, determination of water pollution or tracking changes in seabed. The scope of this work is to classify seabed images with fewest possible mistakes and compare precision of random forests (RF) and support vector machines (SVM) for seabed views segmentation to five specific classes (such as sand, stones and brown, green, red seaweeds), and also to determine problems related with segmentation errors – class recognition mismatches.

Keywords: Seabed image segmentation, support vector machines, random forests, machine learning.

1. Introduction

Images of terrestrial environment are being used for different purposes since the beginning of last century; however image based maps of seabed are still rare. Although the amount of photo and video seabed images is increasing progressively, their processing is extremely labour intensive, while automatic seabed views recognition systems yet are very rare [1], [2]. On another hand, rapid and accurate interpretation of such images is crucially important for understanding of seabed nature, taxation of biological resources, distribution of sediment types and life forms, environmental impact assessments, and other applied and theoretical tasks. Acoustic sea bed segmentation methods are useful for primer (mud, sand gravel, rock) classification [3], [4], [5]. SOMF neural network has been implemented as a classifier for distinguishing up to 5 classes of the grey scale seabed images with accuracy ranging from 89 % to 93 % [6]. The additive colour model RGB based classification approach yet is rarely being used for automatic analysis of underwater images [7].

This article represents RGB seabed coating classification, implemented by using trainable segmentation idea with RF and SVM. Coating

classification from RGB images is the main difference from recently mentioned works, where the scope is to classify a primer.

2. Data

Mosaics of seabed views which were composed from photos taken in Norwegian Sea are used for seabed image recognition. These mosaics are used to create two matrixes of seabed views for solving recognition problem. Every matrix consists of 15 (3x5) different views. Matrix width and height is 1025x826 pixels, in total one matrix consists of 846650 pixels. Colour depth of single RGB pixel in image is 24-bit.

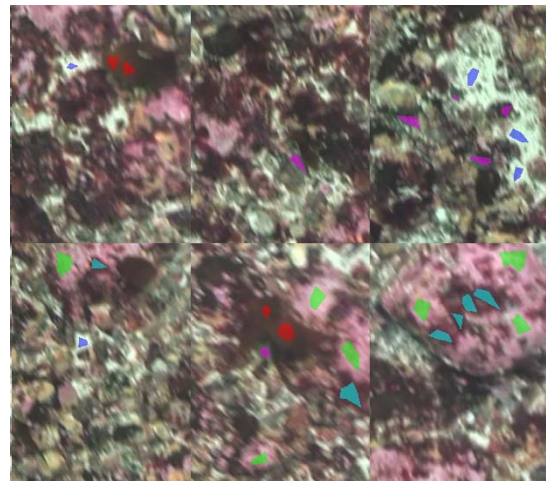


Fig. 1. Part of seabed image matrix with marked regions of prototype classes

There are selected 5 types of coating (such as sand, stones and brown, green, red seaweeds) in seabed and in seabed views. Therefore purpose of this work is to classify all pixels in matrix to five classes. In every seabed view matrix 50 regions of interests (ROI) are marked, 10 for each class. In total 100 ROI (17048 pixels) are marked for both matrixes. The area of

marked regions is different for every region in a general case.

3. Features

One of the most important criteria for pattern recognition is extraction of features. Every single pixel of original image is transformed by using various transformations [8] to create features vector. This vector is formed of 186 elements (number of features obtained by using every transformation presented in the brackets): Original image (1), Gaussian blur (5), Sobel filter (6), Hessian (48), Difference of Gaussians (10), Membrane projections (6), Maximum (5), Variance (5), Median (5), Mean (5), Minimum (5), Anisotropic diffusion (10), Bilateral (4), Lipschitz filter (5), Kuwahara filter (3), Structure filter (20), Neighbors (40), Hue (1), Saturation (1), Brightness (1). Small part of feature vector is presented in Fig. 2.

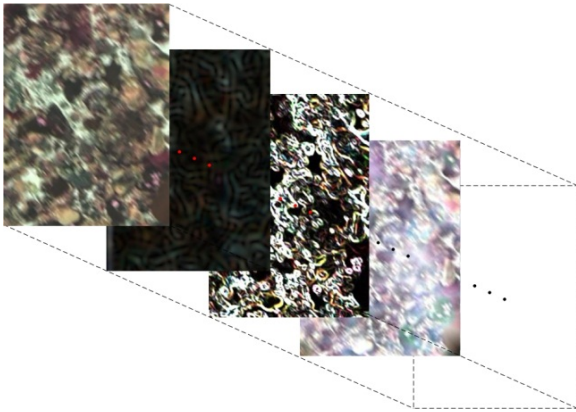


Fig. 2. Small segment of features vector

4. Classification

A RF and SVM are used for classification. As mentioned before trainable segmentation idea is used to solve segmentation problem. As it is shown in Fig. 1 classes of prototype are marked in seabed views matrix. Five different types of classes mean that classifier is trained to segment whole image to five classes using marked examples. An example of such classification result in training or testing phases is represented in Fig. 4. Afterwards trained classifier is applied to get results of classification from second (unseen) seabed views matrix.

4.1. Random forests

One classification tree as a classifier is quite weak. But large group of such classifiers creates a powerful tool called random forest. Operating principles of random forest [9] are based on putting input vector to the top of each tree and all trees are voting- the most frequent vote assigns to corresponding class. Two thirds of training input data are used to construct trees, one third is left for testing [10]. In this way constructed classifier does not need to be cross validated, after training phase classifier returns training (out of bag) error. Two main

parameters must be tuned in random forest: number of trees in the forest and number of features to be randomly selected from all available set of features (in this work 186).

4.2. Support vectors machines

The SVM is a successful modelling and prediction tool because of several reasons: ability to learn even with a small number of free parameters, robustness against model violations and outliers, computational efficiency [11]. The key idea of SVM is to construct a set of hyperplanes in higher dimension space which are used for classification in our work. Hyperplane must be organized to maximize margins between different input data sets (classes). SVM could be used with various (polynomial, multilayer perceptron, fourier series, splines) types of kernels [11]. One of the most popular and the only one used in this work is a radial basis function (RBF). The RBF kernel function is

$$K(\mathbf{x}_i, \mathbf{x}_j) = \exp\left(-\gamma \|\mathbf{x}_i - \mathbf{x}_j\|^2\right) \quad (1)$$

$$\gamma = \frac{1}{2\sigma^2} \quad (2)$$

where, σ is standard deviation.

The SVM and a RBF kernel function tuning of parameters consists of two tuning of parameters called hyperparameters C and γ . Parameter C shows how algorithm is strict to errors/margin errors. Gamma (γ) controls the degree of nonlinearity of the hyperplanes. The higher value of C - the stricter model, the higher value of γ - the nonlinear hyperplane separates different classes more.

5. Getting results

In testing phase classifier is applied for unseen image. After this phase classifier creates a probability map for each class as a result of classification. Example of probability map is represented in Fig. 3. Probability map consists of several probability parts (maps)-one map for each class. Every single pixel in each map obtains value which shows probability that the pixel belongs to corresponding class. Sum of one pixel values in all probability maps is equal to 1. The higher pixel value shows the bigger probability that corresponding pixel belongs to class. Pixels with the highest values compose segmented image. Example of segmented image is represented in Fig. 4.

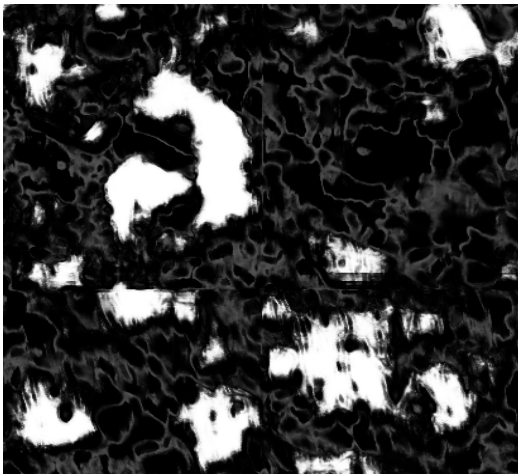


Fig. 3. Probability map example

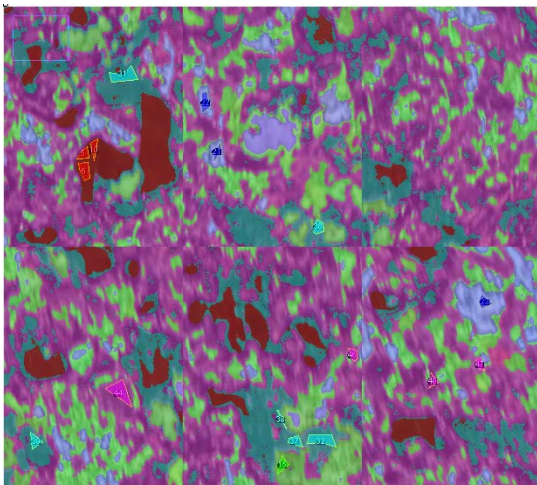


Fig. 4. Part of segmented seabed image

Every ROI pixel value in segmented image is checked and accuracy is calculated. Average recognition accuracy of two seabed views matrixes is calculated. Detailed RF and SVM classification accuracy dependences reviewed in next sections.

5.1. Results using Random forests

There are two parameters (features number and trees in forest number) tuned for better RF performance. Marked ROIs have different number of pixels for each class I general case; this means that some classes get better abilities to be learned. The same importance is given to all classes used homogeneous distribution of samples [8]. Three types of experiments are made to find out parameters impact on classification accuracy. Firstly the number of trees in RF is tuned when the number of features is randomly selected from the available set of features, where each node is equal to 13. Number of features is selected around (13) square root from all features (186) [10]. Best performance (82,38 %) is reached when tree number is 300. Figure 6 represents RF recognition accuracy dependent from randomly selected number of features per node with 300 trees in RF. As it is shown in Fig. 6 (green bars) accuracy is decreasing if number of features is

increasing (for samples without homogenization). If training samples are homogenized-accuracy increases if features number increasing. RF seabed views recognition accuracy is bigger if the same quantity training pixels assigned to all classes.

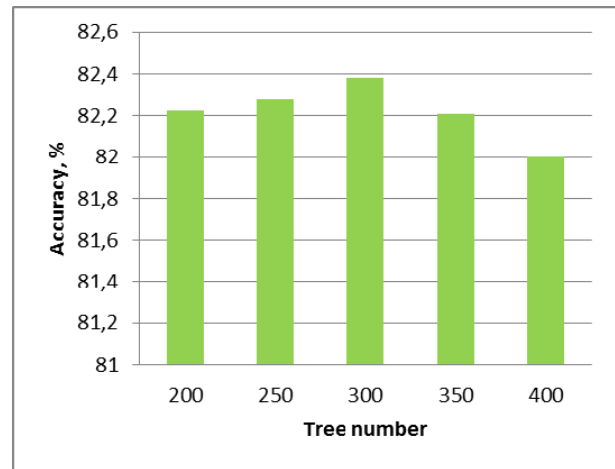


Fig. 5. RF accuracy dependency from tree number in RF

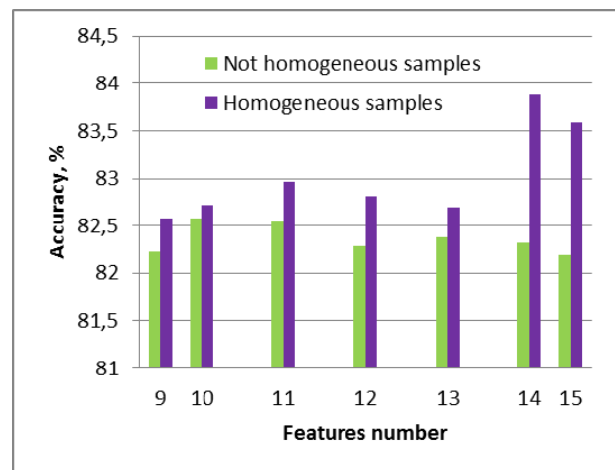


Fig. 6. RF accuracy dependency from features number

The best performance of RF (brown seaweeds 85,06; stones 89,51 %; sand 95,08 %; red seaweed 85,20; green seaweed 58,73 %; in general 83,88 %) reached with following RF parameters: number of trees 300, number of homogeneous features for node 14. The best precisions get with RF by classifying sand, the worst by green seaweeds.

5.2. Results using Support vector machines

For better SVM performance homogeneous distribution of samples are used and two parameters are tuned: C and γ . Figure 7 represents SVM recognition accuracy dependent from error tolerance parameter C. Best performance is reached with C = 200, experiments are made when $\gamma = 0,005$. Figure 8 shows SVM recognition accuracy dependent from hyperplane nonlinearity parameter γ . Best performance is reached with $\gamma = 0,003$, experiments are made when C = 200. The best performance of SVM with RBF kernel (brown

seaweeds 96,98; stones 90,84 %; sand 60,93 %; red seaweed 91,72; green seaweed 9,69 %; in general 77,23 %) is reached with following SVM parameters: C 200, γ 0,003. The best precisions get with SVM by classifying brown seaweeds, the worst by green seaweeds.

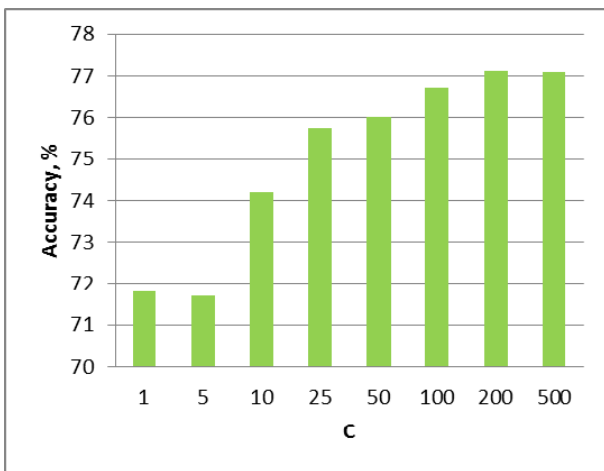


Fig. 7. SVM accuracy dependency from C

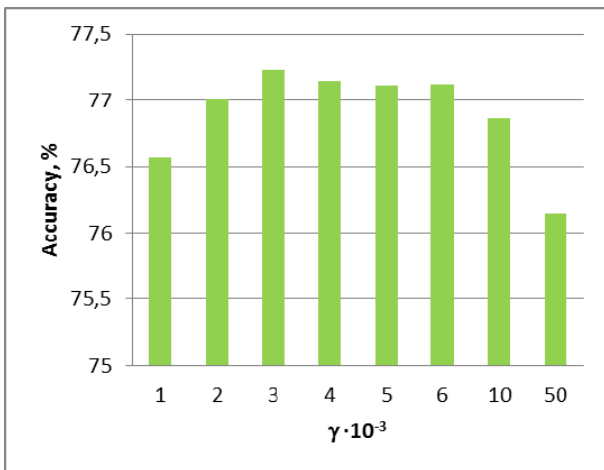


Fig. 8. SVM accuracy dependency from γ

Comparing best performances (RF 83,88 % and SVM 77,23 %) RF reaches better results by 6,65 %.

6. Conclusions

RF and SVM are effective tools for seabed classification. Seabed classification based on trainable segmentation idea using RF and SVM has been tuned for the best exploration of parameters sets. Every set of parameters has been tested and performance has been assessed. According to achieved results, RF classifies seabed images with bigger accuracy than SVM with RBF kernel do. It is easiest to recognize brown seaweeds and stones for both classifiers. Green seaweeds is the most difficult class to recognize. RF classification accuracy is better talking about sands, red seaweeds and green seaweeds, and SVM is better talking about brown seaweeds and stones. Therefore combination of classifiers could be used for better recognition performance. Every single pixel in probability maps would be assignable for corresponding

class with some weight according to classifier with better performance for that class.

7. References

1. Enomoto K.; Toda M.; Kuwahara Y, "Bottom Sediment Classification Method from Seabed Image for Automatic Counting System of Scallop" Proceedings of ISOT' 12, Inti. Symposium on Optomechatronic Technologies, Oct 2012
2. Rzhanov, Y. and Mayer, L. and Beaulieu, S. and Shank, T. and Soule, S. A. and Fornari, D. J, "Deep-sea Geo-referenced Video Mosaics" Proceedings of International Conference "Oceans 2006" Sep 2012.
3. Huseby R.B.; Milvang, O.; Solberg, R.; Bjerde, K.W., "Seabed classification from multibeam echosounder data using statistical methods," OCEANS '93. Engineering in Harmony with Ocean. Proceedings, vol.3, 18-21 Oct 1993 p. III/229,III/233
4. Hamilton L.J., "Topics In Acoustic Seabed Segmentation – Current Practice, Open Software, and Data Fusion" Proceedings of International Conference "Acoustics, Development, and the Environment - 2012" Fremantle, 2012.
5. Lubniewski, Z.; Chybicki, A., "Seabed classification using multibeam echosounder," Proceedings of International Conference "Information Technology, 2008", Gdansk, 18-21 May 2008., pp.1,4.
6. Jianhu Z.; Hongmei Z., "Seabed Classification Based on SOFM Neural Network," Proceedings of International Conference "Computer Science and Software Engineering, 2008" Wuhan, 12-14 Dec. 2008., vol.4, pp.902,905
7. Jerosch, K. , Lüdtkke, A. , Schlüter, M. and Ioannidis, G. T., "Automatic content-based analysis of georeferenced image data: detection of Beggiatoa mats in seafloor video mosaics from the Håkon Mosby Mud Volcano", Journal Computers & Geoscience, 33 , pp. 202-218, 2006
8. Carreras I.A. ; Cardona A.; Kaynig V., "Advanced Weka Segmentation (Fiji)" 2011, http://fiji.sc/wiki/index.php/Advanced_Weka_Segmentation#Training_features
9. Verikas A.; Gelzinis A.; Bacauskiene M., "Mining data with random forests: A survey and results of new tests" Pattern recognition, vol. 44, pp. 330-349, Feb. 2011
10. L. Breiman, "Random forests", Machine Learning vol. 45, pp. 5–32, Oct. 2001
11. Vapnik V. N., "Statistical Learning Theory", Wiley, New York, 1998.

THE METHOD FOR HUMAN-COMPUTER INTERACTION BASED ON HAND GESTURE RECOGNITION

Vidas RAUDONIS, Domas JONAITIS
Kaunas University of Technology, Lithuania

Abstract: This paper gives an overview of gesture recognition concept and the usefulness of the human - computer interaction in today`s society. Most popular methods are observed and their practical applicability. The paper presents the algorithm for computer control based on hand gestures captured using standard web-camera. The methods for hand gesture and analyzed and experimentally investigated in this work. This paper also takes into account the fact that gesture recognition and interpretation takes place in real time in a changing environment. The experiments show the advantages and disadvantages of tested gesture recognition method: the ability to adapt in changing environments, commands precision, accuracy and command recognition speed.

Keywords: Real-time hand gesture recognition, hand segmentation, human-computer interaction.

1. Introduction

Computer human interaction is a very promising field of research. One of the most popular ways is the control of computer (machine) with hand gesture. With such rapid advances in technology, we can find dozens of this method advantages. Such as, for example: a) The computer input device such like mouse or keyboard would become redundant, and computer(machine) management can become much simpler;b)it is possible to use this method like a form of entertainment(for computer games); c)The household routine could become also much simpler: it is possible to apply this method with special combination of hand gesture for example: to lock or unlock the door, open the garage, or turn off the lights, and for many other everyday things.d) After development of this method, after reach the high reliability of this method, it is possibly to use this method as a way to contact between people with disabilities (for example deaf people) and many other advantages.

Hand gesture recognition is one way of the explorations of the human-computer interaction. It is studied in many directions. It is very difficult and there is not one method, for realizing this procedure. It is very difficult to overlook all attempts to study, or realize this method, because there are a lot of different ways, in different countries, in different time, in different ideas. It is possible; just overlook the main evolution steps, to take the idea from them, and to adapt the principal features in our gesture recognition algorithm. This work amount is limited, so we can mark just some of historical events, trying to analyze this method.

As a good start, we can highlight an algorithm of skin color segmentation in the HSV color space and using a back propagation neural network to recognize gestures from the segmented images. This method was suggested by Kjeldsen and Kender1. We can also exclude a system, which was offered by Yoon2, and which was consisting of three different modules: hand localization; tracking and gesture spotting. Xiaoming and Xing suggested an RCE neural network- based color segmentation algorithm for hand segmentation, extract edge points of fingers as points of interest and match them based on the topological features of the hand, such as the center of the palm 3, and other ways for this method, which is really difficult to overlook. But we can signify the most important thing if we want to improve reliability of this method. We must find the most easy and comfortable way to realize the control of computer with hand gesture.

The aim of this paper is to develop and experimentally investigate a method for computer control based on hand gesture recognition. We will need just standard equipment, for our test: laptop with integrated webcam. With that idea, that hand gesture could be a great computer input device; the experiment is combination in different time of the day, adjusting speed and accuracy of the control commands, using the standard lighting in the room. In this experiment used two methods Statistical Gaussian and transformation.

2. State of the art

Most popular hand tracking and gesture recognition methods are overviewed in this chapter. We can exclude some big parts of analyze of this method: 3D model-based (a) skeletal) volumetric); appearance-based (a) deformable 2D-templates b) image sequences). Our method uses a 2D image information, so we will not go into the other above-mentioned methods for hand gesture detection. Anyway, to realize this method, we need to adapt one of mathematical algorithms. So the aim of this chapter is to overlook existing mathematical algorithms;

Hidden Markov Model (HMM) – is one of the most popular and interesting technique for gesture recognition. This technique is a statistical Markov model in which the system being modeled is assumed to be a Markov process with unknown parameters. An HMM can be considered as the simplest dynamic Bayesian network. The mathematics behind the HMM was developed by L. E. Baum and others [45, 67, 8]. Purpose-to recognizes the hidden parameters from visible data. Recognize state of a HMM data can be applied to dynamic Bayesian network. In a hidden Markov model, the state is not directly visible, but output, dependent on the state, is visible. Each state has a probability distribution over the possible output tokens. Therefore the sequence of tokens generated by an HMM gives some information about the sequence of states. Note that the adjective 'hidden' refers to the state sequence through which the model passes, not to the parameters of the model; even if the model parameters are known exactly, the model is still 'hidden'. Also hidden Markov model can be adapt to difficult distribution processes, where the states emit the observations according to some probability distribution. One way is to use Gaussian distribution for this model.

Eickeler, Kosmala and Riggol analyzed gesture recognition system using HMM, and they made several improvements of the system: the improvements include position-independent recognition, rejection of known gestures, and continues online recognition of spontaneous gestures. This solution makes the system much comfortable to work online [9]. Mahmoud Elmezain, Ayoub Al-Hamadi, Jörg Appenrodt, Bernd Michaelis suggested an automatic system that recognizes both isolated and continuous gestures for Arabic numbers (0-9) in real-time based on Hidden Markov Model (HMM). To handle isolated gestures, HMM using Ergodic, Left-Right (LR) and Left-Right Banded (LRB) topologies with different number of states ranging from 3 to 10 is applied [10]. Yona Falinie Abdul Gaus and Farrah Wong suggested a hand gesture recognition system to recognize isolated Malaysian Sign Language (MSL). The system consists of four modules: collection of input images, feature extraction, Hidden Markov Model (HMM) training, and gesture recognition. HMM fitted to recognize the input gesture. The gesture to be recognized is separately scored against different states of HMMs. The model

with the highest score indicates the corresponding gesture [11].

Bayesian network (BN) – is probabilistic graphical model that represents a set of random variables and their conditional dependencies via a directed acyclic graph (DAG). For example it is possible to force a signal with hand gesture in different ways. The model which can learn is called dynamic Bayesian network. Heung-II Suk, Bong-Keel Sin and Seong-Whan Lee analyzed method for recognizing hand gestures in a continuous video stream using a dynamic Bayesian network or DBN model. The method of DBN-based inference was preceded by steps of skin extraction and modeling, and motion tracking. Then we develop a gesture model for one- or two-hand gestures. They are used to define a cyclic gesture network for modeling continuous gesture stream algorithm for hand gesture recognition [12].

Artificial Neural network are composed of interconnecting artificial neurons (programming constructs that mimic the properties of biological neurons) for solving artificial intelligence problems without creating a model of a real system. Neural network algorithms abstract away the biological complexity by focusing on the most important information. This method is also studied in different directions, and is very comfortable for gesture recognition. John Weissmann, and Falf Salomon, analyzed this method for virtual reality applications. For the application, specify hand gestures, such as “fit”, “index finger”, and “victory sign”, have been defined. Their method compares the performance of different neural network models, such as back-propagation and radial-basis functions, which are used by the recognition system to recognize the actual gesture [13]. Baran Çürüklü, Johan Hägg, Batu Akan and Lars Asplund proposed a system which can learn a first time user's hand gestures rapidly. Artificial neural networks trained with the evolution strategy technique. The gesture recognition system is an integrated part of a larger project for addressing intelligent human-robot interaction using a novel multi-modal paradigm [14]. Chun Zhu and Weihua Sheng proposed an online hand gesture recognition algorithm for a robot assisted living system. Neural network-based gesture spotting method is combined with the hierarchical hidden Markov model (HHMM) to recognize hand gestures. In the segmentation module, the neural network is used to determine whether the HHMM-based recognition module should be applied. In the recognition module, Bayesian filtering is applied to update the results considering the context constraints [15]. Chang Tan and Nanfeng Xiao suggested a new method; they conduct an adjustment algorithm for the traditional RCE neural network. The new RCE neural network runs faster and performs better in anti-noise than the traditional one. Firstly, they applied the improved RCE neural network to hand image segmentation. Secondly, they used Freeman chain code to extract the distance from hand edge to the palm-center as feature vectors. Finally, they use those feature vectors as the input of RBF neural network and train the RBF neural network [16]. Hui Zhang, Yongqi Wang, Chen Deng studied an

algorithm of gesture recognition based on simulated annealing BP neural network. This algorithm extracts the edge outline by skin color division and recognition feature of the distance between center and edge of binary gesture image. And it combines simulated annealing with BP neural network, which has both the learning ability and robustness of the neural network and the global optimization of simulated annealing, avoids the slow convergence and prevents it from falling into local minimum [17].

This is just some method of hand gesture detection. All mentioned methods have their personal advantages and disadvantages. It should be very difficult to cut out one method, because all of the mentioned methods were tested in many ways.

3. Algorithm for hand gesture recognition

a) Hand contour extraction

For hand gesture detection, we use a background subtraction method. This is the difference between the real-time image and the background. Our model uses Gaussian method. Background is a static image which we get with a webcam. Therefore, the hand contour is identified by the program as some changes in the background. An image is divided into N regions by color, which is described by a Gaussian distribution function. Therefore, program code, detecting a contour of the hand (this is a learned gesture) can carry out the assigned command. We want to signify some important features of this method, the hand and the background color must be significantly different, because in different ways it is difficult for program to recognize the gesture. Also very important is the lighting, which also has a significant impact, for the program.

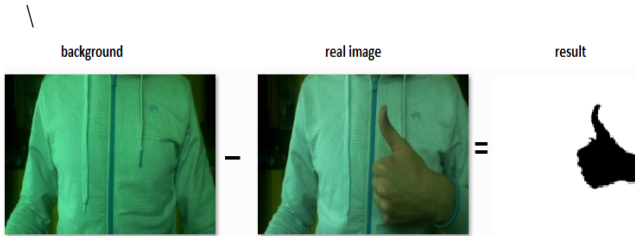


Fig. 1. Background subtraction main visual steps

The Gaussian background model describes the color distribution of the image region. Calculate the distribution of the parameters, we need to calculate μ_c of the color channel i^{th} and the matrix K_i between color channels of i^{th} region of the image.

$$\mu_c(u, v) = \frac{1}{N} \sum_i^N B_c(u, v, i), \quad (1)$$

$$K = \begin{bmatrix} V_{11} & V_{21} & V_{31} \\ V_{12} & V_{22} & V_{32} \\ V_{13} & V_{23} & V_{33} \end{bmatrix}, V_{ij} = cov(C_i, C_j) \quad (2)$$

For each region we are using Gaussian distribution function:

$$\Psi = \exp[-(\mathbf{c} - \boldsymbol{\mu}_i)^T \mathbf{K}_i^{-1} (\mathbf{c} - \boldsymbol{\mu}_i)], \quad (3)$$

$$p_i(\mathbf{c}) = \frac{1}{(2\pi)^2 \sqrt{\det(\mathbf{K}_i)}} \cdot \Psi \quad (4)$$

V_{ij} -covariance value between two color channels.

$C(c)$ -[RGB]-matrix of the pixels values.

$R(r)$, $G(g)$, $B(b)$ -pixels values,

$l=3$ - number of the channels.

Each new image is recognized as the background image if it satisfies a condition:

$$\begin{cases} 0 & \text{if } \sum_{i=1}^M p_i < \theta \\ 1 & \text{otherwise} \end{cases} \quad (5)$$

$M(u, v)$ - mapping matrix.

Mapping image (in Fig. 1 called "result") is filtered from the noise and extracting only the hands contour if it is identified, we actuating the command, which is attached to that gesture.

b) Control algorithm

For this experiment, we are using a laptop with an integrated webcam, but in any case, this model can be adapted for a lot of kinds of machines, with equipped web camera. Prerequisites - the camera view must be complete outline of the hand. In this case, the background is a t-shirt, worn by the user. The problem with this approach, t-shirt color bitmaps do not coincide with the hand.

Our experiment is mouse control with hand gesture. Commands used in this experiment are as follows: forward, backward, left, right, left mouse click, and right. (Fig. 2)

Each control command, use the appropriate hand gesture. For Gesture recognition is using Discrete Fourier Transformation (DFT). This method is designed to normalize the x and y coordinates.

Hand gesture similarity we obtain using the formula of Euclidean distance .

$$\sqrt{\sum_{k=0}^n (F_k - F_k^i)^2} \quad (6)$$

F^i -template coefficients, F - new real time coefficients, k -index of element in F vector.

Gesture is recognized when the minimum value found among all measurements (ϵ). Gesture is identified by a class Y that satisfy the condition:

$$Y = \begin{cases} i & \min_i(\epsilon) < \theta_\epsilon \\ 0 & \text{otherwise} \end{cases} \quad (7)$$

θ_ϵ - Threshold value of the similarity measure.

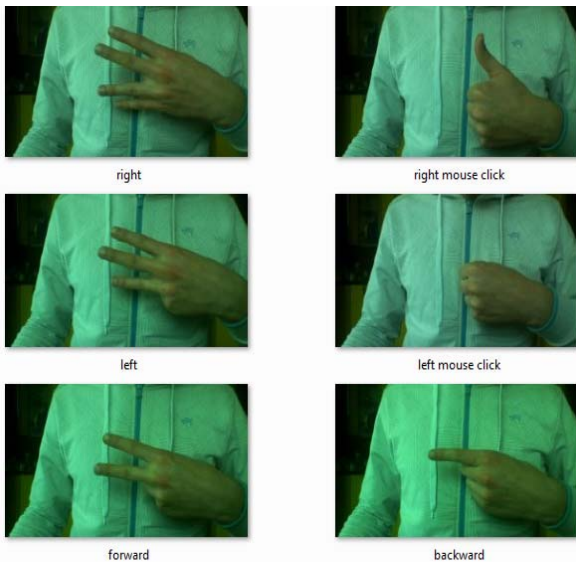


Fig. 2. Possible variations of hand gestures used in this work

4. Results

Experiment can be divided into several major stages: First stage: a training phase in which the contour of the hand is formulated, and saved the coefficient of the hand gesture for the further stage.

Second stage: System testing, in which users give certain commands with hand gestures to computer. In this stage it is possible to see reliability of the method, and control commands accuracy.

Aim of this paper is hand gesture recognition accuracy, and commands rating. 15 persons were participating in this experiment. The first stage of the experiment training, was executed by a single person, but the second stage (control with hand gesture) were tested of 15 persons. During the experiment has been observed that the team accuracy increases when the threshold is higher than 150. Hand gesture contour was saved in training phase by one person, so it is not surprising that some control commands have not always been recognized, because of hand contour difference. But the experimental results are good enough, as exceeds 90 percent. All control commands were repeated 20 times, by each person, and we can make conclusion that recognition rating, depends, of accuracy of repeating more similar gesture like in training stage.

The first table (Fig. 3) were tested all learned control commands. Each person, tested all command 20 times. So in this table we see a percentage of commands accuracy.

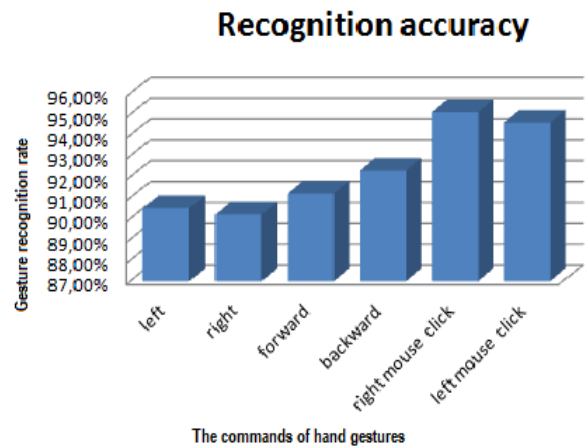


Fig. 3. Commands accuracy

In that idea that we are planning to adapt this method, for everyday routine, this experiment was also repeated on a regular basis at different illumination without affecting the experimentation results with any additional light sources. The results are not very good, that means that there are a lot of prospective works for the future.

This test was performed on the same principle as the first, but the task was repeated at different times: starting in the morning and ending in the evening, to get a curve (Fig. 4) which reflected the impact of illumination for hand gesture recognition.

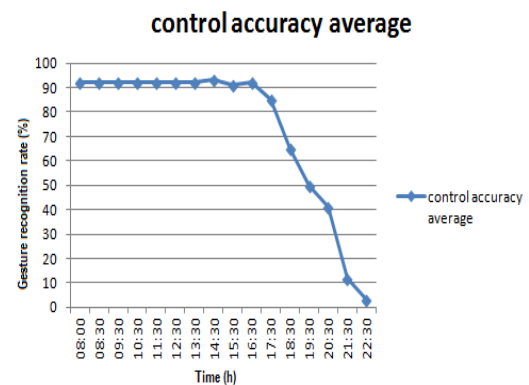


Fig. 4. Lighting influence for gesture recognition

5. Conclusions

In this paper, one method of human – computer interaction was presented. For our method are very important few things: hand contour form, recognition accuracy, lighting, and speed of the recognition and execution of the command. Our control algorithm is able to process about 10 frames per second. It is quite good result.

Hand gesture algorithm using Gaussian method with sufficient accuracy can realize commands that were assigned during training time. However, the necessary conditions - ideal day lighting, and different shades of colors between the background and the contour of the hand. Therefore, to apply this method at home, or

industry, we have to solve these problems (For example to adapt mathematical algorithm, which can adapt in changing lighting). If the terms of the ideal conditions, then perform commands accuracy is high enough, the command execution speed is also very good.

In order to improve the accuracy of the command carried out, it should be a few important things: to improve and optimize the hand gesture detection algorithm that would recognize the circuit with different hand angles, and use a new type of sensor Canon camera that can record video at 0.03 lux. This device allows you to remove noise contained from the video in the bad illumination.

6. References

1. R. Kjeldsen and J. Kender, "Finding skin in color images," IEEE Second International Conference on Automated Face and Gesture Recognition, Killington, VT, USA, pp. 312- 317, October 1996.
2. Ho-Sub Yoon, Jung Soh, Younglae J. Bae, Hyun Seung Yang, "Hand gesture recognition using combined features of location, angle and velocity" ,South Korea, pp.1491-1501,2001.
3. Xiaming Yin and Xing Zhu, "Hand Posture Recognition in Gesture-Based Human-Robot interaction", Industrial Electronics and Applications,2006 1st IEEE Conference, pp.1-6.
4. Baum, L. E.; Petrie, T. (1966). "Statistical Inference for Probabilistic Functions of Finite State Markov Chains". The Annals of Mathematical Statistics **37** (6): pp. 1554–1563.
5. Baum, L. E.; Eagon, J. A. (1967). "An inequality with applications to statistical estimation for probabilistic functions of Markov processes and to a model for ecology". Bulletin of the American Mathematical Society **73** (3): pp. 360-363.
6. Baum, L. E.; Sell, G. R. (1968). "Growth transformations for functions on manifolds". Pacific Journal of Mathematics **27** (2): pp.211–227.
7. Baum, L. E.; Petrie, T.; Soules, G.; Weiss, N. (1970). "A Maximization Technique Occurring in the Statistical Analysis of Probabilistic Functions of Markov Chains". The Annals of Mathematical Statistics **41**: pp.164-171.
8. Baum, L.E. (1972). "An Inequality and Associated Maximization Technique in Statistical Estimation of Probabilistic Functions of a Markov Process". Inequalities **3**: pp.1–8.
9. S. Eickeler, A. Kosmala, G. Rigoll. "Hidden Markov Model based Continuous Online Gesture Recognition". IEEE Pattern recognition, 1998, Proceedings, Fourteenth International Conference, pp. 1206-1208 vol.2.
10. Mahmoud Elmezain, Ayoub Al-Hamadi, Jörg Appenrodt, Bernd Michaelis. "A Hidden Markov Model – Based Continuous gesture recognition System for hand Motion Trajectory". Pattern recognition, 2008. 19th International conference. pp. 1-4.
11. YonaFalinie Abdul Gaus, Farrah Wong. "Hidden Markov Model- based Gesture Recognition with Overlapping Hand- Head/hand-Hand Estimated using Kalman Filter". Intelligent Systems, Modelling and Simulation (ISMS), 2012 Third International Conference. pp. 267-267.
12. Heung –II Suk, Bong-Kee Sin and Seong –Whan Lee, "Hand gesture recognition based on dynamic Bayesian network framework". Pattern recognition, Volume 43, Issue 9, September 2010, pp.3059-3072.
13. John Weissmann, Falf Salomon "Gesture Recognition for Virtual reality Applications Using Data Gloves and Neural Networks" neural networks, 1999, IJCNN'99. International Joint Conference. pp.2043-2046 vol.3
14. Baran Çürüklü, Johan Hägg, Batu Akan and Lars Asplund. "Gesture recognition using Evolution Strategy neural network". Emergin technologies and Factory automation, 2008, ETFA, IEEE International Conference, pp. 245-248
15. Chun Zhu and Weihua Sheng. "Online Hand Gesture Recognition Using neural network Based Segmentation". Intelligent Robots and Systems, 2009, IROS 2009. IEE/RSJ International conference, pp 2415-2420.
16. Chang Tan and Nanfeng Xiao "Improved RCE Neural Network and Its Application in Human-Robot Interaction Based on Hand gesture Recognition". Information Science and Engineering (incise), 2010 2ND International Conference. pp 1260-1263.
17. Hui Zhang, Yongqi Wang, Chen. "Application of gesture Recognition Based on Simulated Annealing BP Neural Network". Electronic and Mechanical Engineering and Information technology (EMEIT), 2011 International Conference. pp.178-181
18. http://news.cnet.com/8301-11386_3-57572446-76/canon-video-sensor-prototype-can-see-in-the-dark/, 2013.04.04

REAL-TIME VIBRATION REDUCTION IN UAV'S IMAGE SENSORS USING EFFICIENT HOUGH TRANSFORM

David AFOLABI¹, Zhun SHEN², Tomas KRILAVIČIUS^{3,5}, Vladimir HAHANOV⁵, Eugenia LITVINOVA⁵,
Svetlana CHUMACHENKO⁵, Ka Lok MAN^{1,4,5}, Hai-Ning LIANG¹,
Nan ZHANG¹, Tomas ŽALANDAUSKAS⁵

¹Xi'an Jiaotong-Liverpool University, Suzhou, China

²IBM China, Suzhou, China

³Vytautas Magnus University, Kaunas, Lithuania

⁴Kharkov National University of Radioelectronics, Kharkov, Ukraine

⁵Baltic Institute of Advanced Technologies, Lithuania

Abstract: This paper explores use of Hough transform to detect and track angular changes between a series of images acquired by vision sensors attached to unmanned aerial vehicles (UAV) and are used in traffic surveillance. The small size and atmospheric conditions can lead to unstable flying and this can induce vibration to the pictures. In this research it is proposed that the vibration in the acquired images can be reduced by using the angular variation as feedback to stabilize the motion of the UAV as it captures subsequent frames.

Keywords: Vibration reduction, image/vision sensor, UAV stabilization, traffic surveillance.

1. Introduction

Two main types of digital image sensors are charge-coupled device (CCD) and complementary metal-oxide semiconductor (CMOS). These devices work by converting the amount of light energy sensed on each pixel's photodiode into voltages which is converted into digital information. These technologies produce quality images with good signal-noise-ratio but they are still susceptible to vertical smear and rolling shutter effect.

The negative effects are caused by the image acquisition scheme in which the sensor sequentially scans each line of the image's frame vertically or horizontally. The effect is significant if the read-out time is slow, the image contains fast moving objects, or the UAV (unmanned aerial vehicle) flight is unstable with high frequency vibration.

In this paper, Hough transform is applied for line detection that is used to improve flight stability in real-time by providing feedback about the amount of distortion in the acquired images.

In the particular use-case of vehicle traffic surveillance [1] the image is usually comprised of straight lines from road marking, road signs, and other stationary objects in which line features can be extracted and measured for angular variation. The data from this process is then transmitted to the actuator of the UAV. In our test CMOS cameras are used because they are smaller, consume less power, and have a faster read-out speed.

2. Proposed methods

In computer vision and image processing, there are various methods for line/circle/feature detection. Hough transform (HT) has been applied in motion analysis, shape extraction and image registration [2] [3]. HT identifies lines within an image by superimposition with the Hough space defined by the following formula:

$$\mathbf{r}(\theta) = x_0 \cdot \cos \theta + y_0 \cdot \sin \theta \quad (1)$$

Data points are determined to be a line if they contain distance, r , and angle, θ , that correlate (*see Fig. 1*).

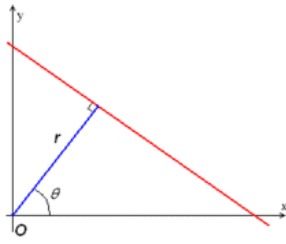


Fig. 1. Polar coordinate of Hough transforms

Fig. 2 shows the Hough transform of a simplified street image showing three distinct correlating points which are the two edges of the road and the road surface marking. The process involves running an edge detection technique (such as Canny edge detection) on an image to produce data points along the boundary of different blobs in the image. The data points are then accumulated in the Hough transform matrix and if the value of an element of the matrix is greater than desired threshold, it is then identified as a line in the image. The distance, r , and angle, θ , for each line is now obtainable.

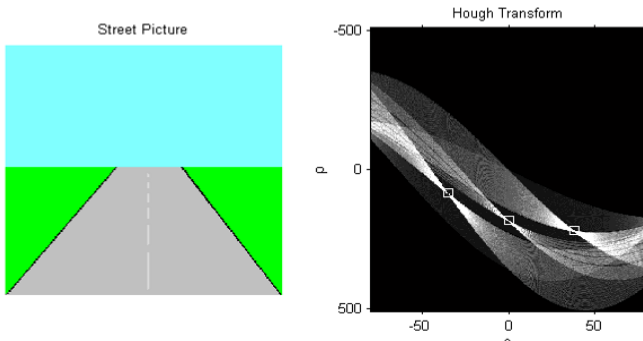


Fig. 2. Hough transform (*right*) of street picture (*left*) showing detected lines

After selecting the prominent lines from the first image, in subsequent images these lines are then continuously monitored for angular changes. Image registration is the process of overlaying a series of images taken from different viewpoints by the image sensor in order to match them to a reference (base image). The images acquired from the UAV's camera will be geometrically distorted (i.e. rotated, translated, skewed, scaled) due to the vibration. Therefore the measured angle, θ , needed for proper image registration is used as a parameter to calculate and adjust the speed of the servomotors of the UAV, consequently fine tuning its roll, pitch, and yaw (*see Figure 3*).

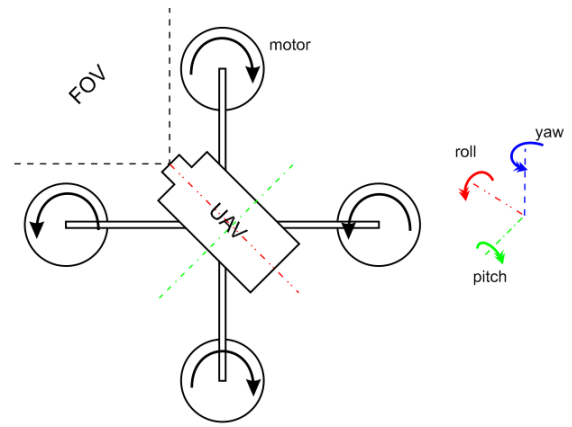


Fig. 3. A quadcopter UAV

3. Implementation and evaluation

The proposed method for vibration reduction was implemented in MATLAB as follows:

- Step 1: Convert image to grayscale
- Step 2: Apply edge detection technique to highlight image intensity boundaries.
- Step 3: Compute HT over a range of θ (in order to exclude horizontal line for instance)
- Step 4: Select n numbers of prominent line (houghpeaks)
- Step 5: Choose the longest line which will be continuously tracked while it remains in the scene.
- Step 6: Extract only the segment of the image containing the line (to eliminate time wasted on computing the other pixels in the image)
- Step 7: Continuously track the rotation in the selected segment on subsequent image
- Step 8: Return the output of angular displacement
- Step 9: Use the detected angular displacement as a feedback to the motors of the UAV.

At first, in order to track the rotation MATLAB's `vision.GeometricTransformEstimator` function was applied; it uses RANdom SAMpling Consensus (RANSAC) algorithm to compute similarity transformations. From Fig. 4 it can be seen that the algorithm detected matching points, and was able to recover the scale and rotation of 1.058 and 7.153 from the original deformation input of 1.1 and 6, respectively.

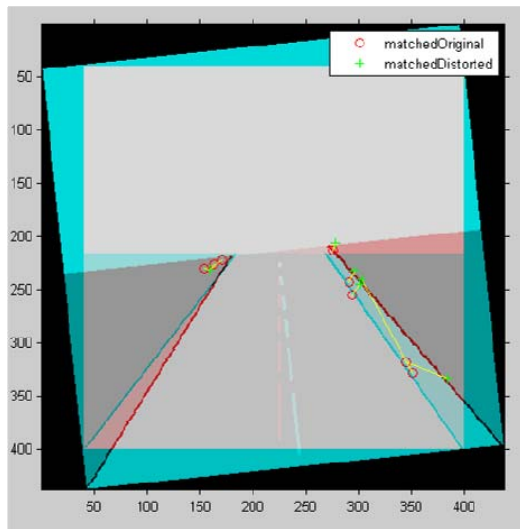


Fig. 4. Application of MATLAB image registration function

Whilst this method provided a relatively close result, it could not be applied on a smaller segment of the image as a result of limited information for matching the two images. Therefore a simpler but more efficient method for detecting the image transformations within a small segment will be necessary as it speeds up the time needed to recover the distortion angles during the UAV flight for adequate feedback.

4. Analysis of results

After hundreds of trials the average θ (theta) error was significantly low when the angle of distortion was less than 10 degrees. The scale and theta values were generated randomly and it was noted that some angles and scales were unsolvable. Therefore the above algorithm can be improved by recomputing HT to find another prominent line in the scene if the original line is lost due to scale or rotation as the UAV moves. In addition, the above method uses random sampling to detect matching points, thus it can be improved by searching neighboring angles incrementally for the displaced line because the vibrations distortion affects image pixels in close proximity.

5. Conclusion and future work

In this paper, the use of Hough transform to reduce the image vibration in unmanned aerial vehicles to support the monitoring of road traffic by selecting the most prominent line in the scene for stability feedback during flight was proposed.

An implementation of a working prototypical system based on the proposed solution is planned. After accomplishing the set objective further research can be carried out on predicting the vibration effects in

subsequent frames using the information from the current time window, and also computational parallelizing of HT [4], and finally to develop hardware that are optimized to process HT in real time [5].

6. Acknowledgements

The research work presented in this paper was partially supported by research development funding of Xi'an Jiaotong-Liverpool University Final Year Project Fund and. Transcend Epoch International Co., Ltd, Hong Kong.

7. References

1. Afolabi D., Man K.L., Liang H.L., Lim G.L., Shen Z., Lei C., Krilavičius T., Yang Y., Cheng L., Hahanov V., and Yemelyanov I. A WSN Approach to Unmanned Aerial Surveillance of Traffic Anomalies: Some Challenges and Potential Solutions "10th East-West Design & Test Symposium – EWDTs'12", Kharkov, Ukraine, September, 2012, pp. 91-95.
2. Nash J, Carter J., and Nixon M. The velocity Hough transform: a new technique for dynamic feature extraction, "Image Processing, 1997. Proceedings, International Conference, 26-29 Oct 1997, pp. 386-389.
3. Sarvaiya J., Patnaik S., and Kothari K. Feature Based Image Registration Using Hough Transform "Integrated Scientific, Engineering and Management (ISEM)" URL: <http://isems.org/images/extraimages/50.pdf>, (Accessed 25 January 2013)
4. Satzoda R., Suchitra S., Srikanthan T. Parallelizing the Hough Transform Computation, "Signal Processing Letters IEEE", 2008. vol. 15, pp. 297-300.
5. Nakanishi M. and Ogura T. Real-time line extraction using a highly parallel Hough transform board "Image Processing, 1997. International Conference – 26-29 Oct 1997", vol. 2, pp. 582-585.
6. Duan D., Xie M., Mo Q., Han Z. and Wan Y. An improved Hough transform for line detection, "Computer Application and System Modeling (ICCSM), 2010 International Conference", vol. 2, pp. V2-354-V2-357.
7. Lefevre S., Dixon C., Jeusse C. and Vincent N., A Local Approach for Fast Line Detection "RFAI publication: IEEE International Conference on Digital Signal Processing", Santorini (Greece), July 2002, pp. 1109-1112
8. Wikipedia (2013), "Image Sensor", URL:http://en.wikipedia.org/wiki/Image_sensor (Accessed 25 January 2013)

THE APPLICATION OF STABLE AND SKEW T-DISTRIBUTIONS IN PREDICTING THE CHANGE IN ACCOUNTING AND GOVERNANCE RISK RATINGS

Leonidas SAKALAIUSKAS*, Zivile KALSYTE**, Ingrida VAICIULYTE*, Irmantas KUPCIUNAS**
*Vilnius University, Institute of Mathematics and Informatics, Lithuania; **Kaunas University of Technology,
Department of Electrical & Control Equipment, Lithuania

Abstract: The parameters of the stable distribution collectively and skew t-distribution, calculated on the basis of stock data (Close and Volume), have been used as Random Forests inputs and applied to predict the direction of the change in future AGR rating (AGR rating will rise, drop or remain unchanged). Three models have been developed: 1) Model 1 uses the present-day AGR rating, Close and Volume parameters as well as the stable distribution parameters defining the past changes in stock; 2) Model 2 uses the present-day AGR rating, Close and Volume parameters as well as the skew t-distribution parameters defining the past changes in stock; 3) Model 3 uses the present-day AGR rating, Close and Volume parameters as well as the stable distribution and skew t-distribution parameters defining the past changes in stock.

Keywords: Random Forests, stable distribution, skew t-distribution, prediction, AGR rating.

1. Introduction

It emerged that when one attempts to apply the Gaussian distribution in a stock market with great price leaps, the curve continuity disappears. Thus, the Gaussian distribution is, generally, inapplicable in an analysis of economic indicators. Moreover, that law takes no account of asymmetry between the investors' expectations and financial results. An investor seeks to know as much as possible about investment alternatives, however, this is not always possible.

The investors' opinion about the change in the enterprise's results is described by the parameters of two distributions (stable and skew t-distribution) that are calculated on the basis of stock price data (Close and Volume). These distributions have been chosen because of the fact that stock price distributions are characterised by asymmetry and a heavy tail.

Mean of distributions points to the prevailing investor expectations from the point of view of the enterprise,

i.e. whether the majority of investors assess the activity of the enterprise and its prospects positively or negatively. Tails of distributions indicate the instability of the investors' opinions about the enterprise's results and its prospects. This may be related to an incorrect provision of the enterprise's results, which is reflected by the AGR rating.

The proprietary Accounting & Governance Risk (AGR) rating is a measure of corporate integrity based on forensic accounting and corporate governance metrics as well as an indicator of aggressive corporate behaviour, which can put stakeholders at risk. The AGR score is based on a quantitative model that weights specific accounting and governance metrics derived from corporate reporting. The score ranges from 0 to 100, with lower scores indicating higher risk [5, 10, 11]. Thus, the history of AGR rating reflects the practice of presenting enterprise's financial data (financial statements). If in the past an enterprise was presenting its data incorrectly, then one may expect that it will continue doing so in the future. The parameters of distributions calculated from stock data reflect the change in investors' opinions.

2. Random Forests

Random Forests consist of an ensemble of separate decision trees. Each decision tree is trained by separating at random from the training sample a certain part (two thirds) of the data, while the rest of the data (Out of Bag (OOB) data) is used for testing. An error of the tested part of the data decreases while increasing the number of decision trees [3].

Importances of the features are measured by using the OOB data. The selected features depend on the amount of the data falling into OOB. Therefore, while selecting the most important features, 7 different amounts of the data falling into OOB were taken. If the number of features is marked as N , then the number of the features falling into OOB was selected as

follows: $\sqrt{N}-2, \sqrt{N}-1, \sqrt{N}, \sqrt{N}+1, \sqrt{N}+2$. The mean of importances of the features was calculated for the OOB data. By employing the backward elimination of features, each 5% of the least important features were removed until there would remain only 1 feature. It was sought to find out under which set of features the Out of Bag error was lowest. Such features and were considered to be the most important ones [6, 7].

3. Stable distribution

The authors start from the Close and Volume empirical data analysis, by estimating the mean, variance, skewness and asymmetry. Then, they fit data series to the normal and α -stable distributions.

Following the well-known definition, see [2, 3], a random vector X has stable distribution and denotes $X = S_\alpha(\sigma, \beta, \mu)$, here S_α is the probability density function, if X has a characteristic function (2) of the form:

$$\phi(t) = \begin{cases} \exp\left\{-\sigma^\alpha \cdot |t|^\alpha \cdot \left(1 - i\beta \operatorname{sgn}(t) \tan\left(\frac{\pi\alpha}{2}\right)\right) + i\mu t\right\}, & \text{if } \alpha \neq 1 \\ \exp\left\{-\sigma \cdot |t| \cdot \left(1 + i\beta \operatorname{sgn}(t) \frac{2}{\pi} \cdot \log|t|\right) + i\mu t\right\}, & \text{if } \alpha = 1 \end{cases} \quad (1)$$

Each stable distribution is described by 4 parameters: the first one and most important is the stability index $\alpha \in (0; 2]$, which is essential when characterizing financial data. The others, respectively are: skewness $\beta \in [-1, 1]$, a position $\mu \in \mathbf{R}$, the parameter of scale $\sigma > 0$.

The probability density function of α -stable distribution is:

$$p(x) = \frac{1}{2\pi} \int_{-\infty}^{+\infty} \phi(t) \cdot \exp(-ixt) dt \quad (2)$$

In the general case, this function (2) cannot be expressed in closed form. The infinite polynomial expressions of the density function are well known, but it is not very useful for Maximal Likelihood Estimation (MLE) because of the error estimation in the tails, the difficulties with truncating the infinite series, and so on. The authors use an integral expression of the PDF in standard parameterization and Zolotarev-type formula [8, section 2.1]. The p^{th} moment of any random variable X exists $E|X|^p = \int_0^\infty P(|X|^p > y) dy$ and is finite only if $0 < p < \alpha$. Otherwise, it does not exist. So, if α parameter of some series is less than 2 it is understood that the variance does not exist, and if it is less than 1, the mean cannot be used as a positional characteristic of such variable.

4. Skew t-distribution

In general, skew t-distribution is represented by a multivariate skew-normal distribution with the

covariance matrix, depending on the parameter distributed according to the inverse-gamma distribution. According to this representation, the density of skew t-distribution as well as the likelihood function is expressed through multivariate integrals that are convenient to be estimated by the maximum likelihood method [4].

There are examples where skew t-distribution is applied in biological research, localization of infectious agents or the prediction of the actual statistical properties of financial markets in statistical literature and so on [1, 2, 4, 8, 9]. It will be demonstrated that skew t-distribution reflects the difference between the investors' expectations and results, since in this distribution data is described by the Gaussian distribution with a random vector of mean and random variance.

The skew t-variable is denoted by $ST(\mu, \Sigma, \Theta, b, \eta)$. A multivariate skew t-distribution defines a random vector X that is distributed as a multivariate Gaussian vector:

$$f(x, a, t, \Sigma) = (t/\pi)^{\frac{d}{2}} \cdot |\Sigma|^{\frac{1}{2}} \cdot e^{-t(x-a)^T \cdot \Sigma^{-1} \cdot (x-a)}, \Sigma \geq 0, \quad (3)$$

where the vector of mean a , in its turn, is distributed as a multivariate Gaussian $N(\mu, \Theta/2t)$, $\Theta \geq 0$ in the cone $\eta \cdot (a - \mu) \geq 0$, $\eta \subset R^d$, where d is the dimension, and the random variable t follows from the Gamma distribution:

$$f_1(t, b) = \frac{t^{\frac{b}{2}-1}}{\Gamma(b/2)} \cdot e^{-t}. \quad (4)$$

By definition, d -dimensional skew t-distributed variable X has the density as follows:

$$\begin{aligned} p(x, \mu, \Theta, \Sigma, b, \eta) &= 2 \cdot \int_{0, \eta(a-\mu) \geq 0}^\infty \int f(x, a, t, \Sigma) \cdot f(a, \mu, t, \Theta) \cdot f_1(t, b) da dt = \\ &= \int_{0, \eta(a-\mu) \geq 0}^\infty \int \frac{2}{\pi^{\frac{d}{2}} \cdot |\Sigma|^{\frac{1}{2}} \cdot |\Theta|^{\frac{1}{2}} \cdot \Gamma\left(\frac{b}{2}\right)} \cdot t^{\frac{b}{2}+d-1} \times \\ &\quad \times e^{-t \cdot \left\{ (x-a)^T \cdot \Sigma^{-1} \cdot (x-a) + (a-\mu)^T \cdot \Theta^{-1} \cdot (a-\mu) + 1 \right\}} da dt, \end{aligned} \quad (5)$$

where $\Sigma \geq 0$, $\Theta \geq 0$ are the full rank $d \times d$ matrices.

In the equation $\eta \cdot (a - \mu) \geq 0$, $\eta \subset R^d$ defines an area of investors' expectations, which may be represented graphically.

The estimation of parameters $\mu, \Sigma, \Theta, b, \eta$ will be examined by following the maximum likelihood approach. The log-likelihood function can be expressed as

$$L(\mu, \Sigma, \Theta, b, \eta) = - \sum_{i=1}^K \ln(p(X^i, \mu, \Sigma, \Theta, b, \eta)) \rightarrow \min_{\mu, \Sigma, \Theta, b, \eta}. \quad (6)$$

The optimality conditions in this problem are derived by taking and setting the first derivatives with respect to parameters to be estimated as equal to zero.

But, first, the transformation of the data is carried out: the mean of the sample is subtracted from the data and divided by variance. The present case requires centring and scaling in order to ease the running of the minimisation program (otherwise the program would have to optimise according to the parameters of a very different scale). After having centred and scaled the data and having solved the minimisation task, the initial scales are resumed, i.e., the data is decentred and descaled backwards.

5. The data

The financial data of the enterprises under examination comprises the period from 2007 to 2009. That is the period of the economic recession, starting by the end of 2007. The year of 2008 was characterised by particularly pronounced problems of liquidity, while towards the end of 2009 the economic hardship assumed a different character.

The enterprises whose stock data have been used for the experiments belong to the following sectors: Diagnostic Substances; Drug Manufactures, Major; Drug Manufactures, Other; Health Care Plans; Hospitals; Medical Instruments and Supplies; Medical Laboratories and Research; Medical Appliances and Equipment; Specialized Health Services; Biotechnology in the US healthcare industry.

6. Methodology

1) Stable distribution is defined by the following parameters: alpha (characteristic exponent), beta (skewness), gamma (scale) and delta (location). Stable distribution parameters are calculated from stock price data—Close (4 parameters) and Volume (4 parameters): $x_j^{stbl}, j = 1, \dots, 8$;

2) skew t-distribution is defined by the following parameters:

μ - vector of mean,

Σ, Θ - covariance matrices,

b - the extinction degree,

η - scalar, enabling to establish the area of preferences (priorities).

Skew t-distribution parameters are calculated from stock price data—Close (5 parameters) and Volume (5 parameters): $x_j^{skw}, j = 1, \dots, 10$;

3) additional parameters describing the present-day situation: AGR rating and stock-defining parameters—Close and Volume: $x_j^o, j = 1, \dots, 3$;

4) three Random Forests classification models are created, which permit to predict the direction of the future change in AGR y_j^{AGR} (AGR rating will rise, drop or remain unchanged). The models differ among themselves by their input parameters:

$$- x_j^{M_1} = \{x_j^{stbl}, x_j^o\} \text{ (Model_1),}$$

$$- x_j^{M_2} = \{x_j^{skw}, x_j^o\} \text{ (Model_2),}$$

$$- x_j^{M_3} = \{x_j^{stbl}, x_j^{skw}, x_j^o\} \text{ (Model_3).}$$

7. Experiments

It is aimed at finding out as to which features had the greatest impact on predicting the future AGR class (AGR will rise, drop or remain unchanged). The features with a negative impact are removed. The experiments are carried out by employing for the input data three different sets of features: $x_j^{M_1}, x_j^{M_2}, x_j^{M_3}$.

The table below shows the Out of Bag errors when all the features are used (OOB^{All}) as well as when the most important ones (OOB^{select}) are selected.

Table 1. The OOB error when all the features OOB^{All} are used as well as when the selected features OOB^{select} are used in the cases of different sets of features: $x_j^{M_1}$ (Model_1), $x_j^{M_2}$ (Model_2), $x_j^{M_3}$ (Model_3) being employed for the input data

	OOB^{All}	OOB^{select}
Model_1	0.19	0.16
Model_2	0.20	0.17
Model_3	0.21	0.15

The selection of features has improved the results of predicting the AGR direction in regard to all the three models. The difference in errors is marginal when different combinations of input data are used for the classificatory. This may suggest that stock data can be equally well defined by both stable distribution and skew t-distribution.

As to which features are the most important in predicting the direction of the change in the future AGR rating in the cases when different sets of features— $x_j^{M_1}$

(Model_1), $x_j^{M_2}$ (Model_2), $x_j^{M_3}$ (Model_3)—are

used for the input data can be represented as follows:

Alpha1, Beta1, Gamma1, Delta1—stable distribution parameters calculated from Close data;

Alpha2, Beta2, Gamma2, Delta2—stable distribution parameters calculated from Volume data;

miu1—mean of the skew t-distribution Close parameter;
miu2—mean of the skew t-distribution Volume parameter;

sigma1— Σ Close;

sigma2— skew t-distribution covariance of Σ matrix of Close and Volume data;

sigma3— Σ Volume;

$$\Sigma = \begin{pmatrix} \text{Sigma1} \\ \text{Sigma2} \\ \text{Sigma3} \end{pmatrix} = \begin{pmatrix} \text{cov}_{\Sigma}(\text{Close}, \text{Close}) \\ \text{cov}_{\Sigma}(\text{Close}, \text{Volume}) \\ \text{cov}_{\Sigma}(\text{Volume}, \text{Volume}) \end{pmatrix}$$

$$\Theta = \begin{pmatrix} \text{Teta1} \\ \text{Teta2} \\ \text{Teta3} \end{pmatrix} = \begin{pmatrix} \text{cov}_{\Theta}(\text{Close}, \text{Close}) \\ \text{cov}_{\Theta}(\text{Close}, \text{Volume}) \\ \text{cov}_{\Theta}(\text{Volume}, \text{Volume}) \end{pmatrix}$$

teta1— Θ Close;
 teta2—skew t-distribution covariance of Θ matrix of Close and Volume data;
 teta3— Θ Volume;

b —skew t-distribution extinction degree;
 eta—skew t-distribution scalar enabling to establish the area of preferences (priorities), in other words—the angle between axis Ox and line $\eta \cdot (a - \mu)$.

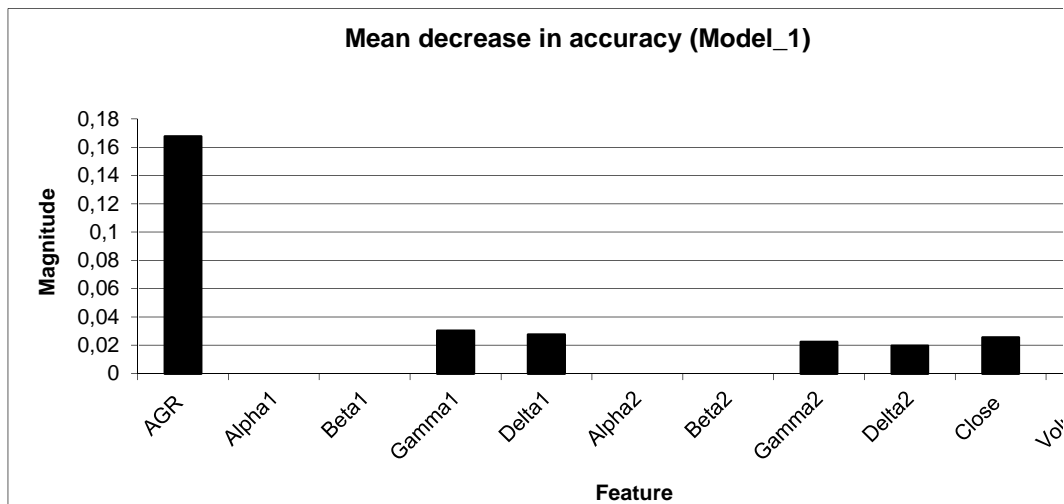


Fig. 1. Features when using the set of parameters of Model_1

When creating the model the present-day parameters (AGR rating, Close, Volume and stable distribution parameters), defining past changes in stock prices and volume, are used, the greatest impact in taking a decision concerning the future direction of AGR rating is made by the present-day AGR rating. A significant

impact is made by the present-day stock price Close and Volume parameters as well as the stable distribution parameters that are calculated from Close and Volume data and correspond to the mean and variance.

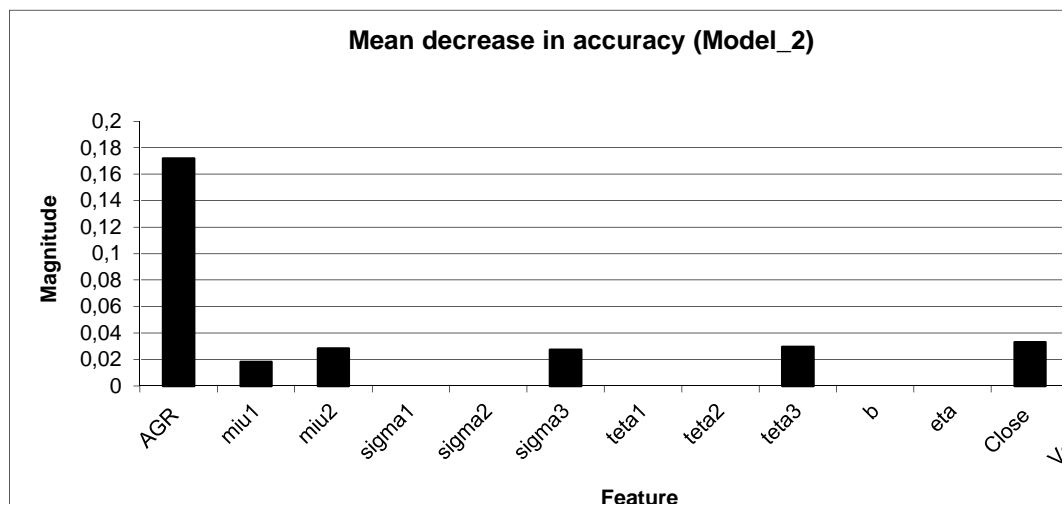


Fig. 2. Features when using the set of parameters of Model_2

When creating the model the parameters describing the present (AGR, Close, Volume) as well as the skew t-distribution data are used, as in the case of Model_1, the greatest impact is made by the present AGR rating, with the present stock price Close and Volume parameters being significant as well. A great impact in taking a

decision concerning the tendencies of future AGR rating is made by the Volume covariance matrix elements sigma3 and teta3, meanwhile Close covariance matrix elements appeared to be insignificant. Consequently, Model_2 is more affected by the intensity of the past investors' reaction, rather than by

the amplitude of the rise or fall of the stock price itself. Nevertheless, it needs to be noted that, in defining the present, the Volume parameter, reflecting the intensity

of investors' reaction, as well as the stock price (Close) are significant.

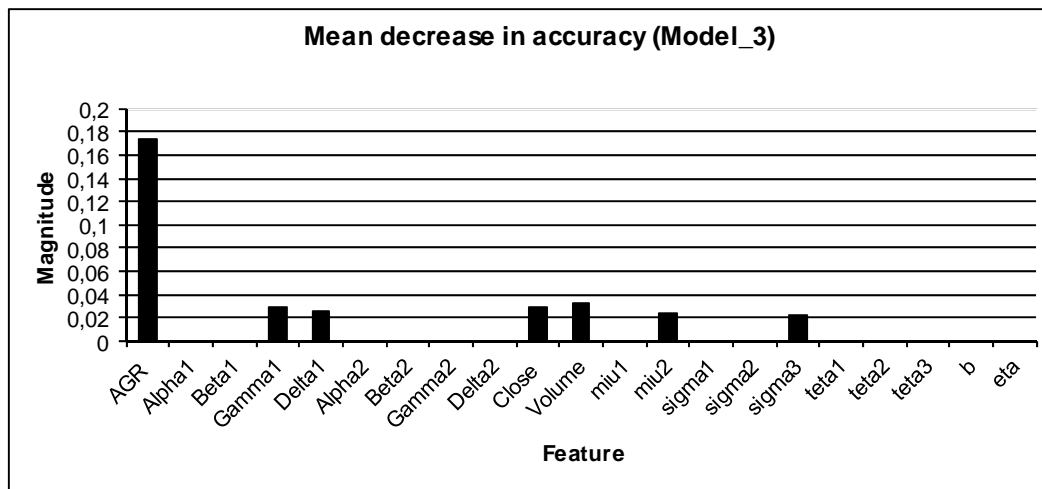


Fig. 3. Features when using the set of parameters of Model_3

When using for the model input data the parameters describing the present (AGR, Close, Volume) as well as the skew t-distribution and stable distribution parameters reflecting the change in past stock prices, once again the greatest impact on decision-making is made by the present-day AGR rating. The present-day Close and Volume parameters have remained to be significant as well.

Meanwhile, the stable distribution parameters calculated from Volume data have been found to be insignificant, although in the case of Model_1 they constituted important parameters.

From among skew t-distribution parameters, as in the case of Model_2, the sigma3 parameter remained to be important. Whereas, miu2 was not important when skew t-distribution was used alone, while when using the parameters of skew t-distribution and stable distribution together, miu2 appeared to be important. Meanwhile, in the case of Model_3, the teta3 parameter was not important, though it was important in the case of Model_2.

Consequently, when parameters of skew t-distribution and stable distribution are used together, stable distribution better reflects the amplitude of stock prices (Close), while skew t-distribution better reflects the intensity of investors' reaction. Therefore, in order to better describe the intensity of investors' reaction as well as the amplitude, it would be more expedient to employ skew t-distribution and stable distribution parameters collectively rather than to use them separately.

8. Conclusions

The financial data of the enterprises falling under examination comprised the period from 2007 to 2009. That was the period of the economic recession, which started by the end of 2007. The year of 2008 was characterised by particularly pronounced problems of

liquidity, while towards the end of 2009 the economic hardship assumed a different character.

It was sought to predict the direction of the change in the Accounting and Governance Risk (AGR) rating (AGR will rise, drop or remain unchanged). Three models were created, for the input data of which the present-day AGR rating, the stock price and volume as well as the distribution parameters defining the change in stock (Close and Volume) were used. These models differ among themselves according to the type of distribution being used: Model_1 employs alpha stable distribution parameters; Model_2—skew t-distribution parameters, while Model_3 takes up the parameters of both distributions. The results show that the errors of all the three models differ inconsiderably. It follows, then, that stable distribution as well as skew t-distribution is appropriate for describing the changes in stock.

The most important features were selected from the input data of Model_1, Model_2 and Model_3, with the aim of disclosing thereby the mutual dependency between the change in AGR rating and the change in stock parameters. In all the three models, the present-day AGR rating had the greatest impact. Consequently, if an enterprise is currently providing its financial data in a non-transparent manner, there is a high probability that it will do so in the future. Also, in all the three models, stock Volume and Close parameters remained to be among most important. From among the parameters defining stable distribution, the gamma and delta parameters (both Close and Volume ones), corresponding to the mean and variance, were most important. Since investors, while assessing the enterprise's financial situation, refer to its financial data, whilst if that data is not provided transparently (which is shown by the AGR rating), so then it becomes difficult for those investors to assess the enterprise's actual prospects. Thus, the fact of discrepancy in opinions becomes distinct, which is defined by the parameter corresponding to variance.

As it turned out during the selection of features, stable distribution parameters are more useful for describing the change in the amplitude of stock prices, whereas skew t -distribution parameters better describe the change in the intensity of investors' reaction.

9. References

1. Azzalini A. and Capitanio A. Distributions Generated by Perturbation of Symmetry with Emphasis on a Multivariate Skew t Distribution. *Journal of the Royal Statistical Society: Series B (Statistical Methodology)*, 65, 2003. p. 367-389.
2. Azzalini A. and Genton M. G. Robust Likelihood Methods Based on the Skew- t and Related Distributions. *International Statistical Review*. 76, 1, 2008. p. 106-129.
3. Breiman L. Random forests. *Machine Learning*. 45, 2001. p. 5-32.
4. Cabral C. R. B., Bolfarine H. and Pereira J. R. G. Bayesian Density Estimation Using Skew Student- t -Normal Mixtures. *Computational Statistics and Data Analysis*. 52, 12, 2008. p. 5075-5090.
5. EON, Audit Integrity's 'AGR' Rating Outperforms Leading Academic Accounting Risk Measures, Independent Study Finds. 2010. Available at (Enhanced Online News, EON): <http://eon.businesswire.com/news/eon/20100315006063/en>
6. Guyon I. Practical Feature Selection: from Correlation to Causality. *NATO Science for Peace and Security*. Vol. 19 of D: Information and Communication Security, IOS Press, 2008, Ch. 3, p. 27-43.
7. Kalsyte Z., Verikas A., Bacauskiene M. and Gelzinis A. A novel technique to design an adaptive committee of models applied to predicting company's future performance. *Expert Systems with Applications*, Volume 40 Issue 6, 2013. p. 2051-2057.
8. Kim H. M. and Mallick B. K. Moments of Random Vectors with Skew t Distribution and their Quadratic Forms. *Statistics & Probability Letters*. 63, 2003. p. 417-423.
9. Panagiotelis A. and Smith M. Bayesian Density Forecasting of Intraday Electricity Prices Using Multivariate Skew t Distributions. *International Journal of Forecasting*. Nr. 24, 2008. p. 710-727.
10. Price R.A., Sharp N.Y. and Wood D.A. Detecting and Predicting Accounting Irregularities: A Comparison of Commercial and Academic Risk Measures. *Social Science Research Network*. 2011. Available at SSRN: <http://ssrn.com/abstract=1546675>
11. Spellman G. K. and Watson R. Corporate Governance Ratings and Corporate Performance: An Analysis of Governance Metrics International (GMI) ratings of US Firms. 2009. 2003 to 2008 Available at SSRN: <http://ssrn.com/abstract=1392313>

APPLICATION OF UPPAAL FOR HEATING SYSTEMS TEMPORAL BEHAVIOR ANALYSIS

Paulius STANKEVIČIUS*, Gintarė SUKAREVIČIENĖ*, Tomas KRILAVIČIUS*, Henrikas PRANEVIČIUS**
* Vytautas Magnus University, Lithuania; ** Kaunas University of Technology, Lithuania

Abstract: Within the field of intelligent house and home automation, intelligent control of heating systems has become the most promising approach to provide all required services and conform to robustness and safety requirements at the same time. However, it remains unclear how such a system can meet such requirements. The aim of this paper is to describe an application formal modeling tool for behavioral analysis of heating system consisting of internal/external sensors, controller, and heater. Results show, that application of formal modeling tool allows analyzing systems at an early stage, checking its consistency and conformance to requirements.

Keywords: systems simulation, Uppaal tool, intelligent house, home automation, intelligent control, modeling.

1. Introduction

Nowadays intelligent houses and home automation are becoming reality and one of the key elements, heating systems, play a significant role within this area. Unfortunately, ensuring efficiency of such systems could be influenced not only by the quality of multiple elements of the heating system itself but also by various possible ways in which the system could be controlled. Thus, efficiency of the heating systems could be increased by introducing new control techniques and algorithms that mainly focus on maintaining the desired temperature inside the buildings and reducing heating costs.

Traditionally there are three inevitable parts within control design cycle: modeling, simulation and synthesis. In order to do rigorous modeling and analysis of diverse systems, formal methods could also be used. Formal methods could be useful for several reasons:

- Unambiguous models. Formal modeling languages allow defining systems unambiguously, because syntax and semantics are defined formally, and that includes means to define non deterministic and stochastic behavior precisely, too. Moreover, for the same reasons, unambiguous refinement and code generation techniques can be applied.

- Strict analysis techniques. Because models are defined using languages with strict semantics, rigorous reasoning about models is possible. E.g., model checking, theorem proving and specifically designed algorithms can be used.

Quite a few techniques and tools were defined over the year, e.g. process algebras [4-8], timed automaton [9], hybrid automaton [10], SPIN [11], Uppaal [2] tools and much more (see [12] for wider overview). Successful application of formal techniques is reported in different areas, e.g. automotive industry [13], electronics [14], industrial devices control [15], healthcare [16] and other.

In this paper we investigate applicability of timed automaton [1] and Uppaal tool [2] for the design and simulation of an intelligent home heating system. Uppaal is an integrated tool environment for modeling, validation and verification of real-time systems modeled as networks of timed automaton, extended with data types and other convenient constructions [2]. Based on two reasons above, we also use formal methods for analysis.

2. Home heating system

Analyzed home heating system (see Fig. 1) consists of the following components:

- Inside temperature sensor.
- Outside temperature sensor.
- Heater.
- Heating controller.

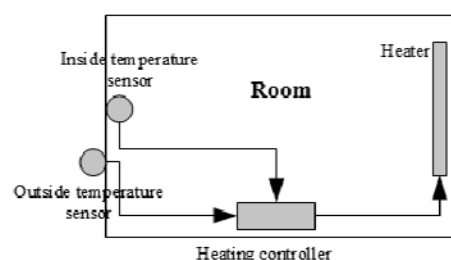


Fig. 1. Home heating system

Inside temperature sensor is used to sense temperature inside the room, outside temperature sensor is used to sense temperature outside the room, heater with fixed power controls “on/off” operations and heating controller system controls the whole heating process. Basically, controller is used to manage transient processes of heating system but the need of energy must be evaluated by sensors. It is essential to evaluate need of energy constantly in order to achieve and maintain temperature that is specified in the task.

In order to get better results and greater opportunities to use these tools in the future for other heating systems:

- control by switching “on/off” was used instead of direct control by changing the heating element power was adopted.
- demand for heating was evaluating not by heating element power or the need of energy for the system, but by heating element operation time.

3. Timed automaton and Uppaal

Timed automaton [1] is one of the most popular techniques for modeling and analysis of the real-time systems. We present a version of automata used in Uppaal [2], an integrated tool environment for the modeling, simulation and verification of real-time systems. It is well-suited for systems that can be modeled as a collection of nondeterministic processes with finite control structure and real valued clocks, communicating through channels or shared variables.

3.1. Definition 1

Let (1) be a set of clocks and $B(C)$ be the set of clock restrictions of the form $g, h \doteq x \lt c \mid x - y \lt c \mid g \wedge h$ with $x, y \in C, c \in \mathbb{N}$ and $\lt \in \{<, \leq, =, \geq, >\}$:

$$C = \{x, y, z, \dots\}. \quad (1)$$

3.2. Definition 2

Timed automata can be represented as in Fig. 2. Locations are drawn as nodes in the graph, and the initial location is usually marked with a double circle.

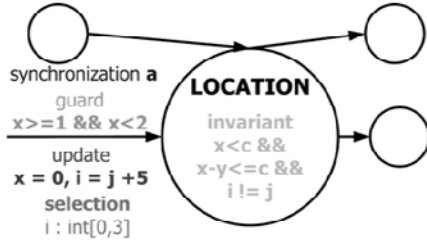


Fig. 2. Timed automata

We will call timed automaton a finite directed graph over C and $B(C)$:

$$A = (L, l_0, \mathcal{A}, E, I), \quad (2)$$

where L is a finite set of locations; $l_0 \in L$ is the initial location; \mathcal{A} is a finite set of action names and $E \subseteq L \times$

$B(C) \times \mathcal{A} \times 2^C \times L$ is a finite set of edges, $I: L \rightarrow B(C)$ assigns invariants to locations.

We will write $l \xrightarrow{g,a,r} l'$ instead of $(l, g, a, r, l') \in E$. For such an edge, l is called the source location of the state, g is the guard, a is the action, r is the set of clocks to be reset and l' is the target location.

3.3. Definition 3

Let (3) be a timed automaton over C :

$$A = (L, l_0, \mathcal{A}, E, I). \quad (3)$$

We define the timed transition system generated by A as $T(A) = (S, Act, \xrightarrow{tr})$ where:

- $S = L \times (C \rightarrow \mathbb{R}_{\geq 0})$ is a set of locations (l, v) , where l is a location of the timed automaton and v is a clock valuation satisfying the invariant of l ;
- $Act = \mathcal{A} \cup \mathbb{R}_{\geq 0}$ is the set of labels;
- Two types of transitions are defined:
 - Action transitions $(l, v) \xrightarrow{a} (l', v')$ such that exists an edge $(l \xrightarrow{g,a,r} l') \in E$ where v satisfies g , v' satisfies $v[r]$ and v' satisfy $I(l')$,
 - Delay transitions $(l, v) \xrightarrow{d} (l, v')$ if $\forall d' \in [0, d] \Rightarrow v + d'$ satisfies $I(l)$.

Let v_0 denote the valuation with $v_0(x) = 0$ for all $x \in C$. If it satisfies the invariant of the initial location, we will call (l_0, v_0) the initial state of $T(A)$.

In Uppaal, timed automata are composed into a network, consisting of n timed automata:

$$A_i = (L_i, l_i^0, \mathcal{A}, E_i, I_i), i = 1 \dots n. \quad (4)$$

Let $l = (l_1, \dots, l_n)$ be a location of the network, then invariants are composed using conjunction $I(\bar{l}) = \bigwedge_{i=0}^n I_i(l_i)$.

3.4. Definition 4

Let (5) be a network of n timed automata:

$$A_i = (L_i, l_i^0, \mathcal{A}, C, E_i, Inv_i), i = 1 \dots n. \quad (5)$$

Let $\bar{l}_0 = (l_1^0, \dots, l_n^0)$ be the initial location vector. The semantics is defined as a transition system (S, s_0, \rightarrow) , where $S = (L_1 \times \dots \times L_n) \times \mathbb{R}^C$ is the set of states, $s_0 = (\bar{l}_0, v_0)$ is the initial state and transition relation combines 3 transitions types:

- time flow transitions (6), if $\forall d' \in [0, d]$ holds $v + d' \models Inv(\bar{l})$:

$$(\bar{l}, v) \xrightarrow{d} (\bar{l}, v + d); \quad (6)$$

- discrete transitions:
 - synchronized:

$$\begin{aligned} & ((l_1, \dots, l_i, \dots, l_j, \dots, l_n), v) \\ & \xrightarrow{\tau} ((l_1, \dots, l'_i, \dots, l'_j, \dots, l_n), v'), \end{aligned} \quad (7)$$

if $\exists i \neq j, \exists (l_i \xrightarrow{a^1, g_i, r_i} l'_i) \in E_i, \exists (l_j \xrightarrow{a^2, g_j, r_j} l'_j) \in E_j, v \vdash g_i \wedge g_j, v' \vdash v[r_i \cup r_j]$ and $v' \vdash I_i(l_i) \wedge I_i(l_i) \wedge \bigwedge_{k \neq i, j} I_k(l_k)$;

o asynchronous:

$$((l_1 \dots, l_i, \dots, l_n), v) \xrightarrow{\tau} ((l_1 \dots, l'_i, \dots, l_n), v'), \quad (8)$$

if $\exists (l_i \xrightarrow{\tau, g, r} l'_i) \in E_i, v \vdash g, v' \vdash v[r]$ and $v' \vdash Inv_i(l_i) \wedge \bigwedge_{k \neq i} Inv_k(l_k)$.

Uppaal is based on the theory of timed automata; however it's modeling language offers additional features such as bounded integer variables, urgency, and more [1]. Properties to be verified are specified using a subset of Computation Tree Logic (CTL) [1-3]:

- $A[]$ property invariant, property always holds in all paths;
- $A<>$ property eventually, property holds in all paths at some moment;
- $E<>$ property possibly, property eventually holds at some state, at least in one path;
- $E[]$ property potentially always, property eventually holds from some state, at least in one path;
- $p \rightarrow q$ leads to, whenever p holds eventually q will hold;
- *deadlock true*, if *deadlock state* is reachable;
- $P.state$ certain properties hold in the selected state.

4. Formal modeling of home heating system using Uppaal

It is a simplified version of the home heating system as defined in Sect. 2. We made imitation of model without real count of heating time algorithm.

We present a work in progress, an abstract version of an intelligent home heating system, defined in Sect. 2. Uppaal model consists of the following components:

- Real temperature changes imitation and day time counter (see Section 4.1);
- Temperature sensors (inside and outside) for imitation of temperature sensor work (see Section 4.2);
- Heater that gets command from controller and change heater status (see Section 4.3);
- Heater controller that sends values of inside and outside temperature to heater (see Section 4.4).

4.1. Real temperature change imitation

Model of real temperature changes imitation (see Fig. 3) calculates a graph of outside temperature according to pre-defined outside temperature:

```
void OutSideTemp(){
  int k = dayInt*tempReC/pHour;
  int k2 = 0;
  int x1 = k*pHour/tempReC;
  int x2 = (k+1)*pHour/tempReC;
  dayHour = k;
  if (k+1 < 24)
```

```
  k2 = k+1;
  outTemp = ((outTempLine[k]-outTempLine[k2])/(x1-x2))*
(dayInt-x1)+outTempLine[k];}
```

In Fig 3, *dayInt* and *dayHour* refer to the time of day, *dayInt* is an index of temperature conversion and variable *dayHour* refers to hour of the day.

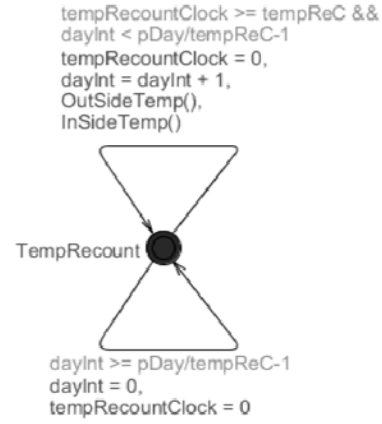


Fig. 3. Model of real temperature changes imitation

Temperature inside is function of loss of energy depending on inside and outside temperature, and power of heater:

```
void InSideTemp(){
  int dT = (inTemp - outTemp)/lostT;
  inTemp = inTemp - dT+ sHeater * hinT;}
```

Values of inside and outside temperature are stored in global variables. Uppaal does not support floats, but it simulated by the clocks and by scaling integers to provide sufficient precision (i.e. 1.001 becomes 1001).

4.2. Temperature sensors

Inside and outside temperature sensors are similar (see Fig. 4 and Fig. 7 for the details):

- Init: sensor's initialized.
- Idle: sensors are waiting for requests of temperature.
- ReadTemperature: location in which the values of temperature are read.

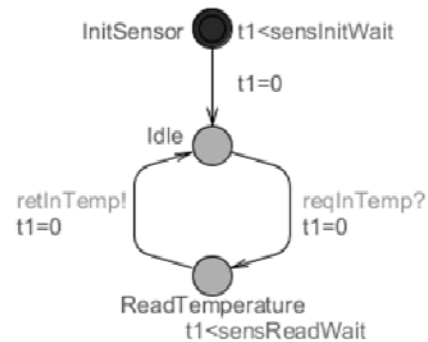


Fig. 4. Sensor automaton

In order to reduce number of controller location, an intermediate automata was developed. It performs scan of values of inside and outside temperatures (see Fig. 5).

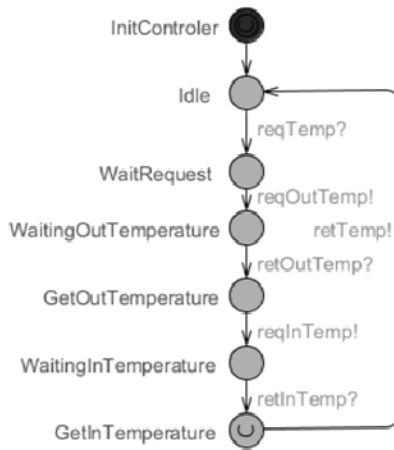


Fig. 5. Intermediate model

4.3. Heater

Heater has two locations: *on* and *off*, that are indicated by the global variable *sHeater*. Despite the fact that at the beginning of simulation heater's symbolic state is *off* in *InitHeator* location, it could perform two actions: *doOn* and *doOff* independent of the state of the heater (see Fig. 6).

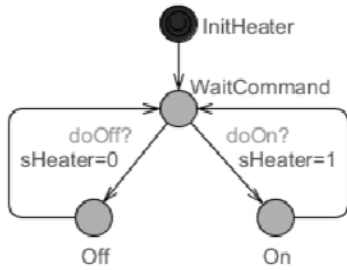


Fig. 6. State of the heater

Heater just switches between two modes - *on* and *off*, changes values of *sHeater*, and *idles* in *idle* location.

4.4. Heating controller

An Uppaal model of the heating controller is depicted in Fig. 7. It consists of two main functional parts:

- The part for maintain fixed temperature (on the right of Fig. 7). In this part for maintain fixed temperature, parameters of controller are initialized in *InitController* location, where *task temperature*, *next task temperature* and *next task time* are set, and automata moves to from *StartControl* to *TemperatureSet*. *TemperatureSet* and sends command *reqTemp* requesting inside and outside temperatures. Controller waits for *retTemp* on to receive temperature change and move to *GetTemperatures1*. Then it counts and evaluates time between recent and next task and moves to *ControlType* location; if the absolute value of the time is larger than the value of the time until the next task, controller moves to *HeaterChange* location and sends command to heater with the values of recent inside temperature and temperature specified in the task. Afterward controller moves to *StartControl*.

- The part of adaptive controlling of intermediate processes (left side of Fig. 7). In this part for adaptive controlling of intermediate processes adaptive control of intermediate process starts when absolute value of the time is lower or equal than value of the rest time till the next task:

- (a) if the estimated time is positive, controller sends command *doOn* and increase inside temperature while temperature becomes the same as specified in the next task.
- (b) if the estimated duration is negative, controller sends *doOff* and operates in similar manner as while increase temperature.

Upon completion of the intermediate processes, controller moves to the *Adaption* location. Finally, after that it returns to the *StartControl* location.

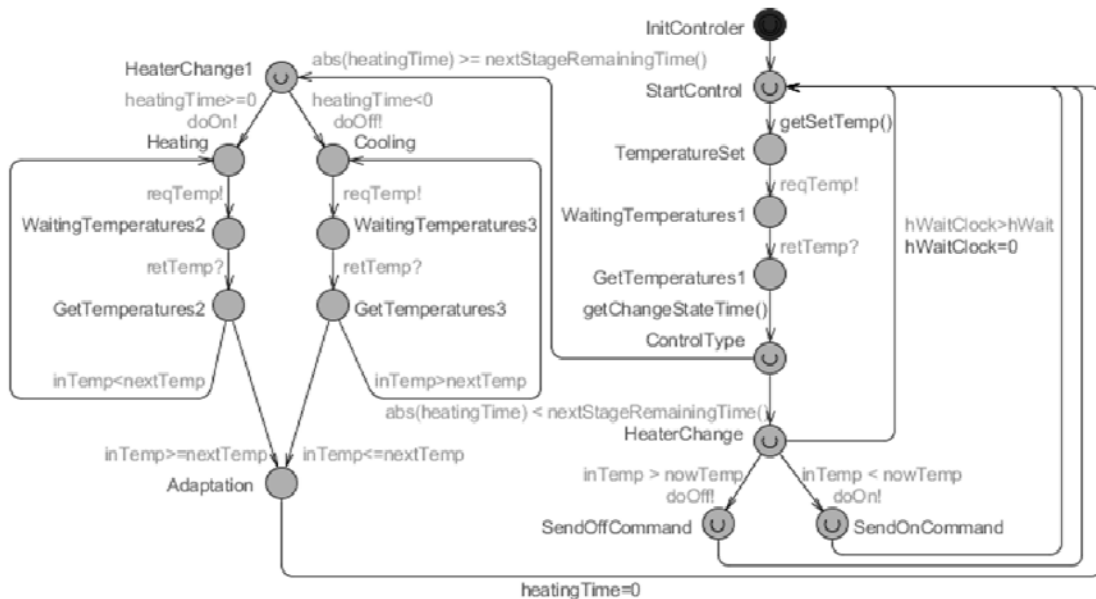


Fig. 7. An Uppaal model of the heating controller

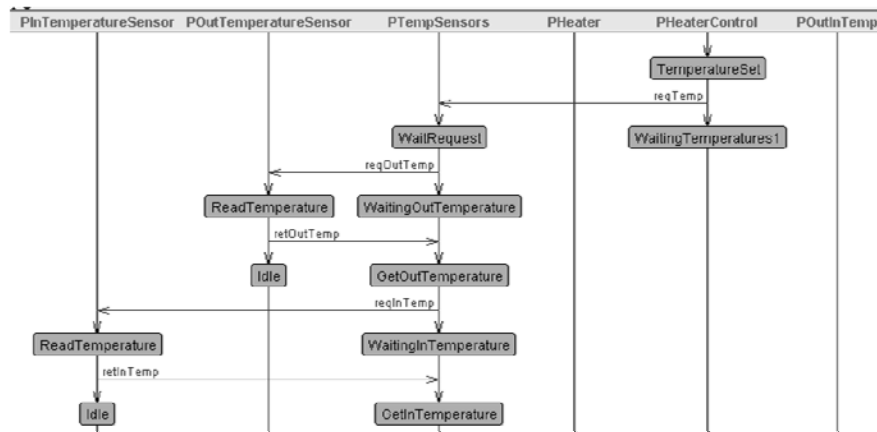


Fig. 8. Simulation Heating System

4.5. Model simulation

Simulation results, e.g. see Fig. 8, show, that system behaves according to requirement, i.e. switching occurs at required time. Unfortunately, the system is too complex for deadlock check.

5. Conclusions

Uppaal tool was applied for modeling and analysis of an intelligent heating system with an internal and external sensors, controller, heater and external/internal temperature change trajectories simulation. We investigated conformance of the model to the requirements. Results show that system (model) conforms to requirements. Moreover, paper shows how Uppaal can be used for analysis of cyberphysical systems during design and development process. It could be a great relevance to further researches within this area.

Future plans include hybrid and continuous modeling of heating system, verification of modified model using Uppaal and experiments with an implementation in laboratory conditions.

6. References

- Alur R. and Dill D. The Theory of Timed Automata. In Real-Time: Theory in Practice, LNCS. Springer Berlin, 1992, vol. 600, pp. 45–73, 10.1007/BFb0031987. [Online].
- Behrmann G., David A., and Larsen K. G. A Tutorial on UPPAAL. In Formal Methods for the Design of Real-Time Systems: 4th Int. School on Formal Methods for the Design of Computer, Communication, and Software Systems, SFM-RT 2004, ser. LNCS, M. Bernardo and F. Corradini, Eds., no. 3185, sep 2004, pp. 200–236. [Online].
- Krilavičius T. and Man K. Timed Model of the Radiation Therapy System with Respiratory Motion Compensation. In Proc. of the 6th Int. Conf. on Electrical and Control Technologies (ECT 2011), 2011, p. 6.
- Milner R. Communication and Concurrency. Prentice-Hall, Inc., 1989. 272 p.
- Hoare C.A.R. Communicating Sequential Processes. Prentice-Hall, Inc., 1985. 256 p.
- Brinksma E., Krilavičius T. and Usenko Y.S. Process Algebraic Approach to Hybrid Systems. Proc. of the 16th IFAC World Congress, Prague, 2005, 6 p.
- Krilavičius T. Hybrid Techniques for Hybrid Systems. PhD thesis, Univ. of Twente, 2006. 192 p.
- Man Beek D., Man K., Reniers M., Rooda J. and Schiffelers R. Syntax and Consistent Equation Semantics of Hybrid Chi. Tech. Rep., Tech. Univ. of Eindhoven (TU/e), Eindhoven, 2004. 119 p.
- Alur R. and Dill D. The Theory of Timed Automata. Proceedings of Real-Time: Theory in Practice, Springer, 600, LNCS, 1994, p. 45–73.
- Alur R., Courcoubetis C., Henzinger T. and Ho P.-H. Hybrid Automata: an Algorithmic Approach to the Specification and Verification of Hybrid Systems. Hybrid Systems, vol. 736, 1993, p. 209–229.
- Holzmann G.J. The SPIN Model Checker: Primer and Ref. Manual. Addison-Wesley, 2003. 608 p.
- Bowen J.P. and Hinchey. Ten Commandments of Formal Methods...Ten Years Later, Computer, vol. 39, no.,1 IEEE, January, 2006, p. 40–48.
- Gebremichael B., Krilavičius T. and Usenko Y.S. A Formal Model of a Car Periphery Supervision System in UPPAAL. Proc. of Workshop on Discrete Event Systems, Sep 22–24, 2004, France, pp. 433–438.
- Man K.L. and Krilavičius T. Case Studies with Process Analysis Toolkit (PAT). International SoC Design Conference, BEXCO, Busan, 2009, 4 p.
- Groote J.F, Pang J. and Wouters A.G. A Balancing Act: Analyzing a Distributed Lift System. Proc. of the 6th Int. Workshop on Formal Methods for Industrial Critical Systems FMICS'2001, France, 2001, p.1–12.
- Krilavičius T., Kaiyu Wan, Lee, K., Man, K.L.. Specification and Verification of Radiation Therapy System with Respiratory Compensation using Uppaal. In the Int. Journal of Design, Analysis and Tools for Integrated Circuits and Systems - IJDATICS, 3(1):8–13, 2012.

INVESTIGATION OF DEPENDENCIES BETWEEN VIRTUAL 3D FACE STIMULI AND EMOTION-BASED HUMAN RESPONSES

Egidijus VAŠKEVIČIUS, Aušra VIDUGIRIENĖ, Vytautas KAMINSKAS
Vytautas Magnus University, Faculty of Informatics, Lithuania

Abstract: Virtual environment is an important part of everyday life, as lots of children and adults engage themselves in social networks, internet applications as well as computer games. The influence that is done to the person through those activities in the virtual environment is important for their daily life and psycho-emotional state. In the paper, the dependencies between the features of virtual dynamic object (3D virtual face) as stimulus and corresponding human psycho-emotional state parameters (engagement/boredom, excitement, and frustration) are modeled. Model validation shows that output signals can be predicted when using least squares method for unknown parameter estimation.

Keywords: Virtual 3D face, psycho-emotional state, EEG, Least Squares method.

1. Introduction

Nowadays a lots of children and adults engage themselves in social networks, internet applications and computer games, so different kinds of virtual environment becomes usual in our daily life and it is even difficult to imagine a world without the new technologies. However, virtual environment influences a psycho-emotional state of a person and it is important to evaluate it for different reasons: to examine the quality of new interfaces of various software products [1], to prevent children or adults from using the applications that gives harmful effects to one's health [2][3], to use virtual environments for military or other training [4] or serves as mediators [5]. One of the usual virtual objects that can be investigated is an avatar. A number of studies have been performed for exploring influence of avatars in various aspects. R. Bailey et al. [6] investigate the influence of interactive game on children cognition and emotion through skin conductance comparing the effects when an avatar is assigned, chosen or self-designed. A self-designed avatar determines a higher skin conductance values and higher arousal. Another study [7] introduces generation of virtual emotional 3D faces with asymmetric features according to valence-arousal coordinate system, to

make the visualizations more realistic. Emotional avatars are constructed using different technologies [8]. Human face is one of the most important means for non-verbal information transferring to another person [9]. We have chosen to investigate the influence of a 3D female avatar face and to measure EEG signals of a human.

Our previous studies were dedicated to investigate if a 3D avatar (male and female) faces have influence on the emotional state of the volunteers who are observing the changing features of a 3D faces [10]. Four volunteers (only male) have been included into this investigation. The experiments were set up to observe an output signal when an input is male or female 3D face with different and changing features.

This paper presents an investigation of the data observed during a set of experiments that were dedicated to explore the dependencies between three 3D face features – distance between eyes, nose width, chin width – and human emotions as a response to a given stimuli.

2. Observations and data

The investigations were performed using the following input and output: virtual 3D face (distance between eyes, nose width, and chin width) for input and excitement, frustration, engagement/boredom signals of a person as output from preprocessed EEG data (see Fig. 1.). The input and output signals were collected using Emotive Epoc device. The device is capable to record raw EEG data and gives already preprocessed signals (excitement, frustration, engagement/boredom). The device records EEG inputs from 14 channels (according to international 10-20 locations): AF3, F7, F3, FC5, T7, P7, O1, O2, P8, T8, FC6, F4, F8, AF4 [11].

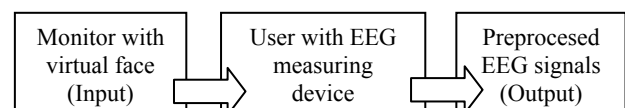


Fig. 1. Input-output scheme of the data recording

Modifications of 3D woman face were used for the input. The faces were created with Autodesk MAYA and imported to Unity 3D engine for programming the required animations using *morphtarget's* method. The “neutral” face is shown in Fig. 2.



Fig. 2. A woman 3D virtual face with “neutral” features

There were two kinds of input signal. In the first case a face were changing smoothly from “neutral” to “large distance-between-eyes”, “wide nose” or “wide chin” then came back in the same manner to “neutral” and changed smoothly to “small distance-between-eyes”, “thin nose” and “thin chin”.

In the second case, a “neutral” face was shown for some period of time, then the picture was changed suddenly to “large distance-between-eyes”, “wide nose” or “wide chin” with a sudden change in a signal pattern, and then after some period of time to “neutral” or “small distance-between-eyes”, “thin nose” or “thin chin” and so on. A numerical value of “neutral” face was 0, increased in the case of “large distance-between-eyes”, “wide nose”, “wide chin” and decreased in the case of “small distance-between-eyes”, “thin nose” and “thin chin”.

Six feature signals were constructed for input - two kinds for every of three features. Only one feature was changing in a face at the same time.

The limiting face feature changes are shown in visual form in figs. 3-5.



Fig. 3. Distance-between-eyes: largest (left) and smallest (right)



Fig. 4. Nose width: wide (left) and thin (right)



Fig. 5. Chin width: wide (left) and thin (right)

Output signals – excitement, engagement/boredom and frustration – varied from 0 to 1. If excitement, frustration and engagement was low, the value was 0 or close to 0 and if they were high, the values of

parameters were 1 or close to 1. The signals were recorded with the sampling period of $T_0=0.5$ s. There were 5 volunteers (2 male and 3 female) tested. A person was watching 6 animated scenes of approximately 1 minute in a row, the EEG signals were measured using Emotiv Epoc and the preprocessed recorded signals were stored for later analysis.

3. Model of dependencies between virtual object stimuli and human psycho-emotional state

The dependencies between virtual object stimuli and human psycho-emotional state are described as follows [12]:

$$\begin{aligned} A(z^{-1})y_t &= B(z^{-1})x_t + \varepsilon_t \\ B(z^{-1}) &= b_0 + b_1z^{-1} \\ A(z^{-1}) &= 1 + a_1z^{-1} \end{aligned} \quad (1)$$

where $A(z^{-1})$ and $B(z^{-1})$ are the model polynomials, y_t is an output (excitement, engagement/boredom or frustration) and x_t is an input (changing 3D face features) signals respectively calculated as

$$y_t = y(tT_0), \quad x_t = x(tT_0) \quad (2)$$

with sampling period T_0 , ε_t corresponds to noise signal and z^{-1} is the backward-shift operator $z^{-1}x_t = x_{t-1}$.

Eq. (1) can be expressed in the following form:

$$y_t = b_0x_t + b_1x_{t-1} - a_1y_{t-1} + \varepsilon_t \quad (3)$$

The parameters of the model $c^T = [b_0, b_1, a_1]$ are unknown. They have to be estimated according to the observations obtained during the experiments with volunteers. Cross-correlation functions between input and output signals and autocorrelation function of input signals are used for this purpose:

$$R_{xy}[\tau] = \frac{1}{N} \sum_{t=1}^{N-\tau} (y_t - \bar{y})(x_{t+\tau} - \bar{x})$$

and (4)

$$R_{xx}[\tau] = \frac{1}{N} \sum_{t=1}^{N-\tau} (x_t - \bar{x})(x_{t+\tau} - \bar{x})$$

where

$$\bar{x} = \frac{1}{N} \sum_{t=1}^N x_t$$

and (5)

$$\bar{y} = \frac{1}{N} \sum_{t=1}^N y_t$$

are the averages of input and output and $\tau = 0, \pm 1, \dots$. It is not difficult to show that in the case of using the model, the following relationship exists between correlation functions:

$$R_{yx}[\tau] = b_0 R_{xx}[\tau] + b_1 R_{xx}[\tau - 1] - a_1 R_{yx}[\tau - 1] \quad (6)$$

Equation (6) can be expressed as a linear regression equation:

$$R_{yx}[\tau] = \beta_\tau^T \mathbf{c} \quad (7)$$

where

$$\beta_\tau^T = [R_{xx}(\tau), R_{xx}(\tau - 1), -R_{yx}(\tau - 1)] \quad (8)$$

For the estimation of unknown parameter vector \mathbf{c} we use a method of least squares. The parameter estimates $\hat{\mathbf{c}}^T = [\hat{b}_0, \hat{b}_1, \hat{a}_1]$ of a model are expressed as follows [12]:

$$\hat{\mathbf{c}} = \mathbf{Q}^{-1} \mathbf{q} \quad (9)$$

where a matrix \mathbf{Q} and a vector \mathbf{q} are calculated using the following equations:

$$\mathbf{Q} = \sum_{\tau=-M}^M \beta_\tau \beta_\tau^T \quad (10)$$

$$\mathbf{q} = \sum_{\tau=-M}^M R_{yx}[\tau] \beta_\tau$$

where M is a number of correlation function values used.

4. Model validation

The model was validated through the output signal (excitement, frustration, engagement/boredom) prediction analysis. The predicted signals of the model have the following expression:

$$\hat{y}_t = \hat{b}_0 x_t + \hat{b}_1 x_{t-1} - \hat{a}_1 y_{t-1} \quad (11)$$

The predicted signal is compared to the observed output signal.

Model was constructed for every of five volunteers between every input (distance between eyes, nose width and chin width) signal and every corresponding output signal (excitement, frustration, and engagement/boredom).

When estimating the parameters of the model using eq. (10), $M=30$. When calculating correlation functions using eq. (4), $N=120$.

Two kinds of inputs were used. The input of Type 1 is shown in Fig. 6 (top). Here signal values are changing suddenly and then is of the same value for some interval of time. The input of Type 2 is shown in Fig. 6 (bottom). It is changing smoothly during all the experiment time.

The values of the vector $\hat{\mathbf{c}}$ when input Type 1 is used are given in Table 1. The corresponding predicted signals are shown in the figs. 7-11 below. Observed output signal is marked with a solid line, and predicted output signal with a dotted line.

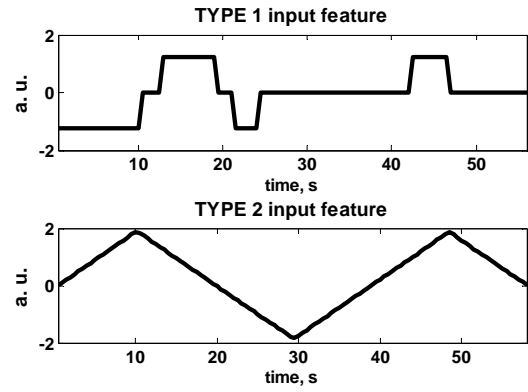


Fig. 6. Type 1 and Type 2 input features

Table 1. Estimated model parameters for different Type 1 input and output signal combinations and volunteers. User no. is followed by the notations f-female and m-male.

User no.	Input feature	Output feature	\hat{b}_0	\hat{b}_1	\hat{a}_1
1 (f)	Nose	Excitement	-0,06	0,03	-0,97
2 (f)	Eyes	Excitement	-0,01	0,05	-0,98
3 (f)	Nose	Frustration	0,06	-0,05	-0,99
4 (m)	Nose	Engagement /Boredom	0,01	0,02	-0,99
5 (m)	Chin	Frustration	0,00	0,02	-0,94

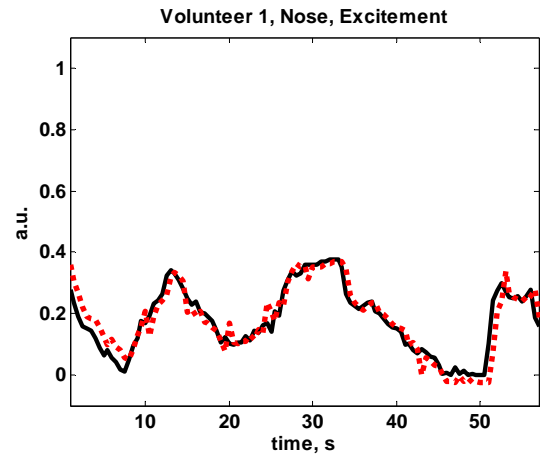


Fig. 7. Volunteer 1, Nose width input, Excitement output signal

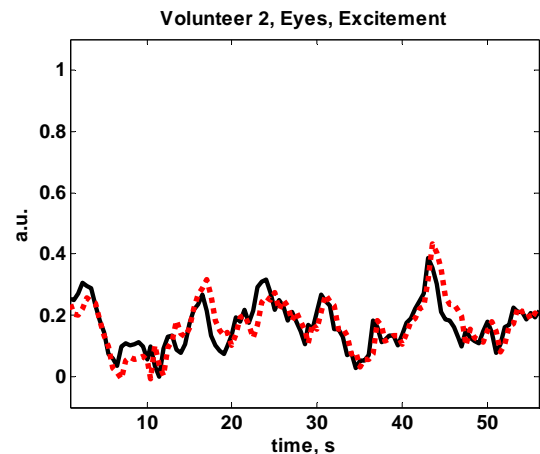


Fig. 8. Volunteer 2, Distance-between-eyes input, Excitement output signal

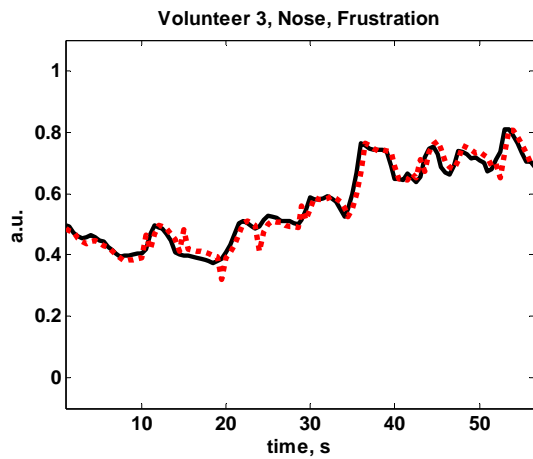


Fig. 9. Volunteer 3, Nose width input, Frustration output signal

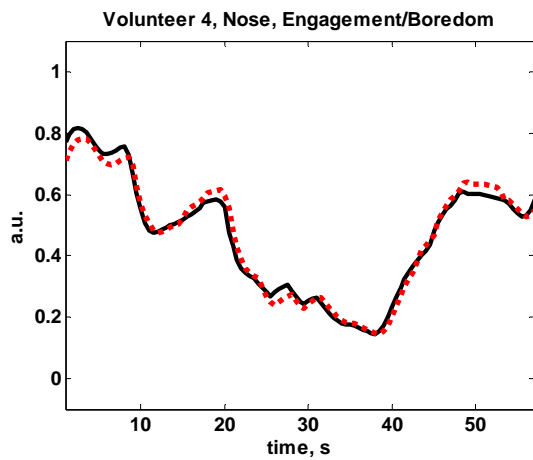


Fig. 10. Volunteer 4, Nose width input, Engagement/Boredom output signal

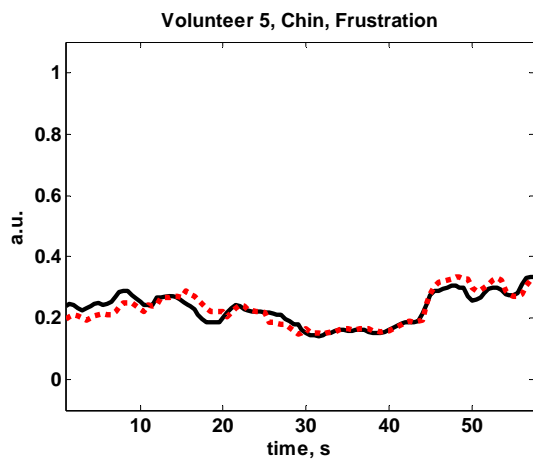


Fig. 11. Volunteer 5, Chin width input, Frustration output signal

It can be noted that excitement and frustration signals are predicted in the larger accuracy than meditation and engagement/boredom.

The values of the vector \hat{c} when input Type 2 is used are given in Table 2. The corresponding predicted signals are shown in the figs. 12-19. Observed output signal is marked with a solid line, and predicted output signal with a dotted line.

Table 2. Estimated model parameters for different Type 2 input and output signal combinations and volunteers. User no. is followed by the notations f-female and m-male.

User no.	Input feature	Output feature	b_0	b_1	a_1
1 (f)	Eyes	Excitement	0,05	-0,07	-0,96
2 (f)	Eyes	Excitement	0,23	-0,21	-1,00
5 (m)	Eyes	Excitement	0,04	-0,05	-1,00
4 (m)	Eyes	Excitement	0,46	-0,49	-1,00
4 (m)	Nose	Excitement	0,16	-0,18	-1,00
4 (m)	Chin	Excitement	-0,65	0,61	-0,97
2 (f)	Chin	Frustration	0,17	-0,19	-1,00
2 (f)	Chin	Engagement /Boredom	-0,14	0,14	-0,99

When analyzing the same parameter for different volunteers (both male and female), it can be seen, that Excitement parameter signal is predicted in acceptable accurately in the analyzed cases (Figs. 12-14).

When analyzing different input parameters for the same output parameter for the same volunteer, it can be also seen, that Excitement parameter signal is predicted accurately in all the cases that are being analyzed here (Figs. 15-17).

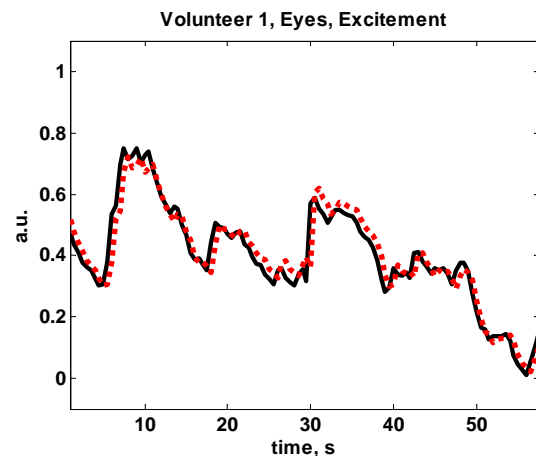


Fig. 12. Volunteer 1, Distance-between-eyes input, Excitement output signal. Recorded output signal – solid line, predicted output signal – dotted line

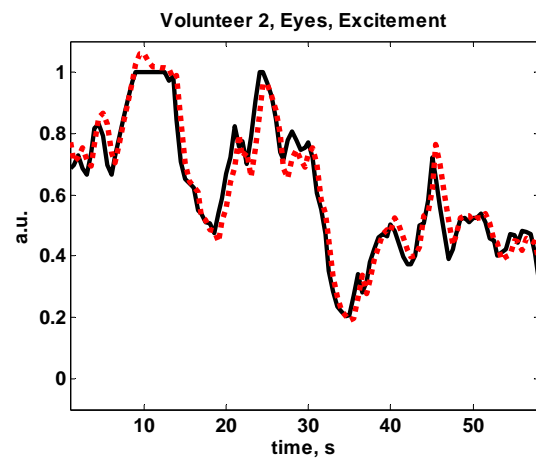


Fig. 13. Volunteer 2, Distance-between-eyes input, Excitement output signal. Recorded output signal – solid line, predicted output signal – dotted line

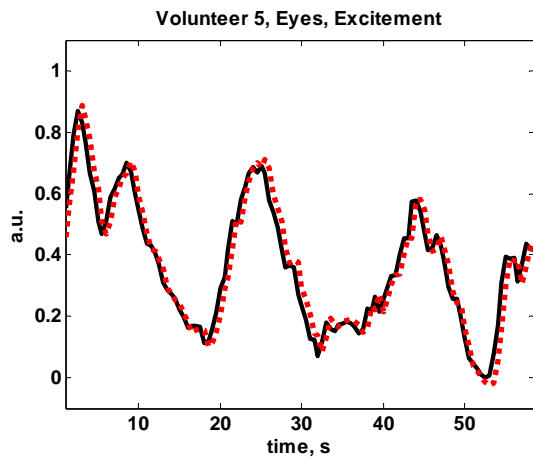


Fig. 14. Volunteer 5, Distance-between-eyes input, Excitement output signal. Recorded output signal – solid line, predicted output signal – dotted line

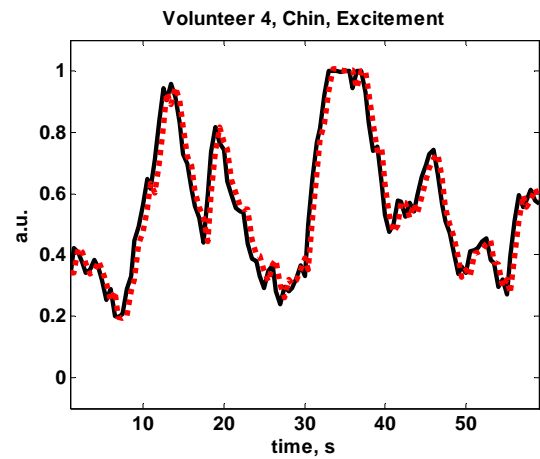


Fig. 17. Volunteer 4, Chin width input, Excitement output signal. Recorded output signal – solid line, predicted output signal – dotted line

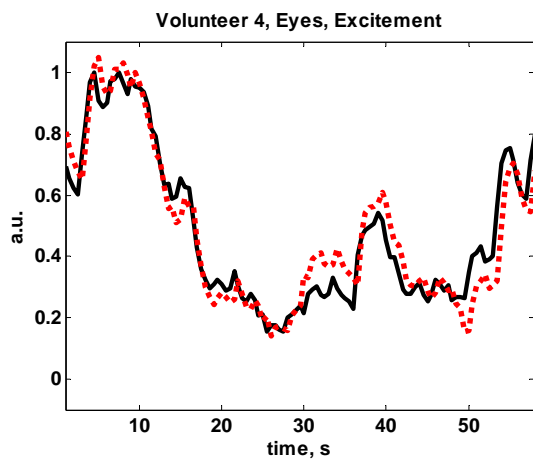


Fig. 15. Volunteer 4, Distance-between-eyes input, Excitement output signal. Recorded output signal – solid line, predicted output signal – dotted line

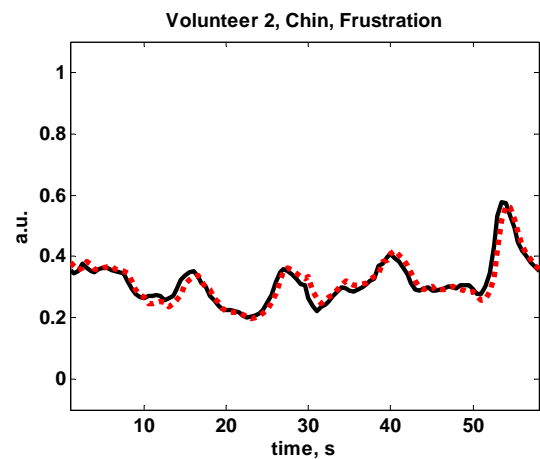


Fig. 18. Volunteer 2, Chin width input, Frustration output signal. Recorded output signal – solid line, predicted output signal – dotted line

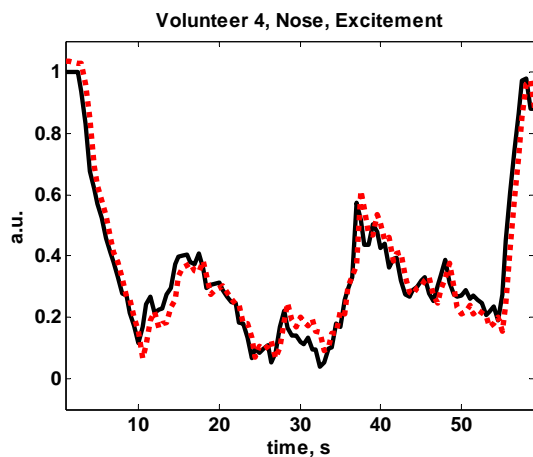


Fig. 16. Volunteer 4, Nose width input, Excitement output signal. Recorded output signal – solid line, predicted output signal – dotted line

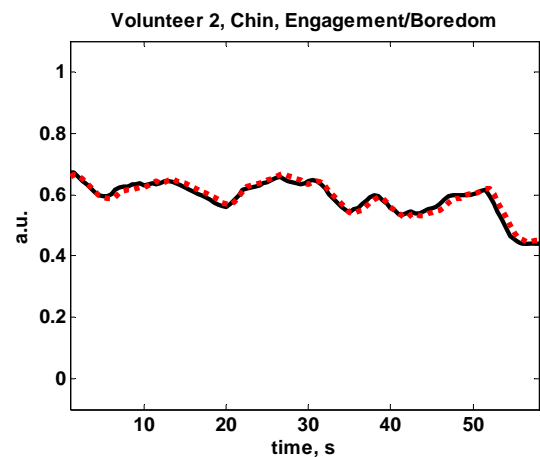


Fig. 19. Volunteer 2, Chin width input, Engagement/Boredom output signal. Recorded output signal – solid line, predicted output signal – dotted line

Frustration and Engagement/Boredom output signals are predicted accurately as well (Fig. 18 and Fig. 19 respectively). Frustration parameter has a larger variation in values and Engagement/Boredom is of a lower variation in values.

5. Conclusions

The mathematical model was constructed that allows describing the dependencies between visual stimuli (virtual 3D face that changes during time) and the reaction to them.

The validation of the model showed that it describes the dependencies between every input (distance between eyes, nose width and chin width) signal and every corresponding output signal (excitement, frustration, and engagement/boredom) for every of five volunteers in an acceptable accuracy.

Excitement parameter was predicted in a better accuracy in comparison to the frustration parameter. Prediction of the engagement/boredom parameter was predicted in the lower accuracy than frustration parameter.

Excitement parameter was equally well predicted for different volunteers and for different input (distance between eyes, nose width, and chin width).

6. Acknowledgements

Postdoctoral fellowship of Aušra Vidugirienė is being funded by European Union Structural Funds project "Postdoctoral Fellowship Implementation in Lithuania" within the framework of the Measure for Enhancing Mobility of Scholars and Other Researchers and the Promotion of Student Research (VP1-3.1-ŠMM-01) of the Program of Human Resources Development Action Plan.

7. References

1. G. Drettakis NIEVE: Navigation and Interfaces in Emotional Virtual Environments, 2010
2. M. H. Depledge, R. J. Stone, W. J. Bird. Can Natural and Virtual Environments Be Used To Promote Improved Human Health and Wellbeing? Environmental Science & Technology, 2011
3. P.J. Costello, Health and Safety Issues associated with Virtual Reality - A Review of Current Literature, 1997
4. A. Rizzo, J. Ford Morie, J. Williams, J. Pair, J. Galen Buckwalter, Human Emotional State and its Relevance for Military VR Training, The Proceedings of the 11th International Conference on Human Computer Interaction, 2005
5. J. Renny Octavia, K. Luyten, J. Vermeulen, B. Mommen, K. Coninx, Exploring Psychophysiological Measures for the Design and Behavior of Socially-Aware Avatars in Ubicomp Environments, CHI, 2010, USA
6. R. Bailey, K. Wise, and P. Bolls, How Avatar Customizability Affects Children's Arousal and Subjective Presence During Junk Food-Sponsored Online Video Games, CYBERPSYCHOLOGY & BEHAVIOR, Volume 12, Number X, 2009
7. Ahn J., Gobron S., Silvestre Q., and Thalmann D. Asymmetrical Facial Expressions based on an Advanced Interpretation of Two-dimensional Russell's Emotional Model. Proceedings of ENGAGE, Zermatt, Switzerland, 2010.
8. M. Mancini, B. Hartmann, C. Pelachaud, A. Raouzaïou, K. Karpouzis, Expressive avatars in MPEG-4, IEEE, 2005
9. Mehrabian A. Silent messages: Implicit communication of emotions and attitudes. Belmont, CA: Wadsworth, 1981
10. E. Vaškevičius, E. Bazevičius, A. Vidugirienė, V. Kaminskas, „Investigation of Avatar's Face Features Influence on User's Emotional State Using Neuro-Feedback“, Proc. of the 7th Int. Conf. on Electrical and Control Technologies (ECT 2012), p. 99 – 104
11. Emotiv EPOC specifications, Brain-computer interface technology, Emotiv 2012, internet access: <http://www.emotiv.com/upload/manual/sdk/EPOCspecifications.pdf>
12. V. Kaminskas. Dynamic Systems Identification via Discrete-Time Observations, Part1. Statistical Method Foundations. Estimation in Linear Systems, "Mokslas", 1982, (in Russian).

COMPARISON OF STATE ESTIMATION TECHNIQUES FOR BIOTECHNOLOGICAL PROCESSES

Vytautas GALVANAUSKAS*, Rimvydas SIMUTIS*,
Donatas LEVIŠAUSKAS*, Jolanta REPŠYTĖ*, Andreas LÜBBERT**
*Process Control Department, Kaunas University of Technology, Lithuania
**Martin Luther University Halle-Wittenberg, Halle/S., Germany

Abstract: In this article, application of state estimation techniques for indirect measurement of biomass concentration and specific growth rate in a typical fed-batch biotechnological process is discussed. Two state-of-the-art algorithms were implemented: Extended Kalman Filter (EKF) and feed-forward artificial neural networks (ANN) of various structures. Oxygen uptake rate (OUR), carbon dioxide production rate (CPR), and base consumption rate (BCR) along with their integrated quantities were used as direct reference measurements. The influence of measurement noise, experimental database size used for the model identification, and of the utilized input variables on the estimation quality was investigated. Recommendations for the application of the elaborated soft-sensors are given.

Keywords: state estimation, biotechnological processes, biomass concentration, specific growth rate, Extended Kalman Filter, artificial neural networks.

1. Introduction

Due to the rapid evolution of biotechnological industry in the recent decades, its importance for the global economy has tremendously increased. Nowadays, this branch of industry produces high-value pharmaceuticals, food additives and fine chemicals. One of the important segments of this industry is recombinant protein production. These biotechnological processes are especially complicated and require real-time monitoring and control that increases their repeatability, productivity and safety. Unfortunately, till now there are few direct measurements for the important biotechnological quantities, e. g., biomass concentration and specific growth rate, which are reliable, robust and applicable online on industrial scale [1]. Therefore, it is of advantage to apply state estimation approaches based on softsensors that utilize data from other measurements available online. The

available approaches are analyzed in literature [1, 2], in which their practical application is discussed in details. In this paper, a typical fed-batch biotechnological process for recombinant protein production is investigated. A first-principle mathematical model of the process is used for generation of the datasets necessary to perform training, testing and validation of the elaborated soft-sensors. Two state-of-the-art algorithms are implemented: Extended Kalman Filter (EKF) and feed-forward artificial neural network (ANN). Various measurement noise intensities and combinations of the input variables are tested. Finally, the obtained results are discussed and recommendations for the application are given.

2. Materials and methods

2.1 Biotechnological process

Escherichia coli B carrying the plasmid pUBS 520 was used as the host. A second plasmid p12023, which is a derivate of the pKK223-3 was introduced into the strain. The bacterium is able to express the Fv-fragment of the antibody MAK33 under the control of the tac-promoter.

The culture was cultivated in a series of fed-batch processes on a defined medium. Initially, the culture was grown on a glucose-based medium until the glucose was depleted and the biomass concentration reached a value of about 1-2 [g kg⁻¹]. Then, the production of the recombinant protein was induced by addition of the lactose, which was then utilized by the cells simultaneously as inducer and carbon source. The biomass growth and product formation were controlled by means of feeding rate (F_S and F_L) and dissolved oxygen (O_2) concentration control. Additional details on the experimental set-up for the analyzed process are given elsewhere [4]. Based on real experimental data, a mechanistic process model was developed and process optimization procedure was performed [3,4].

Subsequently, special “synthetic” data sets were generated for the state estimation studies presented in this article.

Typical trajectories of an optimized process are presented in Fig. 1. They were generated using the model [3, 4] which parameters were identified from the real experimental data. Additionally, white Gaussian noise of a given intensity was added to the simulation data. The process can be divided into two distinct phases: 1) biomass (X) growth on glucose (S) and 2) biomass growth on lactose (L) with the simultaneous product (P) formation. In the first phase, during the biomass growth on glucose, acetate (A) is built. Its production rate can be described by means of the bottleneck kinetics. In the second part of the first phase (3.0-6.0 cultivation hours), when the glucose consumption rate drops below the critical value to

substrate limitation, acetate is gradually consumed. In the first phase, there is no product generation as the inducer (lactose) is not present in the medium. In the second phase, which starts immediately after the glucose and acetate are consumed and lactose is fed, the production of the recombinant protein (P) is induced. The protein specific production rate (q_p) depends on many factors, but the most important ones are: relatively high specific growth rate ($\mu \geq 0.4$ [h⁻¹]) and sufficient inducer (lactose) concentration ($L \geq 1.0$ [g kg⁻¹]). The process was optimized with respect to given technological and physiological constraints and with the aim to maximize the amount of the target product (PW) at the end of the cultivation process.

More details about the cultivation conditions and measurement techniques are provided elsewhere [3, 4].

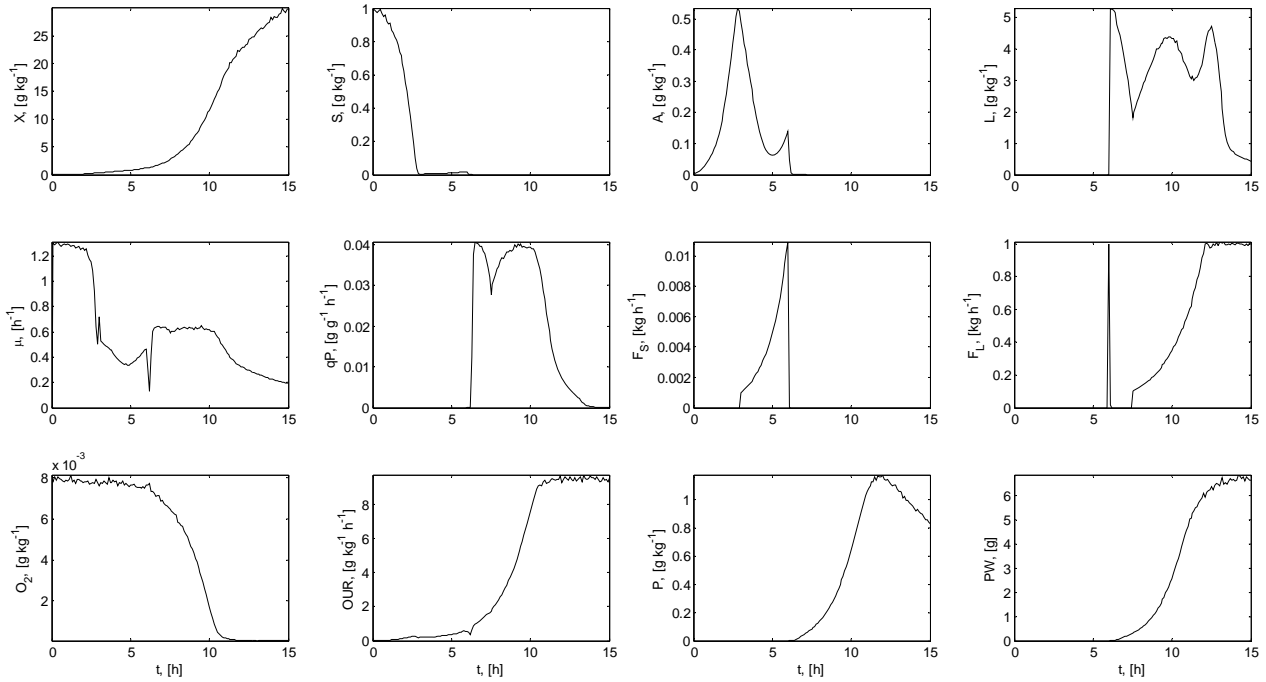


Fig. 1. An optimized fed-batch process of MAK33 recombinant protein production

2.2 Mathematical model of the process

Original first-principle mathematical model of the fed-batch cultivation process consists of differential equations for the main state variables: biomass (X), glucose (S), acetate (A), lactose (L), target product (P), dissolved oxygen (O), and broth weight (W). Additionally, the specific reaction rates for biomass growth, glucose and lactose consumption, acetate production/consumption as well as for the target product formation were built using the main mechanistic laws, e. g., Monod, Haldane, Moser, and Pirt-type kinetics. More details about the mathematical model are provided elsewhere [3, 4].

For the state estimation studies presented in this article, a simplified process model was used. In this study, only those equations are presented that are directly related to the soft-sensor development and/or explain the relationships between directly measured and indirectly estimated process variables.

The elaborated soft-sensors should estimate the biomass concentration and its specific growth rate. Let's analyze the following two equations of the model [3, 4]:

$$\frac{dX}{dt} = \mu X - \frac{F}{W} X, \quad (1)$$

where X is biomass concentration, W is cultivation broth weight, F is total flow into the bioreactor, and μ is biomass specific growth rate:

$$\mu = \frac{q_L}{Y_{LX}} + \frac{q_S}{Y_{SX}} + \frac{q_{Acc}}{Y_{AccX}} + \frac{q_{Acp}}{Y_{AcpX}} - m. \quad (2)$$

μ depends on the substrate/byproduct consumption rates q_L , q_S , q_{Acc} , byproduct production rate q_{Acp} , and maintenance term m . The appropriate yield coefficients Y take into account the conversion rates of the particular reactions. As it can be seen from the equations (1-2),

they can be used together with the whole process mathematical model [3, 4] only, having initial conditions of the state variables, calculated reaction rates and measured flows, but the equations (1-2) cannot be straightforwardly applied in the soft-sensors as these equations contain some quantities that cannot be measured online (e. g., substrate consumption rates that depend on the concentrations of the substrates). Therefore, one has to choose the process measurements that are accurate enough, are carried out online and can be correlated with the biomass concentration and specific growth rate.

2.3 Soft-sensors

The suitable input variables can be oxygen uptake rate (OUR), carbon dioxide production rate (CPR), and base consumption rate (BCR), along with their integrated values. The correlations between the abovementioned variables, X and μ can be defined as follows [5]:

$$OUR = Y_{orX} \mu X + Y_{om} X, \quad (3)$$

$$CPR = Y_{crX} \mu X + Y_{cm} X, \quad (4)$$

$$BCR = Y_{brX} \mu X W. \quad (5)$$

The yield coefficients Y are different for each phase of the process and were identified from the specially design experiments, during which a constant specific growth rate was maintained within sufficiently long time period. Other important quantities, which can be utilized in the soft-sensors, are the integrals (totalized values) of the variables described by equations (3-5) with respect to the total weight of the cultivation broth:

$$OUR_t = \sum_{i=1}^n OUR_i W_i \Delta t_i, \quad (6)$$

$$CPR_t = \sum_{i=1}^n CPR_i W_i \Delta t_i, \quad (7)$$

$$BASE = Y_{brX} X_i W_i. \quad (8)$$

The variables defined by the equations (3-8), cultivation broth weight W , and the process time are used as the input variables of the soft-sensors.

2.3.1 Extended Kalman Filter

Extended Kalman Filter (EKF) is an optimal model-supported on-line estimator of state and process variables. It makes use of a dynamic model, its estimated uncertainty, as well as of the online measured process measurement data together with their associated uncertainties.

EKF makes a one-step-ahead prediction of the vector \mathbf{x} to be estimated. The task for the EKF discussed in this article is to estimate one state variable, the biomass concentration X , and one of the most important process variables, the specific growth rate μ . OUR, CPR, and BCR along with their integrated values and dilution rate D are considered to be available online. In every time

moment k , D can be calculated from the culture broth weight W :

$$D_k = \frac{W_k - W_{k-1}}{0.5 \Delta t_k (W_k + W_{k-1})}. \quad (9)$$

Let's assume that the quantities to be estimated are denoted by a vector \mathbf{x} with two elements:

$$\mathbf{x} = [X \ \mu]^T, \quad (10)$$

where X is measured offline only and the specific growth rate μ , which cannot be measured directly, is considered a (nearly) constant parameter within short time period. The idea behind the EKF is to make use of measurement data and a process model to perform one-step-ahead predictions for the estimation variable vector \mathbf{x}_k at time t_k starting from the last estimated value \mathbf{x}_{k-1} . The relevant process model for EKF is:

$$\frac{d\mathbf{x}}{dt} = \mathbf{M} + \mathbf{w} = \frac{d}{dt} \begin{pmatrix} X \\ \mu \end{pmatrix} = \begin{pmatrix} \mu X - DX \\ 0 \end{pmatrix} + \begin{pmatrix} w_1 \\ w_2 \end{pmatrix}, \quad (11)$$

where \mathbf{M} is the right hand side of the model differential equation, w_1 and w_2 are assumed to be white noise, describing the modeling error or uncertainty.

Since the biomass X and also the specific growth rate μ cannot be measured directly online, these quantities must be related to the available measurement data. This is done by means of the separate measurement model. In the analyzed case, the optimal structure of the measurement model was found to be the following:

$$\mathbf{y} = \mathbf{N} + \mathbf{v} = \begin{pmatrix} OUR \\ CPR \\ BASE \end{pmatrix} = \begin{pmatrix} Y_{orX} \mu X + Y_{om} X \\ Y_{crX} \mu X + Y_{cm} X \\ Y_{brX} X W \end{pmatrix} + \begin{pmatrix} v_1 \\ v_2 \\ v_3 \end{pmatrix}, \quad (12)$$

where $\mathbf{v} = [v_1 \ v_2 \ v_3]^T$ is a noise vector containing white noise errors v_1 , v_2 and v_3 . The parameters Y were identified in advance from the specially designed exploratory experiments.

Initial values for the state variables are considered to be distorted by the white noise signal values p_1 and p_2 :

$$\mathbf{x}(t=0) = [X_0 \ \mu_0]^T + [p_1 \ p_2]^T. \quad (13)$$

I. e., the sequences w_1 , w_2 , v_1 , v_2 , v_3 , p_1 , and p_2 are assumed to be normally distributed random numbers with zero mean, and the corresponding covariance matrices \mathbf{W} , \mathbf{V} and \mathbf{P} , respectively, are build with the squares of these values as diagonal elements.

The Extended Kalman Filter makes a one-step-ahead prediction. It first predicts the elements of the state vector \mathbf{x} at time step k , denoted X_{pk} and μ_{pk} , from the estimates for the previous time step $t_{k-1} = t_k - \Delta t$ using the discrete form of the model \mathbf{M} :

$$\mathbf{x}_{pk} = \mathbf{x}_{k-1} + dt \mathbf{M}_D = \begin{pmatrix} X_{pk} \\ \mu_{pk} \end{pmatrix} = \begin{pmatrix} X_{k-1} \\ \mu_{k-1} \end{pmatrix} + dt \begin{pmatrix} (\mu_{k-1} - D_{k-1}) X_{k-1} \\ 0 \end{pmatrix}. \quad (14)$$

Using the predicted values \mathbf{x}_{pk} (X_{pk} and μ_{pk}) in the measurement model, the result of the next measurement is predicted by:

$$\mathbf{y}_{pk} = \mathbf{N}(\mathbf{x}_{pk}) = \begin{pmatrix} OUR_{pk} \\ CPR_{pk} \\ BASE_{pk} \end{pmatrix} = \begin{pmatrix} Y_{orX}\mu_{pk}X_{pk} + Y_{om}X_{pk} \\ Y_{crX}\mu_{pk}X_{pk} + Y_{cm}X_{pk} \\ Y_{brX}X_{pk}W_{k-1} \end{pmatrix}. \quad (15)$$

Realization of Extended Kalman Filter algorithms can now be performed in following steps:

a) covariance matrix of the process model is estimated

$$\mathbf{P}_{pk} = \Phi_{k-1}\mathbf{P}_{k-1}\Phi_{k-1}^T + \mathbf{W}_k, \quad (16)$$

where $\Phi_{k-1} = \frac{\partial \mathbf{x}_{pk}}{\partial \mathbf{x}_{k-1}} = \begin{pmatrix} 1 + (\mu_{k-1} - D_{k-1})\Delta t & X_{k-1}\Delta t \\ 0 & 1 \end{pmatrix}$; (17)

b) covariance matrix of the predicted measurements is estimated

$$\mathbf{Q}_k = \mathbf{C}_k\mathbf{P}_{pk}\mathbf{C}_k^T + \mathbf{V}_k, \quad (18)$$

where $\mathbf{C}_k = d\mathbf{N}(\mathbf{x}_{pk})/d\mathbf{x}_{pk}$; (19)

c) Kalman gain is estimated

$$\mathbf{K}_k = \mathbf{P}_k \frac{1}{\mathbf{Q}_k} \mathbf{C}_k^T = \frac{\mathbf{P}_k \mathbf{C}_k^T}{\mathbf{C}_k \mathbf{P}_{pk} \mathbf{C}_k^T + \mathbf{V}_k}; \quad (20)$$

d) state estimate is determined

$$\mathbf{x}_k = \mathbf{x}_{pk} + \mathbf{K}_k (\mathbf{y}_k - \mathbf{y}_{pk}); \quad (21)$$

e) finally, since the improved estimates for \mathbf{x}_k are now available, one can update the covariance matrix \mathbf{P}_k of the state vector \mathbf{x}_k by

$$\mathbf{P}_k = \mathbf{P}_{pk} - \mathbf{K}_k \mathbf{C}_k^T \mathbf{P}_{pk}. \quad (22)$$

The square roots of the diagonal elements of the corrected state covariance matrix \mathbf{P}_k are coarse indicators of the accuracy of the state estimate.

The EKF algorithm was used for indirect estimation of biomass concentration X and specific growth rate μ of the MAK33 recombinant protein production process. Various combinations of initial conditions, feeding strategies and noise intensities were tested.

2.3.2 Feed-forward artificial neural network

As a second alternative, soft-sensors based on the application of feed-forward artificial neural networks (ANNs) were elaborated, trained and validated.

The ANNs used in the study have one hidden layer with fast hyperbolic tangent activation functions and the output layer with linear activation functions. Furthermore, tests have proven that one node in the hidden layer was optimal to guarantee the required training/validation quality. The data supplied for

training/validation was generated using the simulation data covered by the white Gaussian noise signal of various intensities. Before using as ANN inputs and outputs, all the data was normalized to zero mean and unit variance. For training purposes, Levenberg-Marquardt algorithm was used.

Various combinations of the input variables were tested. After performing sensitivity analysis, the following set of input variables was chosen: OUR_t , CPR_t , $BASE$ and process time t . The structure of the ANN is presented in Fig. 2.

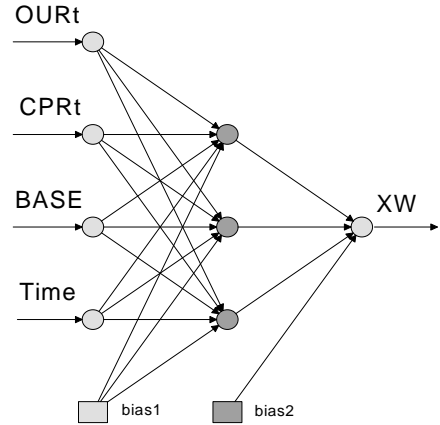


Fig. 2. Structure of the ANN

The single output variable was the total biomass amount XW . After estimating the XW value, the first variable of our interest, i. e. biomass concentration X was calculated dividing the XW values by the corresponding online measured W values. The second variable of the soft-sensor, specific growth rate μ , was calculated from the following equation:

$$\begin{aligned} \mu &= \frac{d(XW)}{dt} \frac{1}{XW} \cong \frac{\Delta(XW)}{\Delta t} \frac{1}{XW} = \\ &= \frac{X_i W_i - X_{i-1} W_{i-1}}{\Delta t_i} \frac{1}{0.5(X_i W_i + X_{i-1} W_{i-1})}. \end{aligned} \quad (23)$$

3. Results and discussion

Quality of the elaborated EKF and ANN soft-sensors was evaluated by calculating the root mean square errors for X and μ :

$$RMSE_X = \sqrt{\frac{\sum_{i=1}^N (\bar{X}_i - X_i)^2}{N}}, \quad (24-25)$$

$$RMSE_\mu = \sqrt{\frac{\sum_{i=1}^N (\bar{\mu}_i - \mu_i)^2}{N}},$$

where \bar{X}_i and $\bar{\mu}_i$ are the values of the variables estimated by the appropriate soft-sensors, X_i and μ_i are the values of the variables obtained from the process, and N is the number of samples.

Acceptable estimation RMSE for X in the most practical applications (when the highest biomass concentration is within the range of 20-40 [g kg⁻¹]) varies between 0.5 and 1.0 [g kg⁻¹]. Realistic relative measurement noise intensity in most cases does not exceed 0.02-0.025.

Acceptable estimation RMSE for μ in the most practical applications (when the highest specific growth rate is within the range of 1-1.5 [h⁻¹]) varies between 0.2 and 0.3 [h⁻¹].

In the analyzed case, 440 different experiments were generated using full mechanistic model [3, 4], 150 measurement points per experiment ($\Delta t=0.01$ [h]).

During the generation of data sets, white Gaussian noise signals (0.005, 0.01, 0.025 and 0.05 intensities relatively to the average value of the state variables within moving window) were added.

The application results of EKF-based soft-sensor are presented in Fig. 3-4.

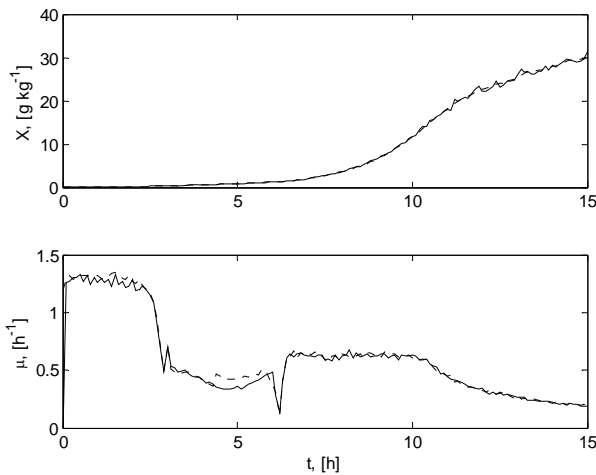


Fig. 3. EKF state estimation quality in a typical optimized experiment. Solid lines represent reference values of the variables X and μ ; dotted lines represent the estimated values

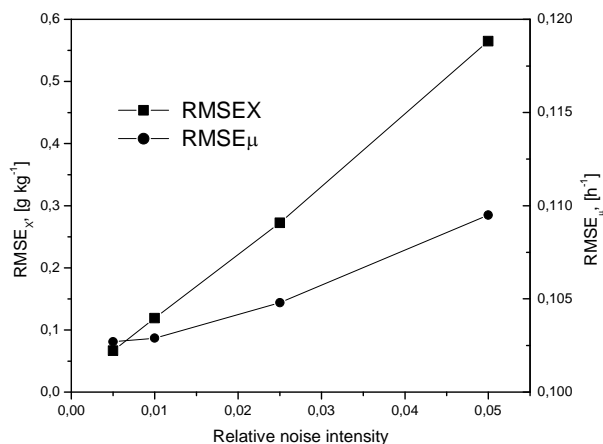


Fig. 4. RMSE_X and RMSE_μ as a function of relative noise intensity of the experimental data

Fig. 3 shows the estimation quality of a typical optimized experiment (EKF-based soft-sensor validation results). Data supplied for the soft-sensor was generated using 0.025 relative noise intensity.

Soft-sensor validation results: RMSE_X=0.28 [g kg⁻¹]; RMSE_μ=0.1 [h⁻¹]. The estimation results show that the biomass concentration and specific growth rate are estimated with sufficiently precision within the investigated span of noise intensity. Both estimation errors (see Fig. 4) meet the requirements for practical application.

The application results of ANN-based soft-sensors are summarized in Fig. 5-7.

During the ANN training procedure, 5, 10, 15 or 20 randomly chosen experiments were used. During the ANN validation procedure, the same numbers of experiments from the remaining data set was chosen.

The prediction quality in validation experiments was evaluated from the equations (24-25).

Fig. 5 shows the estimation quality of a typical optimized experiment (soft-sensor validation results). The data used for soft-sensor training: 0.01 relative noise intensity; 20 randomly chosen experiments. Soft-sensor validation results: RMSE_X=0.25 [g kg⁻¹]; RMSE_μ=0.2 [h⁻¹]. The results show that the biomass estimation quality is highly satisfactory. The specific growth rate estimation results show significant noise due to numerical differentiation according to the eq. (23). Nevertheless, in the given example, the estimation error is within the acceptable limits and the soft-sensor is suitable for practical application.

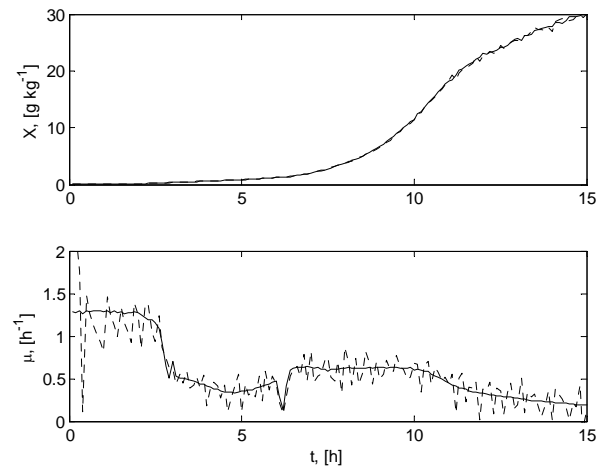


Fig. 5. ANN state estimation quality in a typical optimized experiment. Solid lines represent reference values of the variables X and μ ; dotted lines represent the estimated values

Fig. 6-7 show the contour surfaces of RMSE for biomass concentration X and specific growth rate μ as a function of applied relative noise intensity and the number of experiments used for ANN training/validation. The results presented in Fig. 6 show that X estimation error gradually increases with the increasing noise intensity and decreasing data sample size. Taking into account the acceptable range of estimation errors, the estimation quality of the soft-sensor for biomass concentration within the working range is considered acceptable. The X estimation quality of both analyzed approaches is also comparable with the results achieved by means of other biomass estimation techniques that are presented in literature [2].

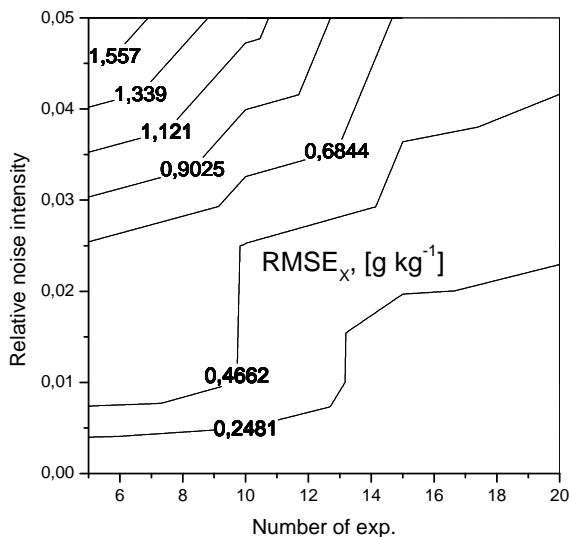


Fig. 6. Contour surface of $RMSE_X$ as a function of relative noise intensity and number of experiments used for ANN training/validation

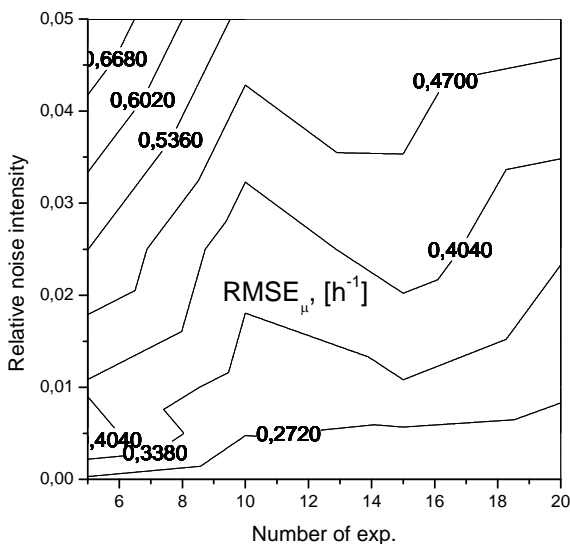


Fig. 7. Contour surface of $RMSE_\mu$ as a function of relative noise intensity and number of experiments used for ANN training/validation

The results presented in Fig.7 show that μ estimation quality follows the same law as in the case of X estimation. Nevertheless, the influence of measurement noise is less than in the case of X . Taking into account the acceptable range of μ estimation errors, the estimation quality of the ANN-based soft-sensor for specific growth rate is acceptable only in presence of a moderate relative noise intensity (up to 0.01) and having relatively high number of experiments for ANN training purpose.

4. Conclusions

The comparison results show that both EKF and ANN soft-sensors can assure comparable estimation quality

and are suitable for practical applications. Nevertheless, the approaches suffer from distinct limitations, which may limit their application under certain conditions.

Under all tested conditions (0.005-0.05 relative noise intensities), the EKF algorithm assured a state estimation quality that is adequate for practical applications. The application of EKF is of advantage when the information about the statistical noise measures is known in advance and the parameters of the measurement models are correctly identified.

The ANN-based soft-sensors can be successfully applied when sufficiently large amount of training/validation data is available. In the analyzed case, the threshold value of the training dataset size was ~ 10 experiments, below which the estimation error of the specific growth rate could exceed the acceptable value of 0.3 $[h^{-1}]$ when higher relative noise intensity (>0.01) is present. Hence, additional filtering techniques should be applied in order to reduce the estimation RMSE of the specific growth rate. This topic is currently under investigation and will be presented in a separate study.

5. Acknowledgements

This research was funded by a grant (No. MIP-056/2013) from the Research Council of Lithuania.

6. References

1. Sonnleitner B. Instrumentation of Biotechnological Processes. In: Advances in Biochemical Engineering and Biotechnology. Vol. ed.: Sonnleitner B., Springer, 1999, 66:3-54.
2. Galvanauskas V., Simutis R., Lübbert A. Direct comparison of four different biomass estimation methods against conventional dry weight measurements. Process control and quality, 1998, 11(2), 119-124, DOI: 10.1163/156856698750247786
3. Levišauskas D., Galvanauskas V., Simutis R., Lübbert A. Model Based Calculation of Substrate/Inducer Feed-Rate Profiles in Fed-Batch Processes for Recombinant Protein Production. Biotechnology Techniques, 1999, 13(1), 37-42, DOI: 10.1023/A:1008887514011
4. Galvanauskas V., Volk N., Simutis R., Lübbert A. Design of Recombinant Protein production Processes. Chemical Engineering Communications, 2004, 191(5), 732-748, DOI: 10.1080/00986440490276056
5. Galvanauskas V., Simutis R., Volk N., Lübbert A. Model Based Design of a Biochemical Cultivation Process. Bioprocess and Biosystems Engineering, 1998, 18(3), 227-234, DOI: 10.1007/s004490050435

FORECASTING OF DEVICE COMPONENT FAILURES BY ADVANCED ALGORITHMS

Saulius ŽIŪKAS, Vygandas VAITKUS
Kaunas University of Technology, Lithuania

Abstract: Companies around the world are facing storage management problem. To solve this problem, companies should use the spare parts demand forecast, or in other words, to predict equipment failures. Failures of various equipment components can be forecasted by adapting advanced algorithms. This paper introduces how to implement two regression models and multi-layer feedforward artificial neural network on automated teller machines components failures in detail, including model identification, forecasting and analysis of forecasting errors.

Keywords: Automated teller machine, data mining, artificial neural network, regression, decision tree.

1. Introduction

Machinery maintenance practices have changed greatly over the years. Usually, a machine would fail before maintenance is performed. It is reactive maintenance and it is still the predominant mode of maintenance. The advantage of this mode is low cost and less staff. But also it has a disadvantages and they are:

- Increase of cost due to unplanned downtime of equipment.
- Increase of labor cost, especially if overtime is needed.
- Cost involved with repair or replacement of equipment.
- Possible secondary equipment or process damage from equipment failure.
- Inefficient use of staff resources.

Second mode is preventive maintenance. Preventive maintenance can be defined as actions performed on a time - or machine-run-based schedule that detect, preclude, or mitigate degradation of a component or system with the aim of sustaining or extending its useful life through controlling degradation to an acceptable level. Its advantages are:

- Cost effective in many capital-intensive processes.
- Flexibility allows for the adjustment of maintenance periodicity.

- Increased component life cycle.
- Energy savings.
- Reduced equipment or process failure.

And disadvantages:

- Catastrophic failures still likely to occur.
- Labor intensive.
- Includes performance of unneeded maintenance.
- Potential for incidental damage to components in conducting unneeded maintenance.

While preventive maintenance is not the optimum maintenance program, it does have several advantages over that of a purely reactive program. By performing the preventive maintenance (lubrication, filter change, etc.) as the equipment designer envisioned, it will extend the life of the equipment closer to design.

Third and possibly the most effective maintenance mode is predictive. Predictive maintenance can be defined as follows: Measurements that detect the onset of system degradation (lower functional state), thereby allowing causal stressors to be eliminated or controlled prior to any significant deterioration in the component physical state. Basically, predictive maintenance differs from preventive maintenance by basing maintenance need on the actual condition of the machine rather than on some preset schedule. The advantages of predictive maintenance are:

- Increased component operational life/availability.
- Allows for preemptive corrective actions.
- Decrease in equipment or process downtime.
- Decrease in costs for parts and labor.
- Better product quality.
- Improved worker and environmental safety.
- Improved worker morale.
- Energy savings.

Disadvantages are:

- Increased investment in diagnostic equipment.
- Increased investment in staff training.

There are many advantages of predictive maintenance. A well-organized predictive maintenance program will

eliminate catastrophic equipment failures. Staff will be able to schedule maintenance activities, to minimize or delete overtime costs, to minimize inventory and order parts to support maintenance needs. It becomes possible to optimize the operation of the equipment, saving energy cost and increasing plant reliability.

Our investigation object is automated teller machine (ATM) failures. ATM (Fig.1) consists of more than 20000 parts, so a wide variety of failures can occur. Usually parts of ATM are divided in main classes, then subclasses and so on. It is done because of variety of spare parts and maintenance simplicity. Co-operating in research a joint stock company is using hybrid maintenance mode. It is a combination of reactive and preventive modes. In reality after failure only one small part of the main component could be changed and the problem is fixed, but sometimes cost less to replace whole braked component by new one. Spare parts cost strongly depends on business case and usually consist of spare part price also delivering, storing, replacement and sometimes other components of service prices. So maintenance and repairs are the priority activities of the service companies and spare parts suppliers and as it was mentioned above they are trying to make planning for down time of ATM. To reach that goal they need to forecast time till failure or in other words they need to switch current maintenance mode to predictive mode. In collaboration with ATM service companies the data of ATM service and repair records were received.



Fig. 1. Automated teller machine back side view

2. Data Mining

Like many areas of industry, data is collected but very little is converted to useful information. Data mining is extracting or “mining” knowledge from large amounts of data. Data mining is very important with the ever-growing amounts of stored data. It automates the analysis of large volumes of data to produce useful information. There are two kinds of models in data mining, predictive and descriptive. The descriptive model summarizes data illustrating subgroups of data.

The predictive model makes predictions based on historical data. This model may be able to determine a time of ATM component failure. Next section describes material and methods for predictive modeling.

3. Material and methods

Ensemble methods that build multiple trees can dramatically reduce the error, but usually result in huge structures that are incomprehensible. Breiman (1996) [3] describes a Bagging (*Bootstrap Aggregating*) procedure. Schapire (1990) [5] introduced boosting, which was later enhanced in Freund & Schapire (1995) [4].

Boosting algorithms are a class of general methods used to improve the general performance of regression analysis. The main idea is to maintain a distribution over the train set.

Bagging predictors is a method for generating multiple versions of a predictor and using these to get an aggregated predictor. The aggregation averages over the versions when predicting a numerical outcome and does a plurality vote when predicting a class. The multiple versions are formed by making bootstrap replicates of the learning set and using these as new learning sets. Tests on real and simulated data sets using classification and regression trees and subset selection in linear regression show that bagging can give substantial gains in accuracy. The vital element is the instability of the prediction method. If perturbing the learning set can cause significant changes in the predictor constructed, then bagging can improve accuracy.

All boosting and bagging algorithms are based on tree learners.

Bagging algorithms generally constructs deep trees. This construction is both time consuming and memory-intensive. This also leads to relatively slow predictions. Bagging predictors is a method for generating multiple versions of a predictor and using these to get an aggregated predictor. The aggregation averages over the versions when predicting a numerical outcome and does a plurality vote when predicting a class.

Boosting algorithms generally use very shallow trees. This construction uses relatively little time or memory. However, for effective predictions, boosted trees might need more ensemble members than bagged trees.

Artificial neural networks are modeling techniques that are capable of modeling extremely complex functions and analyse large amounts of data to discover the predominant features and patterns within it.

3.1. Decision trees

Decision tree learning is a method for approximating discrete-valued target functions, in which the learned functions is represented by a decision tree. Learned trees can also be re-represented as sets of *if-then* rules to improve human readability. These learning methods are among the most popular of inductive inference algorithms and have been successfully applied to a broad range of tasks from learning to diagnose various cases. This method constructs trees that have only binary splits. This restriction simplifies the splitting criteria

because there is not needed a penalty for multi-way splits. Furthermore, if the label is binary, the binary split restriction allows decision tree to optimally partition categorical attributes to two subsets of values in time that is linear time in the number of attribute values. The restriction has its disadvantages, however. The tree may be less interpretable with multiple splits occurring on the same attribute at adjacent levels. There may be no good binary split on an attribute that has a good multi-way split, which may lead to inferior trees.

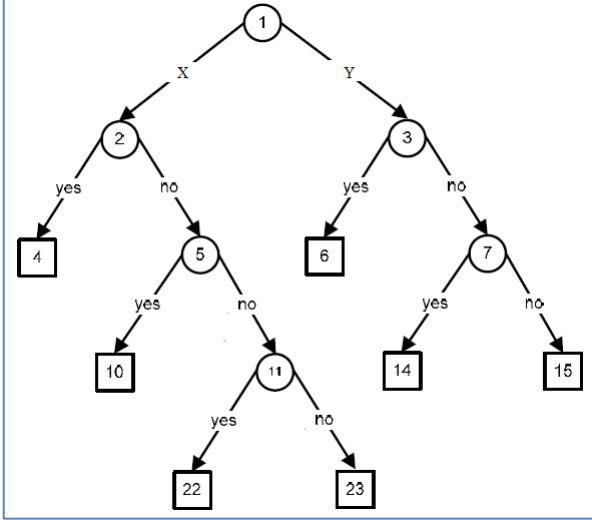


Fig. 2. Example of a binary decision tree

3.2. Least squares boosting for regression

The idea of boosting is to increase the strength of a weak learning algorithm. For a binary classifier, the weak learning hypothesis is getting 50% right. Boosting trains a weak learner a number of times, using a reweighted version of the original training set. Boosting trains the first weak learner with equal weight on all the data points in the training set, then trains all other weak learners based on the updated weight. The data points wrongly classified by the previous weak learner get heavier weight, and the correctly classified data points get lighter weight. This way, the next classifier will attempt to fix the errors made by the previous learner.

This algorithm (“*LSBoost*”) iteratively call a base learning algorithm L (also called *weak learner*) of a weighted training sample. The base learner is expected to return in each iteration t a hypothesis h_t from some hypothesis that has small *weighted training error* which is the weighted number of false predictions in classification and weighted estimation error in regression.

The algorithm “*LSBoost*” is from Friedman’s gradient-based boosting strategy, using square loss $L = (y - r)^2/2$ where r is the actual training label and y is the current cumulative output:

$$y_i = c_0 + \sum_{j=1}^{i-1} c_j h_j + c_i h_i = y_{i-1} + c_i h_i \quad (1)$$

The new training labels r should be set to the direction that minimizes the loss, which is the negative gradient with respect to y evaluated at y_{i-1} .

Then $r = [-\partial L / \partial y]_{y=y_{i-1}} = r - y_{i-1}$ which is the current residual error. Substituting into the loss, we get the training error:

$$E = \sum_{t=1}^N [c_t h_t^t - r^t] \quad (2)$$

where r^t are the current residual labels. The combination coefficients c_i are determined by solving $\partial E / \partial c_i = 0$.

3.3. “Bagging” algorithm for regression

A learning set of L consists of data $\{(y_n, x_n), n = 1, \dots, N\}$ where the y ’s are either class labels or a numerical response. Assume we have a procedure for using this learning set to form a predictor $\varphi(x, L)$ — if the input is x we predict y by $\varphi(x, L)$. Now, suppose we are given a sequence of learning sets $\{L_k\}$ each consisting of N independent observations from the same underlying distribution as L . Mission is to use the $\{L_k\}$ to get a better predictor than the single learning set predictor $\varphi(x, L)$. The restriction is that all we are allowed to work with is the sequence of predictors $\{\varphi(x, L_k)\}$.

If y is numerical, an obvious procedure is to replace $\varphi(x, L)$ by the average of $\varphi(x, L_k)$ over k , i.e. by $\varphi_A(x) = E_L \varphi(x, L)$ where E_L denotes the expectation over L , and the subscript A in φ_A denotes aggregation. If $\varphi(x, L)$ predicts a class $j = \{1, \dots, J\}$, then one method of aggregating the $\varphi(x, L_k)$ is by voting. Let $N_j = nr \{k; \varphi(x, L_k) = j\}$ and take $\varphi_A(x) = \text{argmax}_j N_j$, that is, the j for which N_j is maximum.

Usually, though, we have a single learning set L without the luxury of replicates of L . Still, an imitation of the process leading to φ_A can be done. Take repeated bootstrap samples $\{L^{(B)}\}$ from L , and form $\{\varphi(x, L^{(B)})\}$.

If y is numerical, take φ_B as $\varphi_B(x) = \text{avg}_B \varphi(x, L^{(B)})$.

If y is a class label, let the $\{\varphi(x, L^{(B)})\}$ vote to form $\varphi_B(x)$. This procedure is called “*bootstrap aggregating*” and uses the acronym *bagging*.

The $\{L^{(B)}\}$ form replicate data sets, each consisting of N cases, drawn at random, *but with replacement*, from L . Each (y_n, x_n) may appear repeated times or not at all in any particular $L^{(B)}$. The $\{L^{(B)}\}$ are replicate data sets drawn from the bootstrap distribution approximating the distribution underlying L .

3.4. Multi-layer feedforward neural network

The multi-layer perceptron is the most popular neural network. Its structure has an input layer which presents data to the network for processing in one or more hidden layers of neurons. Every neuron in a layer is connected to every neuron in the adjacent layers. The data is weighted to modify its strength as it is passed from one neuron to the next. Each neuron sums the weighted data from neurons in the previous layer to produce a new value, passing this on to the next layer of neurons. Output layer produces a classification.

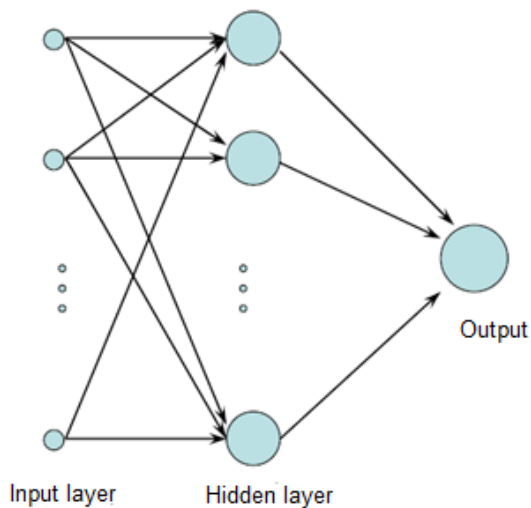


Fig. 3. Multi-layer feedforward neural network

4. Experimental investigation

Three experiments were designed to evaluate the performance of techniques described. First, comparing the mean absolute percentage error of the least squares boosting using different number of decision trees. Second, examining bagging algorithm with the same error evaluation and number of decision trees. Third, applying multi-layer feedforward neural network with different number of nodes in the hidden layer. Experimental calculations, programming and modeling was performed by using *Matlab* software.

4.1. Description of data

The database contains different ATM's component failures that is registered by specialists after each failure appears.

It contains nearly 5000 records. The database includes failure records dating from 2003 to 2011. The columns in database are:

- *DefectDate* – date of failure recording.
- *YearMade* – year of component manufacturing.
- *DeviceCode* – type of ATM.
- *DeviceSerialNr* – serial number of ATM.
- *ModuleCode* – type of the component.
- *ModuleName* – name of the component.
- *ModuleSerialNr* – serial number of the component.
- *PartCode* – type of the specific part in component.
- *PartName* – name of the specific part in component.
- *Part Q-ty* – quantity of parts that was changed after failure.
- *Outdoor* – environment of ATM maintenance (inside or outside of the building).
- *WorkDaysTillDefect* – days that specific component worked before failure.
- *RepairCount* – times that specific component was repaired overall.
- *ModuleVendor* – manufacturer of the specific component.

Data collected improperly results an invalid data being stored in the database. The invalid records are excluded in this analysis. Improper data can cause bad accuracy of forecasting, so it is needed to select only correct input values or create new ones from existing records. 85 percent of data received for analysis was discarded (excluded) from “correct” data because of lack of information in some rows, incorrect failures registration (human-factor), data repeatability or lack of logical thinking.

Similar problems have the most big companies in the world because of very big number of records, which may be not correct. Data may be coded differently by each staff member or grammatical errors done because of possible different levels of education, place of residence in the region or language habits. Comments next to recorded failure may be understood differently because of different human thinking, understanding events and its importance evaluation for future maintenance.

Taking into account all that features of the database presented next chapter describes what data filtering was performed.

4.2. Data analysis and preparation

First of all it was deleted blank rows because they give absolutely no information.

Excluded data that contains repeatable “*RepairCount*” value sorted by “*ModuleSerialNr*”. Repeatable data is not needed. This could be a mistake of “human-factor”. The first value of each ATM's component in “*RepairCount*” column sorted by “*ModuleSerialNr*” must be “0”, because we need to know number of days till the first failure appears. Excluded “non-zeros” from dataset.

There should not be any gaps between each component failures in “*RepairCount*” column sorted by “*ModuleSerialNr*”, i.e. [0, 1, 2, ... ,n-1, n]. Excluded data that is recorded after a gap appears.

If there is a „*WorkDaysTillDefect*“ value “0” in line with “*RepairCount*” value “0”, all data excluded that comes after that point, because there is no guarantee that the following information is correct.

4.3. Important features identification

For experimental investigation four main components of ATM were selected. These four components had a sufficient amount of data to perform prediction efficiency evaluation. The component selected are:

1. *Card Reader*.
2. *Double Extractor*.
3. *Stacker Transport*.
4. *Thermal Receipt Printer*.

4.4. Inputs and output

There were six conditionally important inputs selected for time till failure modeling.

Inputs:

1. *Outdoor*.
2. *RepairCount*.
3. *YearMade*.
4. *DeviceID*.
5. *LifeCycle1* (Table 1).
6. *LifeCycle2* (Table 2).

First four inputs were taken directly from data base presented by service companies. Last two variables “*LifeCycle1*” and “*LifeCycle2*” were calculated from “*WorkDaysTillDefect*” column data.

Input “*LifeCycle1*” is the number of days worked before the previous failure. If the new component is installed then its “*LifeCycle1*” is equal to zero. It should be noted that variable “*WorkDaysTillDefect*” is calculated again from zero after each failure. Illustration of variable “*LifeCycle1*” calculation is presented below in table 1.

Table 1. Illustration of input “*LifeCycle1*” calculation.

Module SerialNr	Work Days Till Defect	Repair Count	Life Cycle 1
010150	2413	0	0
010150	162	1	2413
010150	335	2	162
010150	356	3	335

Input “*LifeCycle2*” is the number of days worked from its first installation till previous failure. This variable is increasing after each failure. Illustration of variable “*LifeCycle2*” calculation is presented below in table 2.

Table 2. Illustration of input “*LifeCycle1*” calculation.

Module SerialNr	Work Days Till Defect	Repair Count	Life Cycle 1
0012974761	460	0	460
010150	2413	0	2413
010150	162	1	2575
010150	335	2	2910
010150	356	3	3266

Output of the model is saved in variable “*WorkDaysTillDefect*”, which is the number of days each component worked until the failure occurs. The more accurate results, the more likely necessary maintenance will be done before failure will shut down ATM’s operation and cause unwanted financial expenditure.

5. Results and discussions

For prediction models investigation 232 training points and 115 testing points were used for card reader, 12 training points and 6 testing points for double extractor, 181 training points and 91 testing points for stacker transport, 41 training points and 21 testing points for thermal receipt printer.

There were made 1000 iterations for each different number of decision trees.

This number of iterations taken as maximum because more iterations taking a lot of time resources for calculations and higher load of processor.

The same 1000 iterations were made for each multi-layer feedforward neural network with different number of nodes in the hidden layer.

For prediction accuracy evaluation mean absolute percentage error (MAPE) were used. It is calculated by equation:

$$MAPE = \frac{1}{n} \left[\sum_{i=1}^n \left| \frac{A_i - F_i}{A_i} \right| \right] \times 100, \quad (3)$$

where A_i – actual value, F_i – forecast value.

Below the experimental investigation results are presented in tables and figures.

Table 3. Mean absolute percentage error (MAPE) of regression ensemble prediction with “*LSBoost*” algorithm for all four components time till failure.

Decision trees	MAPE			
	Card Reader	Double Extractor	Stacker Transport	Thermal Receipt Printer
1	462.86	579.18	1286.3	407.48
5	352.28	576.09	792.57	476.67
10	397.93	85.55	725.55	326.51
20	372.81	110.86	524.25	333.55
50	364.41	72.46	428.07	270.83
100	358.89	58.99	359.15	262.53
200	330.19	56.21	315.35	249.85
400	303.58	56.08	304.97	249.44
700	295.51	56.08	324.65	249.39
1000	300.33	56.08	349.79	249.39

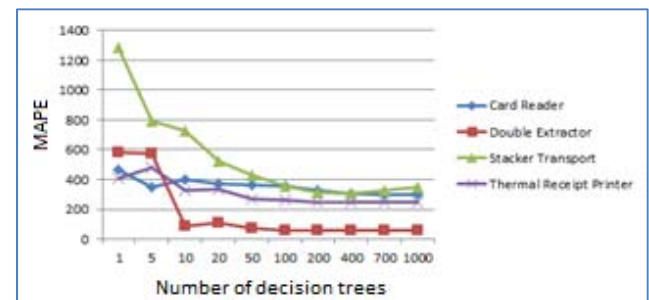


Fig. 4. Graphical results comparing main components forecasting by regression ensemble with “*LSBoost*” algorithm

Table 4. Mean absolute percentage error (*MAPE*) of regression ensemble with “*Bagging*” algorithm for all four components.

Decision trees	MAPE			
	Card Reader	Double Extractor	Stacker Transport	Thermal Receipt Printer
1	350.62	1236.7	1060.51	495.27
5	359.49	1271.3	963.47	463.51
10	340.48	1190.7	952.28	483.92
20	345.52	1206.2	954.98	470.21
50	347.51	1195.1	956.47	468.58
100	345.12	1190.2	956.18	468.35
200	345.28	1209.5	954.45	470.71
400	346.92	1213.1	958.72	474.11
700	345.78	1209.2	959.93	473.62
1000	345.25	1219.4	951.41	472.14

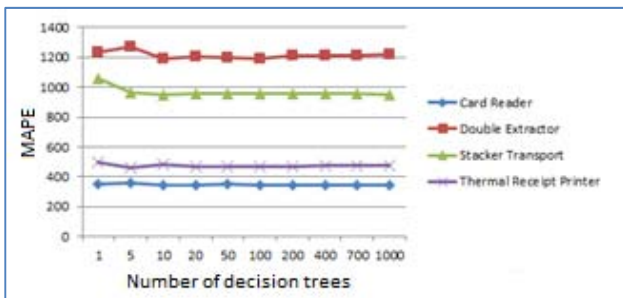


Fig. 5. Graphical results comparing main components forecasting by regression ensemble with “*Bagging*” algorithm

Table 5. Mean absolute percentage error (*MAPE*) of Multi-layer feedforward neural network algorithm.

Nodes	MAPE			
	Card Reader	Double Extractor	Stacker Transport	Thermal Receipt Printer
1	107.48	56.76	103.67	68.55
2	118.65	45.82	100.33	57.26
3	103.78	45.35	87.81	65.72
4	113.19	31.71	79.69	67.44
5	106.88	51.45	79.94	67.86
6	107.23	44.44	86.88	57.61
7	118.29	44.08	86.81	56.09
8	120.46	48.97	75.28	70.05
9	119.09	47.07	81.89	93.07
10	112.64	49.87	83.09	62.85

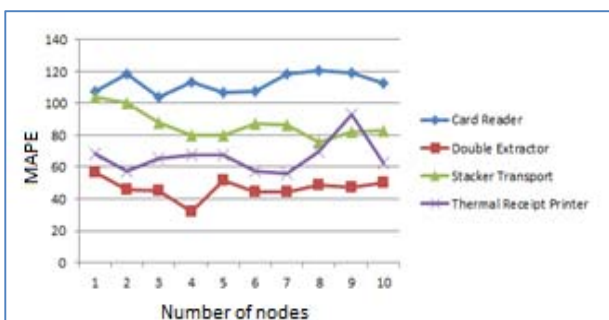


Fig. 6. Graphical results comparing main components forecasting by neural network algorithm

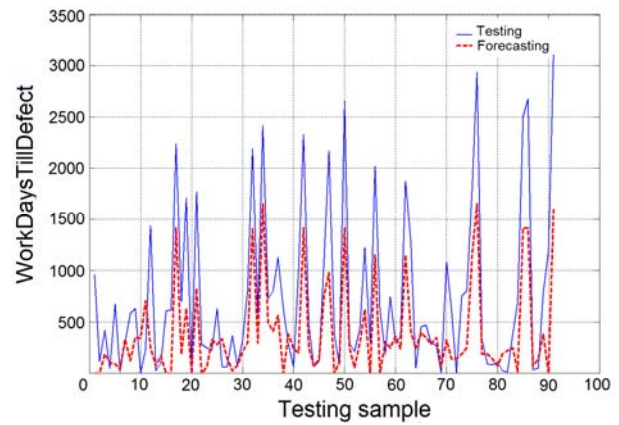


Fig. 7. Graphical results of neural network testing points and forecasting for stacker transport

Investigation results showed that best accuracy on all four components was achieved by multi-layer feedforward neural network.

Analysis of decision trees for regression models application for components time till failure prediction showed that increase of decision trees number does not have a significant impact on accuracy of prediction but time for model training is increasing dramatically.

Analysis of feed-forward neural network application showed that it is rational to use not less than 4 and not more than 8 nodes in hidden layer. Exact number of nodes depends on component type and need to be selected only after short experimental tests.

It is clear that better results may be achieved by additionally checking raw data, searching for new informative input variables and increase of training data amount.

Despite the fact that additional studies are needed this paper showed promising results in failure prediction. Service companies’ specialists appreciated investigation results and concluded that the initial prediction software prototype for service engineers’ decision support could be made.

6. References

1. Verikas A. Computational intelligence systems. Research Overview. Kaunas University of Technology. 2009. ISSN 2029-3151 p. 98-103.
2. Verikas A., Gelzinis A. Neuroniniai tinklai ir neuroniniai skaičiavimai. Kaunas University of Technology. [Kaunas : Technologija]. 2008.
3. Breiman L., Bagging Predictors. Mach. Learning 24 (2) (1996) 123-140.
4. Freund Y., Schapire R. E. A decision-theoretic generalization of on-line learning and an application to boosting. In European Conference on Computational Learning Theory p. 23-27, 1995.
5. Schapire E. The Strength of Weak Learnability. Machine Learning. Boston, MA: Kluwer Academic Publishers 5 (2): p. 197–227. 1990

EMBEDDED PLATFORM HARDWARE IMPLEMENTATION FOR OBJECT COUNTING USING VIDEO DATA PROCESSING

Paulius LENGVENIS, Audrius BUKIS, Rimvydas SIMUTIS
Process Control Department, Kaunas University of Technology, Lithuania

Abstract: The main goal of this work was prototyping hardware system for the counting of moving objects, port it to a low cost embedded Linux platform, and evaluate the recognition accuracy (count accuracy) in static and dynamic background environments, performance (we target a real-life processing), as well as the power consumption in real-life applications. The proposed system was structured to be capable (if necessary) to transfer the selected data to any server via internet protocols for additional data mining, generating of reports for various objects groups, doing analytics and so on. In the article, the authors present the proposed system structure and hardware implementation, measured characteristics, proprietary algorithm and the experimental evaluation in real-life (not laboratory) conditions.

Keywords: Distributed computing, Hardware, Microprocessors, Mobile computing, Image processing.

1. Introduction

The growing popularity, performance and effectiveness of embedded systems are having its impact on various areas of the market, from small microcontrollers to quad core mini computers. Unfortunately most of the software development was (and still are) done for the cumbersome PC or specialized PLC platforms, without the optimization necessary for non-specialized embedded modules. As in the topic of this article, video data processing is typically done on desktop PC, often on standalone servers, with large distance data submissions frequently non-real-time, and most sometimes even making the approach cumbersome and hard to implement in specific areas and applications (i.e. mostly in moving objects). Most modern embedded systems have the advantages of small size and low power consumption, as well as reasonable performance. Having this in mind, we have set a task to build and embedded system for the tracking of moving object in dynamically changing environments. Our system was structured to be capable (if necessary) to transfer the

selected data to any server via internet protocols for additional data mining, generating of reports for various objects groups, doing analytics and so on. One of the application we have done was the counting of people (clients) in a shopping center (usually a reasonably large area) and using the gathered results for a real-time management of sales staff and service personnel, as well as the technical part, i.e. the control of air conditioning, lighting, etc.

2. State of the art

Authors created accurate multiple object detection under multiple cameras algorithm, but his main disadvantage is slow processing speed [1], human detection and tracking with mobile robots using a SoS design based on contour classification using template matching [2]. Another real time active vision system which can track a moving object from 1 meter to 200 meters [3] or real-time (49.721 ms for one frame) eye detection realization on smart camera [4]. Solution to track particularly selected moving object in an environment of multiple moving objects [5]. Innovative NOVEL object tracking scheme that exploits the geometrical structure of Riemannian manifold and piecewise geodesics under a Bayesian framework for visible and infrared cameras [6]. For contentious object tracking can be used Continuous Object Tracking Algorithm (COTA) witch adaptively schedule a sensor's activity on the grounds of an object's movement to increase performance [7] or algorithm which can track people under various environments in real-time using active shape model [8]. To increase low accuracy in a complex environment authors created CAMSHIFT algorithm, which can track the moving target successfully in different scenarios and it can handle target with scale, orientation, and view changes, moreover, it has better robustness and accuracy of object tracking [9], additional frameworks which integrates object-model knowledge with the perceptual organization process [10] or recognize gestures of the objects of interest (the human whole body) [11]. Other

authors present a method of point feature tracking and online identification using SIFT (Scale Invariant Feature Transform) which works robustly for multi-persons tracking and identification [12]. Moving object segmentation based on motion vector for fast acting algorithm [13] or based on clustering MVs and Markov Random Field (MRF) iterations [14]. Looking from technical side we can find interesting tries to extract moving objects when video data is transferred from Camera Link bus to Xilinx development board SP605 and results are displayed in LCD monitor [15], hi scale interpolation with hardware-aware median filter [16], or speedy results of GPU calculation power for motion estimation [17]. Alternative solution for camera-based system for tracking and position estimation of humans [18].

3. System structure and hardware implementation

Object counting is usually considered as a distributed task problem as the perceived results are often structured together, unified, and used for analytical purposes, prognosis and similar goals. We have tried to create a system structure with a user-oriented and user-friendly interface, capable of integration of remote objects into the network of processing and communication.

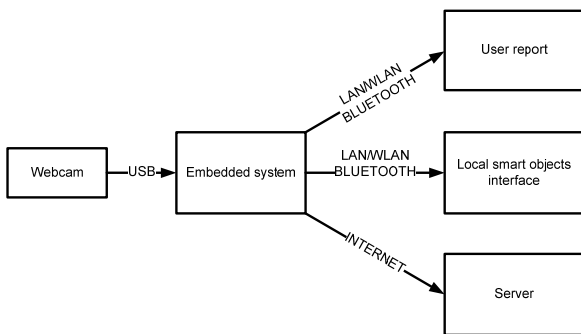


Fig. 1. A structure of system interface

The structure in principle is very simple. An ordinary camera (i.e. webcam via usb) is connected to the embedded platform capable of real-time communicating via built-in communication port (Ethernet, Bluetooth or Wi-Fi) and generating real-time results, reports or just transferring specific data to other smart objects in the area for further processing or other tasks and applications – thus forming a biggest advantage – the physical, real-time speed of local information exchange, by providing a single component embedded system with a minimum load on the internet and local communications.

The brain of our embedded platform was a PandaBoard ES board equipped with Core Logic OMAP4460 applications dual-core processor running at up to 1.2 GHz each, 1GB low power DDR2 RAM and a 8 GB SDHC class 10 card which was used as a storage for our own optimized Linux operating system build. Video data collecting was done with USB webcam C310 from Logitech. PandaBoard ES platform was selected as it offered wide connectivity possibilities from LAN to

WLAN 802.11 b/g/n as well as Bluetooth v2.1 + EDR as well as it was cheap to implement (official listed price was 130 euro at a time of submission) on a larger scale.

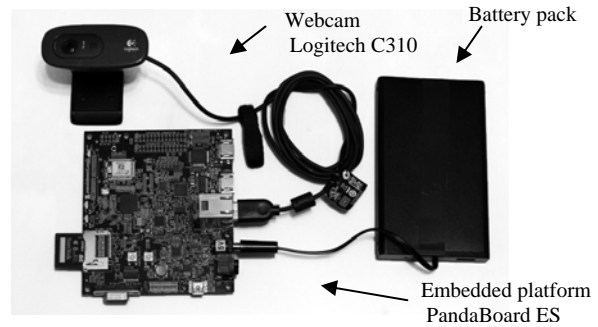


Fig. 2. Hardware implementation

As we have set our self a goal of reasonably low platform power dissipation we have measured the power consumption prior building the final system and doing the experimental research. Fig. 3. shows the power dissipation on a system load (video data processing) with 2 options: with Wlan module on and Wlan module off. System power dissipation was promising, especially compared with middle level notebook or similarly capable Intel Atom ITX board, as this embedded system's power dissipation was around 8-10 times lower making it more appropriate for 24/7/365 applications and green environmental politics of EU. To test a system ability of full autonomous work, we have picked two 3.6V Lithium-thionyl chloride spiral (Li-SOCI2) batteries connected consistently with nominal capacity of 13.0Ah

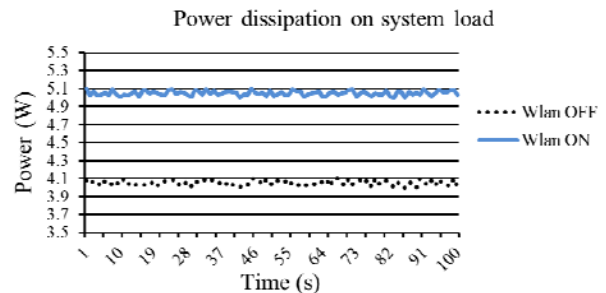


Fig. 3. Power consumption chart

Using our battery pack from Li-SOCI2 batteries, we measured discharge characteristics, on average of about ~1000mA with Wlan and 800mA without. In reality during our experimental evaluations we were able to calculate objects over 8 hours timeframe (with Wlan), which means that this system in principle could be used as full portable stand-alone platform without a power supply with a total weight of less than 800 grams (with batteries and plastic enclosure).

To evaluate the algorithm we have analyzed the performance of a system (we have measured how much video data (length in different resolution settings) a system can process during a predefined time-frame). For this reason we have set up two identical systems in

parallel one working in a resolution of 320x240 pixels and the other in 640x480 pixels resolution. The results of system counting algorithm performance in static environments are illustrated in Fig. 4.

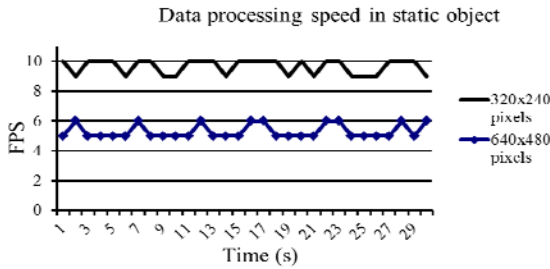


Fig. 4. Data processing performance working in static environments at VGA and QVGA resolutions

Maximum processing speed of embedded system working 320x240 pixel resolution were 10 frames per second, which is enough for a proper counting in static object.

Comparing a processing speed of 640x480 and 320x240 video material the performance dropped nearly 2 times (10 fps vs 5 fps), difference in data amount is 4 times, so if pixel number increase 4 times processing speed drops 2 times.

The performance in the dynamic environments was measured as well though it is important to note, that the algorithm was also using two ROI sets to minimize the number of errors which in the end had an impact on processing time. The results are illustrated in Fig. 5.

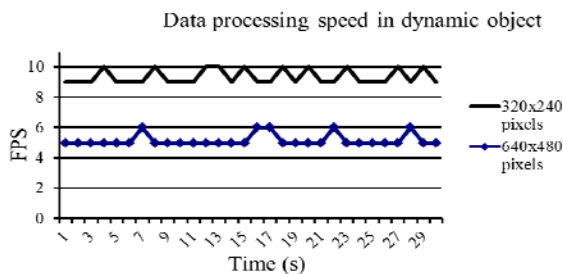


Fig. 5. Data processing performance working in dynamic environments at VGA and QVGA resolutions

We have got quite similar results compared to the tests done in static environment because adding second ROI don't take much time to process, but as before 640x480 resolution processing was too slow for real-time object counting.

4. Test setup and hardware evaluation

The experimental evaluation was done both in real-life static and dynamic environments. For the analysis of static environment we have mounted our equipment above the door in the petrol station and for the dynamic environment in the city bus (public transport bus on an ordinary route). To get most realistic result there wasn't any information given for persons which was calculated. Total 622 counting situations appeared in over 9 hours

continuous tests. Both environments had various light conditions, especially in bus when in every bus stop we get different background, light level and shadows of the bus stop. This test was done in daytime (in bus case some rain periods appear) so test results are as close as possible to real life. The recognition accuracy was also verified with a reference by manually analyzing a parallel video stream (filmed in synchrony using an additional, consumer grade video camera).

Test results done in a static environment are shown in table 1.

Table 1. Static environment detection accuracy

	Situations	Detected	Wrong detected	Missed	Correct Detected	Accuracy
People IN	184	188	10	6	178	97%
People OUT	184	190	15	9	175	95%
Total:	368	378	25	15	353	96%

A total of 368 people entered or leaved the petrol station during this test, though a system detected 378 which is more than correct number, after detailed review we find out that system missed 15 peoples and total 25 wrong detections were maid, they were classified in table 2. Overall system accuracy in static object was 96%.

Table 2. Static environment errors classification

Dramatic light change error	5
People crossed ROI but don't leaved/entered the shop	14
Other	6
Total:	25

Total 5 counting errors were made when dramatic light change appeared in camera view, this number can be lowered by adding normalization operation on input images, but this operation need more system resources, which now are on limit for real time operation. Other 14 errors were when people crossed ROI but don't leaved or entered the petrol station. This number can be lowered by expanding logic or adding additional ROI for verification. This will be done in future work. Test results of the analysis done in dynamic environment are shown in table 3.

Table 3. Dynamic environment detection accuracy

	Situations	Detected	Wrong detected	Missed	Correct Detected	Accuracy
People IN	134	128	11	17	117	87%
People OUT	120	114	9	15	105	88%
Total:	254	242	20	32	222	87%

Total 254 peoples entered or leaved the bus during this test, system detected 242 witch is less than correct number, after detailed review we find out that system missed 32 peoples and total 20 wrong detections were maid, they were classified in table 4. Overall system accuracy in dynamic object was 87%.

Table 4. Dynamic environment errors classification

Dramatic light change error	12
People crossed ROI but don't leaved/entered the bus	3
Other	5
Total:	20

Total 12 counting errors were made when dramatic light change in bus stops, other 3 errors were when people crossed ROI but don't leaved or entered the bus. Main problem where that people entered or leaved the bus congestion. In these situations moving peoples filled over 90% of all view and algorithm performed with errors.

5. Conclusions

Embedded systems now are fast enough to precede video data in low resolutions. Our proprietary fast acting algorithm for object counting was realized in embedded platform with Linux arm kernel witch accuracy in dynamic objects was 86% and in static 96%, in future work we try to increase accuracy in dynamic environment by expanding logic and adding additional ROI also try to make auto tune feature. Large advantage of this system was power consumption, size and weight, whole system weight about 800g with batteries on which can perform over 8 hours (only 4W power dissipation).

6. References

1. Susheel K., Prasad S., Saroj P. K., Tripathi R. C. Multiple Cameras Using Real Time Object Tracking for Surveillance and Security System. *Emerging Trends in Engineering and Technology (ICETET)*, 2010, p. 213–218.
2. Bowen R. M., Cinar E., Sahin F. System of systems approach to a human tracking problem with mobile robots using a single security camera. *Soft Computing, Computing with Words and Perceptions in System Analysis, Decision and Control (ICSCCW)*, 2009, p. 1–4.
3. Yan G., XiaoLin Z. Real time tracking of a remote moving object by active zoom cameras. *IEEE International Conference on Intelligence and Security Informatics (ISI)*, 2010, p. 162–164.
4. Mehrubeoglu M., Linh Manh Pham, Hung Thieu Le, Muddu R., Dongseok Ryu. Real-time eye tracking using a smart camera. *IEEE International Conference on Applied Imagery Pattern Recognition Workshop (AIPR)*, p. 1–7.
5. Hyung-Bok Kim, Kwee-Bo Sim. A particular object tracking in an environment of multiple

- moving objects. *Conference on Control Automation and Systems*, 2010, p. 1053–1056.
6. Khan Z. H., I.Y.-H Gu. Tracking visual and infrared objects using joint Riemannian manifold appearance and affine shape modeling. *IEEE International Conference on Computer Vision Workshops (ICCV)*, 2011, p. 1847–1854.
7. Yun Xu, Wei Bao, Hongli Xu. An Algorithm for Continuous Object Tracking in WSNs. *International Conference on Research Challenges in Computer Science (ICRCCS)*, 2009, p. 242–246.
8. Dongeun Lee, Sunghoon Choi. Multisensor fusion-based object detection and tracking using Active Shape Model. *International Conference on Digital Information Management*, 2011, p. 108–114.
9. Qiu Xuena, Liu Shirong, Liu Fei, Zhu Weitao, Du Fangfang. A moving object tracking method based on sequential detection scheme. *Control Conference (CCC)*, 2010, p. 2991–2996.
10. Gaurav H., Rajesh B., Santanu C. Using Object Models as Domain Knowledge in Perceptual Organization: An Approach for Object Category Identification in Video Sequences. *International Conference on Computing: Theory and Applications (ICCTA)*, 2007, p. 650–654.
11. Joseph C. N., Kokulakumaran S., Srijevanthan K., Thusyanthan A., Gunasekara C., Gamage C. D. A framework for whole-body gesture recognition from video feeds. *International Conference on Industrial and Information Systems*, 2010, p. 430–435.
12. Yang Liu, Xiaonian Wang, Jie Yang, Lixiu Yao. Multi-objects tracking and online identification based on SIFT. *International Conference on Multimedia Technology*, 2011, p. 429–432.
13. Wei Chen, Quan-Xi Yang, Ke-Wei Lin, Sheng-Yu Wang, Chung-Lin Huang. Human and car identification using motion vector in H.264 compressed video. *IEEE Visual Communications and Image Processing (VCIP)*, 2011, p. 1–4.
14. Jong Yih Kuo, Tai Yu Lai, Fu-Chu Huang, Liu K. The color recognition of objects of survey and implementation on real-time video surveillance. *IEEE Systems Man and Cybernetics (SMC)*, 2010, p. 3741–3748.
15. Kryjak T., Komorkiewicz M., Gorgon M. Real-time moving object detection for video surveillance system in FPGA. *Design and Architectures for Signal and Image Processing*, 2011, p. 1–8.
16. Perez J.M., Sanchez P., Martinez M. Low-cost bayer to rgb bilinear interpolation with hardware-aware median filter. *Electronics, Circuits, and Systems (ICECS)*, 2009, p. 916–919.
17. Rahman A., Houzet D., Pellerin D., Agud L. GPU implementation of motion estimation for visual saliency. *Design and Architectures for Signal and Image Processing*, 2010, p. 222–227.
18. Hartmann R., Al Machot F., Mahr P., Bobda C. Camera-based system for tracking and position estimation of humans. *Design and Architectures for Signal and Image Processing*, 2010, p. 62–67.

CALCULATION OF LOW VOLTAGE ELECTRIC CABLES ZERO SEQUENCE PARAMETERS

Gytis SVINKUNAS
 Kaunas University of Technology, Lithuania

Abstract: Low voltage electric cables zero sequence estimation is very important for short circuit current calculation in low voltage electric power networks. Tables of zero sequence calculation in literature often are old and not include data of modern power cables with plastic insulation. In this research analysed and compared cables zero sequence parameters in various sources of literature, model of low voltage cable zero sequence calculation is proposed.

Keywords: Low voltage cable, zero sequence parameters, short current, IEC909-2 standard.

1. Introduction

Impedance of zero sequence low voltage cables is very important for short current calculation. Calculation of zero sequence impedance high voltage lines is widely described in literature, but low voltage lines and cables impedance analyzing is less than it is necessary. But calculation of one phase short current in low voltage electric power network is very important for fuses and miniature circuit breaker sensitive checking, so zero sequence parameters are very important. In this research zero sequence impedance calculation is proposed, is analyzed and compared low voltages cables zero sequence impedance tables in Russian federation and West European countries standards.

2. Russian federation low voltage cable zero impedance data

Method of calculation of low voltage short circuits is described in Russian federation standard [1]. In this standard special tables of low sequence zero impedance is described. But these tables include some incorrections (see Table 1 and Table 2).

Prima facie these tables seems detail and right. But are some problems when tables data is applied to practice.

1. Cables in table 1 are with three wires. Where forth return wire? In the table 1 no mention about return wire size and other parameters. May be like return wires are

used steel constructions of building (this cheap solution was used in old Soviet enterprises). Now electric power nets without special return wire are forbidden.

2. Now all low voltage cables are with non-conductive sheath, made from plastic, steel and lead sheaths are not used in new cable lines.

3. At present all low voltage electric cables have four conductors. In literature [1] are not dates of cables with non-conductive sheath and four conductors.

Table 1. Parameters of 3 wires cable in Russian federation standard [1]

Cross-section of conductor	Resistance and inductance of 3 wires cable with aluminum conductors and lead sheath			
	R1	X1	R0	X0
3×4	9.61	0.092	11.6	1.24
3×6	6.41	0.087	8.38	1.2
----	----	---	---	---
3×185	0.208	0.056	1.69	0.606
3×240	0.16	0.055	0.55	0.535

Table 2. Parameters of 4 wires cable in Russian federation standard [1]

Cross-section of conductor	Resistance and inductance of 4 wires cable with cooper conductors and steel sheath			
	R1	X1	R0	X0
4×6	3.53	0.1	4.42	1.49
4×10	2.13	0.095	2.28	1.34
----	----	---	---	---
4×150	0.14	0.07	0.45	0.28
4×185	0.115	0.069	0.37	0.27

Destination of research in literature [2] is calculation of zero sequence parameters of modern cables. Calculations was done for zero sequence parameters of plastic cables, witch were not included in standard [1]. But solution is not right, because for a calculation was used non-correct model.

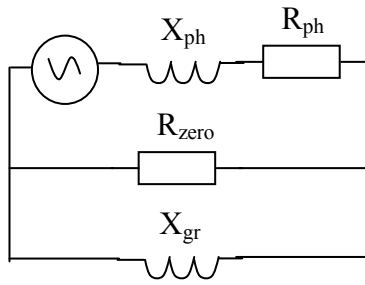


Fig. 1. Zero sequence calculation cable model in literature [2], R_{ph} and X_{ph} are resistance and inductance of cable phase conductor, R_{zero} – resistance of return conductor, X_{gr} – inductance of ground return path

In this model most interesting part is inductance of ground return path. Value of parallel ground return path X_{gr} is 0.6 Ω /km. This value is small; according this, influence of ground return for low voltage cables is significant. According this model, in literature [2] tables of modern low voltage cables zero sequence resistance and inductance are calculated.

But after several years research [3] with serious critics of article [2] was published. Main target of critic was zero ground return value 0.6 Ω /km. Simple ground return circuit consists of two earthing resistances and ground resistance and other earthing resistance. Self-resistance of earthing is minimum 10 Ω , so resistance of all circuit is much more than 0.6 Ω /km. According [3], value $X_{gr} = 0.6 \Omega$ /km is for steel sheath cables where sheathed cable lie under the ground and pass current in its entire sheath. So, for modern plastic cable this value is unacceptable. But calculation of new resistance and inductance's tables in this job isn't done.

3. Low voltage cable zero sequence parameters in Europe standard IEC909

A best table of low voltage cables zero sequence resistance is in IEC 909 standard [4].

Table 3. Parameters of cables in IEC909 standard [4]

Cross-section of conductor	Zero and direct resistance and inductance proportions of 4 wires cable with aluminum conductors and non conductive sheath			
	With ground and neutral return		Return only in neutral	
	R0/R1	X0/X1	R0/R1	X0/X1
4×25	1.8	16.5	4	4
4×35	2	15.5	4	3.9
4×50	2.5	12	4	3.7
4×70	3.0	8.5	4	3.6
4×95	3.1	6.3	4	3.6
4×120	3.2	5.6	4	3.6
4×150	3.3	4.7	4	3.6
4×185	3.4	4.3	4	3.6
4×240	3.4	4	4	3.6

In this standard two cases of neutral grounding were separated: system without grounding and system with in both ends grounded neutral. So, it table is best source of

zero sequence cables parameters in literature. Separation of return path allows calculate and compare zero sequence parameters in all possible conditions. But inductance of cable with ground return increasing very much in this table, so it is useful to create model of cable zero sequence parameters and calculate impedance.

4. Models of cable zero sequence parameters calculation without ground circuit

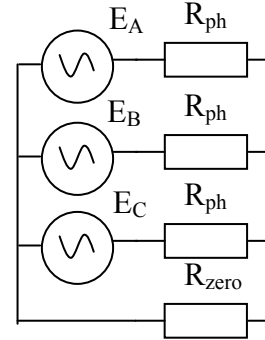


Fig. 2. Calculation model of zero sequence resistance: R_{ph} is resistance of cable phase conductor, R_{zero} – resistance of return conductor, $E_A=E_B=E_C$ – zero sequence voltages

According Fig.2., simple equation for cable zero sequence resistance R_0 is written, when all cable ground return current flow in the fourth conductor.

$$R_0 = R_{ph} + 3 \times R_{zero} . \quad (1)$$

This equation is very important for estimation of zero sequence data. If all conductors in cable have same cross-section, proportion between zero and positive sequence is constant:

$$R_{ph} = R_{zero}; R_{ph} = R_1; \frac{R_1}{R_0} = 4; \quad (2)$$

So, this value is very close to Table 3 data.

According calculation result of (2) equation, cables parameters in table 1 and 2 are calculated with Fig. 1 model, because when cross-section is small, proportion $R_0/R_1=1.2$, when cross-section is bigger, R_0/R_1 is about 3÷4. It's means, current flow not only return conductor, but in other return resistance, independent from cable cross-section.

Inductance of low voltage cable is calculated according model in Fig. 3.

For these calculations is expedient to use methodic of multiwired conductor system inductance calculation, described in [5]. Inductance of multiwired system is calculated like two wires system inductance: one wire (a) consist from three conductors (A, B and C) and second (b) is one conductor N. Total system inductance L_{ABCN} is:

$$L_{ABCN} = \frac{\mu_0 l}{2\pi} \left(\ln \frac{d_{ab}^2}{d_a \cdot d_b} \right); \quad (3)$$

where d_a , d_b – average geometric shapes distance himself from his; d_{ab} – average geometric two shapes distance between each other, l – length of conductor, μ_0 – magnetic constant.

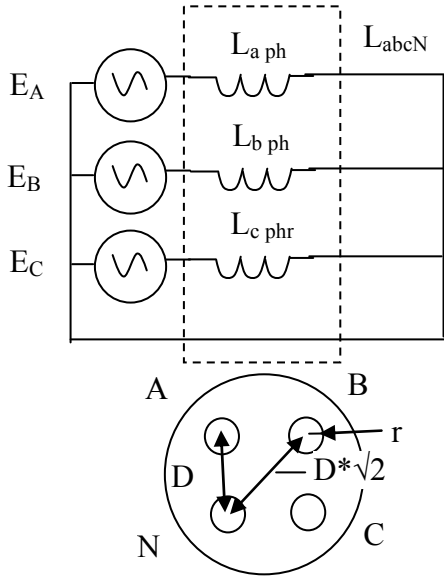


Fig. 3. Calculation model of zero sequence inductance: L_{ph} is inductance of cable phase an neural loop, M_{AB} – Mutual inductance between phases conductors, $E_A=E_B=E_C$ – zero sequence voltages, D – distance between conductors, r – radius of conductor

According [5] distances d_a , d_b and d_{ab} are calculated: circle average geometric shapes distance himself from his is equal its radius [5];

$$d_b = r. \quad (4)$$

Distance himself from his for three wires system is calculated like product of all wire distance himself from his r and all wires distances between each other.

$$d_a = \sqrt[9]{r \cdot D \cdot D \cdot \sqrt{2} \cdot r \cdot D \cdot D \cdot r \cdot D \cdot D \cdot \sqrt{2}} = \left(r^3 \cdot D^6 \cdot 2 \right)^{\frac{1}{9}}. \quad (5)$$

Distance between two wires system is calculated like product distances of all conductors between each other:

$$d_{ab} = \sqrt[3]{D \cdot D \cdot \sqrt{2} \cdot D} = D \sqrt[3]{2}. \quad (6)$$

$$L_{ABCN} = \frac{\mu_0 l}{2\pi} \left(\ln \frac{D^{\frac{12}{9}} \cdot 2^{\frac{2}{9}}}{r^{\frac{4}{3}}} \right) = \frac{\mu_0 l}{2\pi} \left(\ln \frac{D^{\frac{4}{3}}}{r^{\frac{4}{3}}} \right) + \quad (7)$$

$$\frac{\mu_0 l}{2\pi} \left(\ln 2^{\frac{2}{9}} \right) = \frac{4}{3} \cdot \frac{\mu_0 l}{2\pi} \ln \frac{D}{r} + \frac{2}{9} \cdot \frac{\mu_0 l}{2\pi} \ln 2.$$

Inductance of one phase and zero sequence is equal:

$$L_{oABCN} = L_{Aph} = 3 \cdot L_{ABCN} = \frac{2\mu_0 l}{\pi} \ln \frac{D}{r} + \frac{\mu_0 l}{3\pi} \ln 2. \quad (8)$$

Direct sequence inductance of 4 wires phases cable is calculated [5]:

$$L_1 = \frac{l}{2 \cdot \pi} \left(\mu_0 \ln \frac{D}{r} + \frac{1}{4} \right). \quad (9)$$

Calculation of proportion between 4 wire cable zero and direct sequence inductances was done for aluminum 4 wire cable with conductor cross-section $S=35\text{mm}^2$, its parameters (see Fig. 3) $r=3.5\text{mm}$, $D=9\text{mm}$. According (8) and (9) is:

$$\frac{L_0}{L_1} \approx 3.4$$

So, this value is very close to Table 3 data.

5. Models of cable zero sequence parameters calculation with ground circuit

Resistance of grounded low voltage system is calculated with model including grounding resistance. Current from return wire flow to the ground and return to wire throw eathing, with resistance minimum 10Ω . Earthing is connected to neutral wire periodically, in every place where customers are connected to the cable.

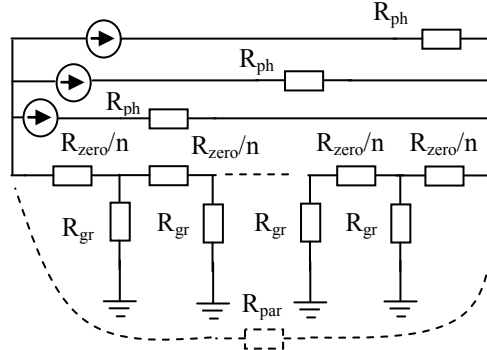


Fig. 4. Calculation model of low voltage net zero sequence resistance with $n-1$ earthings: R_{ph} – phase conductor resistance; R_{zero} – return conductor resistance; R_{gr} – earthing resistance (10Ω)

Typical length of low voltage cable net about 500m. To this cable about 20 – 30 customers are connected, so there are to 30 earthings ($n=30$). Typical cross section of aluminum cable is 95mm^2 .

For this conditions calculated R_0/R_1 proportion is 3.8 (in Table 3 $R_0/R_1=3.1$). For cable 25mm^2 calculated R_0/R_1 proportion is 3.48 (in Table 3 $R_0/R_1=1.8$). So difference between standard values and simulation is significant. Influence of all earthing is possible to estimate with one parallel resistance of earthings, R_{par} . Meaning of $R_{par}=8 \div 10.4\Omega$ (for 0.5 km length line).

Using methods of multiwired system inductance calculations is possible to calculate inductance of various systems of grounding. First case is three-wire

system, when return conductor wired separate from all phases conductors.

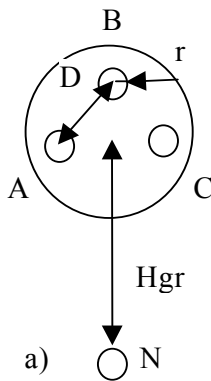


Fig. 5. Calculation model of zero sequence inductance: a) three wire cable with separate neutral wire; b) four wire cable with two neutral wires

For three wire cable in Fig. 5. a) distances d_a , d_b and d_{ab} are calculated:

$$d_b = r \quad (10)$$

$$d_a = \sqrt[3]{r \cdot D \cdot D \cdot r \cdot D \cdot D \cdot r \cdot D \cdot D} = \left(r^3 \cdot D^6 \right)^{\frac{1}{9}} \quad (11)$$

$$d_{ab} \approx \sqrt[3]{H_{gr} \cdot H_{gr} \cdot H_{gr}} \quad (12)$$

$$L_{ABC+N} = \frac{\mu_0 l}{2\pi} \left(\ln \frac{H_{gr}^2}{r^{\frac{1}{3}} \cdot D^{\frac{2}{3}}} \right) = \quad (13)$$

$$\frac{\mu_0 l}{2\pi} \ln \left(\frac{H_{gr}}{r^{\frac{1}{6}} \cdot D^{\frac{1}{3}}} \right)^2 = \frac{\mu_0 l}{\pi} \ln \left(\frac{H_{gr}}{r^{\frac{1}{6}} \cdot D^{\frac{1}{3}}} \right)$$

Inductance of one phase and zero sequence is equal:

$$L_{oABC+N} = 3 \cdot L_{ABC+N} = \frac{3\mu_0 l}{\pi} \ln \left(\frac{H_{gr}}{r^{\frac{1}{6}} \cdot D^{\frac{1}{3}}} \right) \quad (14)$$

Calculation of L_0/L_1 proportion for three wires cable $S=35\text{mm}^2$, with separate return wire if distance $H_{gr}=1\text{m}$ give value $L_0/L_1=12.6$, if $H_{gr}=10\text{m}$, $L_0/L_1=24.6$. So, zero sequence inductance is big and dates or Table 1 are similar to be true.

For four-wire cable with separate grounding wire zero sequency calculation model in Fig.6 is proposed. Model consists of paralel connection of two models in Fig.3 and Fig. 5 a). In this model is necessary estimate distribution of currents in both neutral wires, so to create one complex impedance model it is necessary.

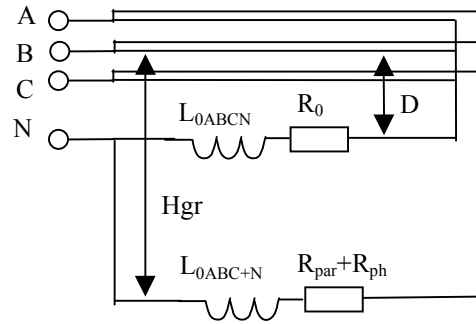


Fig. 6. Calculation model of zero sequence impedance Z_{0ABC+N} for four wire cable with ground return

$$Z_{0ABC+N} = \frac{(R_0 + j\omega L_{0ABCN})(R_{par} + R_{ph} + j\omega L_{0ABC+N})}{R_0 + j\omega L_{0ABCN} + R_{par} + R_{ph} + j\omega L_{0ABC+N}} \quad (15)$$

Calculation of cable with $S=185\text{mm}^2$, $r=7.5\text{mm}$, $D=19\text{mm}$, $H_{gr}=10\text{m}$ give value $L_0/L_1=3.03$. This value is far from 4.3 in table 3. For cable $S=35\text{mm}^2$, $r=3.5\text{mm}$, $D=9\text{mm}$, $H_{gr}=10\text{m}$ value $L_0/L_1=4.50$. This value is not similar to 16.5 in table 3. Main reason of dissimilarity is big resistance R_{par} of ground return path.

6. Conclusions

The best source of low voltage cables zero sequence impedances data is standard IEC 909-2. Zero sequence parameters of the cables in IEC 909-2 without ground return circuit are accurate and correct. Zero sequence parameters of the cables in IEC 909-2 with ground return circuit raises some doubts. Influence of ground return circuit for low cable zero sequence parameters is less significant than it is in [2] and [4].

7. References

- ГОСТ 28249-93. Короткие замыкания в электропроводках. Методы расчета в электроустановках переменного тока напряжения до 1 кВ.
- Каменский М.К., Холодный С.Д. Силовые кабели 1–10 кВ с пластмассовой изоляцией. Расчет активного и индуктивного сопротивлений // Новости ЭлектроТехники. – 2005. – № 4(34)..
- Владимир Фишман. Силовые кабели до 1 кВ. Расчет сопротивлений нулевой последовательности. Новости ЭлектроТехники. – 2007. – № 2(44).
- IEC 909-2. Electrical equipment - Data for short-circuit current calculations in accordance with IEC 909 (1988). Copyright International Electrotechnical Commission. First edition. 1992-08.
- Калантаров П. Л., Цейтлин Л. А. Расчет индуктивностей: Справочная книга. — 3-е изд., перераб. и доп. Л.: Энергоатомиздат. Ленингр. отд-ние, 1986.

INVESTIGATION OF COMPATIBILITY OF THE VARIABLE SPEED PUMPED STORAGE UNIT AND WIND POWER PLANTS IN THE POWER SYSTEM

Rimantas Pranas DEKSNYS, Darius ALIŠAUSKAS
Kaunas University of Technology, Lithuania

Abstract: Compatibility of the variable pumped storage unit and wind power plants while balancing active power in the power system are analyzed in this article. Structural and functional peculiarities of the excitation control system of the pumped storage unit are applied in the analysis in the regimes of generator and pump. Oscillations of wind plant parks active power in the power system are being modeled for probability. Active power flows in the power system are determined by iterational method. Numerical integrations method for determining parameters and characteristics is applied for modeling pumped storage unit and its excitation control system. We determine distribution of active power flows and influence of variable pumped storage unit on active power balance in the power system.

Keywords: Variable speed pumped storage unit, power system regime, wind power plants, systems compatibility.

1. Introduction

New variable speed units are being installed in the pumped storage plants of Europe. The variable speed units can work as the generator and the pump regimes. These units are recommended as having high reaction in powers variation of the power system. It ensures stability of the power system compares with the synchronous units.

Nowadays the renewable energy is being installed in the power systems broadly. These are sun, wind plants. Those plant parks are generating the variable active power which depends on conditions of the nature. This event is originating the balancing problem of the power system [1].

The fundamental principles of the asynchronous machines are applied for the variable speed units. These principles are perfecting the exciter control system of the variable speed units and searching for the new solutions. One of solution ensures compatibility of systems between the variable speed unit and wind plants [2].

The fundamental theory of the automation control, which is certificate IEEE, is applied for structure of the exciter control system [3, 4].

2. Dynamic model of the system of the variable speed pumped storage unit

The systems of the algebraic and differential equations are describing models. The methods of numerical integration and iteration are applied for system analysis [5, 6].

Dynamic mathematical model of the variable speed pumped storage unit is described the system of differential equations of positive and negative sequences Fig. 1.

$$\left\{ \begin{array}{l} \underline{e}_{ds} = \underline{i}_{ds} r_s + \frac{d\underline{\psi}_{ds}}{dt} + j\omega_s \underline{\psi}_{qs} \\ \underline{e}_{qs} = \underline{i}_{qs} r_s + \frac{d\underline{\psi}_{qs}}{dt} + j\omega_s \underline{\psi}_{ds} \\ \underline{e}_{dr} = \underline{i}_{dr} r_r + \frac{d\underline{\psi}_{dr}}{dt} - j(\omega_s - \omega_r) \underline{\psi}_{qr} \\ \underline{e}_{qr} = \underline{i}_{qr} r_r + \frac{d\underline{\psi}_{qr}}{dt} - j(\omega_s - \omega_r) \underline{\psi}_{dr} \end{array} \right. ; \quad (1)$$

where $\underline{i}_s, \underline{i}_r$ are currents' vectors of stator and rotor; $\underline{e}_s, \underline{e}_r$ are electromotive vectors of stator and rotor; $\underline{\psi}_s, \underline{\psi}_r$ electromagnetic flow vectors of stator and rotor; r_s, r_r active resistance of stator and rotor; ω_s, ω_r angle frequency of stator and rotor.

For determining mechanic angle we express movement equation of rotor:

$$\frac{d\theta_r}{dt} = \frac{T_e \pm T_m + D\theta_r}{J}; \quad (2)$$

where T_e, T_m are electromagnetic and mechanical driving torques moment; D is damping factor, J is mechanic movement moment.

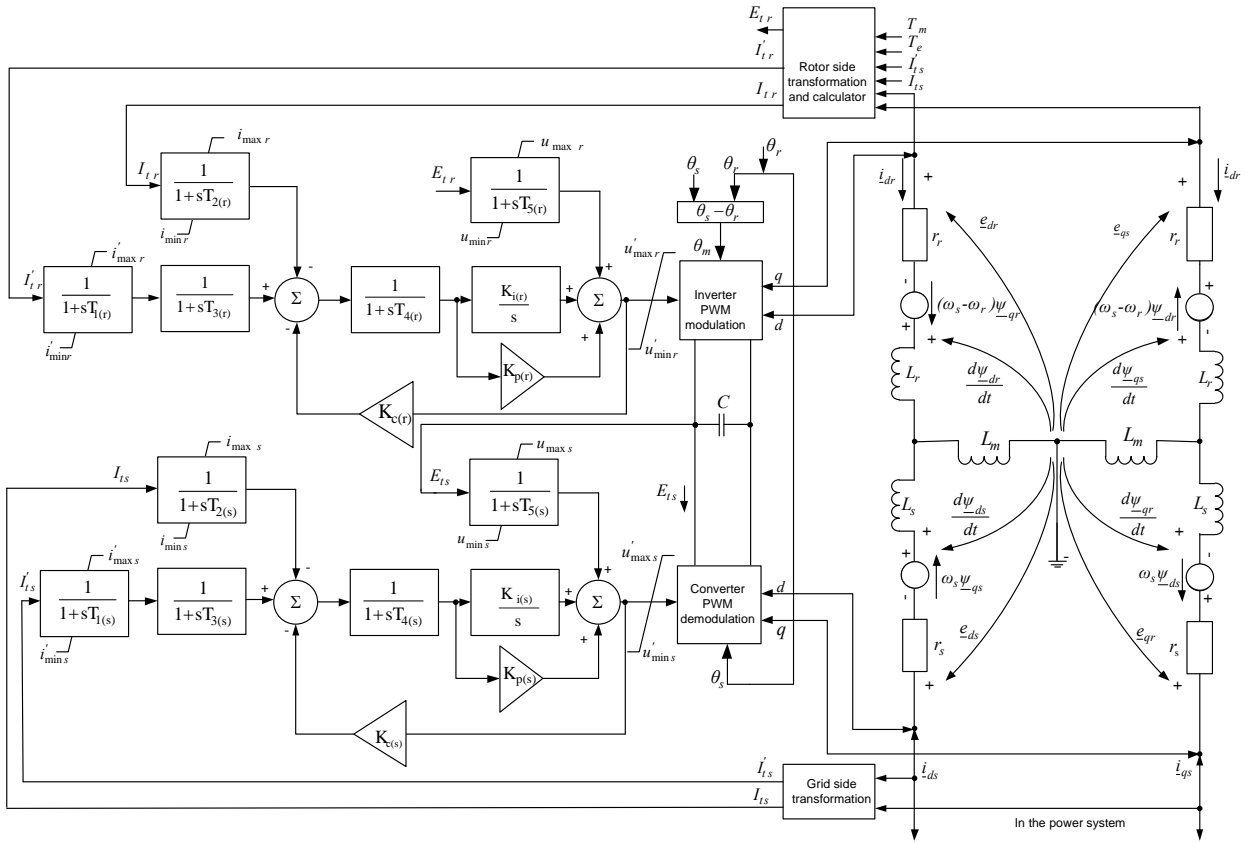


Fig. 1. Structural scheme of the exciter control of the variable speed pumped storage unit

Then differential equation (1) we transform from polar coordinates to space Park's coordinates' system in matrix form:

$$\begin{bmatrix} \dot{i}_{ds} \\ \dot{i}_{qs} \\ \dot{i}_{dr} \\ \dot{i}_{qr} \end{bmatrix} = \begin{bmatrix} \left(r_s + \frac{d}{dt}L_s\right) & \theta_s L_s & \frac{d}{dt}L_m & \theta_s L_s \\ -\theta_s L_s & \left(r_s + \frac{d}{dt}L_s\right) & -\theta_s L_s & \frac{d}{dt}L_m \\ \frac{d}{dt}L_s & \theta_m L_m & \left(r_r + \frac{d}{dt}L_r\right) & \theta_m L_r \\ -\theta_m L_m & \frac{d}{dt}L_s & -\theta_m L_r & \left(r_r + \frac{d}{dt}L_r\right) \end{bmatrix}^{-1} \begin{bmatrix} e_{ds} \\ e_{qs} \\ e_{dr} \\ e_{qr} \end{bmatrix} \quad (3)$$

where L_s , L_r are inductions of stator and rotor; L_m is mutual connection induction.

Given matrix (3) and movement equation (2) we rearrange into state space equations. Having applied Cauchy's state space equation we express variable solutions of angle rotor and current of stator and rotor:

$$\begin{cases} \underline{i}(t) = e^{\mathbf{A}(t)} \underline{i}(t) + \int_0^t \left(e^{\mathbf{A}(t-\tau)} \mathbf{B} e(\tau) \right) d\tau \\ \theta_r(t) = e^{\mathbf{A}(t)} \theta_r(t) + \int_0^t \left(e^{\mathbf{A}(t-\tau)} \right) d\tau \end{cases} \quad (4)$$

where \mathbf{A} , \mathbf{B} are state equation matrixes; τ is time change.

Angle frequency ω_s , ω_r is integrated for determining angle relations of variable speed pumped storage unit between mutual conditions of stator and rotor:

$$\begin{cases} \theta_s = \int \omega_s dt \\ \theta_r = \int \omega_r dt \\ \theta_m = \theta_s - \theta_r \end{cases} \quad (5)$$

where θ_s , θ_r or θ_m are angle frequency of stator, rotor and mechanical.

From the first differential equation we express induction and angle frequency of inside rotor and stator is substituted by electrical and mechanical angles (3).

From this solution (4) we express electro motion vectors:

$$\begin{bmatrix} e_{ds} \\ e_{qs} \\ e_{dr} \\ e_{qr} \end{bmatrix} = \begin{bmatrix} \left(r_s + \frac{d}{dt}L_s\right) & \theta_s L_s & \frac{d}{dt}L_m & \theta_s L_s \\ -\theta_s L_s & \left(r_s + \frac{d}{dt}L_s\right) & -\theta_s L_s & \frac{d}{dt}L_m \\ \frac{d}{dt}L_s & \theta_m L_m & \left(r_r + \frac{d}{dt}L_r\right) & \theta_m L_r \\ -\theta_m L_m & \frac{d}{dt}L_s & -\theta_m L_r & \left(r_r + \frac{d}{dt}L_r\right) \end{bmatrix} \begin{bmatrix} \dot{i}_{ds} \\ \dot{i}_{qs} \\ \dot{i}_{dr} \\ \dot{i}_{qr} \end{bmatrix} \quad (6)$$

Summary active power P_e may be computed by use of proposed mathematical model of variable speed pumped storage unit power circuits and method of solution:

$$P_e = 3 \begin{bmatrix} e_{ds} & e_{qs} & e_{dr} & e_{qr} \end{bmatrix} \cdot \begin{bmatrix} \dot{i}_{ds} \\ \dot{i}_{qs} \\ \dot{i}_{dr} \\ \dot{i}_{qr} \end{bmatrix} \quad (7)$$

Active power of the variable speed pumped storage unit depends on water potential power. We are expressing moments of driving of electromagnetic and mechanic:

$$\begin{cases} T_e = \frac{P_e}{\omega_s} \\ T_m = \frac{kG\sqrt{H^3}}{\omega_m} \end{cases}, \quad (8)$$

where k is the proportionality factor, H is the pressure height and G is a factor position of deflection wheel. According to this described mathematic model when the meanings of electro motion, current vectors and condition angle meanings are known we establish active as well as reactive power in variable speed pumped storage unit in pump and generator work regimes [7]. Variable speed pumped storage unit structure of excitation control system has analogical mathematically described control elements as well as control system of wind power station [8].

Dynamic mathematic model excitation control stabilization structures made of grid side and rotor side control blocks. Grid side control block is integrated into converter demodulator and rotor side control block is inverter modulator. Modulator and demodulator are controlled by impulse width modulation. Excitation control structure has to ensure stable functioning of pumped storage unit.

Stator's and rotor's control currents $\underline{i}_{(dq)s} \rightarrow I_{ts}$, $\underline{i}_{(dq)r} \rightarrow I_{tr}$ as well as rotor's voltage $\underline{e}_{(dq)r} \rightarrow E_{tr}$ are transformed. Control system grid's and rotor's sides elements' basic constant parameters are time constants $T_{x(s,r)}$, integration factors $K_{i(s,r)}$, proportion factors $K_{p(s,r)}$ and negative feedback compensation factors $K_{c(s,r)}$. Calculation rotor side parameters are reconciled with mechanic parameters of pumped storage unit and electromagnetic and mechanic driving torques.

The control exciter system structures of synchronous blocs are created from mathematical equation to describe function blocs. These function blocs are widely investigated. Calculation of parameters is executed by standard fundamental theoretical electronical methods. Variable speed pumped storage unit with excitation control system are integrated into power system.

3. Model of generate the active power of the wind power plants

Wind power plant's on dominant wind speed which depends on the season. A 24 hours load graphic and generated power by other generators are also evaluated. According to meteorological prognosis paying attention to seasons wind power generated power is described using probability Weibull's distribution [9]:

$$H_{VPP} = \left(\left(\frac{k}{\frac{v_{vid}}{\Gamma(\frac{2}{k})}} \right)^{k-1} \cdot \frac{v}{\frac{v_{vid}}{\Gamma(\frac{2}{k})}} \right)^k, \quad (9)$$

$$P_{VPP} = P_{VP(nom)}^n H_{VPP}$$

where H_{VP} is Weibull's parameter for wind power station, $P_{VP(nom)}$ nominal power of wind power plants, P_{PVV} generate active power of wind power plants, Γ is gamma function, k is form factor, v is v_{vid} wind and medium wind speed, n number of wind power plants. We are expressing moments of driving of electromagnetic of wind power plants:

$$T_{VPP} = \frac{P_{VPP}}{\omega_s}. \quad (10)$$

Then electromagnetic moment is to terminals of variable speed pumped storage unit (before terminals):

$$T_e' = T_L - T_{VPP}; \quad (11)$$

where T_L is electromagnetic moment of load.

We are accepting that electromagnetic and mechanic moments are approximately equal:

$$T_e' \approx T_e \approx T_m. \quad (12)$$

This equation (12) is ensure balance of moments.

4. Results of analysis

For selected the variable speed pumped storage units and their systems' excitation control and the wind power plants work regimes are established limits of mathematic models algebraic and solutions of differential equations convergence. The wind power plants and the variable speed pumped storage units parameters are substituted by per units' system.

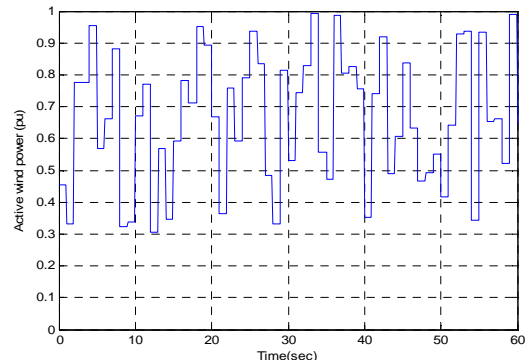


Fig. 2. Active power of wind power plants

Numerical integration method is applied for establishing and the variable speed pumped storage units systems of excitation control operation characteristics of dynamic processes. In 60 seconds the wind power plants generated medium active power are mathematically simulation Fig.2.

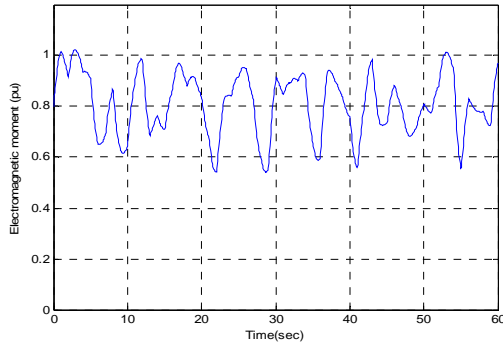


Fig. 3. Electromagnetic moment of before terminals

Having identified balance of electromagnetic moments between variable speed pumped storage unit and wind power plants in the system is simulated mathematically Fig. 3.

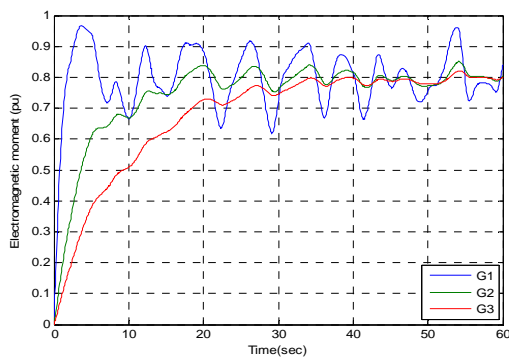


Fig. 4. Electromagnetic moment of behind terminals

We are changing factor position G of deflection wheel in equation (8). From here we are debugging to compatibility and to balance of electromagnetic moments between variable speed pumped storage unit and wind power plants. Sensibility adjustment and position of deflection wheel allows reconciling excitation control so that in variable speed pumped storage units turbines would not intervene water hammer.

Mechanical moment and its control system compensate and stabilize fluctuations of electromagnetic moment Fig. 4. Adequately they react to electromagnetic moment fluctuations.

The exciter control system sensitivity to variable speed pumped storage unit allows to react adequately to electromagnetic moment variations of the wind power plants.

5. Conclusions

1. Created variable speed pumped storage unit and its excitation control system's mathematic model allows investigating and controlling dynamic processes.
2. Model of the exciter control system sensitivity to variable speed pumped storage unit allows to react adequately to electromagnetic moment variations of the wind power plants.
3. Variable speed pumped storage units ensure effective active power balance.

6. References

1. The Strategy approved by Resolution No XI-2133 of the Seimas of the Republic of Lithuania of 26 June 2012. Available: <http://www.lrv.lt/EP/strategija-EN.pdf>
2. Suul, J. A., Uhlen, K., Undeland, T. Variable speed pumped storage hydropower for integration of wind energy in isolated grids – case description and control strategies. Proc. Nordic Workshop on Power and Industrial Electronics, *NORPIE/2008*, June 9–11, 2008, Espoo, Finland, 8 p.
3. J. Rodriguez, S. Bernet, W. Bin, J. O. Pontt, and S. Kouro, "Multilevel Voltage-Source-Converter Topologies for Industrial Medium-Voltage Drives," *IEEE Trans. Ind. Electron.* Vol. 54, No. 6, pp. 2930–2945, December 2007.
4. IEEE Recommended Practice for Excitation System Models for Power System Stability Studies, *IEEE Standard 421.5-1992*.
5. Lung, J.-K., Lu, Y., Hung, W.-L., Kao, W.-S. Modeling and dynamic simulations of doubly fed adjustable-speed pumped storage units. *IEEE T. Energy Conver.*, 2007, 22(2), 250–258
6. Nagura, O., Higuchi, M., Tani, K., Oyake, T. Hitachi's adjustable-speed pumped-storage system contributing to prevention of global warming. *Hitachi Review*, 2010, 59(3), 99–105.
7. Lung, J.-K., Lu, Y., Hung, W.-L., Kao, W.-S. Modeling and dynamic simulations of doubly fed adjustable-speed pumped storage units. *IEEE T. Energy Conver.*, 2007, 22(2), 250–258.
8. Takahashi, R., Tamura, J., Tada, Y., Kurita, A. Model derivation of an adjustable speed generator and its excitation control system. 14th *Power Systems Computation Conference (PSCC)*, 24–28 June 2002, Seville, Spain, 1, 200–205.
9. I. Munteanu, I. U. Bratcu, N. A. Cutululis, and E. Ceanga, *Optimal Control of Wind energy Systems*. Springer, 2008.

ELECTROSTATIC FIELD OF AXIALLY SYMMETRICAL ELECTRODE SYSTEM “NEEDLE NEAR THE PLATE”

Povilas MARČIULIONIS, Stasys ŽEBRAUSKAS
Department of Electrical Engineering, Kaunas University of Technology, Lithuania

Abstract: Electrode system “needle near the plate” electrostatic field is shown. Laplace equation in finite difference form of axial symmetry electrostatic field is presented. Numerical modeling with Comsol Multiphysics 3.5 program package by finite difference method is introduced. Comparison of results computed with both methods is accomplished. Analysis of electrostatic field of electrode system “needle near the plate” is also performed. The results of potential and electric field strength distribution of axial symmetry needle near the plane and plane parallel wire near the plane fields are compared.

Keywords: Axial symmetry electrostatic field, Laplace equation, finite difference method, numerical methods.

1. Introduction

Corona field is applied to electrostatic precipitators, electric spraying, ion induced fans, powdery materials separation, biological application [8], drying in electrohydrodynamic field [4] and other.

Authors underline a small power needs using electrostatic or corona discharge field [1, 4]. Corona discharge takes place in a small inter-electrode space therefore it must be very careful model and simulation to obtain desired process. Corona discharge electric field depends upon polarity of corona electrode, a set voltage, the geometry of electrodes.

There is various electrode systems most adapted for each application. Most popular electrode systems are wire-to-plane, group of parallel wires at the plane, needle-to-plane [1, 2]. Authors foreground that in industrial application there must be a set of wires or needles, because of to meet the needs of mass productions [4]. Each electrode system has its own advantages and shortages in using areas of industrial processes. Most of authors simulate electric field in two dimensions because of economy of computational time and computer resources [1, 2, 3]. Electrode systems wire near the plate or needle near the plate has great attitude of the scientists [4, 5, 6, 7]. In some cases,

when concentrated electric field is needed at small volume, needle has advantage over wire-to-plane.

Corona discharge electric field is constant at the surface of electrode according Kaptzov's assumption, which states that the electric field strength on the surface of wire electrode at the corona discharge is constant and equal to its value E_0 corresponding to the inception voltage U_0 of the discharge. The initial field strength E_0 is determined from Peek's formula. When field strength near corona discharge electrode-needle is less than initial field strength E_0 in inter-electrode space would be electrostatic field with no space charge. It is first step for complicated corona discharge electric field analysis. Goal of this paper is to set Laplace equation finite difference formulas for axial symmetry field to calculate electrostatic field. Finite element method in Comsol Multiphysics is used to check the accuracy of solution.

2. Axial symmetry electrode system needle near the plane

Selected electrode system needle near the plane is shown in Fig. 1. Parameters of the needle: thickness 0,2 mm, sharpness is 1 cm (from the tip of the needle grows up 1 cm to 0,2 mm at the thickest spot). Computational domain area is 5x5 cm. The needle is 1 cm above the plane. Because of axial symmetry of electrode system chosen coordinate system of computation is the polar one. Calculations are carried out in the r and z directions. There is no variation of the potential in the direction of φ $\left(\frac{\partial V}{r\partial\varphi} = 0\right)$ because the field in electrode

system needle near the plate is of axial symmetry.

Boundary conditions for Laplace equations are of type Dirichlet: points on the surface of the needle potential is uniform and equal to set voltage $V = U$, points on the surface of the plane potential $V(z = 0) = 0$, plane is grounded.

Labels of the field boundaries are shown in Fig. 1. Boundary AB is the symmetry line of the field and $r_0 = 0$, $V_K = V_D$. Boundary BC is the surface of the needle and all points laying on this surface has potential equal

to set voltage U . Boundaries CD and DE are external borders of the field and voltage vary directly. Boundary AE is surface of the plate. All nodes of the computational grid at the initial stage of computation are equal to zero except the boundary on the surface of emitting electrode.

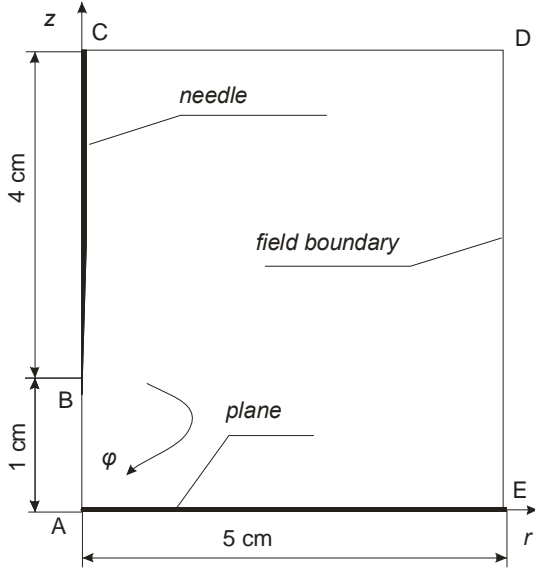


Fig. 1. Electrode system needle near the plane

3. Laplace equation of axial symmetry field in finite difference form

Laplace equation has main form:

$$\Delta V = 0. \quad (1)$$

In axial symmetry field where is no variation in φ direction Laplace equation has the partial derivative form:

$$\frac{\partial^2 V}{\partial r^2} + \frac{1}{r} \frac{\partial V}{\partial r} + \frac{\partial^2 V}{\partial z^2} = 0. \quad (2)$$

Polar coordinate system is chosen to compute the solution. Finite difference method is selected to compute distribution of potential in inter-electrode space. Computational grid becomes rectangular spread in r and z coordinates. Element of computational grid is shown in Fig. 2.

Partial derivative form of Laplace equation outspread in finite difference form for regular distances is:

$$V(i, j) = \frac{1}{4} (V(i+1, j) + V(i, j+1) + V(i-1, j) + V(i, j-1)) + \frac{a}{2 \cdot r} (V(i+1, j) - V(i-1, j)) \quad (3)$$

Computational node potential value is average of four surrounding nodes plus derivative in r axis product unit divided by distance from axis of symmetry to computational node.

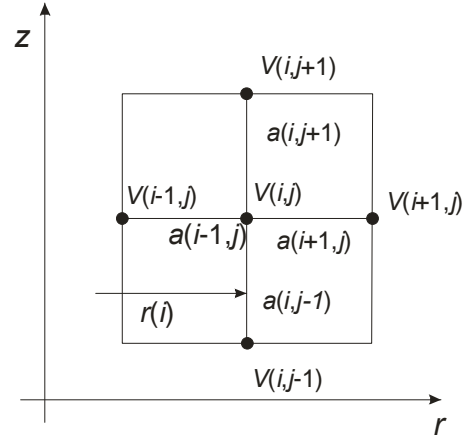


Fig. 2. Nodes of finite difference mesh

Numerical algorithm is shown in Fig. 3.

Boundary conditions are described in second part of the paper. Initial values in all nodes of computational grid are zero except nodes located at the surface of the needle. These nodes have set value potential all computational time.

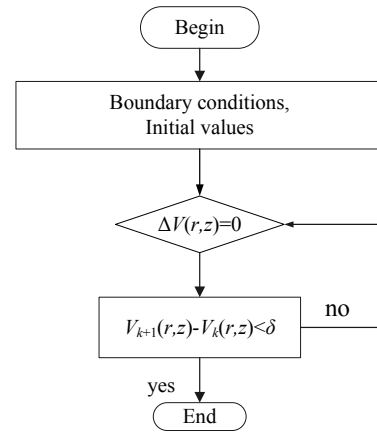


Fig. 3. Numerical algorithm for calculation the electrostatic field in electrode system needle near the plate

The calculation process is at the z direction computational grid line counted all nodes potentials from first plane node $i=1, j=1$ to exterior field boundary CD line point. Then get back to the beginning and compute next line $j+1$. When all points are counted condition of convergence is tested. Calculations are completed if condition is satisfied, if not calculation is repeated from beginning.

4. Results

Computed results of potential and electric field strength distribution of axial symmetry needle near the plane and plane parallel wire near the plane fields must be compared to investigate field strength and potential distribution at the symmetry line of the field where is strongest electric field. Wire near the plane was computed in cylindrical coordinate system. Computational algorithm, finite difference approximation and computational grid are shown in paper [1].

Computed results of electrode system needle near the plane with 200x200 computational grid nodes are shown in Fig. 4. Calculation was verified with finite element method program package Comsol Multiphysics 3.5. Boundary conditions in finite element problem are the same as described in section 2.

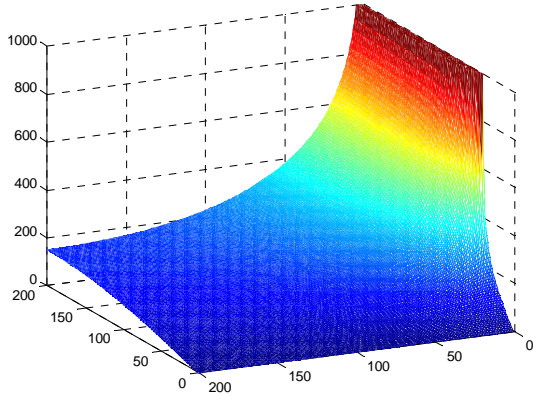


Fig. 4. Distribution of potential in electrode system needle near the plane computed by finite difference method

Computed results with finite element method of electrode system needle near the plane are shown in Fig. 5.

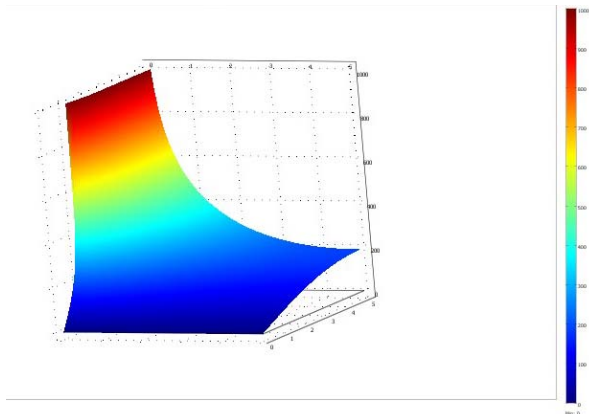


Fig. 5. Distribution of potential in electrode system needle near the plane computed by finite element method

It is clear from Fig. 4 and Fig. 5 that solutions in both methods are the same. Potential vary with a few percent accuracy at any point of the field.

Electric potential is decreasing sharply near the surface of the needle. Component of the Laplace equation product of potential derivative to r axis with unit divided by $r \frac{1}{r} \frac{\partial V}{\partial r}$ has significant influence to potential

reduction in axial symmetry field near the symmetry line because of small value of distance from symmetry line r . Far from symmetry line the influence of derivative of potential value is less. At the symmetry line of the electrode system a short distance from the needle potential falls rapidly, at the on-tenth of the distance losing more than half of the value, it is clear from Fig. 6.

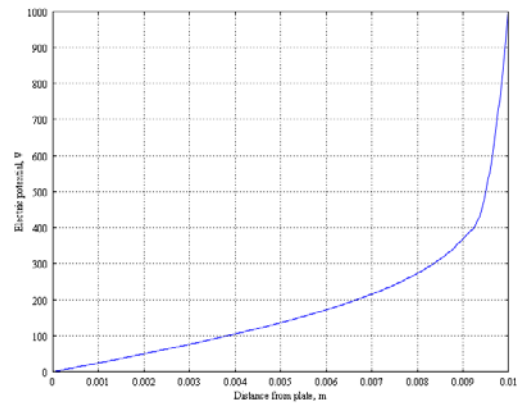


Fig. 6. Distribution of potential at the symmetry line in electrode systems wire near the plane and needle near the plane computed by finite element method

Potential distribution on symmetry axis shown in Fig. 7 corresponds to the values of wire radius $r = 0,025, 0,05$ and $0,1$ mm. Potential distribution in electrode system needle near the plane is shown there also. Distance from wire center to plane is 1 cm.

This figure shows that the electric potential rapidly declines from point of the surface of the wire to the plane at the lower radius of the wire. At the electrode system needle near the plane electric potential declines even faster and potential value stays lesser in all points of the symmetry line as in electrode systems wire to plane.

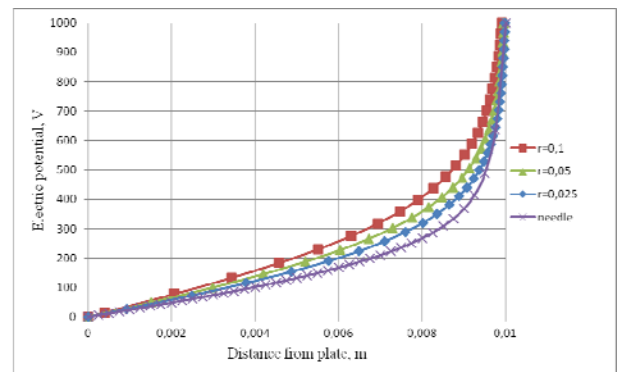


Fig. 7. Distribution of potentials at the symmetry line in electrode systems wire near the plane and needle near the plane computed by finite difference method

The main characteristic of the electrode systems is distribution and character of the electric field strength. Space charge density value depends on electric field strength value at the surface of corona electrode according Kaptzov's assumption. Also in some electric field applications it is essential to know electric field distribution and values in the space.

Distribution of electric field strength at the symmetry line in electrode systems wire near the plane and needle near the plane computed by finite difference method is shown in the Fig. 8. All values of the first node from wire or needle are computed at the $z = 0.00975$ mm distance from the surface of plate. This avoids additional errors of the electric field strength which vary exponentially near the surface of corona electrode.

Electric field strength is greater with smaller radius of the wire. Field strength near the surface of the needle is greater than $r = 0.05$ and 0.1 mm and less than $r = 0.025$. Receding from the surface of corona electrode electric field strength is greater with wire to the plane electrode system for a few points of the computational grid. Below is lower than electric fields of the electrode system wire to the plane.

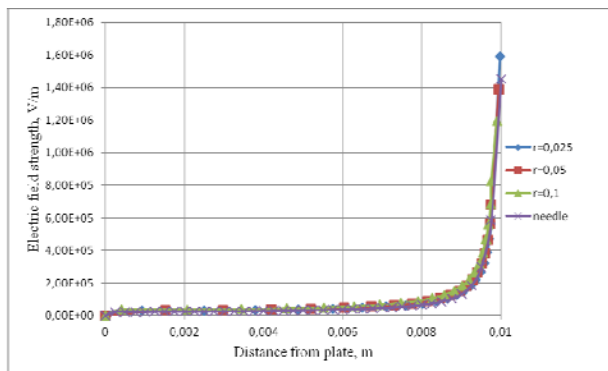


Fig. 8. Distribution of electric field strength at the symmetry line in electrode systems wire near the plane and needle near the plane computed by finite difference method

5. Conclusions

Calculation of the electrostatic field of the axial symmetry electrode system needle near the plane by finite difference method is presented.

Verification of the results with program package Comsol Multiphysics 3.5 by finite element method is performed, because of no analytical solution.

Potential and electric field strength values of the electrode systems needle near the plane and wire near the plane are compared.

At the electrode system needle near the plane electric potential declines faster and potential value stays lesser in all points of the symmetry line than in electrode systems wire to plane.

Near the surface of corona electrode electric field strength is greater in wire to the plane electrode system for a few points of the computational grid. In points below field strength is lower than electric field of the electrode system wire to the plane.

6. References

1. P. Marčiulionis, S. Žebrauskas. Numerical analysis of spatial force components in direct current corona field // *Electronics and Electrical Engineering = Elektronika ir elektrotechnika*. Kaunas : Technologija. ISSN 1392-1215. 2009, nr. 8(96), p. 3-8.
2. Laurentiu Marius Dumitrana, Pierre Atten, Petru V. Notingher, Lucian Dascalescu. 2-D corona field computation in configurations with ionising and non-ionising electrodes. *Journal of Electrostatics* 64 (2006) 176–186.
3. Zhao L., Adamiak K. Numerical Simulation of the Electrohydrodynamic Flow in a Single Wire-Plate Electrostatic Precipitator. *IEEE Transactions on Industry Applications*, Vol. 44, No. 3, p. 683-691.
4. F. C. Lai, R. K. Sharma. EHD-enhanced drying with multiple needle electrode. *Journal of Electrostatics*. 63 (2005) p. 223–237.
5. L. Zhao, K. Adamiak. EHD flow in air produced by electric corona discharge in pin–plate configuration. *Journal of Electrostatics*. 63 (2005) p. 337–350.
6. H. Kawamoto, S. Umezū. Electrostatic micro-ozone fan that utilizes ionic wind induced in pin-to-plate corona discharge system. *Journal of Electrostatics* 66 (2008) 445–454.
7. Matthew Rickard, Derek Dunn-Rankin. Numerical simulation of a tubular ion-driven wind generator. *Journal of Electrostatics* 65 (2007) p. 646–654.
8. Masao Washizu. Biological applications of electrostatic surface field effects. *Journal of Electrostatics* 63 (2005) p. 795–802

INVESTIGATION OF ELECTRIC FIELD UNDER THREE-PHASE LINE

Ramūnas DELTUVA, Gabija NEDZINSKAITĖ, Juozapas Arvydas VIRBALIS
Department of Electronics Engineering, Kaunas University of Technology, Lithuania

Abstract: The paper offers mathematical analysis of the electric field strength in high-voltage outdoor switchgears with phase voltages. The methodology of mathematical calculations allows for estimation of the electric field distribution in the surroundings of open switchgears. Based on this methodology of mathematical calculation it is possible to theoretically estimate and determine the electric field strength at the workplace, and its dependencies on distance and voltage, while comparing calculated values with the valid regulated standard values. Knowing the electric field strength distribution in high-voltage switchgears makes it possible to undertake precautions to diminish its potential effects.

Keywords: electric field distribution, the method of images, permissible electric field strength values.

1. Introduction

The Hygiene Norm HN110:2001 “The electromagnetic field of industrial frequency (50 Hz) in the workplace” has been valid in Lithuania until 2012 providing that the human exposure to highly intensive electric field can involve only short periods of time. However, these EMF values are way too high and must be reduced in accordance with the Directive 2004/40/EC of the European Parliament and of the Council valid since 30/04/2012. In compliance with this particular Directive valid for member states of EU, the electric field strength of industrial frequency (50 Hz) must not exceed 10 kV/m in the workplace [1].

All the high-voltage units have been previously designed irrespective of this requirement. For this reason, it is necessary to explore if workplaces exceeding the recommended electric field strength value by the respective EU Directive exist in the territory of the Republic of Lithuania, and undertake necessary means for ensuring compliance with this particular requirement.

The operative 330 kV open-type outdoor switch-gears are considered to be the most hazardous among high-voltage installations. For this reason, the electric field generated by these switchgears was investigated in the first place.

Within the operating switchgear employees are allowed to stay on the ground only, consequently the investigation of electric field values found in the territory of the switchgear up to 2 m in height above the ground surface is of utmost importance [2].

2. Presumptions for calculating the electric field strength

The wavelength of the electric field of industrial 50 Hz frequency is approximately 6000 km, whereas measurements of the workplace are incomparably smaller. Thus the electric field can be assumed to be evenly distributed over the entire space of switch gear at any moment in time. Therefore, we can use methods of electrostatic field for electric field distribution investigation. In high-voltage outdoor switchgears, wires are usually arranged in one plane parallel to the ground surface.

Thus, we suppose that distances of the conductors of all three phases to the ground surface are equal and amount. We calculate the electric field strength in the observation point O with distance y_0 at earth surface (see Fig. 1). The distance between phase wires is also known, l_0 . The electric field strength created by three-phase line in the observation point we calculate using the method of image charges. We suppose that the charge densities created in the phase wires are equal to q_i ($i=A, B, C$). By image charge method the image charges (see Fig. 1) have the same charge densities but opposite signs $-q_i$ ($i=A^*, B^*, C^*$).

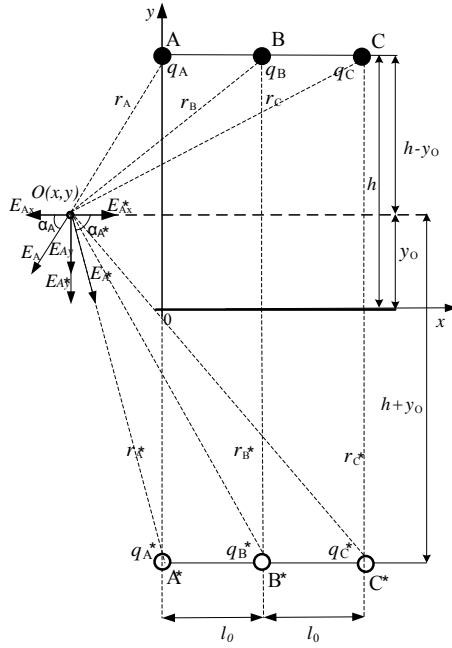


Fig. 1. Scheme used to calculate the electric field strength vectors at the point O

The electric field strength can be found from a well-known expression of the electrostatic field potential:

$$E_i = \frac{\pm q_i}{2\pi\epsilon_r\epsilon_0} \cdot \frac{1}{r_i}; \quad (1)$$

where $\epsilon_0=8,85 \cdot 10^{-12}$ F/m – dielectric constant, ϵ_r – relative dielectric constant; r – the distance between the charge and the observation point.

3. Calculation of the electric field strength using the method of image charges

Knowing potentials of the current leads it is necessary to find the electric field strength, E . Although potentials of current leads or their charges are already known, however distribution of the charge density over the surface of the current lead is unknown.

When the electric field is being generated by charges of the three-phase line q_i ($i=A, B, C$), the total strength of the resultant field is equal to the sum of field strengths of the individual charges as follows:

$$\mathbf{E} = \mathbf{E}_A + \mathbf{E}_B + \mathbf{E}_C; \quad (2)$$

where $\mathbf{E}_A, \mathbf{E}_B, \mathbf{E}_C$ is the electric field strength generated by phases conductors A, B, C charges and its images. The total field can be calculated more conveniently within the orthogonal coordinate system as follows:

$$E = \sqrt{E_x^2 + E_y^2}. \quad (3)$$

The components of the electric field strength of the three-phase conductor system are as follows at the point O: in a horizontal direction E_x , and in the vertical

direction E_y . The components for each phase of the electric field strength generated by the three-phase conductor system can be calculated as follows:

$$E_x = E_{Ax} + E_{A^*x} + E_{Bx} + E_{B^*x} + E_{Cx} + E_{C^*x}, \quad (4)$$

$$E_y = E_{Ay} + E_{A^*y} + E_{By} + E_{B^*y} + E_{Cy} + E_{C^*y}. \quad (5)$$

The constituents of the electric field strength of the three-phase electric power system can be expressed through geometrical parameters of the line as follows:

$$E_{Ax} = \frac{q_A}{2\pi\epsilon_r\epsilon_0} \left(\frac{x_0}{(h-y_0)^2 + x_0^2} - \frac{x_0}{(h+y_0)^2 + x_0^2} \right), \quad (6)$$

$$E_{Bx} = \frac{q_B}{2\pi\epsilon_r\epsilon_0} \left(\frac{x_0+l_0}{(h-y_0)^2 + (x_0+l_0)^2} - \frac{x_0+l_0}{(h+y_0)^2 + (x_0+l_0)^2} \right), \quad (7)$$

$$E_{Cx} = \frac{q_C}{2\pi\epsilon_r\epsilon_0} \left(\frac{x_0+2l_0}{(h-y_0)^2 + (x_0+2l_0)^2} - \frac{x_0+2l_0}{(h+y_0)^2 + (x_0+2l_0)^2} \right), \quad (8)$$

$$E_{Ay} = \frac{q_A}{2\pi\epsilon_r\epsilon_0} \left(\frac{(h-y_0)}{(h-y_0)^2 + x_0^2} + \frac{(h+y_0)}{(h+y_0)^2 + x_0^2} \right), \quad (9)$$

$$E_{By} = \frac{q_B}{2\pi\epsilon_r\epsilon_0} \left(\frac{(h-y_0)}{(h-y_0)^2 + (x_0+l_0)^2} + \frac{(h+y_0)}{(h+y_0)^2 + (x_0+l_0)^2} \right), \quad (10)$$

$$E_{Cy} = \frac{q_C}{2\pi\epsilon_r\epsilon_0} \left(\frac{(h-y_0)}{(h-y_0)^2 + (x_0+2l_0)^2} + \frac{(h+y_0)}{(h+y_0)^2 + (x_0+2l_0)^2} \right); \quad (11)$$

where $h-y_0$ – the distance between the line wires plane and the observation point O; $h+y_0$ – the distance between the line wires plane and the plane of the images; l_0 – the distance between wires of phases A and B between wires of phases B and C.

The components of the vector of electric field strength E_x and E_y are calculated using the Equation (2) as follows:

$$E_x = E_{Ax} + E_{Bx} + E_{Cx}, \quad (12)$$

$$E_y = E_{Ay} + E_{By} + E_{Cy}. \quad (13)$$

The following denominations of the geometric parameters of the line are introduced:

$$A_x = \left(\frac{x_0}{(h-y_0)^2 + x_0^2} - \frac{x_0}{(h+y_0)^2 + x_0^2} \right),$$

$$B_x = \left(\frac{x_0+l_0}{(h-y_0)^2 + (x_0+l_0)^2} - \frac{x_0+l_0}{(h+y_0)^2 + (x_0+l_0)^2} \right),$$

$$C_x = \left(\frac{x_0+2l_0}{(h-y_0)^2 + (x_0+2l_0)^2} - \frac{x_0+2l_0}{(h+y_0)^2 + (x_0+2l_0)^2} \right),$$

$$A_y = \left(\frac{(h-y_0)}{(h-y_0)^2 + x_0^2} + \frac{(h+y_0)}{(h+y_0)^2 + x_0^2} \right),$$

$$B_y = \left(\frac{(h-y_0)}{(h-y_0)^2 + (x_0+l_0)^2} + \frac{(h+y_0)}{(h+y_0)^2 + (x_0+l_0)^2} \right),$$

$$C_y = \left(\frac{(h-y_0)}{(h-y_0)^2 + (x_0+2l_0)^2} + \frac{(h+y_0)}{(h+y_0)^2 + (x_0+2l_0)^2} \right).$$

Taking into consideration expressions (6-11) with the above-introduced denominations, equations (4) and (5) are rewritten as follows:

$$E_x = \frac{1}{2\pi\epsilon_r\epsilon_0} [q_A A_x + q_B B_x + q_C C_x], \quad (14)$$

$$E_y = \frac{1}{2\pi\epsilon_r\epsilon_0} [q_A A_y + q_B B_y + q_C C_y]. \quad (15)$$

The potentials of conductors V_i ($i=A, B, C$) are associated with their charge densities q_i ($i=A, B, C$) using Maxwell's equations as follows:

$$[q_i] = [c_i] \cdot [V_i]; \quad (16)$$

where:

$$q_i = \begin{bmatrix} q_A \\ q_B \\ q_C \end{bmatrix}, \quad c_i = \begin{bmatrix} c_{11} & c_{12} & c_{13} \\ c_{21} & c_{22} & c_{23} \\ c_{31} & c_{32} & c_{33} \end{bmatrix}, \quad V_i = \begin{bmatrix} V_A \\ V_B \\ V_C \end{bmatrix},$$

where c_{kn} ($k=1,2,3; n=1,2,3$) are capacitance coefficients. They can be expressed via the potential coefficients p_{kn} ($k=1,2,3; n=1,2,3$) evaluating $[c]^{-1}=[p]^{-1}$ as follows:

$$c_{kn} = \frac{\det p_{kn}}{\det p}. \quad (17)$$

The potential coefficients are expressed via the geometrical parameters [2]. The coefficients $p_{11}=p_{22}=p_{33}$ can be found from the following equation:

$$p_{11} = \frac{1}{2\pi\epsilon_r\epsilon_0} \cdot \ln \frac{2h}{r}; \quad (18)$$

the coefficients $p_{12}=p_{21}=p_{23}=p_{32}$ can be found as follows:

$$p_{12} = \frac{1}{2\pi\epsilon_r\epsilon_0} \cdot \ln \frac{b_{AB^*}}{a_{AB}}; \quad (19)$$

where $a_{AB}=a_{BC}$ is the distance between the wire phases A and B, where as b_{AB^*} is the distance between the phase A wire and the image B* of the phase B wire. The coefficients $p_{13}=p_{31}$ can be calculated in this way:

$$p_{13} = \frac{1}{2\pi\epsilon_r\epsilon_0} \cdot \ln \frac{d_{AC^*}}{c_{AC}}; \quad (20)$$

where c_{AC} is the distance between the wire phases A and C, where as d_{AC^*} is the distance between the phase A wire and the image C* wire of the phase C.

Knowing values of the electric charges q_A, q_B, q_C , and taking into consideration expressions (14) and (15), the electric field generated by phases A, B, and C in directions of axes x and y can be formulated as follows:

$$E_{Ax} = q_A A_x = V(c_{11} + c_{12} + c_{13}) A_x, \quad (21)$$

$$E_{Ay} = q_A A_y = V(c_{11} + c_{12} + c_{13}) A_y, \quad (22)$$

$$E_{Bx} = q_B B_x = V(c_{21} + c_{22} + c_{23}) B_x, \quad (23)$$

$$E_{By} = q_B B_y = V(c_{21} + c_{22} + c_{23}) B_y, \quad (24)$$

$$E_{Cx} = q_C C_x = V(c_{31} + c_{32} + c_{33}) C_x, \quad (25)$$

$$E_{Cy} = q_C C_y = V(c_{31} + c_{32} + c_{33}) C_y. \quad (26)$$

Potentials of the phase current leads are defined by phase voltages of the line that are expressed as follows [3]:

$$\begin{cases} V_A = u_{A0} = U_m \sin \omega t; \\ V_B = u_{B0} = U_m \sin(\omega t - 120^\circ); \\ V_C = u_{C0} = U_m \sin(\omega t + 120^\circ). \end{cases} \quad (27)$$

where U_m is amplitude of phase voltage.

Let V be the potential effective value. The instantaneous values of electric field strength are:

$$E_x(t) = V \cdot \sqrt{2} \begin{bmatrix} (A_x c_{11} + B_x c_{21} + C_x c_{31}) \sin \omega t + \\ A_x c_{12} + B_x c_{22} + C_x c_{32} \sin(\omega t - 120^\circ) \\ + (A_x c_{13} + B_x c_{23} + C_x c_{33}) \sin(\omega t + 120^\circ) \end{bmatrix}, \quad (28)$$

$$E_y(t) = V \cdot \sqrt{2} \begin{bmatrix} (A_y c_{11} + B_y c_{21} + C_y c_{31}) \sin \omega t + \\ A_y c_{12} + B_y c_{22} + C_y c_{32} \sin(\omega t - 120^\circ) \\ + (A_y c_{13} + B_y c_{23} + C_y c_{33}) \sin(\omega t + 120^\circ) \end{bmatrix}. \quad (29)$$

Using the equations:

$$\sin(\omega t - 120^\circ) = -0,5 \sin \omega t - \frac{\sqrt{3}}{2} \cos \omega t, \quad (30)$$

$$\sin(\omega t + 120^\circ) = -0,5 \sin \omega t + \frac{\sqrt{3}}{2} \cos \omega t, \quad (31)$$

we can write the following:

$$E_x(t) = V \sqrt{2} \begin{bmatrix} \left(A_x (c_{11} - 0,5c_{21} - 0,5c_{31}) \right) \sin \omega t \\ + B_x (c_{21} - 0,5c_{22} - 0,5c_{23}) \\ + C_x (c_{31} - 0,5c_{32} - 0,5c_{33}) \end{bmatrix}, \quad (32)$$

$$E_y(t) = V \sqrt{2} \begin{bmatrix} \left(A_y (c_{11} - 0,5c_{21} - 0,5c_{31}) \right) \sin \omega t \\ + B_y (c_{21} - 0,5c_{22} - 0,5c_{23}) \\ + C_y (c_{31} - 0,5c_{32} - 0,5c_{33}) \end{bmatrix} + \frac{\sqrt{3}}{2} \begin{bmatrix} A_x (c_{13} - c_{12}) \\ + B_x (c_{21} - c_{22}) \\ + C_x (c_{33} - c_{32}) \end{bmatrix} \cos \omega t. \quad (33)$$

Noting $N_{AS} = c_{11} - 0,5c_{12} - 0,5c_{13}$,
 $N_{BS} = c_{21} - 0,5c_{22} - 0,5c_{23}$, $N_{CS} = c_{13} - 0,5c_{32} - 0,5c_{33}$,
 $N_{AC} = c_{13} - c_{12}$, $N_{BC} = c_{21} - c_{22}$, $N_{CC} = c_{33} - c_{32}$, and
involving by second power we obtain:

$$E_x^2(t) = 2V^2 \begin{bmatrix} (A_x N_{AS} + B_x N_{BS} + C_x N_{CS})^2 \sin^2 \omega t \\ + \frac{3}{4} (A_x N_{AC} + B_x N_{BC} + C_x N_{CC})^2 \cos^2 \omega t \\ - \sqrt{3} (A_x N_{AS} + B_x N_{BS} + C_x N_{CS}) \\ \cdot (A_x N_{AC} + B_x N_{BC} + C_x N_{CC}) \sin \omega t \cos \omega t \end{bmatrix}, \quad (34)$$

$$E_y^2(t) = 2V^2 \begin{bmatrix} (A_y N_{AS} + B_y N_{BS} + C_y N_{CS})^2 \sin^2 \omega t \\ + \frac{3}{4} (A_y N_{AC} + B_y N_{BC} + C_y N_{CC})^2 \cos^2 \omega t \\ - \sqrt{3} (A_y N_{AS} + B_y N_{BS} + C_y N_{CS}) \\ \cdot (A_y N_{AC} + B_y N_{BC} + C_y N_{CC}) \sin \omega t \cos \omega t \end{bmatrix}. \quad (35)$$

The trigonometric functions obtained from equations (34) and (35) for the electric field strength constituents E_x and E_y , can be expressed as $\sin^2 \omega t = 0,5 - 0,5 \cos 2\omega t$ and $\cos^2 \omega t = 0,5 + 0,5 \cos 2\omega t$, then the electric field strength generated around phase conductors can be calculated as follows:

$$E^2 = V^2 \begin{bmatrix} 0,5 \cdot \left((A_x N_{AS} + B_x N_{BS} + C_x N_{CS})^2 \right. \\ \left. + (A_y N_{AS} + B_y N_{BS} + C_y N_{CS})^2 \right) \\ + 0,375 \cdot \left((A_x N_{AC} + B_x N_{BC} + C_x N_{CC})^2 \right. \\ \left. + (A_y N_{AC} + B_y N_{BC} + C_y N_{CC})^2 \right) \end{bmatrix}. \quad (36)$$

4. Expression for electric field strength calculation in any observation point

Total sum of coefficients A_x ; A_y ; B_x ; B_y ; C_x ; C_y , that are used to take into consideration the geometric position of the phase wires A, B, C and the point O in the space, are expressed as follows:

$$E^2 = V^2 \begin{bmatrix} C_A^2 (A_x^2 + A_y^2) + C_B^2 (B_x^2 + B_y^2) + \\ C_C^2 (C_x^2 + C_y^2) + C_{AB} (A_x B_x + A_y B_y) + \\ C_{BC} (B_x C_x + B_y C_y) + C_{AC} (A_x C_x + A_y C_y) \end{bmatrix}; \quad (37)$$

where, $C_i = (0,5N_{is}^2 + 0,375N_{ic}^2)$ and
 $C_{ij} = 2(0,5N_{is}N_{js} + 0,375N_{ic}N_{jc})$

$$A_x^2 + A_y^2 = \frac{C_A^2 a_4}{x_o^4 + a_{A2}x_o^2 + a_{A0}},$$

$$B_x^2 + B_y^2 = \frac{C_B^2 a_4}{x_o^4 + a_3x_o^3 + a_{B2}x_o^2 + a_{B1}x_o + a_{B0}},$$

$$C_x^2 + C_y^2 = \frac{C_C^2 a_4}{x_o^4 + 2a_3x_o^3 + a_{c2}x_o^2 + a_{c1}x_o + a_{c0}},$$

$$A_x B_x + A_y B_y = \frac{C_{AB}(a_4x_o^4 - a_3x_o^3 + a_{AB2}x_o^2 - a_1x_o + a_{AB0})}{(x_o^4 + a_{A2}x_o^2 + a_{A0})(x_o^4 + a_3x_o^3 + a_{B2}x_o^2 + a_1x_o + a_{B0})},$$

$$A_x C_x + A_y C_y = \frac{C_{BC}(a_4x_o^4 + 2a_3x_o^3 + a_{AC2}x_o^2 + a_1x_o + a_{AC0})}{(x_o^4 + a_3x_o^3 + a_{c2}x_o^2 + 2a_1x_o + a_{c0})(x_o^4 + a_{A2}x_o^2 + a_{A0})},$$

$$B_x C_x + B_y C_y = \frac{C_{AC}(a_4x_o^4 + 3a_3x_o^3 + a_{BC2}x_o^2 + a_{BC1}x_o + a_{BC0})}{(x_o^4 + a_3x_o^3 + a_{B2}x_o^2 + a_{B1}x_o + a_{B0})(x_o^4 + a_3x_o^3 + a_{c2}x_o^2 + a_{c1}x_o + a_{c0})}.$$

Values of the coefficients along axes x and y are determined by the position of phase wires A, B, C and the point O in the space, as well as by the structural parameters of the three-phase above-ground line. The structural parameters can be expressed through polynomials: the coefficients of denominator:

$$\begin{cases} a_3 = 4l_0, & a_0 = (h^2 - y_0^2)^2, & a_{A2} = 2(h^2 + y_0^2), \\ a_{B2} = 2(h^2 + y_0^2 + 3l_0^2), & a_{C2} = 2(h^2 + y_0^2 + 12l_0^2); \\ a_{B1} = 4l_0(h^2 + y_0^2 + l_0^2), & a_{C1} = 8l_0(h^2 + y_0^2 + 4l_0^2); \\ a_{B0} = a_0 + l_0^2(2h^2 + 2y_0^2 + l_0^2), & a_{C0} = a_0 + 8l_0^2(h^2 + y_0^2 + 2l_0^2). \end{cases}$$

The coefficients of numerator:

$$\begin{cases} a_4 = 4y_0^2, & a_3 = 8y_0^2l_0, & a_1 = 8y_0^2l_0(h^2 + y_0^2); \\ a_{AB2} = 4y_0^2(2h^2 + l_0^2 + 2y_0^2), & a_{AC2} = 4y_0^2(2h^2 + 4l_0^2 + 5y_0^2); \\ a_{BC2} = 4y_0^2(2h^2 + 13l_0^2 + 2y_0^2), & a_{BC1} = 24y_0^2l_0(h^2 + y_0^2 + 2l_0^2); \\ a_{AB0} = 4y_0^2(h^2 + y_0^2) - 4y_0^2l_0^2(h^2 + y_0^2); \\ a_{AC0} = 4y_0^2(h^4 - 5y_0^2h^2 - y_0^4) - 4y_0^2l_0^2(h^2 + y_0^2); \\ a_{BC0} = 4y_0^2l_0^2(4l_0^2 + 3h^2 + 5y_0^2) + 4y_0^2(h^2 - y_0^2). \end{cases}$$

5. Conclusions

The methodology for the mathematical calculation has been developed enabling to analytically estimate the electric field strength in the surroundings of 330 kV electric power transmission line or bus-bar system. Spatial distribution of the electric field strength E generated by the high-voltage power installations is described through A_x ; A_y ; B_x ; B_y ; C_x ; C_y – the coefficients along axes x and y that are dependent on the geometric position of phase wires A, B, C and the point O in the space, as well as on the structural parameters of the three-phase above-ground line.

6. References

1. The Directive 2004/40/EC of the European Parliament and of the Council on the minimum health and safety requirements regarding the exposure of workers to the risks arising from physical agents (electromagnetic fields). Commission of the European Communities. Brussels, 2004
2. R. Deltuva, J. A. Virbalis, S. Žebrauskas. Analysis of Electric Field in 330 kV Overhead Transmission Line // Electrical and Control Technologies. – Kaunas: Technologija, 2011. – No. ISSN 1822-5934. – P. 255-259.
3. R. Deltuva, J. A. Virbalis. Protection against Electric Field of the Outdoor Switch-Gear Workplaces // Electronics and Electrical Engineering. – Kaunas: Technologija, 2011. – No. 6 (112). – P. 11-14.
4. S. Žebrauskas, P. Marčulionis. The Electrostatic Field of the Electrode System “Wire near Cylinder” // Electronics and Electrical Engineering. – Kaunas: Technologija, 2005. – No. 6 (62). – P. 32-36.

DRYING OF PLANTS AND THEIR SEEDS IN THE CORONA FIELD

Stasys ŽEBRAUSKAS*, Ernestas KALINSKAS**

*Kaunas University of Technology, Lithuania; **Aleksandras Stulginskis University, Lithuania

Abstract: Drying rate parameters of herbs and grain of wheat treated by a direct current corona field are discussed. Wheat grain drying rate increases two-fold or three-fold in comparison to free convection conditions. It is slightly slower as the rate achieved by using the electromechanical ventilator if the surface moisture is removed. Drying is two-fold faster in comparison to electromechanical ventilator under volume moisture removal conditions. The drying is rather uniform in all layer of the product due to the action of corona field. Effectiveness of the drying is caused by small energy consumption of the field device.

Keywords: corona field, moisture content, rate of evaporation, energy consumption.

1. Introduction

Electrohydrodynamic drying technique of materials and products is a new modern method of drying enabling to improve the drying quality and to reduce energy consumption. Conventional drying methods usually comprise air moving by fans or ventilators and air temperature elevation. These methods are energy and cost-intensive [1]. Corona field has been found to consume little power compared to conventional drying techniques [2]. Corona field despite being shown to have a low efficiency in creating forced convection, still has the ability to enhance the evaporation significantly with energy consumption equivalent to conventional drying methods [9]. Total chlorophyll and ascorbic acid contents in spinach are substantially higher after electric field drying than after oven drying [4]. Moisture content of the treated wheat grain decreases much faster than that of air-dried samples under free-convection conditions. Average drying rate improves from 1,7 to 2,1 times compared with control samples [5]. Average drying rate of rapeseeds treated at 8, 9 and 10 kV electrostatic fields for 270 min exposure increased by 1,8, 2,1 and 2,5 times, respectively, compared to the control [1]. Electrostatic evaporation systems offer a number of advantages over the drying technologies due to power saving, compactness, reduced cost, and environmental friendliness [6]. It is shown that the

enhancement of drying rate increases with the applied voltage but decreases with the growth of external cross-flow reducing the corona field affect [7]. Although several studies [1-7] demonstrate the feasibility of electro-hydro-dynamically enhanced drying, some fundamental issues about this technique still remain largely unexplored [8]. Moreover, despite the successful demonstration of using the corona field technique for drying of various materials (cookie dough, chopped onion, filter paper, wool, potato slab, apple slice, paper towel, biomass materials, radish, spinach, and okara), its development still remains very much in the laboratory [9]. The following research stage is to scale up the laboratory results to meet the needs of industrial processes. We present in this paper some experimental results of wheat grain and herbs drying in the corona field.

2. Experimental equipment

Our experimental equipment consists of electrode system, high voltage source, kilo-voltmeter and microammeter (Fig. 1). Electrode system is represented by a set of parallel wires with high potential above the grounded plate. Flat container with the uniform layer of wheat grain is placed on the plane electrode.

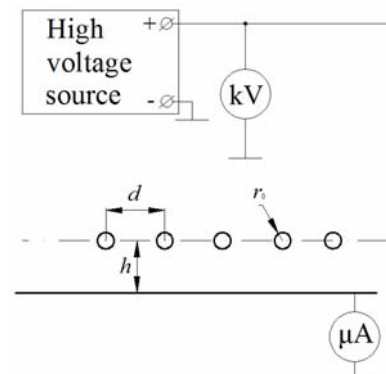


Fig. 1. Scheme of the experimental equipment

Corona discharge current depends on the voltage U , spacing between electrodes h , distance between wires d and wire radius r_0 . Computed and experimental volt-

ampere characteristics are analyzed to determine the proper values of mentioned parameters. Empirical formula of volt-ampere characteristic is the same as in [10]:

$$I_0 = 1,6b\varepsilon_0 \left(1 + 1,12 \frac{d}{h}\right) \left(\pi E_0 \frac{r_0}{2h}\right)^2 \gamma^{1,5}, \quad (1)$$

where I_0 is the corona current per unit wire length, b is the discharge ion mobility (assumed as constant), $b = 2,2 \cdot 10^{-4} \text{ m}^2/\text{V}\cdot\text{s}$ for negative discharge mode, and $b = 1,9 \cdot 10^{-4} \text{ m}^2/\text{V}\cdot\text{s}$ for positive one, ε_0 is the electric constant, $\varepsilon_0 = 8,85 \cdot 10^{-12} \text{ F/m}$, γ is the discharge index:

$$\gamma = \left(\frac{U}{U_0} - 1\right) \left(2\pi \frac{h}{d} - \ln 2\pi \frac{r_0}{d}\right). \quad (2)$$

Onset voltage U_0 for the electrode system “a set of parallel wires above the plate” may be determined as follows:

$$U_0 = r_0 E_0 \left(2\pi \frac{h}{d} - \ln 2\pi \frac{r_0}{d}\right). \quad (3)$$

Initial field strength E_0 is determined from well-known Peek's formula [8].

Computed and experimental volt-ampere characteristics for negative corona are given in Fig. 2. Similar characteristics for positive corona are shown in Fig. 3. Characteristic curves given in Fig. 2 and Fig. 3 correspond to the following values of parameters: $h = 12 \text{ mm}$, $d = 15 \text{ mm}$, $r_0 = 0,025 \text{ mm}$ without treated product.

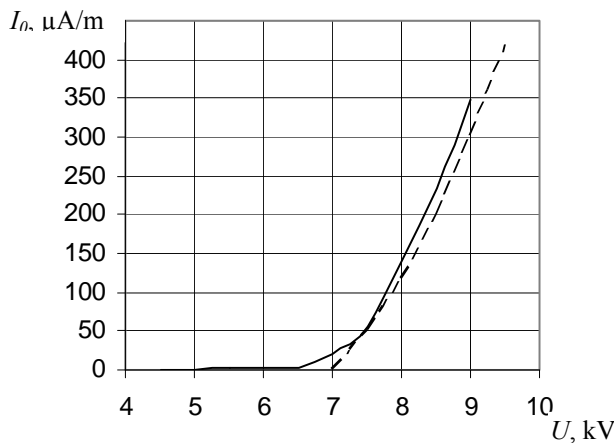


Fig. 2. Volt-ampere characteristic for negative corona:
----- computed, — experimental

Negative corona current exceeds the positive one because they are determined by greater value of negative ion mobility in comparison to positive one.

Experimental curves of volt-ampere characteristics corresponding to wheat grain layer placed on the grounded plane electrode are given in Fig. 4. Total length of emitting wires $l = 2,15 \text{ m}$. Negative corona

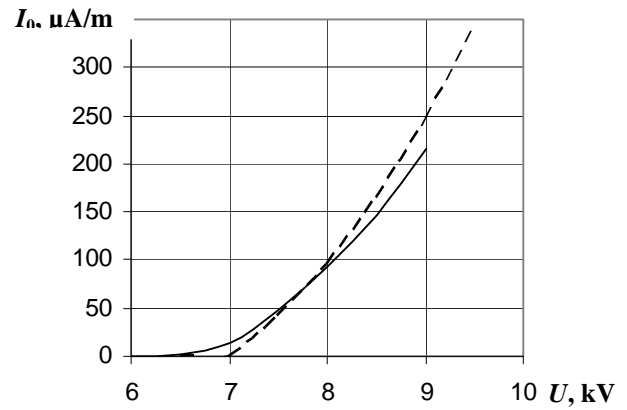


Fig. 3. Volt-ampere characteristic for positive corona:
----- computed, — experimental

current determined from Fig. 4 $I = 480 \text{ }\mu\text{A}$ at $U = 8,0 \text{ kV}$. So, the linear current density $I_0 = I / l = 480/2,15 = 223 \text{ }\mu\text{A/m}$. Although the spacing is the same for curves given in Fig. 2 and Fig 4 ($h = 12 \text{ mm}$) the linear current density value in the system with grain layer considerably exceeds the value in the system without the grain layer. This is because of the roughness of grain layer.

3. Results of drying experiment

Three modes of drying are being performed: drying with corona field, drying with air movement created by electromechanical ventilator and control drying under free convection conditions. Drying experiment is performed under the following ambient air conditions: air temperature $\vartheta = 20 \pm 1 \text{ }^\circ\text{C}$ ($T = -253 \text{ K}$), relative humidity $50 \pm 5 \%$. Power of corona field device is 1 W ($U = 7,2 \text{ kV}$, $I = 0,15 \text{ mA}$), power of electro-mechanical air driver (ventilator TITAN TFD-5010M12Z) is the same ($U = 12,0 \text{ V}$, $I = 0,09 \text{ A}$). Content of removed moisture is determined by weighing with a balance CQT202 (200g max $\pm 0,01 \text{ g}$). Thickness of grain layer

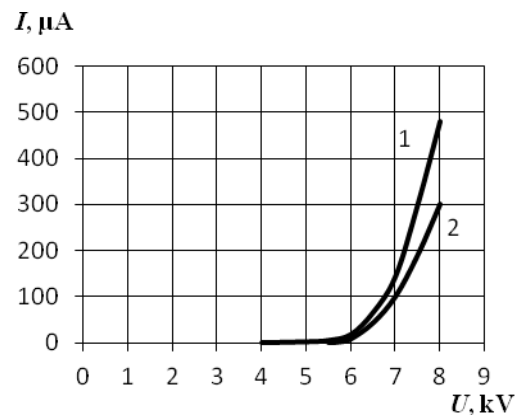


Fig. 4. Volt-ampere characteristics of electrode system with grain layer on the plain electrode; 1 – negative corona, 2 – positive corona

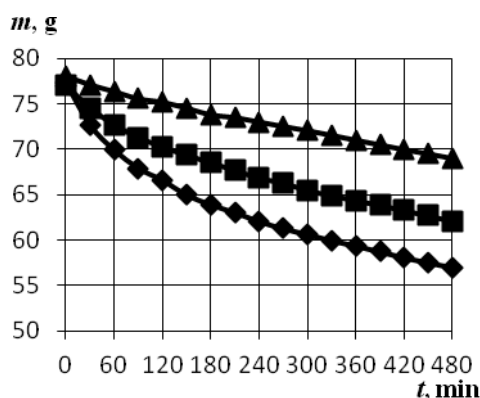


Fig. 5. Grain volume moisture reducing curves: triangles – free convection conditions, squares – tangential air flux driven by ventilator, rhombs – action of positive corona field

in all samples is equal to 10 mm. Volume moisture reducing in wheat grain layer curves are given in Fig. 5. Content of removed moisture varies in time according to exponential law. Time constants of all three curves in Fig. 5 are given in Table 1.

Table 1. Drying time constants corresponding to Fig. 5

Manner of drying	Positive corona field	Cross-flow of air	Control sample
Time const., min	100	200	400

Surface moisture evaporating from wheat grain layer graphics are presented in Fig. 6. Time constants of all three drying processes shown in Fig. 6 are given in Table 2.

Table 2. Drying time constants corresponding to Fig. 6

Manner of drying	Positive corona field	Cross-flow of air	Control sample
Time const., min	60	50	180

Surface moisture evaporating by air cross-flow is slightly more effective in comparison to drying with corona field. On the other hand evaporating of volume moisture in corona field is twofold more effective as compared to drying with the air cross-flow.

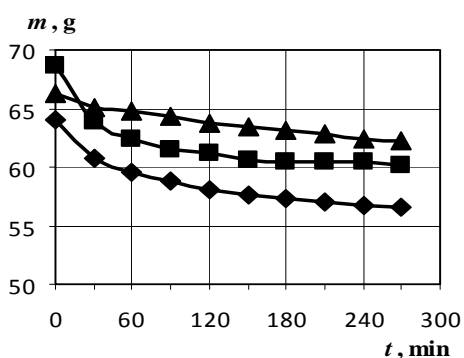


Fig. 6. Grain surface moisture reducing curves: triangles – free convection conditions, squares – tangential air flux driven by ventilator, rhombs – action of positive corona field

Results of herbs drying in the negative corona field are presented in Fig. 7 ($U = 6,8 \text{ kV}$, $I = 0,1 \text{ mA}$).

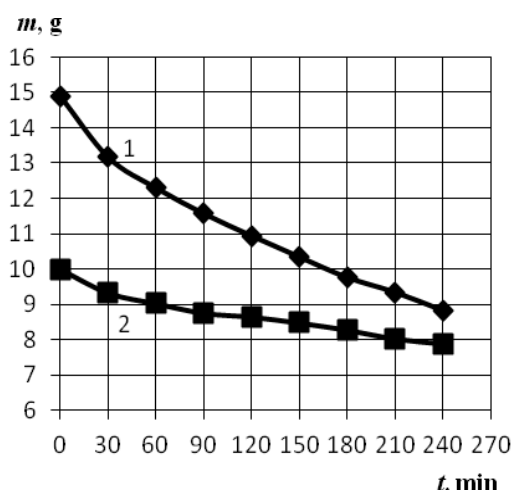


Fig. 7. Herbs drying graphics: rhombs – action of negative corona field, squares – free convection conditions

Time constants for drying processes shown in Fig. 7 are the following: drying by action of negative corona field – $\tau = 110 \text{ min}$, control sample – $\tau = 150 \text{ min}$.

4. Air movement

Distribution of ion-driven air movement velocity vectors in wire-to-plane electrode system at $U = 6,8 \text{ kV}$ is shown in Fig. 8 [11].

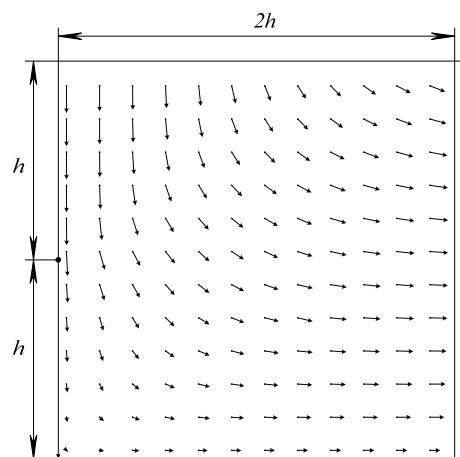


Fig. 8. Distribution of ion-driven air movement velocity vectors in wire-to-plane system, $U = 10 \text{ kV}$, $h = 12 \text{ mm}$, $r_0 = 0,050 \text{ mm}$

Dependence of air velocity at the plane electrode on the voltage is shown in Fig. 9. Air velocity gains the value $1,5 \text{ m/s}$ at the $U = 10 \text{ kV}$.

Position of electro-mechanical ventilator TFD-5010M12Z ($U = 12,0 \text{ V}$, $I = 0,09 \text{ A}$) in the system of coordinates is shown in Fig. 10. Variation of air flow velocity in the direction perpendicular to flow at $x = 1 \text{ cm}$, $x = 2 \text{ cm}$ and $x = 4 \text{ cm} = \text{const.}$ is given in Fig. 11. Ion driven air movement is significantly more uniform as compared to ventilator air movement.

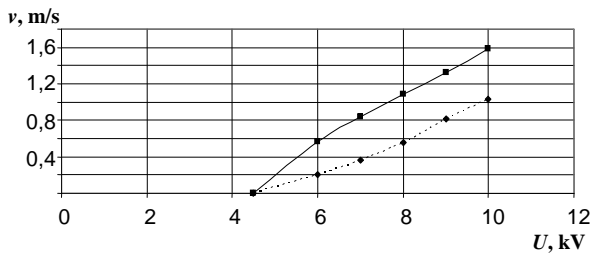


Fig. 9. Ion-driven air velocity chart: squares – computed values, rhombs – measured values

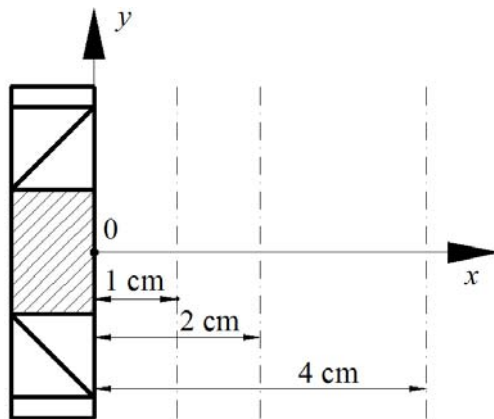


Fig. 10. Position of ventilator TFD-5010M12Z in the system of coordinates

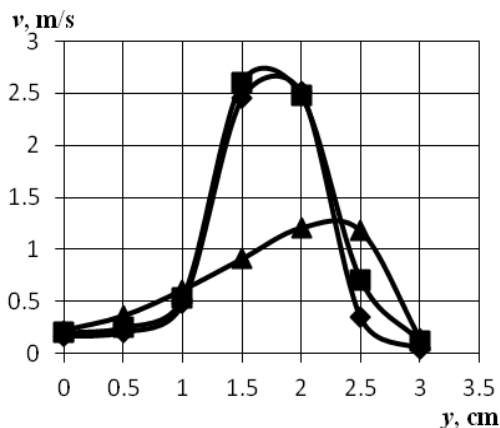


Fig. 11. Variation of air flow velocity in the directions perpendicular to the flow: rhombs – $x = 1$ cm, squares – $x = 2$ cm, triangles – $x = 4$ cm

5. Conclusions

1. Wheat grain surface drying time constant by action of air cross-flow is 50 min, surface drying time constant by action of positive corona field is 60 min.
2. Wheat grain volume drying time constant by action of positive corona field is 100 min, this value of drying by action of air cross-flow is 200 min.

3. Rate of herbs drying by action of negative corona field exceeds the control sample drying by 1,4 times.
4. Ion-driven air flow is significantly more uniform as compared to ventilator-driven flow.
5. Drying action of corona field depends not only on the action of ion-driven air flow but also of the action of electric field. This is a reason why volume drying is effective by action of corona field.
6. Effectiveness of corona field drying is determined by small energy consumption of corona device.

6. References

1. Basiry M., Esehaghbeygi A. Electrohydrodynamic drying of rapeseed. *Journal of Electrostatics*, Vol. 68, 2010, p. 360-363.
2. Alemrajabi A., Lai F.C. EHD-enhanced drying of partially wetted glass beds. *Drying technologies*, Vol. 23, 2005, p. 597-690.
3. Goodenough T.J., Goodenough P.W., Goodenough S.M. The efficiency of corona wind drying and its application to the food industry. *Journal of food engineering*, Vol. 80, 2007, p. 1233-1238.
4. Bajgal T.R., Hashinaga F. Drying of spinach with high electric field. *Drying technologies*, Vol. 19, 2001, p. 2331-2341.
5. Pietrzyk W., Sumorek A., Influence of electric field on wheat grain drying. *International Agrophysics*, Vol. 13, 1999, p. 245-250.
6. Reznikov M.A., Kolessov A., Koziol R. Electrohydrodynamic Enforcement of Evaporation and Gas Flow. *IEEE Transactions in Industry Applications*. Vol. 47, No 2, 2011, p. 1036–1042.
7. Lai F.C., Sharma, R.K. EHD-enhanced drying with multiple needle electrode. *Journal of Electrostatics*, Vol. 63, 2005, p. 223-237.
8. Huang M., Lai F.C. Numerical Study of EHD-enhanced Water Evaporation. *Journal of Electrostatics*, Vol. 68, 2010, p. 364-370.
9. Lai F.C. A Prototype of EHD-enhanced Drying with Multiple Needle Electrode. *Journal of Electrostatics*, Vol. 68, 2010, p. 101-104.
10. Žebrauskas S., Lankevičius G. Intensification of Heat Transfer in Direct Current Corona Discharge. *Proceedings of the 6th International Conference on Electrical and Control Technologies ECT2011*, Kaunas, Technologija, 2011, p. 206-209.
11. Marčiulionis, Povilas; Žebrauskas, Stasys. Numerical analysis of electrohydrodynamic air flow in dc corona field // *Przegląd Elektrotechniczny*. Warsaw :. 2012, Vol. 88, iss. 7b, p. 200-202.

THE NEED TO CONSIDER THE SKIN EFFECT IN THE STUDY OF DIRECT START-UP OF A SQUIRREL-CAGE INDUCTION MOTOR

Julija MAKSIMKINA

Institute of Industrial Electronics and Electrotechnics, Riga Technical University, Latvia

Abstract: Exploitation of squirrel-cage induction motors (SCIMs) is inevitably accompanied by the appearance of the transient processes that critically impact the condition and operation of electrical machines. In the study of transients in induction motors must consider that during the start-up, the rotor parameters (resistance and inductance) are changing due to the skin effect. The current paper is dedicated to the research of the direct start-up of the SCIM with due account for of the current's displacement in the rotor slots. The starting and nominal torque's values of different power SCIMs were calculated. The conclusion about the need to consider the skin effect in the study of direct start-up of SCIMs is given. Calculation and comparison are also given for the dynamic characteristics of SCIMs with constant and variable parameters of the rotor.

Keywords: Induction motors, transient process, current displacement effect, resistance, inductance, slip, starting torque.

1. Introduction

At the motor start-up the slip changes within the range starting from $s = 1$ up till the value of the steady regime $s=0.01\div 0.06$ [1]. During start-up (at slip $s=1$), to a greater or lesser extent, the current's displacement effect in the rotor bars is arises. In this case, the equivalent resistance of the rotor bars increases with the frequency of rotor current increasing [2]. In the majority of cases the current's displacement effect has a positive role by increasing the resistance of the rotor, decreasing the inductance of the rotor and increasing the starting torque of the motor. However, the uneven distribution of current density over a rod of the rotor can lead to undesirable consequences, up to motor failure [3]. Therefore, mathematical models of SCIMs, which do not consider the current displacement effect, may lead to significant errors in the calculations [4 – 7, 12 – 14]. This raises the question, in which range of motors the skin effect plays a significant role in the

start-up, and which range of motors this effect is negligible.

2. Evaluation of motors range liable to skin effect at start-up of SCIM

At start-up of the SCIM occurs starting current, which exceeds the nominal value of 5 – 10 times. Simultaneously with this, there is impact increase motor torque, which is transmitted to the shaft of rotor and through the shaft - on the mechanical part of the drive. That leads to overheating a stator windings and a deterioration of their isolation, as well as shaft breakage from shock and vibration, mechanical deformations of electric parts, etc.[8].

To cushion the shock in the transmissions and to provide smooth acceleration, frequency converters are used, limiting the starting current and torque [9].

Simultaneously with change of frequency should be regulated by a particular law the value of the supply voltage, to provide high stiffness of mechanical characteristics, high power index of SCIM (power factor, efficiency, overload capability) [10].

In order to identify the need to consider the skin effect at start-up the electromagnetic torque of wide range of motors was calculated for the different frequencies f_l of supply voltage at $s=1$ and evaluation of necessity to take into account the effect have been done by comparison of torques obtained with the rated ones for the motors.

The calculations of the electromagnetic torque were based on the equivalent circuit, which is shown in Fig. 1.

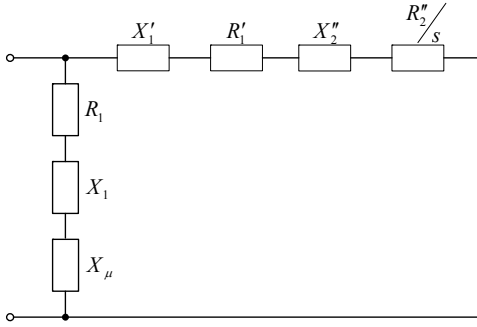


Fig. 1. Γ -shaped equivalent scheme of the induction motor

The parameters of the equivalent scheme $R_1', X_1', R_2'', X_2'', X_\mu$ is shown in the handbook [11] in relative units (r.u.).

The electromagnetic torque developed by the rotor of SCIM is defined by [8]

$$M = \frac{pm_1 U_1^2 \frac{R_2'}{s}}{\omega_1 \left[\left(R_1 + c_1 \frac{R_2'}{s} \right)^2 + (X_1 + c_1 X_2')^2 \right]}, \quad (1)$$

where p – number of pole pairs;

m_1 – number of phases of the stator winding;

U_1 – voltage of stator winding;

R_1 и X_1 – stator resistance and inductance;

$\frac{R_2'}{s}$ и X_2' – rotor resistance and inductance, reduced to the stator winding.

The equivalent circuit parameters should reduce to physical units to determine the electromagnetic torque. The calculation is as follows:

$$\begin{aligned} X_1 &\approx \frac{2X_1' \cdot X_\mu}{X_\mu + \sqrt{X_\mu^2 + 4X_1' \cdot X_\mu}}; \\ R_1 &= \frac{R_1' \cdot X_1}{X_1'}; \quad c_1 \approx 1 + \frac{X_1}{X_\mu}; \\ X_2' &= \frac{X_2''}{c_1^2}; \quad \frac{R_2'}{s} = \frac{R_2''}{s \cdot c_1^2}. \end{aligned} \quad (2)$$

For calculations at frequencies lower as $f_1 < 50$ Hz voltages applied in (1) have been accepted at constant relation of U/f , i.e. assuming for all speed characteristics constant range of speed decreasing.

The dependence $M_{start}/M_{nom}=f(P_2)$ at different frequencies is presented in Fig. 2. Range of motors examined reaches from 0.12 kW up to 315 kW. All motors are with number of pole pairs $p=2$ and rated voltage 380/220 V at $f=50$ Hz.

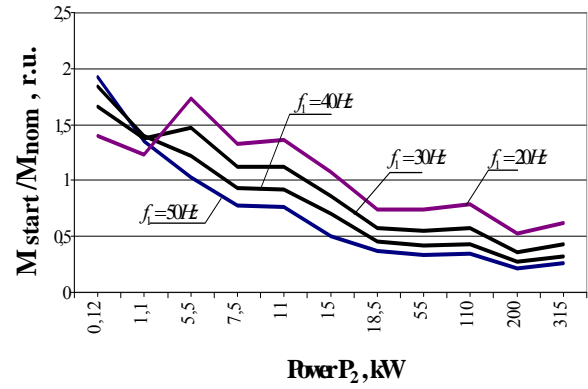


Fig. 2. Dependence of $M_{start}/M_{nom}=f(P_2)$ from P_2 value at different frequencies f_1 of supply voltage for rated power range of motors A4 from 0.12 kW to 315 kW

This dependence (Fig. 2) provides an opportunity to estimate the influence of skin effect to start electromagnetic torque of SCIMs at different frequencies.

At frequency $f_1 = 50$ Hz:

– at power of SCIM $0.12 \text{ kW} \leq P_2 \leq 5.5 \text{ kW}$ starting torque is greater than the nominal ($M_{start}/M_{nom} \geq 1$),

and the effect of current displacement in the rotor bars is weakly expressed. Consequently, in the calculation of dynamic characteristics of $I = f(t)$, $M = f(t)$, $n = f(t)$ of SCIM the surface effect can be ignored;

– at power of SCIM $5.5 \text{ kW} \leq P_2 \leq 315 \text{ kW}$ starting torque is lower than the nominal ($M_{start}/M_{nom} \leq 1$),

begins to appear the effect of the current displacement in the rotor bars, and the more power P_2 , the stronger will appear the surface effect. Consequently, in the calculation of dynamic characteristics of $I = f(t)$, $M = f(t)$, $n = f(t)$ of SCIM ignore of the surface effect can lead to significant errors.

Further on with decreasing frequency f_1 lower range of P_2 , which begins to show the effect of the current displacement, shifting, which reduces to decreasing of P_2 range:

$$\begin{aligned} -f_1 = 40 \text{ Hz} & \quad 7.5 \text{ kW} \leq P_2 \leq 315 \text{ kW}; \\ -f_1 = 35 \text{ Hz} & \quad 11 \text{ kW} \leq P_2 \leq 315 \text{ kW}; \\ -f_1 = 30 \text{ Hz} & \quad 13 \text{ kW} \leq P_2 \leq 315 \text{ kW}; \\ -f_1 = 25 \text{ Hz} & \quad 15 \text{ kW} \leq P_2 \leq 315 \text{ kW}; \\ -f_1 = 20 \text{ Hz} & \quad 18.5 \text{ kW} \leq P_2 \leq 315 \text{ kW}. \end{aligned}$$

It can be concluded, that at smaller supply voltage frequencies accounting of skin effect for start-up processes should be provided only for relative large power motors range, but at frequency 50 Hz range of motors dependent upon the skin effect at start-up is much wider.

3. Model of slot magnetic field of SCIM

It is known that at start-up, when the frequency of the rotor is high ($f_1=f_2$), the current density is distributed over the height of the bar very unevenly. As the motor

acceleration current frequency of the rotor is reduced. When the motor reaches the rated speed, the current frequency of the rotor is very low ($f_2 = s_{nom} \cdot f_1 \leq 1 \div 5$ Hz). In this case the effect of current displacement practically disappears, and the current is distributed evenly over the cross section of the rod [4, 14]. The model of rotor bar for SCIM 4AH355S4U3 315 kW, obtained with program complex *Quick Field 5.5*, is shown in Fig. 3.

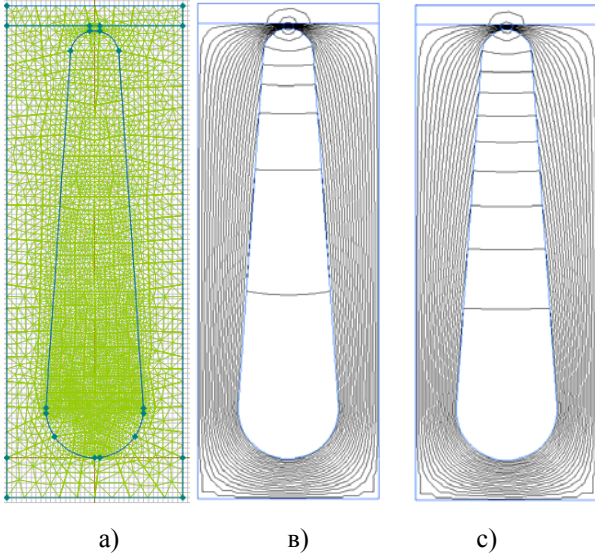


Fig. 3. The model of rotor bar (a), field distribution in the slot at $f_1 = 50$ Hz (b), at $f_1 = 5$ Hz (c)

Current density distribution in height of the rod, based on the program complex *Quick Field 5.5*, is presented in Fig. 4.

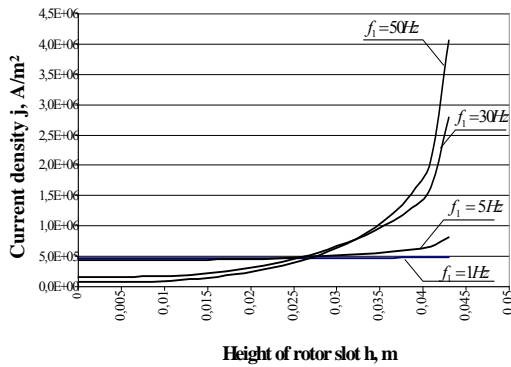


Fig. 4. Current density j as a function of height of rotor slot h at different frequencies f_1 of supply voltage

The obtained results (Fig. 3 and Fig. 4) clearly prove that magnetic field and current density are unevenly distributed in rotor slot. This makes it necessary to consider the skin effect in the rotor slots of SCIM.

4. The calculations of dynamic characteristics of SCIM with variable and constant parameters

To show the current displacement effect on dynamic characteristics, $I = f(t)$, $M = f(t)$, $n = f(t)$ were

calculated for a model of an idealized generalized motor.

The dynamic characteristics with Park-Gorev equations for the chosen SCIM 4AH355S4U3 have been obtained. The Park-Gorev equations in relative units are solved. The proposed IM mathematical model has been developed in coordinate axes $d, q, 0$, i.e. a set of the axes which are static relative to the rotor and rotate relative to the stator with the rotor's rotational speed $\omega_c = \omega_r$.

Therefore, modified Park-Gorev's equations assume the following form [10]:

$$u_{sd} = R_s i_{sd} - \omega_c \Psi_{sq} + \frac{d\Psi_{sd}}{d\tau}; \quad (3)$$

$$u_{sq} = R_s i_{sq} + \omega_c \Psi_{sd} + \frac{d\Psi_{sq}}{d\tau}$$

$$0 = R_r i_{rd} - (\omega_c - \omega) \Psi_{rd} + \frac{d\Psi_{rd}}{d\tau}; \quad (4)$$

$$0 = R_r i_{rq} + (\omega_c - \omega) \Psi_{rq} + \frac{d\Psi_{rq}}{d\tau}$$

$$T_M \frac{d\omega}{d\tau} = [X_{ad}(i_{rd}i_{sa} - i_{rq}i_{sd}) - M_{load}], \quad (5)$$

where u_{sd}, u_{sq} are the stator phase voltages in axes d, q ; i_{sd}, i_{sq} are the stator phase current in axes d, q ; i_{rd}, i_{rq} are the rotor phase current in axes d, q ; R_s, R_r is the respective stator and rotor resistances; Ψ_{sb}, Ψ_{rb} are the respective total flux linkages with phase windings of the stator and rotor; M_{load} is the load torque on the SCIM shaft; T_M is a mechanical time constant; $\tau = \omega t$.

Load simulation in relative units is accepted as follows:

$$M_{load} = M_c + k \cdot \omega^2 \quad (6)$$

where $M_c = 0$ – static torque; $k = 0.702$ – coefficient.

Torque of inertia $J = 5.8 \text{ kg}\cdot\text{m}^2$ is simulated with mechanical time constant:

$$T_M = \frac{J \cdot n_{nom}}{9.55 \cdot M_{nom}} \cdot 314.159 = \frac{5.8 \cdot 1500}{9.55 \cdot 2032} \cdot 314.159 = 0.448 \cdot 314.159$$

Usually, for solving (3) – (5) it is accepted that the rotor's parameters R_r and X_r are constant values. However, this approach is incorrect.

The current paper offers a general approach and presents a numerical method of calculation of the variable parameters of the rotor slots with arbitrary configuration.

The equivalent scheme of rotor circuit with the variable parameters that are influenced by the current's displacement effect could be presented in the form of the multi-link circuit with the constant and independent of the current displacement impedances (Fig. 5) [3].

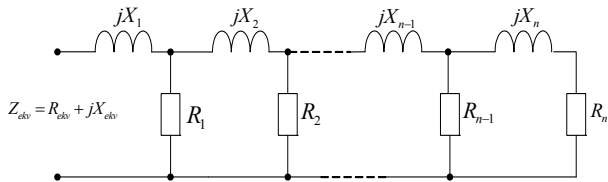


Fig. 5. The rotor bar equivalent scheme

The method for calculation of the rotor bar with a displacement of the electric current density in the multi-link scheme of impedances is as follows. Knowing the configuration of the magnetic lines of flux leakage in the slot, we will present a massive electrical conductor (a squirrel-cage winding rotor bar) divided into a great number of elementary layers isolated from each other by the thin layer of the insulation.

Let us presume that there is a plain-parallel filed in the slot, and electric current density along the line of flux is constant. With regards to a relevantly low height of the elementary layers these allowances do not bring into the calculations any considerable errors. With the account of these assumption allowances the parameters of the equivalent scheme (Fig. 5) are resistance R_i and inductance X_i of the elementary layer i .

$$R_i = \rho_i \cdot l / q_i ; \quad (7)$$

where ρ – resistivity of the rotor bar material;
 q_i – cross sectional area of the i layer;
 l – the length of the i elementary layer.

$$X_i = \omega_2 \mu_0 \lambda_i l = 2\pi f_1 s \mu_0 \lambda_i l ; \quad (8)$$

where ω_2 - current cyclic frequency of the rotor bar;
 λ_i - geometrical conductivity of the magnet tube the borders of which are defined by the i elementary layer.

Then show the current displacement effect on the dynamic characteristics $I=f(t)$, $M=f(t)$, $n=f(t)$ are calculated for the model of idealized generalized IM with the constant parameters of the rotor. SCIM 4AH355S4U3 parameters are used in relative units for nominal mode of operation [11]:

Stator's resistance 0.019;
 Stator's inductance 0.11;
 Rotor's resistance 0.014;
 Rotor's inductance 0.14;
 Magnetizing inductance 4.6.

The comparison the dynamic characteristics are presented in Fig. 6, Fig. 7 and Fig. 8.

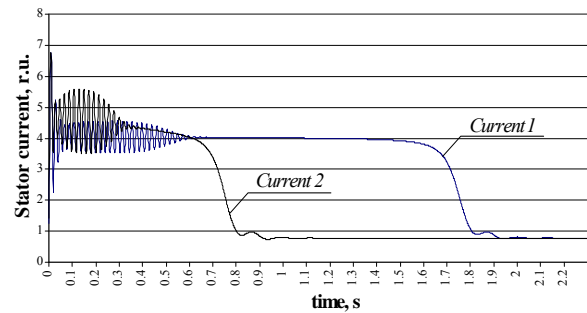


Fig. 6. Stator's current for SCIM 4AH355S4U3:
 1 – mode of operation with constant rotor's parameters R_2 and X_2 ;
 2 – mode of operation with variable rotor's parameters R_2 and X_2

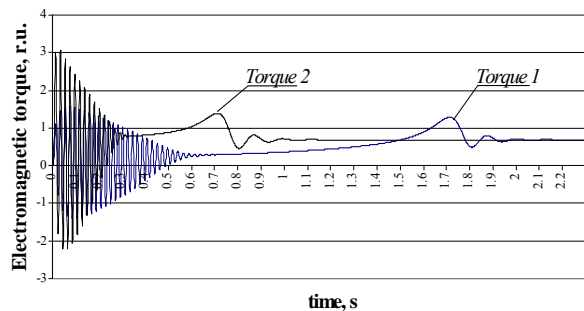


Fig. 7. Electromagnetic torque for SCIM 4AH355S4U3:
 1 – mode of operation with constant rotor's parameters R_2 and X_2 ;
 2 – mode of operation with variable rotor's parameters R_2 and X_2

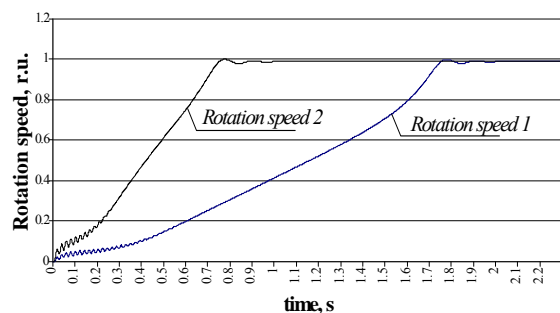


Fig. 8. Rotation speed for SCIM 4AH355S4U3:
 1 – mode of operation with constant rotor's parameters R_2 and X_2 ;
 2 – mode of operation with variable rotor's parameters R_2 and X_2

From the obtained dependence (Fig. 6, Fig. 7, Fig. 8) it is obvious that transient process proceeds quicker in mode with variable rotor's parameters; IM reaches its steady mode of operation during $t_{start}=0.9$ s. In mode of operation with constant rotor's parameters IM reaches its steady mode during $t_{start}=1.8$ s.

As seen from $I=f(t)$ characteristics (Fig. 6), the first current's bursts are the same independently from the mode of operation ($I_{max} = 6.4$ r.u. at $t=0.009$ s). In

steady mode current's values are identical and reach its nominal value $I_{nom}=0.77 r.u.$ Current's relation is:

$$\frac{I_{start}}{I_{nom}} = \frac{6.738}{0.77} = 8.75$$

As seen from $M=f(t)$ characteristics (Fig. 7), in steady mode of operation torque's values are identical and reaches its nominal value $M_{nom}=0.687 r.u.$ However, start torque's value is a lot more in mode of operation with variable rotor's parameters.

Start torque relations are:

$$\frac{M_{start}}{M_{nom}} = \frac{1.61}{0.687} = 2.35 \quad \text{-- mode of operation with}$$

constant rotor's parameters;

$$\frac{M_{start}}{M_{nom}} = \frac{3.059}{0.687} = 4.45 \quad \text{-- mode of operation with}$$

variable rotor's parameters.

This research work is show the variable parameters effect on the dynamic characteristics of induction motor's direct start-up.

5. Conclusions

Based on the results obtained in this work, the following conclusions can be drawn.

With decreasing supply voltage frequency f_1 range of rated power P_2 , for which have to be taken into account the effect of the current displacement is restricted in direction of higher powers, i.e. the effect have to be accounted only for start-up of larger scale motors.

Model of rotor slot obtained by using program complex *Quick Field 5.5*, provides a visual and numerical representation on the distribution of the magnetic flux and the current density in the rotor slots, depending on the frequency f_1 and displacement effect. Accounting for variable parameters of rotor in way of start-up fundamentally changes the course of the SCIM transient process. The start torque's value increases; the duration of the transient process becomes shorter by increasing the average torque developed by SCIM during the start-up.

6. References

- Zviedris A., Maksimkina J. The set of algorithms to calculate the parameters of squirrel cage induction motor // *Elektros enerģetika ir tehnoloģijas*, "Vilnius", Kaunas, Lietuva, 2004, p. 195-200 (in Russian).
- Zviedris A., Maksimkina J. Inventory of different methods of rotor's parameters influence of starting process of induction motor // *Power and Electrical Engineering, RTU, 4. sērija, 18. sējums, Rīga, 2006, p.45-50.*
- Maksimkina J. The Research of the Processes of the Squirrel-cage Induction Motor's Direct Start-up in the Setting of the Rotor's Variable Parameters // *Power and Electrical Engineering, RTU, 30 sērija, Rīga, 2012, p.53-58.*
- Kurnishev B.S. Skin effect in squirrel cage induction // *Young scientist, 2012, №8, p.26-28 (in Russian).*
- Pastuhov V.V., Korneev K.V. The direct start-up of induction motor simulation // *The innovative power, Novosibirsk, 2010, p.242-245 (in Russian).*
- Petrushin V.S., Buhalva Bendhaman, Yakimec A.M. The impact of saturation and current displacement in the rotor winding on the dynamic characteristics of controlled induction motors // *Electrical Engineering and Electronics, 2010, №2, p.21-23 (in Russian).*
- Pastuhov V.V., Korneev K.V. Three slot model for determining the bar parameters of the squirrel cage rotor of induction motor // *Power Engineering, №4, 2011, p.34-39 (in Russian).*
- Voldek A.I. *Electric machines. L., Energy, 1974 (in Russian).*
- Vazhnov A.I. *Transient processes in alternating current machines. L.: Energy, 1980 (in Russian).*
- Kazovskiy E.Y. *Transient processes in alternating current machines. L.: Publisher Academy of Sciences CCCP, 1962 (in Russian).*
- Kravchik A.E. *Induction motor 4A range. reference book. L., Energoatomizdat, 1982 (in Russian).*
- Boglietti A. Skin effect experimental validations of induction motor squirrel cage parameters // *The International Journal for Computation and Mathematics in Electrical and Electronic Engineering, Vol. 29, №5, 2010, p.1257-1264.*
- Cipín R., Běloušek J. Influence of a skin effect in the squirrel cage on a speed – torque characteristics of the induction motor // *Sborník konf. EPVE 08, VUT FEKT Brno, 2008.*
- Benecke M., Doebbelin R., Lindemann A. Skin effect in squirrel cage rotor bars and its consideration in simulation of non-steady-state operations of induction machines // *Progress In Electromagnetic Research Symposium Proceedings, Marrakesh, Morocco, 2011, p.1451-1455.*

SMART SYSTEM FOR CONDITION MONITORING OF THE POWER SYSTEM EQUIPMENTS INSULATION

Alfonsas MORKVENAS, Povilas VALATKA
Department of Electric Power System, Kaunas University of Technology, Lithuania

Abstract: In the power network the insulation condition of electrical equipment is one of the most important factors in guaranteeing the quality and cost efficient operation of the power system. Reliable operation of the electrical equipment relies on the appropriate maintenance and condition monitoring of the equipment, timely repair tasks, also on factors affecting equipment and their nature.

Research results related to smart insulation condition monitoring system and resource assessment system for high-voltage equipment is done according to the processes in the power network and registered factors affecting the insulation, their performance and variations are provided in this paper.

Keywords: Insulation condition, overvoltage, online diagnostics.

1. Introduction

Power system performance usually depends on the reliability of electrical equipment. Electrical equipment condition assessment and arising defects are subject to various periodic or permanent monitoring methods [1, 2, 3, 4,]. Fairly simple and efficient electrical equipment evaluation system is a periodic maintenance of the installation.

In the power system, the insulation condition and duration of reliable operation of high-voltage (HV) electrical equipment is determined by various factors: over-voltage, partial discharges (PD), over current, vibration and so on. The in operation substation and power transmission lines, the high-voltage electrical equipment is continuously affected by the high electric field, surges, discharges, heat, humidity, oxidation, vibration, aging processes and other factors causing various defects. The insulation aging rate and the appearance of defects is mostly due to over-voltages, thermal impact and PD. In the power system the duration and amplitude of the over-voltage can be various. The over-voltage and equipment operating temperature are the key factors accelerating aging processes of electric equipment insulation [1, 5].

In order to ensure reliable operation of electrical equipment, periodic tests and measurements are carried out. They require disconnection of the electrical equipment from power network. This causes temporary changes in the schemes that usually reduce reliability of the power system. Besides this, testing of electrical equipment does not guarantee reliable operation. Therefore it is advisable to develop testing methods that would allow to increase the test efficiency of electrical equipment and to reduce testing costs.

Currently the maintenance of electrical equipment is carried out according periodic schedule - after determined time duration or working hours. Such maintenance method of electrical equipment is not always optimal, because the quality of the insulation can change rapidly and defects can develop very quickly. The key method for optimization of this maintenance technique is to change the maintenance system in which repair frequency of electrical equipment and the scope of work would be determined by the insulation condition of the equipment. Thus an efficient diagnostic system for electrical equipment must be developed that would include monitoring equipment's insulation.

One of the prospective insulation condition monitoring systems for electrical equipment is equipment's in operation testing and monitoring procedures, without disconnecting the operating voltage. If monitoring systems for HV electrical equipment are applied without turning off the operating voltage, in the electrical equipment the characteristics can be monitored according to which the inner insulation and condition of other components can be determined thus technical condition can be evaluated. It is important to develop a monitoring system for high-voltage electrical equipment that would allow to assess the equipment in accordance with processes in the power system and to evaluate external factors: the over-voltage parameters and their effects, the asymmetry, limits of emergency condition and so on.

In this paper is analyzed, summarized and provided the methodology allowing developing electrical equipment smart insulation condition monitoring system wherewith

more accurate assessment of the insulation condition is possible.

2. Methods of electrical equipment diagnostics

In modern power system maintenance systems are important in order to do equipment condition evaluation based on the available relevant information which allows identifying priorities for equipment repair tasks and scope of work depending on the actual device condition. The main goal is to determine the necessary to observe indicators, which enable to relate existing condition information and to evaluate the service life [6].

Electrical equipment condition evaluation, defect identification and prediction are difficult, but important task. Electrical equipment condition often leads to operating conditions and maintenance time. Solid and liquid insulation elements usually form equipment insulation. Most of the researches focus on the voltage effecting the insulation and current interaction between qualitative characteristics.

2.1. Electrical equipment condition assessment characteristic

Analysis of the qualitative changes in the characteristics makes it possible to evaluate the technical condition of the electrical equipment and their reliability. Timely carried out equipment condition assessment, allows avoiding damage and accidents, also limits their consequences. Particularly vulnerable are the power and measurement transformers, 330 kV HV equipment terminals and so on. Studies have shown [7, 30] that up to 90 percent of the accidents can be avoided by improving methods of diagnosis, and 70 percent. – by applying timely repairs of the equipment.

Electrical equipment condition can be evaluated by analyzing various parameters which describe insulation and determination of their development and creating systems which predict the parameters. Once a reliable condition assessment system is arranged it can be used to identify potential arising defects, repair and testing tasks, evaluate operation time until device breakdown.

Main factors effecting equipment aging rate are over-voltage and overloads. Over-voltages directly affect the insulation, increases the PD level, due to the increasing number of defects in insulation and so on. Overloads and short-circuits effects insulation in its thermal way. Recently monitoring systems, continuously evaluating various parameters ($\tan\delta$, gas emissions, and temperature), are being applied [8, 9, 10].

For each type of HV equipment diagnostic methods are applied in line with the insulation characteristics the equipment design and if possible without reducing the resource. Currently the most commonly investigated dielectric diagnostic methods focus on insulation physical and chemical properties.

2.2. Periodic electrical equipment quality performance measurement system

Using a periodic monitoring system is sufficient to assess the power transformer and other equipment insulation condition by dissolved gases. Effect is even greater when the periodic oil dissolved gas monitoring system is supplemented with database which enables to predict the gas extraction rate. By applying periodic monitoring of water content in oil and making the database of the registration results the water quantity can be quite effectively monitored and changes in the critical level of operation regime can be predicted.

3. Smart insulation condition monitoring system

Application of the monitoring systems for HV electrical equipment allow to observe the characteristics of the inner insulation and other components and to evaluate the technical condition also the risk of accident without turning off operating voltage. Most common is dissolved gas chromatographic analysis [5, 11].

HV electrical equipment monitoring system monitors the electrical network elements, operating characteristic (surge parameters and their effects on the duration of the asymmetry of harmonics, emergency mode settings). Power system simulations models are arranged in order analytically investigate the electrical equipment insulation and evaluate the quality of the insulation and the resource. Simulation of PD processes in insulation is being done in insulation models. Using a structured algorithm is easier to create HV simulation models for mathematical investigations and calculations.

3.1. Electrical equipment online condition monitoring system

For in-operation electrical equipment a constant state monitoring systems are installed, which allows to monitor a variety of device's parameters - status indicators. Furthermore, it gives information about the actual state of internal electrical installations, and reduces the potential for damage of equipment, allows better assess the risk of possible failure.

PD is one of the important parameters influencing the isolation of aging. Therefore, using a variety of measurements and fault detection equipment it can be identified faults in electrical equipment. HV electrical equipment PD tracking system indicates the aging processes in electrical equipment insulation, and can act as an early warning system. Broadband electromagnetic interference tracking methods are applied consistently to track and identify the location of fault in cables and connectors. In the distribution network these techniques is being applied for more than 10 years [8]. Currently such methods expand in the transmission network - HV electrical substation electrical equipment with solid insulation continuous condition monitoring systems. In the substations, which use continuous monitoring systems, it must be possible to measure current and voltage and additional measuring devices that are

mounted to the cable line input coupling must be installed.

The structure of the registration equipment for resource expenditure and defect trends investigation according to the isolation and surge characteristics is provided in Fig. 1.

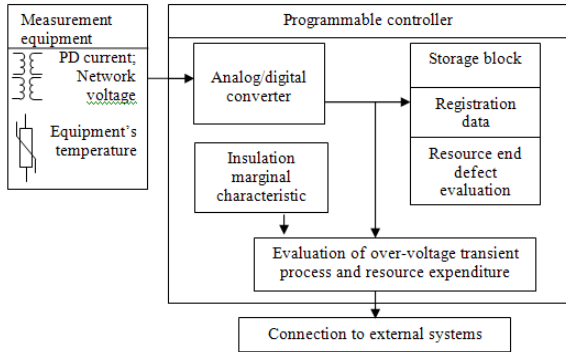


Fig. 1. Structure of the registration equipment for resource expenditure and defect trends investigation according to the isolation and surge characteristics

Device for insulation resource expenditure and defect trend recording and analysis is designed in order to measure electrical quantities in the secondary circuit, which correspond to voltage change processes in the network, and ongoing processes insulation of PD currents. When the voltage exceeds the maximum allowable operation level, measurement data is recorded, changed to digital and voltage changes are stored in the registration data storage block. In the insulation marginal characteristics data base block data is entered and then the data is stored according to the electrical equipment parameters, the registrar's coverage area and insulation resource characteristics are being calculated. In the resource and defect evaluation block surge impact and insulation resource expenditure, for each registration surge, is set and the level and duration of action, assessing PD transient performance indicators are compared with the previous registrations. The arranged surge integral characteristics are attributed to new registrations characteristics and exposure values are calculated. Resource expenditure and defect size assessment results are stored in the memory unit, and a warning signal is activated when values reach marginal levels. Alarm signal is transmitted to external systems. Programmable controller can be connected to the existing HV voltage measuring transformer secondary winding and the newly installed PD current measuring transformer secondary windings.

3.2. Algorithm of smart insulation diagnostic system

In purposed smart diagnostic system device status must be compared with the normalized allowable values specified in the standard, the manufacturer's instructions and regulatory documents. The measurement results and comparison with normalized values allows to assess only one or a few critical parameters level. Qualitative characteristics of the observed variation pattern can be

varied and predicted using mathematical analysis and processing of the measurement data. Electrical equipment insulation condition, in accordance with the recorded PD parameters qualitative characteristics of the complex, can be seen in the Fig. 2.

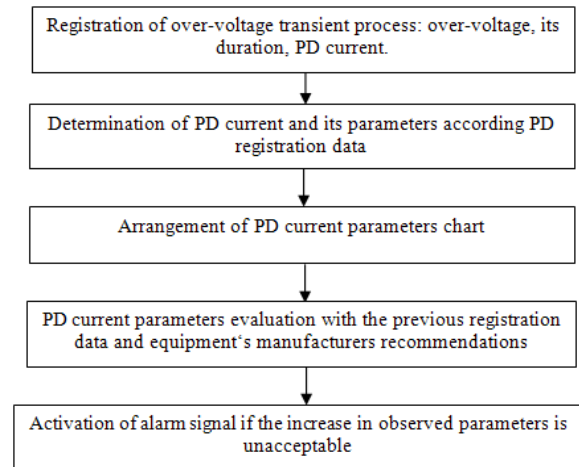


Fig. 2. Structure of condition assessment according to PD parameters

In Fig. 2 the evaluation of qualitative characteristics of the change (from the initial values to the normalized) is shown.

With the development of newer and more reliable monitoring system, which provides detailed information about the changes occurring in insulation, constantly recorded characteristics of patterns and evaluation of its variation allows determining devices operational status. Upgrading of existing facilities allows using additional criteria's to evaluate the equipment performance variation in order to assess the changing nature and the resource of reliable operation.

When the surge impact integral performance characteristic monitoring device is installed, the assessment of electrical equipment insulation and operating over-voltage characteristics can be done. In this way the number of tests can be reduced. This registering device would monitor electrical equipment, its insulation and the factors that affect the integral over-voltage characteristics on-line and resource assessment across a wide range of surge can be done.

3.3. Electrical equipment insulation resource expenditure monitoring algorithm

Equipment's operational resource is determined during the manufacturing and design periods. The initial resource of the equipment must be assessed before the unit is put in operation, the original factory data and qualitative characteristics must be set.

Electrical equipment initial resource can be estimated from (1) equation.

$$R = R_{\infty} \cdot e^{T_a / (T + B \cdot E^2)}; \quad (1)$$

where: R_{∞} – insulation operation until breakdown, T_a – activation temperature, B – basic electrothermal constant, E – strength of electric field, T – temperature. According to the results provided by the manufacturer, electrical equipment insulation resource status should be evaluated in three parameters: R_{∞} , T_a , B . Based on these indicators, and the (1) equation, finite resource surface R_{marginal} can be formed. Electrical equipment resource expenditure can be estimated based on the algorithm provided in Fig 3.

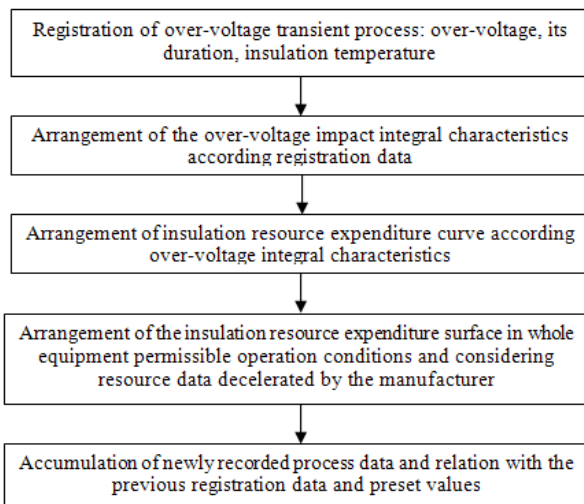


Fig. 3. Algorithm Electrical equipment resource expenditure calculation

According to the algorithm shown in Figure 3 a variety of methods (analytical, operational and numerical) can be applied to investigate with the purposed model. Currently the most commonly used are numerical integration methods. The compliance with the real object can be verified experimentally.

Electrical equipment (power and measurement transformers, switching apparatus, surge protection, and short-circuit equipment, communications equipment, etc.) is composed from more or less components which affect the overall device reliability. Using purposed algorithm, status of the qualitative characteristics can be monitored and evaluated continuously. Qualitative characteristics of the observed quantities and their variation range are quite wide. Evaluation of equipment condition and reliability from the qualitative characteristics should be monitored for changes.

According to the methods mentioned above, it is possible to increase the electrical equipment insulation condition assessment. The effectiveness of not only normalized values, but also changes due to the defect in insulation, influenced by the operating voltage, over-voltage, overload, and other factors that may quickly increase can be assessed. Factors affected by the surge can be accurately identified and defects and their trends in a variety of operating conditions can be evaluated.

4. Insulation investigation with the smart insulation condition monitoring system

According to the over-voltage integral characteristics impact on insulation resource scheme shown in Fig. 1 the electrical equipment insulation diagnosis and resource consumption and assessment smart diagnostic system (SDS) is created. This system can be used for monitoring electrical equipment, potential fault diagnostics and for investigation of affecting factors. Diagnostics can be performed automatically without intervention of service personnel. The observed indicators can be as follows: PD in equipment insulation, over-voltages affecting insulation

With SDS it can be monitored the electrical equipment insulation for those devices which has PD measurement sensors. These sensors must be connected to the inverters, which would change the analog values to digital ones. All measurement data must be collected and processed to programmable controller which can be mounted in substation control panel. This unit can be used as a warning alarm system.

Programmable controller should regularly measure values (PD, operating voltage, temperature) and compare the measurement results with the specified nominal permissible. In addition self-control of SDS should be done. Based on the measured values and the results of self-control, the corresponding messages should be formed for operating a staff.

SDS algorithm should consist of the following operations:

- Measuring equipment condition assessment.
- Selected set of indicators in the measuring objects.
- Evaluation of the measurement data according to the set of functional dependencies.
- Comparison of the measurement results with the preset values.
- Where appropriate, signalization about changes in the results.

Signalization of deviations, which excess the preset levels, can be implemented in three stages: normal mode, warning stage and failure regime.

In the first stage can be in the event when the minor insulation defects are recorded - PD currents values, which are close to noise levels, are recorded. In this step the maximum acceptable values must be set in order to avoid unacceptable false signals. According to the surge effects the insulation resource must have a large margin to the breakdown value.

In the second stage alarm is activated when the PD recorded value exceeds the permitted level and long-term operation is no longer available. If it appears and the observed value is rapidly increasing, an information signal should be activated. When the insulation resource value reaches the maximum acceptable value the emergency signal must be activated.

When the measured values exceeds the maximum permissible insulation resource values or according to registration data it is beyond the permissible limits, electrical equipment operator personnel should be informed about the status of the equipment which is in emergency condition.

According to the measurement and evaluation results the SDS, can form complex equipment isolation and resource expenditure assessment reports, which can be analyzed by the maintenance personnel who can use the necessary additional equipment to evaluate the situation in order to ensure the proper operation of the equipment.

4.1. Results of smart insulation condition diagnostic system

Based on surge effects registrations data, registered surge impact transient process is shown in Fig. 4.

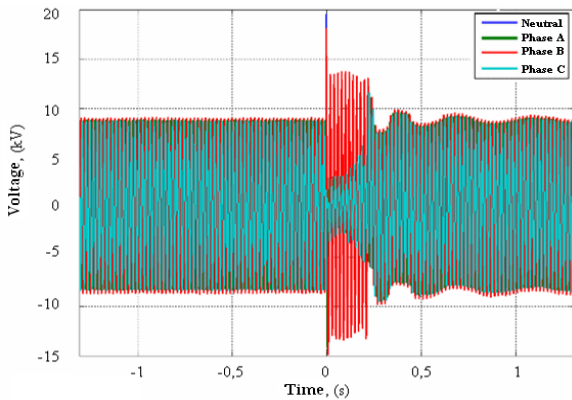


Fig. 4. Transient process registered in the network

Out of all the registered data the important range and the phase in which the process took place when the voltage exceeds the set value is extracted. Data must be recording with prehistory. Interval of single-phase transient process is given in Fig. 5.

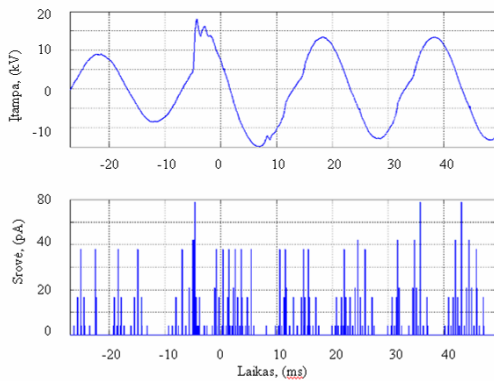


Fig. 5. Results of simulation of the several defects

Registration data is adjusted according to the PD simulation in isolation model, given in Fig. 1. The simulation the results of 0,1 mm, 0,2 mm and 0,3 mm defects are presented in Fig. 5 also.

Analysis results have shown that for transient process, provided in Fig. 4, registration data do not meet the requirements of IEC 60270 standard, (data was recorded at a frequency of 25 kHz), so PD current transient response simulation results are not representative (see Fig. 6).

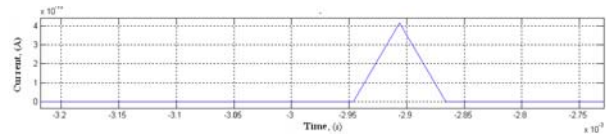


Fig. 6. PD simulation results when over-voltage transient registration results do not meet the IEC 60270 requirements

Part of registration data met the necessary requirements specified in IEC 60270 standard (registrations frequency of 2,5 MHz) (see Fig. 7.) - data recording frequency is satisfactory.

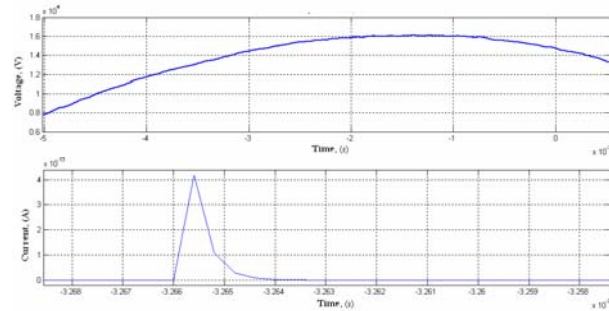


Fig. 7. PD simulation results when over-voltage transient registration results meet the IEC 60270 requirements

With the PD registrations data and based on the methodology presented previously, PD current pulses can be calculated and approximation curves, characterizing the process, can be arranged (see Fig. 8).

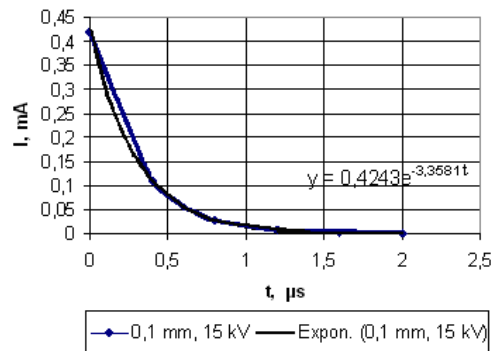


Fig. 8. PD current impulses approximation curve and calculation of PD characterizing index

The analysis of registered data indicated that when the artificial defect increased, the trend of PD current characteristics decreased. If the current samples are selected correctly (with no extraneous noise), there are no cross-sections between different sizes of artificial defects discharge current characteristics trends curves. The increase in discharge current characteristics trend, at the same registered voltage level, can give the indication of defect expansion. This parameter can be assumed as the warning factor for the insulation breakdown.

Registration of the over-voltage in the power network and PD induced current pulses at the same time, and evaluation of the PD current trend characteristics can be used to set up an active insulation condition monitoring system.

4.2. Insulation resource consumption and lifetime assessment with the SDS by the purposed algorithm

The analysis can be drawn according to surge registrations data available in the transient process shown in Fig. 4. The over-voltage impact integral characteristic is formed according data given in Fig. 9.

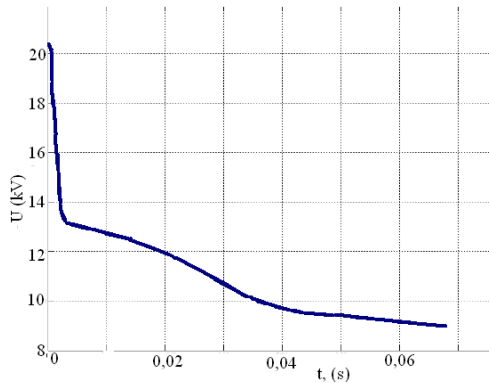


Fig. 9. The integral characteristics of a recorded over-voltage transient, induced by a lightning surge

According to the arranged characteristics the comparison of the integrated resource isolation is formed by the surface of the defined range of the over-voltage and temperature. This data is compared with the levels set for the observed device at the beginning of operation time (see Fig. 10).

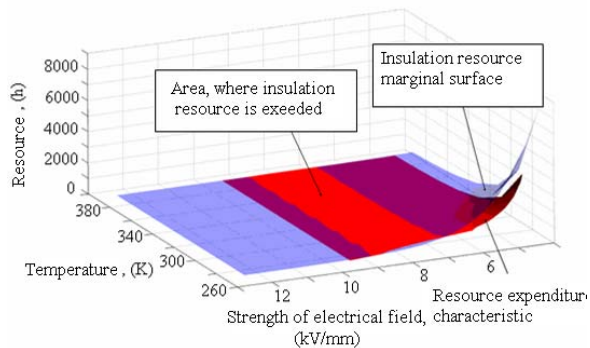


Fig. 10. Relative resource consumption calculated with the model

When accumulated surface exceeds the threshold level, an alert signal is activated. Based on the isolation resource assessment provided in the example, it can be noted that the resource evaluation of the proposed method is superior to other literature review, researchers who investigate the similar techniques. Key advantages and differences are:

- The relative isolation of resource assessment is done considering the electric field strength, and temperature.
- Insulation resource is described by the functional characteristics of dependence between two variables. According to the functional dependence the arranged insulation resource characteristic is the isolation surface is continuous.

5. Conclusions

By registering over-voltage in the power network and partial discharge current pulses, with the developed active monitoring system of insulation condition, it is possible that dangerous insulation quality changes as well as emerging defects can be timely detected. The system is complemented with over-voltage integral characteristics, which enable to assess operation conditions and insulation resource expenditure of the equipment.

6. References

1. Gerhards, J. and Temkins, A. Prognostics of electrical insulation resources: Nordic Insulation Symposium Stockholm, 11–13 June 2001, p. 125–132.
2. Kreuger, F. H. Partial discharges detection high voltage equipment. London: Butterworth & Co. Ltd; 1989, 192 p.
3. Сви, П. М. Контроль изоляции оборудования высокого напряжения. Москва, Энергоатомиздат, 1988, 128 p.
4. Aubin, J.; Gervais, P. On-line monitoring of key fault gases in power transformers and shunt reactors. Sixty-second Annual International Conference of Doble Clients, 1995, p. 122–135.
5. Gudžius, S.; Markevičius, L. A.; Morkvėnas, A.; Navickas, A. S.; Stanionienė, R. The Analysis of the Integral Characteristics of the Overvoltage's Effect Duration. EMD 2006: Proceedings of XVI International Conference on Electromagnetic Disturbances, September 27–29, 2006, Kaunas, Lithuania, Kaunas: Technologija, 2006, p. 72–77.
6. Walker, J. Condition based risk management [interactive] [accessed on 2011-09-10]. <http://scitation.aip.org/getabs/servlet/GetabsServlet?prog=normal&id=PEJOEE00001700000100003400001&idtype=cvips&gifs=yes&ref=no>.
7. Kane, C. The future of predictive technologies is here now. Neta world, 2007 [interactive] [accessed on 2011-09-10]. <http://www.netaworld.org/files/netajournals/NWsp07Kane.pdf>.
8. Cygan, P.; Laghari, J. R.; Models for insulation aging under electrical and thermal multistress. IEEE transactions in electrical insulation. October 1990, Vol. 25 No. 5, p. 923–934.
9. Gibeault, J. P. On-line monitoring of key fault gases in transformer oil. 10th International Symposium on High Voltage Engineering, Montreal, 1997, p. 62–71.
10. Partial discharge measurement using the MPD 600. Omicron magazine, 2011, Nr. 2, p. 32–33.
11. Morais, D. R.; Rolim, J. G. A hybrid tool for detection of incipient faults in transformers based on the dissolved gas analysis of insulating oil. IEEE Transactions on Power Delivery, April 2006, Nr. 21, p. 673–680.

ANALYSIS OF AN ELECTROSTATIC FIELD IN ELECTRODE SYSTEM OF DEVICES FOR DRYING OF POWDERY MATERIALS

Ignas ANDRIJAUSKAS, Stasys ŽEBRAUSKAS
Kaunas University of Technology, Lithuania

Abstract: Electrohydrodynamical drying of moist materials is one of perspective industrial technologies. Electrode system “a set of parallel cylindrical wires above the plane” is often used in drying devices. Results of numerical analysis of the electrostatic field in the system are discussed. Results of the analysis enable to minimize energy consumption to get the maximum drying effect. Comparison of volt-ampere characteristics shows that minimum energy consumption is inherent to the system with thinnest wires.

Keywords: potential distribution, field strength distribution, energy consumption.

1. Introduction

Conventional materials and products drying techniques, which usually involve elevated-temperature treatment and air movement, often produce undesirable changes in physical and chemical properties of materials, especially for food products. Moreover, air flow usually is too large in comparison with needed. Electrohydrodynamically (EHD) enhanced drying is a relatively new, non-thermal drying technique [1]. It utilizes the air flow induced by a high-intensity electric field. This EHD-induced secondary flow is also known as ionic wind or corona wind, which can be analyzed as a micro-jet of fluid moving from a corona electrode to a non-emitting surface. Increasing of moisture removal rate is caused by the complex action of corona field and of induced air movement destabilizing of the boundary layer. This drying technique may be characterized as low-temperature one. Additional increase of drying rate is obtained by dielectrophoresis exhibiting by the drift of dipoles in the gradient of the electric field and directly affecting the water vapor by an external electric field [2]. Main advantages of EHD drying are low energy consumption and higher quality of drying in comparison with conventional methods. [3]. Many authors note the twofold-threefold increase of drying rate compared with free convection drying. Usually EHD drying devices

use needle or wire emitting electrodes. The field of wire electrodes is characterized by rather uniform drying action, the effect of needle-electrode field is more concentrated [4]. Although this technology has been successfully demonstrated using various materials its development still remains very much in the laboratory. Moreover, despite many research results show that using corona field can produce drying enhancement, this does not imply that it is operating at its optimal conditions [5]. Optimization of the operating parameters (corona polarity, applied voltage, cross-flow velocity, surface curvature radii of emitting electrodes and electrode spacing) is critical for a viable commercialization of the technique. Our analysis deals with attempt to determine an influence of electrode dimensions (e.g. radius of emitting wire electrodes) on the operating parameters of the system.

2. Electrostatic field analysis

Our research comprises numerical simulation of electrostatic field in the electrode system “a set of parallel wires above the plate” and a comparative analysis of volt-ampere characteristics in a mentioned electrode system and in a wire-to plate system. Two-dimension view of the wire set-plate system is shown in Fig. 1. Let the distances be $b = 15$ mm, $h = 12$ mm that are usual for the systems operating at the voltages 5–15 kV. Radii of wires are varied from 0,025 mm to 0,100 mm. The field under examination has two axes of symmetry, the first coincides with the coordinate axis y

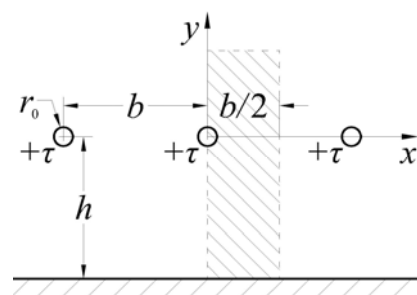


Fig. 1. Arrangement of electrodes

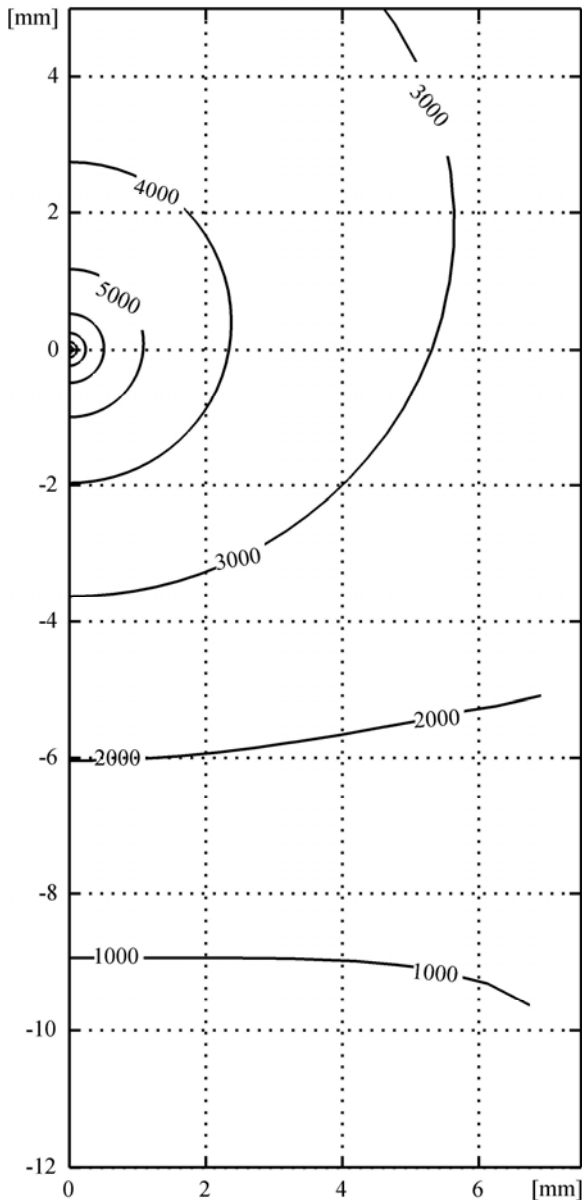


Fig. 2. View of equipotential lines, $r_0 = 0,025$ mm

and the second is vertical line which equation is $x = b/2 = 7,5$ mm. Computational area corresponds to lined rectangular shown in the figure. Finite-difference method of numerical simulation is used. Difference approximation of Laplace's equation is employed in two forms, the first is derived for all nodes of the regular grid occupying the inner part of computational area and the second is used for the nodes of irregular grid near the boundaries $y = -12$ mm = const, $x = b/2 = 7,5$ mm = const and $y = 5$ mm = const. Boundary conditions are the following: potentials of the wire and the plate are 10000 V and 0 correspondingly, potentials of symmetrical nodes to right and to left in respect of symmetry axes $x = 0$ and $x = b/2$ are the same. Boundary condition on the line $y = 5$ mm = const is determined as follows: potential derivatives of the last and the next-to-last nodes of each radial line are the same.

Distribution of equipotential lines for values of wire radii 0,025 and 0,050 mm, $h = 12$ mm, $b = 15$ mm and

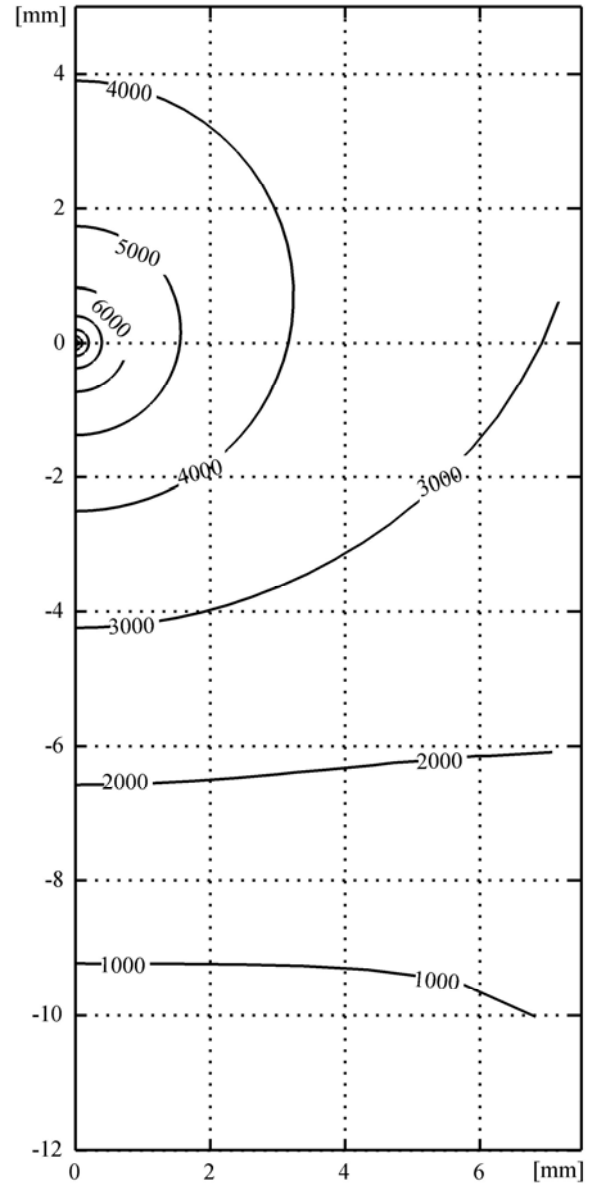


Fig. 3. View of equipotential lines, $r_0 = 0,050$ mm

$U = 10000$ V is shown in the Fig. 2 and Fig. 3. Equipotential lines move away from the wire is radius r_0 is increased.

Distribution of the electrostatic field strength on the surface of the wire is presented in the Fig. 4 and Fig. 5 corresponding to conditions that are noted for Fig. 2 and Fig. 3. Values of electric flux related with the surface of wire are determined from Fig. 4 and Fig. 5:

$$\Psi = \varepsilon_0 \oint_l \mathbf{E} \cdot d\mathbf{l} = 2\varepsilon_0 r_0 \int_0^\pi E \cdot d\alpha. \quad (1)$$

Numerical values of the flux are 71 nC/m and 78 nC/m for the field of Fig. 4 and Fig. 5 correspondingly. So the influence of the wire radius on the electric flux related to the wire isn't essential.

3. Corona field analysis

Onset field strength in electrode system with wire electrodes may be determined by the well-known Peek's formula [6]:

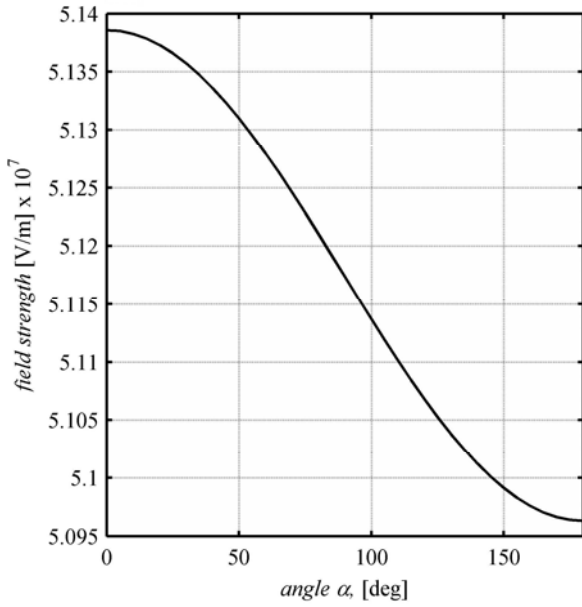


Fig. 4. Distribution of the field strength on the surface of the wire, $r_0=0,025$ mm

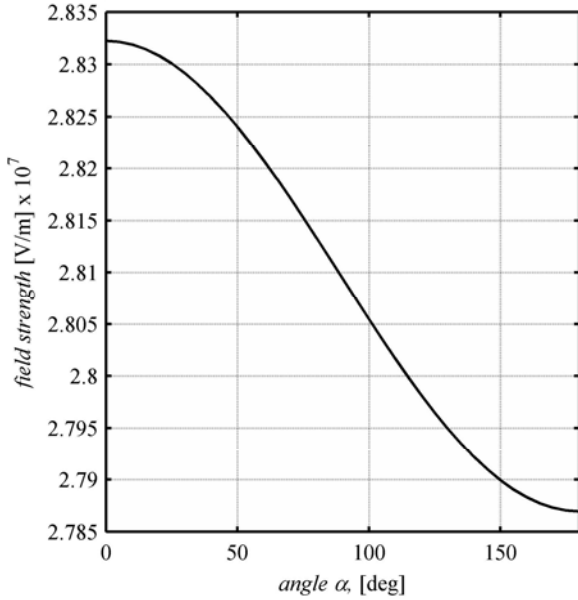


Fig. 5. Distribution of the field strength on the surface of the wire, $r_0=0,050$ mm

$$E_0 = 30,3\delta \cdot \left(1 + \frac{0,298}{\sqrt{r_0\delta}} \right), \quad (2)$$

where r_0 is the radius of the wire, cm, δ is the relative density of air, E_0 is evaluated in kV/cm.

Onset voltage of the discharge U_0 depends not only on radius r_0 , but also on the other geometrical dimensions of the system. For wire-plate electrode system this dependence involves the distance h from the center of wire to the plate [7]:

$$U_0 = E_0 r_0 \cdot \ln \left[\frac{2h}{r_0} \cdot \left(1 - \frac{r_0}{2h} \right) \right]. \quad (3)$$

Onset voltage in the system “a set of wires above the plate” depends also on the distance d between neighbour wires:

$$U_0 = E_0 r_0 \cdot \left[2\pi \cdot \frac{h}{b} - \ln \left(2\pi \cdot \frac{r_0}{b} \right) \right]. \quad (4)$$

Dependences of onset field strength E_0 and onset voltage U_0 on wire radius r_0 for values of variables $h=12$ mm, $b=15$ mm, $\delta=1$ are given in Table 1.

Table 1. Dependences of E_0 and U_0 on r_0

r , mm	E_0 , kV/cm	U_0 , V	
		wire-plate	wire set-plate
0,025	210,9	3620	5054
0,040	173,2	4430	6315
0,050	158,0	4876	7025
0,100	120,6	6605	9888

Approximate empirical equation of current dependence on voltage (volt-ampere characteristic) for wire set-plate electrode system may be written as follows [7]:

$$I_0 = 0,7\epsilon_0 k \cdot \left(1 + 1,12 \cdot \frac{b}{h} \right) \cdot \left[\pi \frac{r_0 E_0}{2h} \right]^2 \cdot \left[(\gamma + 1)^{1,8} - 1 \right] \cdot 10^6, \quad (5)$$

where I_0 is the linear current density, $\mu\text{A}/\text{m}$, ϵ_0 is electric constant, $\epsilon_0 = 8,85 \cdot 10^{-12}$ F/m, k is ion mobility, $k = 2,2 \cdot 10^{-4}$ $\text{m}^2/(\text{V}\cdot\text{s})$ for negative ions, γ is discharge parameter which depends upon the voltage and geometrical dimensions of electrode system:

$$\gamma = \left(\frac{U}{U_0} - 1 \right) \cdot \left(2\pi \cdot \frac{h}{b} - \ln \left(2\pi \cdot \frac{r_0}{b} \right) \right). \quad (6)$$

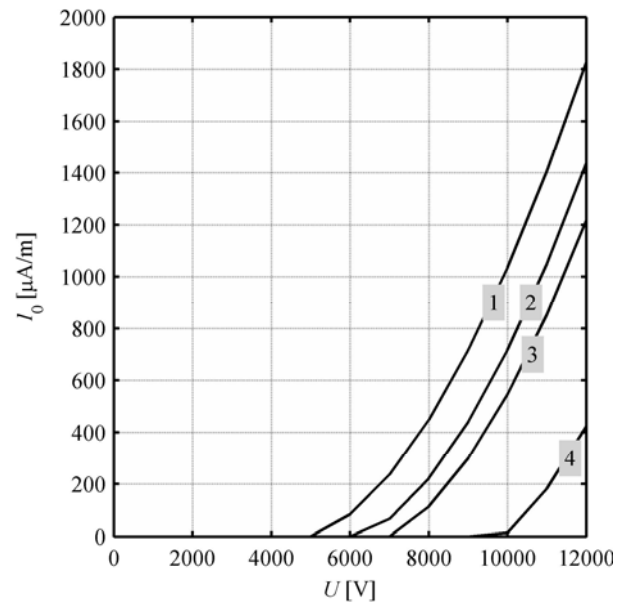


Fig. 6. Volt-ampere characteristics of wire set-plate electrode system: 1 – $r_0 = 0,025$ mm, 2 – $r_0 = 0,040$ mm, 3 – $r_0 = 0,050$ mm, 4 – $r_0 = 0,100$ mm

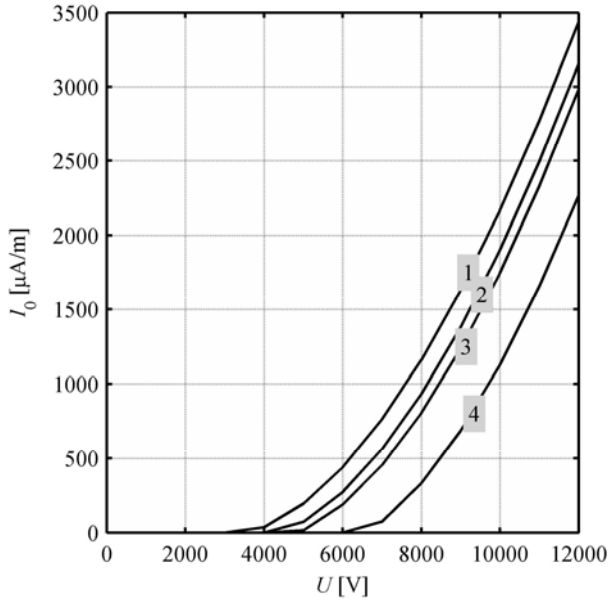


Fig. 7. Volt-ampere characteristics of wire-plate electrode system: 1 – $r_0 = 0,025$ mm, 2 – $r_0 = 0,040$ mm, 3 – $r_0 = 0,050$ mm, 4 – $r_0 = 0,100$ mm

Corresponding formulas for the wire-to-plane electrode system are the following:

$$I_0 = 2,3\varepsilon_0 k \cdot \left[\pi \frac{r_0 E_0}{2h} \right]^2 \cdot [(\gamma + 1)^{1,8} - 1] \cdot 10^6 \frac{\mu\text{A}}{\text{m}}, \quad (7)$$

$$\gamma = \left(\frac{U}{U_0} - 1 \right) \cdot \ln \left(\frac{2h}{r_0} \right). \quad (8)$$

Volt-ampere characteristics corresponding to $b = 15$ mm and $h = 12$ mm in wire set-plate electrode system are shown in Fig. 6. Values of onset voltage U_0 indicating the positions of the point on abscissa axis are given in Table 1. It is obvious that values of the voltage corresponding to the same values of the current increase considerably with increasing the radius of wire. This phenomenon depends on the increase of onset voltage with wire radius growth. Therefore it is desirable to use thin wires in corona field drying devices with minimum energy consumption. Similar characteristics for wire-to-plate electrode system with spacing $h = 12$ mm are presented in Fig. 7. Main difference between curves shown in Fig. 6 and Fig. 7 is almost 3-fold exceeding of current in wire-to-plane system in comparison with wire set-to-plane system at

the same value of voltage. For example, $I_0 = 1200 \mu\text{A/m}$ in the first system, and $I_0 = 450 \mu\text{A/m}$ in the second one at $U = 8000$ V and $r_0 = 0,025$ mm in both cases. So the wire-to-plane electrode system is more desirable to achieve the greater drying effect, and wire set-to plate system is preferable to minimize energy consumption. This conclusion corresponds with the research results of other authors [5].

4. Conclusions

Increasing of wire radius in wire set-to-plate electrode system moves away from the wire equipotential lines of electrostatic field. Variation of wire radius does not affect considerably the electric flux related to the wire. Increasing of wire radius causes the remarkable growth of onset voltage. The current of discharge corresponding to the fixed value of the voltage decreases with growth of wire radius in both electrode systems. Wire-to-plate electrode system is preferable to get the greater drying effect, and wire set-to plate electrode system is better to minimize the energy consumption.

5. References

1. Huang M., Lai F.C. Numerical Study of EHD-enhanced Water Evaporation. *Journal of Electrostatics*, Vol. 68, 2010, p. 364-370.
2. Reznikov M.A., Kolessov A., Koziol R. Electrohydrodynamic Enforcement of Evaporation and Gas Flow. *IEEE Transactions in Industry Applications*. Vol. 47, No 2, 2011, p. 1036–1042.
3. Basiry m., Esehaghbeygi A. Electrohydrodynamic drying of rapeseed. *Journal of Electrostatics*, Vol. 68, 2010, p. 360-363.
4. Lai F.C., Sharma, R.K. EHD-enhanced drying with multiple needle electrode. *Journal of Electrostatics*, Vol. 63, 2005, p. 223-237.
5. Lai F.C. A Prototype of EHD-enhanced Drying with Multiple Needle Electrode. *Journal of Electrostatics*, Vol. 68, 2010, p. 101-104.
6. Zhao L., Adamiak K. Numerical Simulation of the Electrohydrodynamic Flow in Single Wire-Plate Electrostatic Precipitator. *IEEE Transactions in Industry Applications*. Vol. 4, No 3, 2008, p. 683–691.
7. Vereshchagin I.P., Semenov A.V. *Elektricheskije Polja v Ustanovkach s Koronnym Razrjadom*. Moskva, MEI, 1984, 98 p.

OPTIMIZATION OF TRANSMISSION LINE PARAMETERS

Svetlana BERJOZKINA* **, Viktorija NEIMANE***, Antans SAUHATS* **

* Riga Technical University, Institute of Power Engineering, Latvia; ** JSC “Siltumelektroprojekts”, Latvia;

*** Vattenfall Research and Development, Sweden

Abstract: The transmission grid requires the new upcoming electrical connections, resulting in limited capacity of the existing overhead lines. One of the possible solutions of the problem is to build the new overhead lines and substation. Overhead lines designing are associated with several considerable technical, environmental and economical problems. The paper deals with the concept of optimization of the transmission line parameters. There is a real line design case with the main purpose to minimize the total invested capital and maximize net present value of the described competitive variants of overhead high voltage line construction.

Keywords: Design engineering, Pareto optimization, transmission lines.

1. Introduction

A considerable increase in electric power transmission as well as power consumption has been observed over the past twenty years. Furthermore, advanced transmission technologies were implemented, for example, underground and submarine XPLE cables; Gas Insulated Line (GIL); High Temperature Low Sag (HTLS) conductors as well as Flexible Alternating Current Transmission System (FACTS); High Voltage Direct Current (HVDC); real-time technologies [1]. It becomes necessary to optimize these technical solutions for the modernization of energy infrastructures; therefore, several technology options have led to the need to integrate the Smart Grid into the European electricity network.

Since the actual network is getting ready for Smart Grid solutions, the expansion of the transmission grid will be required both from national and international prospects. Thus, it is necessary to implement new transmission line projects in the operation of the grid.

There has not been a significant increase in new EHV lines over recent years, although most grid owners have invested heavily in increasing the capacity of existing lines. The total 380/400kV line length has increased by 3 percent (approximately 3,000 km) over the past 5

years. Main areas of expansion have been: Austria – completion of the 380kV ring to the south east of Vienna; interconnection between Greece and Italy; Spain – a line from Madrid to Aragon, which links with Portugal and the connection of wind farms; Sweden, submarine cable with Poland; UK, submarine cables to the Isle of Man and Northern Ireland [2].

The construction of a new line is a complex arrangement with necessary to fulfill different restrictions like a complex regulatory framework, public opposition, a high population density, intensive use of land, visual impact, environmental issues, grid issues, electromagnetic fields (EMF), difficult terrain and weather, and, of course, commercial problems [3]. Due to these issues many transmission expansion projects have been delayed or even canceled.

Designing of transmission lines is performed by solving an optimization problem with the main purpose of minimizing invested capital by taking into account numerous limitations such as thermal (allowable conductor temperature, load current), mechanical (conductor sag, mechanical tension) as well as environmental (climatic conditions, the impact of the electromagnetic field) limitations [4]. Besides, it is necessary to account for uncertainties and random factors, the random and uncertain nature of which generates the complexity of the formulating and solving the task of optimal designing of expensive power objects, in particular, transmission lines.

The most widely used methods of the transmission line design are based on the cost-benefit analysis and maximization of the net present value (NPV) [5] or minimization of invested capital subject to several restrictions.

There is other problem formulation, for example, in the case of minimizing the payback of a power line [6].

The invested capital for a new line can be assigned to one or more construction years, preceding the start of circuit operation, but generally it is assumed to be sustained in the construction year ($y=0$), where the main cost components are: cost for acquisition of rights of way; cost of acquisition of further portions of land from land owners; cost of purchase of all pieces of equipment

from manufacturers; costs for transportation of materials; costs of civil works; costs of onsite civil and electrical works for installation of equipment; contingency costs; costs for swathe reinstatement at the end of construction works; engineering and project management costs [7].

The optimization procedure can be simplified by using the several software techniques as [8], which provide an opportunity of fast transmission line design according to the installed limitations, climate and geographic conditions.

Since the parameters of a power line are chosen for the long-term perspective (up to 50 years and more), it can be stated that this fact relates to a considerable unpredictability of one of the most influential parameters – the long-term current capacity. For setting this current, there is a prognosis of loads as well as grid topology for the long-term also the repair and emergency modes must be described. In general, the worst-case approach is used, when the long-term current capacity values are largely high, thus increasing the line construction costs.

However, there have been important changes of line construction conditions over the recent years:

1) There are HTLS conductors. The use of HTLS conductors in the existing lines provides a considerably increase of capacity in the line. It becomes realistic to design a power line, with the perspective of replacing existing conductors with such HTLS conductors if necessary.

2) Smart Grid technologies are rapidly developing, thus, the necessity of utilizing worst-case approaches can be impugned in several cases.

This study considers the OHL design method, which is partially based on a stochastic approach and game theory criteria used for the final decision-making. The idea of proposed approach is based on five main stages: at the first designing stage there is the analysis of the development plans of the region the scenarios of loads growth are developed; at the second stage, there is a selection of the variety of competitive structure variants and OHL parameters, the most influential restriction is determined; at the third stage, there is an evaluation of worth of capital costs and NPV of all variants both when the restrictions are performed, or in the case of a disruption of one of them; at the fourth stage, the variety of the competitive decisions is constructed; the last stage describes an assessment of probability of conditions occurrence, which cause the restriction disruption, the consequences of a disruption and its technical and organizational prevention methods.

2. Theoretical background of the proposed optimization task formulation

In order to formulate the tasks of transmission line design taking into account the influence of random and uncertain factors, assume that:

- ✓ Company, the owner of OHL strives to minimize invested capital I_C and increase its revenues R_{ti} (the net cash flow i.e. cash inflow - cash outflow, for each year t_i of the planning period T , $T=m \cdot t_i$).

- ✓ Revenues R_{ti} and invested capital I_C of the company depends on the structure Σ_j and the parameters Π_j of the OHL chosen by this company. The structures Σ_j are described as a set of discrete variables (the number of wires per phase, the height and parameters of the standard towers, conductor area, mechanical and electrical parameters of the conductor etc). Each such structure is called alternative. Assume that N alternatives A_j are considered, $j=1, \dots, N$. The parameters Π_j are described by a set of continuous variables (the span lengths, coordinates for construction of the towers etc.).
- ✓ The freedom of choosing the structures and parameters of the company is limited. Let S_j be the set of all permissible structures and parameters for OHL and $s_j = \{\Sigma_j, \Pi_j\}$ as chosen combination of the structure and parameters, $s_j \in S_j$. The frontier of a space of permissible structures is determined by the inequalities that describe the technical and legislative factors and regulations.
- ✓ OHL functions under the influence of the ambient environment that is characterized by a set of random and uncertain parameters X_{ti} (the load current in a power line, the ambient temperature, the wind speed, the humidity ect). In general case, X_{ti} are changing in time. We assume that during each year t_i , X_{ti} are constant.

Due to the influence of random and uncertain factors, the revenues are also uncertain: in this case the scenario approach in combination with probabilistic variables can be used for solving the planning task. The uncertain information will be always modeled by a number of scenarios. For each scenario SC_n ($n=1, \dots, k$) we can declare that the revenues R_{tij} are the probabilistic values. Hence, we can write the following:

$$R_{tijn} = R_{tijn}(s_j, X_{tijn}) \quad (1)$$

Suppose that distribution functions that have the following form may be assigned to each combination of scenario SC_n and alternative A_j :

$$F_{tijn} = F_{tijn}(R_{tijn}(s_j, X_{tijn}) | SC_n, A_j) \quad (2)$$

If the distribution function is known, the expected value of the revenues for each year t_i , for each scenario SC_n and alternative A_j combination can be determined using the following equation:

$$E[R(s, X)] = \int_{\Omega} R(s, X) dF(R(s, X)), \quad (3)$$

where Ω – an integration area, which is limited by the existence space of the random parameters X . Frontier of the space of the allowable parameters and structures S_j is limited by restrictions:

$$FR(s_j, X) > 0. \quad (4)$$

In the equation (3) the Lebesgue-Stieltjes integral is used.

The knowledge of the expected values of the revenues allows finding the equation for the determination of the net present value (NPV), which serves as main criteria of an optimization:

$$NPV = -I_C + \sum_{i=1}^m \frac{E(R)}{(1+I)t_i} \quad (5)$$

where I_C – investment capital, which is the function of s_j .

Then the task for optimal planning can be presented in the following form:

$$s_{jn}^* = \arg \max \left(-I_C + \sum_{i=1}^m \frac{E(R)}{(1+I)t_i} \right) \quad (6)$$

where arg stands for “the argument for”; the subject of maximization; I is the discount rate.

Solving the task (6) will result in system’s structures and parameters s_{jn}^* that maximize NPV for the planning period T for all selected scenarios SC_n and alternatives A_j . For each combination SC_n and A_j the evaluation of NPV can be determined. Realizing the NPV maximization process the extended space s_{jn}^* is selected additionally with the purpose to determine alternatives and the values of parameters, which is closing to the frontier of the allowable space and beyond its limits, that can be stored. Such parameters R_i will be reviewed as the additional criteria of an optimization. Having as a result the NPV and R_i values for all combinations of scenarios and alternatives, we can get the matrix, which is formulated in Table 1. After that it remains to choose the best of the alternatives. In the given set of alternatives there are even the solutions that lead to violation of the most impacting restriction.

Each of the columns of Table 1 may contain Pareto set; if the indexes R_i consider the second optimization criteria (note that in general case the number of these indexes can be numerous).

The final decision-making based on the decision set in Table 1 in common case is a complex task, for solving which several methods are proposed [9]. When dealing with the specific tasks, as it will be illustrated below, the significant simplifications may occur.

Table 1. Expected values of Net Present Value and Restriction Indicators R_i

Alternatives	Scenario 1	...	Scenario k
A_1	$NPV_{11} R_{11}$...	$NPV_{1k} R_{1k}$
.....
A_N	$NPV_{N1} R_{N1}$...	$NPV_{Nk} R_{Nk}$

3. The selection of the scenarios and alternatives

Due to impact of the uncertainties, there is a need to consider several scenarios for instance for the load increase ratio. After selecting the development scenarios of power system, the numerous alternatives are examined with the purpose of choosing the optimization parameters S_j (see part 2).

The following parameters can be subject of optimization: the nominal voltage of a line, the mechanical and electrical characteristics of a conductor (conductor diameter, cross-section, the coefficient of linear expansion, modulus of elasticity, the allowable conductor temperature as well as the load current, the reduced specific load, linear loads, destructive loads), conductor type, quantity in a phase; tower type, geometry, height, the allowable wind, weight and clearance spans; the insulator type, the damper type; the lightning wire type, the earthing and lightning protection systems; the optimal line route.

Thus, to achieve the best technical and economical solution of the transmission line design, a large number of optimization variables must be taken into account. As mentioned previously, OHL is operated under the influence of the ambient environment that is characterized by a set of random and uncertain parameters X_{ij} . The impacting parameters which describe the OHL operating conditions are the following: climate conditions (ambient temperature, wind speed, wind direction, solar radiation, air humidity, ice thickness); the capacity of the transmission line in the future power system; the forecasted electricity consumption; expansion of the existing interconnection systems; environmental impacts.

To simplify a very complex and labor-consuming procedure of revenues calculation for huge number of the scenarios and of the alternatives combinations, the filtration task of the limited number of the competitive variants may be formulated and solved. Until recently this task was solved using the accumulated experience, which is decrypted in the different guidances, glossaries, descriptions of the standard cooperative solutions and rules as well as the powerful software tools are used, which give the opportunity to form significantly smaller initial set of the competitive alternatives.

Additional diminution of a number of the competitive variants may be achieved by using simplified optimization task form. In this case the task is formulated as following:

$$S_{ij} \approx \arg \min I_C, \quad (7)$$

The equation (7) is much easier to use than (6). Using the simplified formulation of the problem, the obviously non- competitive variants of a project are discarded. Note that considered problem (7) does not take into account the number of important factors (for example, the power losses in a line) and it can be implemented only for reducing the number of the options, which are subject to further consideration with the use (6).

4. The main restrictions during the optimization

The search for the best alternatives of OHL has to take into account several restrictions: thermal (allowable conductor temperature, load current), mechanical (conductor sag, mechanical tension), electrical (insulation levels) and environmental (climatic conditions, the impact of the electromagnetic field) [4]. During designing of the OHL it is necessary to provide adjusted maximum capacity (allowable load current), the ground clearance as well as the clearance to the crossed objects, and the distributions of electric and magnetic fields. In respect that a large number of optimization parameters are discrete, it can be argued that for solving the optimization task formulated in part 2 (6), it is necessary to perform investment calculations for all possible combinations of parameters s_j corresponding to the area that meet the restrictions: $s_j \in S_j$.

In general case, if one of the existing restrictions is not fulfilled, the appropriate alternative is not taken into account. In contradiction to that this study allows to take into consideration the alternatives violating these restrictions, because the development and implementation of new technical possibilities (different monitoring systems as well as existence of HTLS) are giving the additional opportunities to avoid the restrictions violation regimes.

5. Revenues and NPV

The NPV calculation is a difficult and very time-consuming task. There are difficulties that are determined by the following main factors:

- ✓ The price of OHL elements must be taken into account, which will be defined “experimentally” by conducting negotiations with the stakeholders;
- ✓ There is a lack of common recognized methodology of revenue, which occurs in result of the OHL construction calculation.

In this study let us accept the following hypotheses:

- The OHL construction is defined by the necessity of grid development for providing the planned consumption growth and energy transit;
- The construction projects are realized by a coalition, which consist of two companies – C_1 . The owner of existing network and the owner of new objects C_2 , in particular a new power line;
- The new construction provides receiving the additional annual revenue of transmission grid, which is equivalent to the normalized percentage (generally, 7-12 % [2]) of the average cost of energy transit;
- The dividing of total additional revenue R_{ad} and additional revenue of each company R_{C1} and R_{C2} is based on the basis of Shapley distribution, which in case of two players is elementary simple [10]:

$$R_{C1} = R_{C2} = \frac{R_{ad}}{2} \quad (8)$$

In this study suppose that additional income of the transmission grid is distributed among the existing network and newly built objects in the equivalent

proportion, and then we get the amount of annual income:

$$R_{inc} = \left(\frac{I_l}{I_s} \right) \frac{R_{ad}}{2}, \quad (9)$$

where

$$R_{ad} = \beta (E_{an} + E_{antr}), \quad (10)$$

where I_s – annual investment in a transmission grid; I_l – investment in the OHL construction; E_{an} – the annual growth of the power consumption; E_{antr} – transit energy growth; β – rate of the cost of energy.

6. Case study

Consider an example of using the described methodology of optimization of the transmission line design is based on a real project, which will be realized in Latvia.

Power system analysis for scenarios of development of the region resulted in the following alternatives for the new transmission line: 110 kV power line with the maximum current of 1200 A (optimistic scenario 1) or 800 A (pessimistic scenario); 330 kV transmission line with the maximum current of 2000 A (optimistic scenario 2) or 1500 A (pessimistic scenario).

The optimization task of a structure and parameters of new transmission line was formulated. After searching the optimal solutions by using of the software for OHL design, 20 alternatives were selected, formed by realizing the different combinations of examined towers and conductors (see Fig. 1).

For simplifying the posed task at the first stage instead of the NPV maximization according to the part 5 there is the minimization of invested capital. In the final comparison of the options the time-consuming task with the NPV criteria will be used.

For simplifying evaluation of the environment impact, the calculations were done [11]. Verification of the restrictions was simplified due to existence of these results in the evaluation of alternatives. Thus, as the electric field may not satisfy the necessary requirements, the described below solution was proposed for solving the posed problem.

Therefore, the following groups of combinations were selected: V1 and V10; V11 and V20 mean that there are the traditional type conductors for both 110 kV and 330 kV circuits; V6 ÷ V9; V16 ÷ V19 – there are the HTLS conductors for both 110 kV and 330 kV circuits; V2 ÷ V5; V12 ÷ V15 – there are the traditional type conductors with a combination with the HTLS conductors for 110 kV and 330 kV circuits (see Fig. 1).

Fig. 1 reflects the optimum solution results of two-objective optimization by implementing Pareto approach [12], where I_C (p.u.) is the invested capital and E (kV/m) is the strength of the electrical field. As a result, the competitive variants are V6, V7, V9, V10, V15, V17, V19 and V20.

The resulting values of the optimization criteria are summarized in Table 2 (only competitive alternatives are left for farther consideration). Analysis of the table reveals the following:

1. If the “classical” problem formulation, namely maximization of the NPV, complying with all the restrictions would be used, one of the alternatives V10 would be chosen. The final decision would be taken using one of the criteria in [4].
2. If the constraint violation is allowed one of the alternatives V17 or V19 should be chosen.

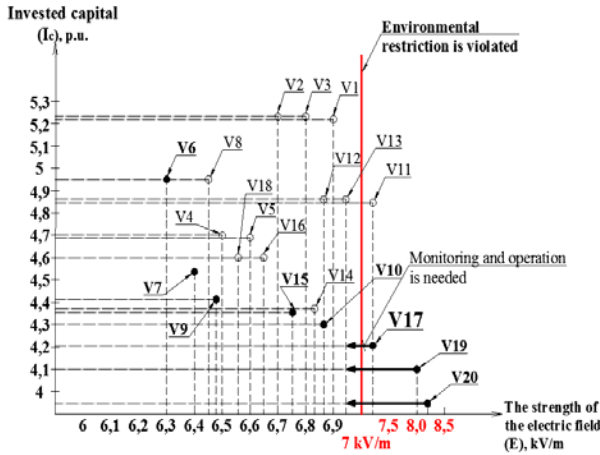


Fig. 1. The diagram of Pareto set for the combination variants

Table 2. Expected Worth of Net Present Value and Restriction Indicators R_i

Alternatives	Optimistic scenario 1	Pessimistic scenario 2
	NPV_{II}/E_{II}	NPV_{II}/E_{II}
V10	4.7 // 6.9	5.4 / 5.0
V17	6.2 // 7.1	5.33 / 5.6
V19	6.7 // 8.0	5.7 / 7.3

The risks of appearance of conditions leading to changes in operation in its turn leading to additional economic losses were estimated in order to make the final decision. Violation of limits for the strength of electric field for the considered example for Latvian climate can arise at the maximum air temperature of +35°C and the maximal load current. The combination of these two conditions has very low probability, for the alternative V10 it is 0,01, while for alternative V17 0,000001 (both probabilities are estimated considering optimistic scenario). After taking into consideration the probabilities mentioned above the alternative V17 was chosen as a final decision for real life realization.

7. Conclusions

The new methods are required able to facilitate decision-making resulting in reduced invested capital and power losses, and improved reliability and power quality.

The problem of optimization of the design of transmission lines is a multi-criteria optimization task with a large number of state and decision variables. This task must be formulated taking into consideration possible influence of random and uncertain parameters. Solution of such problem is associated with considerable mathematical, computational and informational difficulties.

Implementation of the multi-criteria optimization partially based on stochastic approach provides the possibility to consider even the alternatives with constraint violations, which with some additional measures can represent the most cost effective solution.

8. Acknowledgment

This work has been supported by the European Social Fund within the project «Support for the implementation of doctoral studies at Riga Technical University».

9. References

1. A. L' Abbate, G. Migliavacca, T. Pagano, A. Vafeas. Advanced transmission technologies in Europe: a roadmap towards the Smart Grid evolution. Proceedings of International Conference “IEEE PowerTech – 2011”, Trondheim, 2011. p. 1-8.
2. ICF Consulting. (2002, Oct.). Unit Costs of constructing new transmission assets at 380kV within the European Union, Norway and Switzerland, Final Report.
3. P. Buijs, D. Bekaert, S. Cole, D. Van Hertem, R. Belmans. Transmission investment problems in Europe: Going beyond standard solutions. Energy Policy, 2011, doi:10.1016/j.enpol.2011.01.012.
4. Svetlana Beryozkina, Antans Sauhats, Edvins Vanzovichs. Climate Conditions Impact on the Permissible Load Current of the Transmission Line. Proceedings of International Conference “IEEE PowerTech – 2011”, Trondheim, 2011. p. 1-6.
5. King Fahd University of Petroleum and Minerals: Chapter 7 Net Present Value and Other Investment Criteria.
6. Блок В.М., Electrical networks and systems, М.: Высшая школа, 1986, p. 430. [in Russian]
7. Roberto Benato, Domenico Napolitano. Overall cost comparison between cable and overhead lines including the costs for repair after random failures. ELECTRA, N° 265, December 2012. p. 4-13.
8. PLS-CADD™ (Power Line Systems - Computer Aided Design and Drafting).
9. János Fülöp. Introduction to Decision Making Methods.
10. M. Zima-Bockarjova, J. Matevosyan, M. Zima, L. Soder. Sharing of Profit from Coordinated Operation Planning and Bidding of Hydro and Wind Power. IEEE Trans. on Power Systems, vol. 25, no.3, pp.1663-1673, Aug. 2010.
11. Мисриханов М.Ш., Иостсон Ю.А., Рубцова Н.Б., Токарский А.Ю., The electromagnetic parameters of overhead power transmission lines. Certificate of official registration of computer software, No. 2006613744, October 27, 2006. // Official Bulletin of the Federal Service of Intellectual Property, Patents and Trademarks – No. 1 (58) – М. – Federal State Institution “Federal Industrial Property Institute”, – 2007. [in Russian].
12. V. Pareto, Cours D'Economie Politique, Vol. I and II. F. Rouge, Lausanne, 1896.

MODELLING AND ANALYSIS THE COMPENSATION OF POWER FLUCTUATION OF WIND POWER FARM

Rimantas Pranas DEKSNYS, Aldas STANKEVIČIUS
Kaunas University of Technology, Department of Electric Power Systems, Lithuania

Abstract: The model of the power system has been made for the research into the compensation for power generation by wind power plants. Possibilities for compensation for the power fluctuations in wind power plants through combined heat and power plants (CHP) and solar power plants have been examined. Compensation values for power generation over a period of one month in different year seasons have been found.

Keywords: Wind power generation, power compensations, combined heat and power plants.

1. Introduction

Rapidly increasing numbers of wind and solar power plants generating renewable energy as well as variable and only partly predictable power generation and electricity production by these plants raises problems to power systems and electrical power market because makes it difficult to continuously ensure a balance between electrical power generation and demand, the exchange of power generation and trade in electric power with neighbouring countries [1-2].

Successful integration of wind and solar power plants into power systems requires not only for increased power transfer throughput of power systems but also for improved technologies and ability to duly control and adjust variable power generation by wind power plants. Use of combined heat and power plants (CHP) for the stabilization of wind power production supports principles of the distributed generation. For this reason, local CHPs can be used for balancing power in the supply-demand system with varying power production by wind power plants. Normal operation of a combined heat and power plant requires for guaranteed combining of heat demand as the operation of the power plant depends on the heating load. In case of a balancing operation, CHP is capable of generating power at the specifically required time, when this is necessary, i.e., under low electric power production by WPP. When the need for electric power is being satisfied by wind power plants, and combined heat and power plants stand idle,

heat demand can be covered from boilers. Otherwise put, if thermal store is used, the entire heat produced by CHP can be used straight away or stored and used at a later date [3].

2. Model of the system

Model under research is comprised of wind power farm WPP, regional farm of solar power plants PVP, combined heat and power plant CHP used for compensation for the power fluctuations in the former two, and loads of electric power and heating systems of the region concerned. For the purpose of calculations regarding wind power plants, the installed capacity of 30 MW was selected. To satisfy the total demand for heating, the boiler has been modelled with the thermal store (see Fig. 1). The type of fuel used by combined heat and power plant and the boiler – natural gas. Simulation of wind and solar power farms used measurement data of wind speed, total solar radiance and temperature for one hour time-steps recorded by the Lithuanian Hydrometeorological Service (LHMT) in January – June of the year 2011 at Šilutė power plant. Measurements of wind speed were taken at Šilutė hydrometeorological station at the height of 10 m above ground surface. Requirement for power generation in January in the region under research amounts for 15.9 GWh of electric power and 12.1 GWh of heating energy, whereas in June – 13.6 GWh of electric power and 2.3 GWh of heating energy. The selected need for electric power and heating energy in the region under consideration is realistic and consistent with the time of data being modelled.

Need for heating of the power system is comprised of the following: heat required for heating, heat required for hot water, and losses incurred through piping system, recalculated based on the outdoor temperature for the period under research (as of LHMT).

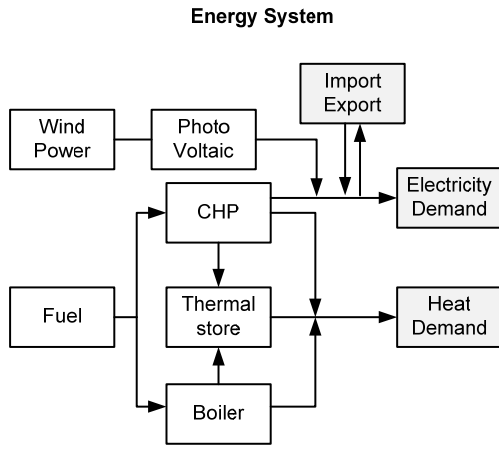


Fig. 1. Schematic representation of the modelled power system

With reference to the suggested model of the system, calculations of the compensation for the power fluctuations were calculated using “energyPRO” software.

3. The methods for calculation of power generation by solar and wind power plants

Power generation by solar and wind power plants can be calculated using the following methods:

Method of solar calculation (Photovoltaic).

The electricity production from a Photovoltaic module, P_{pv} , can be expressed as follows :

$$P_{pv} = P_{max} \cdot \frac{I_s}{I_{STC}} \cdot [1 - \gamma_s \cdot (T_{cell} - T_{STC})]; \quad (1)$$

where P_{max} is the installed capacity, I_s is the solar radiation, I_{STC} is the radiation at standard conditions, γ_s is the temperature coefficient for module efficiency, T_{cell} is the operation cell temperature, T_{STC} is the cell temperature at standard conditions.

The operation cell temperature is calculated by the following formula [4]:

$$T_{cell} = T_{at} + I_s \cdot \left(\frac{NOCT - 20^\circ C}{800W / m^2} \right); \quad (2)$$

where T_{at} is the ambient temperature, $NOCT$ is the Nominal Operating Cell Temperature.

Hereto come losses from the pv-module to the grid, λ_{misc} , such as miscellaneous PV array losses and other power conditioning losses.

The power production at grid becomes:

$$P_{elec} = P_{pv} \cdot (1 - \lambda_{misc}); \quad (3)$$

where P_{elec} is the electricity production to the grid from the photovoltaic plant.

Method of wind warm calculation.

Calculated wind speed at hub height [5]:

$$WS_c(t) = WS_m(t) \cdot \left(\frac{H_h}{H_m} \right)^\alpha; \quad (4)$$

where $WS_c(t)$ is the wind speed calculated at time t , $WS_m(t)$ is the wind speed measured at time t , H_m is the Height of measurements, H_h is the Hub Height, α is the Hellmann coefficient.

Calculation of production at time t :

$$P(t) = PC(WS_c(t)) \cdot P_{Max} / P_{MaxPC}; \quad (5)$$

where $PC(WS_c(t))$ return then power from the power curve based on the calculated wind speed at hub height and linear interpolation on power curve, P_{Max} is the Max Power stated, P_{MaxPC} is the Max power value found in power curve. $P(t)$ is the production at time t .

Based on the data of LHMT, and using above mentioned methods, it was estimated that, in January, operating under its average capacity of 8.52 MW, WPP is supposed to generate 6.34 GWh of electricity, resulting in its installed capacity efficiency of 28.41 %. Fig. 2 depicts varying loads and power generation by power plants. In the same period of time, the regional farm of solar power plants PVP operating under its average capacity of 0.95 MW is supposed to generate 0.71 GWh of electricity, resulting in its installed capacity efficiency of as low as 3.16 %. In June, operating under its average capacity of 7.17 MW, WPP is supposed to generate 5.16 GWh of electricity, resulting in its installed capacity efficiency of 23.88 %. In the same period of time, the regional farm of solar power plants PVP operating under its average capacity of 21.05 MW is supposed to generate 4.55 GWh of electricity, resulting in its installed capacity efficiency of 21.05 %.

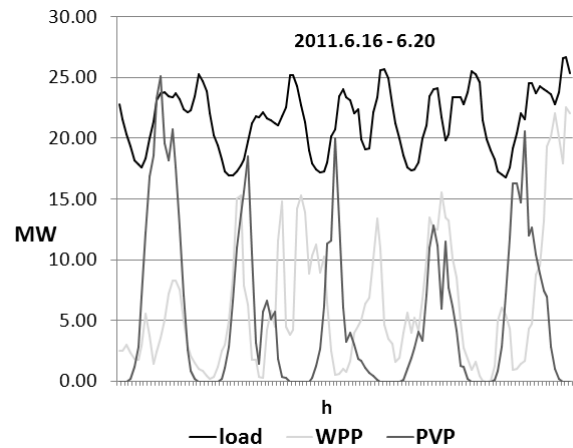


Fig. 2. Fluctuations in power generation of solar and wind power farms

The obtained results show that the fluctuation in average power generation by wind power farms in January was minor when compared to that in June, whereas the average power generation by solar power plants increased by more than six times in June.

4. Investigation the compensation for power fluctuations

To estimate the compensation for the power fluctuations in wind power farm, based on the suggested model of power system, the research was undertaken involving the data of individual periods of time of measurement. Priorities of power generation have been selected for producers as follows: 1 – wind power farm, 2 – regional farm of solar power plants, and the combined heat and power plant (CHP) operating depending on the fluctuation of power generation by former two, considering the electricity and heat demand. The rest of the heat, depending on the demand, is generated in 30 MW boiler. For the balancing of power generation by the combined heat and power to be more effective, a thermal store with capacity of 83.4 MWh is modelled.

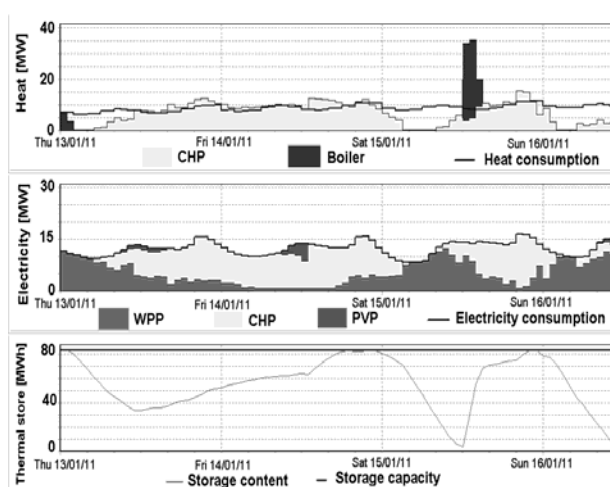


Fig. 3. Compensation for fluctuations in power generation by wind power farm

Analysis of the obtained results (Fig. 3, Table 1) shows that in January, the combined heat and power plant in compensation for fluctuations in power generation by the regional power system (RPS) and operating in accordance with the electricity and heat demand, has produced 8.93 GWh of electricity and the same amount of heat. The rest of the heat, 3.11 GWh, depending on the system demand, has been produced by the boiler. The installed capacity efficiency of the combined heat and power plant amounted for 40.03 % in January. In January, the simulated regional power system is expected to produce 15.63 GWh of the total electricity required for the system, and the total amount of heat necessary for the system.

The total electricity input amounted for 0.35 GWh, and output – for 0.31 GWh of the power system (PS) under consideration. It was estimated, that the simulated RPS in compensation for power fluctuations in wind power farm, has produced 98.1 % of the total electricity needed by the system in January.

In June, while operating under the same regime, the combined heat and power plant has produced 2.27 GWh of electricity and the same amount of heat.

Table 1. Production of electricity and heat

Demand and Production (MWh)	January		June	
	RPS	PS	RPS	PS
Heat demand	12047.6	-----	2277.5	-----
Electricity demand	15942.6	-----	13546.8	-----
Production:				
Wind power farm - "WPP"	6091.4	249.5	4998.6	160.5
Solar power farm - "PVP"	607.1	98.8	3625.7	920.8
CHP electricity	8934.8	-----	2274.1	-----
CHP heat	8934.8	-----	2274.1	-----
Boiler	3112.8	-----	3.4	-----
Total electricity	15633.3	-309.3	10898.4	-2648.4
Total heat	12047.6	-----	2277.5	-----

Consequently, the installed capacity efficiency of the combined heat and power plant amounted for 10.52 %. This decrease was determined by low heat demand characteristic to this season. In June, boiler has produced only 3.4 MWh of heat.

The total electricity input amounted for 1.1 GWh, and output – for 2.65 GWh of the power system under consideration. The total power generated in June by simulated RPS in compensation for power fluctuation in wind power farm amounted for 10.9 GWh, which is equal to 80.4 % of the electricity needed by the energy system under consideration.

In summary of research results, during cold weather season, the combined heat and power plant sufficiently compensates for power fluctuations in wind power plants however in summer time, due to reduced heat demand, its ensured compensation is not sufficient. In June, the increased power generation by solar power plants poorly serves for compensation of fluctuations in power generation by the regional power system, making it necessary to find additional ways for balancing power generation such as integration of electro mobiles or hydrogen production via electrolysis [6].

5. Conclusions

1. It was estimated, that in January, the simulated RPS in compensation for the power fluctuations in wind power farm, has produced 98.1 % of the total electricity needed by the system, out of which 56.0 % has been produced by the combined heat and power plant.
2. It was estimated, that in June, the simulated RPS in compensation for power fluctuations in wind power plants, has generated only 80.4 % of the electricity needed by the system, out of which 26.7 % has been produced by the solar power plants.
3. The combined heat and power plants are suitable for compensation of power fluctuations in wind power plants only in cold weather season, however in

summer time they turn out to be inefficient due to reduced heat demand.

4. Our research found that the increased power generation by solar power plants in hot weather season poorly serves for compensation of fluctuations in power generation by wind power plants.

6. References

1. Deksnys R. P., Staniulis R., Šulga D. Possibilities of wind power plants penetration into electric power system // *Electrical and Control Technologies ECT - 2008: 3rd International conference*. Kaunas: Technologija, 2008. ISBN 978-9955-25-484-3. p. 27-31.
2. Andriuškevičius R., Šulga D., Bikulčius R. Estimation of variation of wind power generation and its impact on performance of the Lithuanian power system // *Power Engineering/The Lithuanian Academy of Sciences*, ISSN 0235-7208. 2004. No. 3. p. 45–50 .
3. Kuhi-Thalfeldt R., Valtin J. Combined heat and power plants balancing wind power // *Oil Shale*, 2009, Vol. 26, No. 3 Special, pp. 294–308 ISSN 0208-189
4. Luque A., Hegedus S. *Handbook of Photovoltaic Science and Engineering*. Books:Wiley, 2003, ISSN 0471491969, p. 1168.
5. Ernst B. Short – Term Power Fluctuations of Wind Turbines from the Ancillary Services Viewpoint. Institut für Solare Energieversorgungstechnik Königstor 59 D-34119 Kassel Germany, <http://www.iset.uni-kassel.de>
6. Support Schemes for Renewable Energy – A comparative analysis of payment mechanisms in the EU. <http://www.ewea.org>.

SIZING OF THE DC CHOPPER PARAMETERS FOR THE GRID-TIED CONVERTER EFFICIENT OPERATION

Česlovas RAMONAS, Vytautas ADOMAVIČIUS
Renewable Energy Centre at Kaunas University of Technology, Lithuania

Abstract: Power conversion processes in the small-scale grid-tied photovoltaic power plant are analysed in the paper. Methodology for determination of the DC chopper inductor's inductance and capacity of power storage capacitor is presented. Mathematical model of the photovoltaic power plant power conversion system is comprised on basis of MATLAB/SIMULINK library SimPowerSystem. Impact of the inductor's inductance and capacity of power storage capacitor to operation of the power conversion system is investigated. Results of the investigation are presented in the conclusions and curves obtained by means of simulation.

Keywords: PV system, DC chopper, inductor, power storage capacitor, grid-tied inverter.

1. Introduction

Electronic converters for the grid integration of small-scale power systems based on the renewable energy sources continue to be one of the main objects of investigation in the field of power electronics. It can be ascertained by looking over the titles of scientific papers in the journals of power electronics and renewable energy [1, 2, 3 and many other]. Unmitigated majority of the scientific prognoses predict further rapid development of renewable power systems in upcoming decades. Development of microgrids [4] and hydrogen power systems also will give additional impulses which will have positive impacts to the increase of cumulative number and capacity of converters used in small-scale power systems including stand-alone systems in remote regions [5].

In this paper we continue investigation of the grid-connected power converter which includes the grid-tied inverter and the DC chopper (or a number of DC choppers connected in parallel). The DC choppers are installed between the primary power source and input terminals of the grid-connected inverter. The primary power source(s) can be the primary energy converters (PV array, wind turbine, FC), a power storage system or any other DC power source of relevant capacity. So, this

converter may have one or more inputs through the DC choppers and one output through the grid-connected inverter. The DC choppers and their number in the converter could be installed as changeable modules of different parameters and supplied according to the requirements of customer.

Results of preceding investigations of the mentioned above converter were published in a number of papers – [6, 7, 8] and other. Results of construction of the methodology for determination of the DC chopper parameters and investigation of the impact of inductor's inductance and capacity's of power storage capacitor to operation of the power conversion system are presented in this paper.

2. Object and goals of the research

Object of research of this paper is a small-scale renewable power system with grid-tied converter, which includes DC chopper, is depicted in Fig. 1. The DC chopper is used for stepping up the input voltage. Power circuits of the proposed small-scale grid-tied PV system consist of the three main units: the PV array, the step up DC chopper and the grid-tied inverter. The PV array has 30 PV modules E_1-E_{10} , $E_{11}-E_{20}$ and $E_{21}-E_{30}$ connected in parallel and shunted by the diodes V_1-V_{30} . The step up DC chopper consists of the shorting transistor V_t , the inductor L_d and flyback diode V_{at} . The main elements of the inverter are the transistors V_1-V_4 with FR diodes $V_{at1}-V_{at4}$ and two reactors L_{f1} -and L_{f2} . Control pulses for the inverter (ICP) and control pulses for the DC chopper transistor V_t (SCP) are generated in the control unit, which is not shown in Fig. 1. Electric load of the PV power system is controlled over the transistor of shorting circuit V_t . DC chopper converts the variable output DC voltage of photovoltaic array to the DC voltage suitable for the grid-tied inverter [6, 7]. The grid-tied inverter transfers energy produced by the photovoltaic array to the grid. Such system has some positive peculiarities [6, 8]. It can be exploited in any power sources having variable DC voltage in the input of the converter.

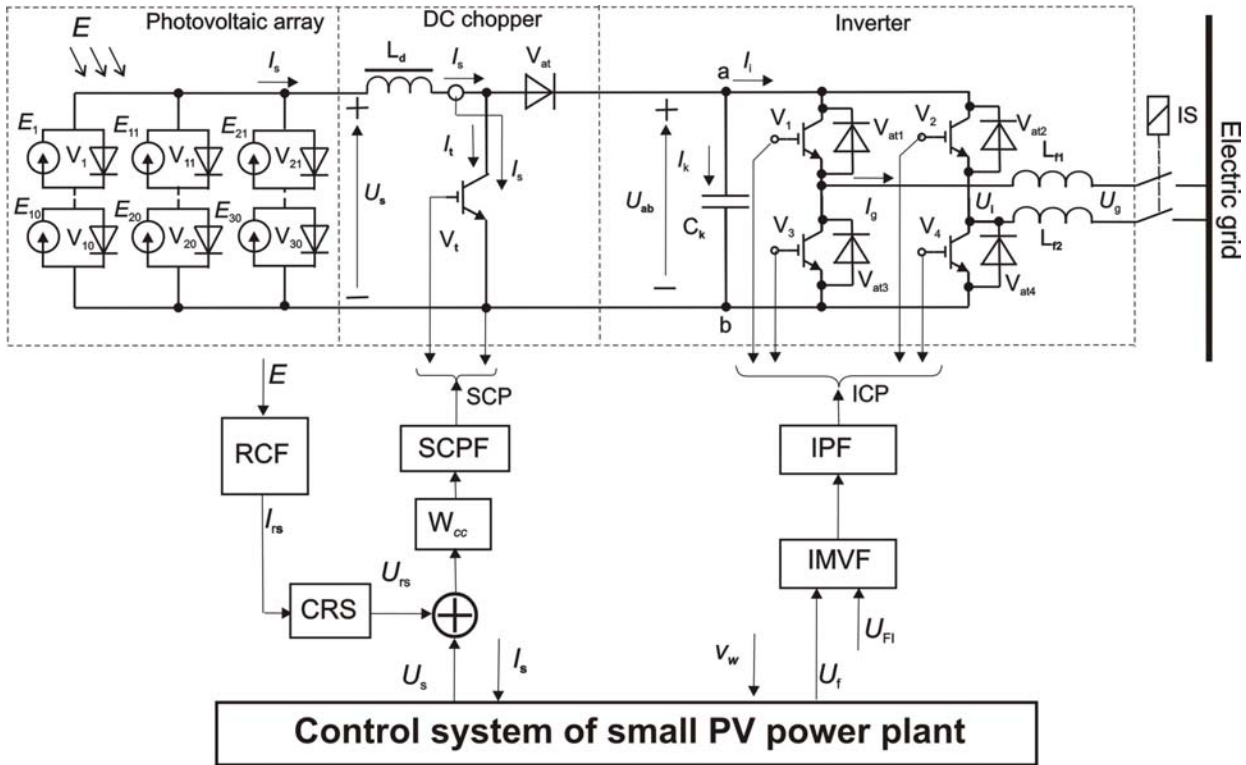


Fig. 1. Simplified electrical scheme of the small scale grid-tied PV power system

Goal of the study is investigation of impact of energy storage elements' parameters, i. e. inductance L_d and capacitance C_k , on the operation quality of the converter and developing of the methodology for calculating of the inductance and capacitance values. Mathematical description of the PV power circuits will be made by using one-line equivalent scheme for average values of the system. Adequacy of the received equations was checked by means of mathematical modelling and using MATLAB/SIMULINK programme package.

3. Parameters of the LC chain

Operation quality of the PV converter significantly depends on the parameters' of energy storage inductor and capacitor. Mathematical description of the PV converter circuit can be simplified by using the one-line equivalent scheme for average values, i. e. neglecting PW operation of inverter circuit (Fig. 2).

Operation of the power converter depends on the DC chopper operation and consists of two intervals: short-circuiting, i. e. energy accumulation in the inductor L_d (switch S_1 is ON) and energy transferring from inductor L_d to the inverter input (switch S_1 is OFF). The amount of accumulated energy can be changed by changing duty cycle of the DC chopper. The duty cycle of DC chopper is expressed as follows:

$$\gamma = \frac{\tau}{T_c}, \quad (1)$$

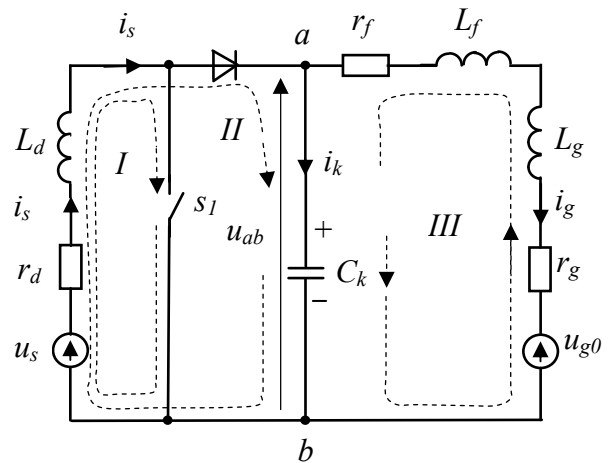


Fig. 2. Equivalent scheme of the small scale grid-tied PV power system

where γ - duty cycle, τ - the time interval when transistor V_t conducts, T_c - the chopping period, $f_c = 1/T_c$ - the chopping frequency. As it is shown in Fig. 2, three contours here can be marked out dependently on the switch S_1 state. First and third contour operates independently one from another when switch S_1 is ON. Mathematical description for the first contour can be expressed as follows:

$$\frac{di_s}{dt} = \frac{1}{L_d}u_s - \frac{r_d}{L_d}i_s. \quad (2)$$

Solution of the equation (2) is presented in the previous paper of authors which is submitted for publication [9]. The equations for calculation of the inductance L_d values are transcendental. Therefore inductance of the

inductor can be calculated by using the approach methodology based on repeated computations. Minimal values of the inductor inductance and capacity of the capacitor can be calculated by using the following formulae:

$$L_{dm} = \frac{2\gamma T_c P_{s \max}}{I_{s \max}^2}, \quad (3)$$

$$C_{km} = \frac{2(1-\gamma)T_c P_{s \max}}{U_{ab}^2}. \quad (4)$$

where $P_{s \max}$ is the maximal power value of PV source, $I_{s \max}$ – the maximal current value of PV source, U_{ab} – the DC voltage on the inverter input.

More detailed analysis and investigations have to be performed on purpose to formulate more convenient methodology for calculation of the mentioned above parameters.

The mathematical description for the third contour can be expressed as follows:

$$\begin{cases} -L_i \frac{di_g}{dt} - r_i i_g + u_c = u_{g0}; \\ C_k \frac{du_c}{dt} = i_k; \\ i_k = -i_g. \end{cases} \quad (5)$$

where u_{g0} – the rectified no load voltage of the grid, C_k accumulating capacitor, $r_i = r_g + r_f$ – the active resistance of the inverter circuit, r_g – the active resistance of the grid, r_f – the active resistance of the filter, $L_i = L_g + L_f$ – the inductance of the inverter's circuit, L_g – the inductance of the grid, L_f – the inductance of the filter, φ_m – phase of the modulation voltage.

The following equations are received taking Laplace transform and considering that $u_{g0} = k_{si} \cdot U_{g0fm} \cdot \cos(\varphi_m)$:

$$\begin{cases} -L_i [s i_g(s) - I_g(0)] - r_i i_g(s) + u_c(s) = \frac{u_{g0}}{s}; \\ u_c(s) = -\frac{i_g(s)}{s C_k} + \frac{U_c(0)}{s}. \end{cases} \quad (6)$$

Solutions of the equations set can be expressed as follows:

$$i_g(s) = I_g(0) \frac{s + b_0}{s^2 + 2\beta s + \omega_0^2} = I_g(0) \frac{s + b_0}{A(s)}; \quad (7)$$

$$u_c(s) = \frac{U_c(0)(s^2 + b_1 s + b_2)}{s A(s)}, \quad (8)$$

where $\beta = r_i / 2L_i$ is the decrement factor, $\omega_0^2 = 1 / L_i C_k$ – natural radian frequency and parameters b_0, b_1, b_2 have to be expressed in this way:

$$b_0 = (U_c(0) - u_{g0}) / (I_g(0) \cdot L_i); \quad b_1 = 2\beta - \frac{I_g(0)}{U_c(0) C_k};$$

$$b_2 = \omega_0^2 - \frac{U_c(0) - u_{g0}}{U_c(0) C_k L_i}.$$

Roots of the nominator polynomial $A(s)$ can be calculated as follows:

$$s_{1,2} = -\beta \pm \sqrt{\beta^2 - \omega_0^2} = -\beta \pm \sqrt{D}. \quad (9)$$

Three cases are available depend on the value of discriminant D : the root of the nominator polynomial will be real negative numbers when $D > 0$; it will be only one root when $D = 0$; and the root will be complex numbers when $D < 0$.

Current $i_g(t)$ and voltage $u_c(t)$ as the time functions can be deduced taking the inverse Laplace transform. The 2, 5 ÷ 7 equations are valid for $0 \leq t \leq \tau = \gamma \cdot T_c$, i. e., during the interval of short-circuiting.

Second and third contours operate when switch S_l is OFF. The energy is being transferred to the inverter input. Mathematical description for this interval is more complicated and can be expressed as follows:

$$\begin{cases} \frac{di_s}{dt} = \frac{1}{L_d} \cdot (u_s - u_{ab}) - \frac{r_d}{L_d} \cdot i_s; \\ \frac{di_g}{dt} = \frac{1}{L_i} \cdot (u_{ab} - u_{g0}) - \frac{r_i}{L_i} \cdot i_g; \\ \frac{du_c}{dt} = \frac{1}{C_k} \cdot i_k; \\ U_c(0) = u_{g0} = k_{si} \cdot U_{g0fm} \cdot \cos(\varphi_m); \\ u_{ab} = u_c; \\ i_k = i_s - i_g. \end{cases} \quad (10)$$

Operation of the scheme (Fig. 2) in the interval of inverting is similar to the operation described above for the III contour; however the power flows from the inductor into the third contour in this case. The LC chain operates in the same manner as it was described above.

Impact of the LC chain parameters to the quality of the system operation will be carried out by using the library SimPowerSystem of digital simulation programme package MATLAB/SIMULINK where models of real power electronics' devices are presented.

4. Mathematical model of the grid-tied PV power system

Mathematical model of small-scale grid connected PV power plant is worked out on the grounds of authors' previous investigations [6–8, 9]. Minimal values of the DC chopper inductor inductance L_{dm} and capacity of the power storage capacitor C_{km} are calculated according the formulas (3) and (4). The recommended values of the same parts of the DC chopper (L_{dr} and C_{kr}) are calculated according the following formulas given below:

$$L_{dr} = (1.2 \div 2.2) L_{dm}, \quad (11)$$

$$C_{kr} = (5.5 \div 16) \cdot C_{km}. \quad (12)$$

Scheme of the PV power system model is depicted in Figure 3. The elaborated model of the PV system has the same units as the real PV system: models of PV array, grid-tied inverter and electric grid, which has its component models of the grid no load voltage U_{g0} , equivalent resistance and inductance of the grid – R_g

and L_g . The model of the PV system also has devices I_g , $\sim U_{g0}$, $\sim U_g$, P and Q for measurement parameters of the system. Results of simulation are being recorded into the Workspace. Virtual oscilloscope (Scope) is used for the expeditious watching of the system's parameters.

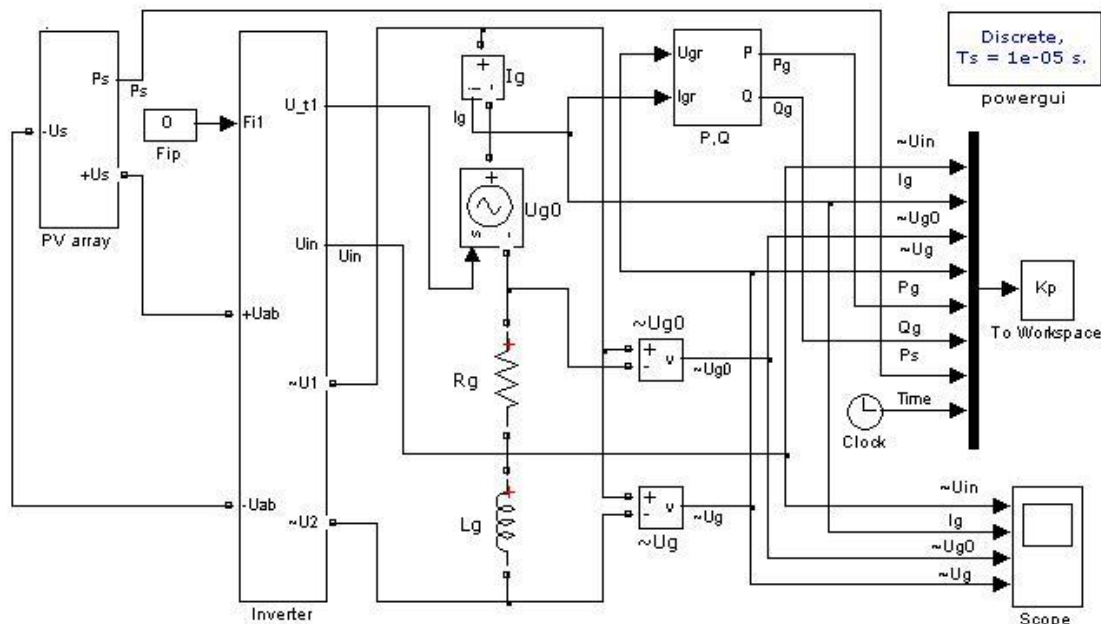


Fig. 3. Scheme of the grid-tied PV power system model

5. Results of the research and discussion

The main results regarding the PV power plant operation quality dependently on the value of capacity of power storage capacitor and the value of DC chopper inductor's inductance L_d , which was kept constant, are reflected in the presented below curves (Fig. 4 – Fig. 6) received by means of simulation.

Figure 4 shows that size of the capacity of power storage capacitor does not have significant impact to the DC power on the terminals of the inverter and active power supplied to the grid from the PV power plant. However, DC voltage on the inverter input terminals strongly depends on the capacity of power storage capacitor. Therefore value of the capacity should be properly chosen in order to avoid unnecessary potentially harmful overvoltages.

Figure 5 shows, that size of the capacity of power storage capacitor has considerable impact into the THD of the grid voltage and inverted current as well. THD of the grid voltage has a clear minimum at the value of the capacity of power storage capacitor $0.5 \cdot 10^{-4}$ F. But THD of the inverted current at the same point is high (about 20 %). This aspect shows that capacity of the power storage capacitor and inductance of the DC chopper inductor as well has to be determined taking into consideration all possible positive and negative consequences and impacts for the efficiency of power conversion system operation.

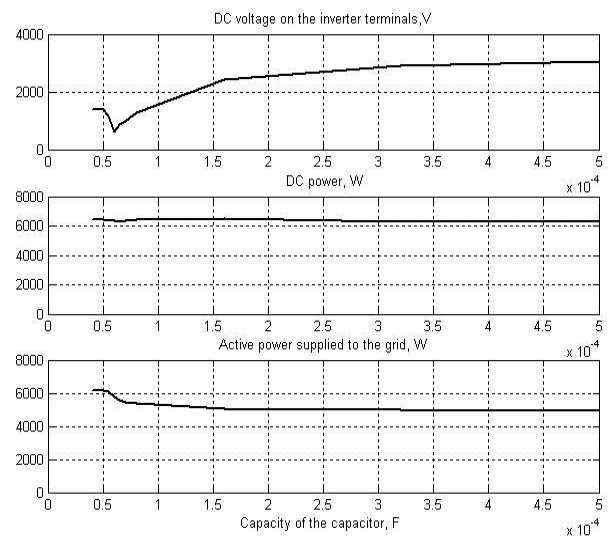


Fig. 4. DC voltage and power on the inverter terminals, active power supplied to the grid versus capacity of the capacitor when inductor's inductance $L_d = 0.015$ Hn

Figure 6 shows that efficiency of the converter depends more on the capacity of capacitor at the low values of the capacity. Efficiency of the converter at the high values of the capacity is not sufficiently good. But there are some possibilities to correct the efficiency of converter by means of adjusting the angle of the inverter modulation voltage what will be disclosed in further discussion of the simulation results.

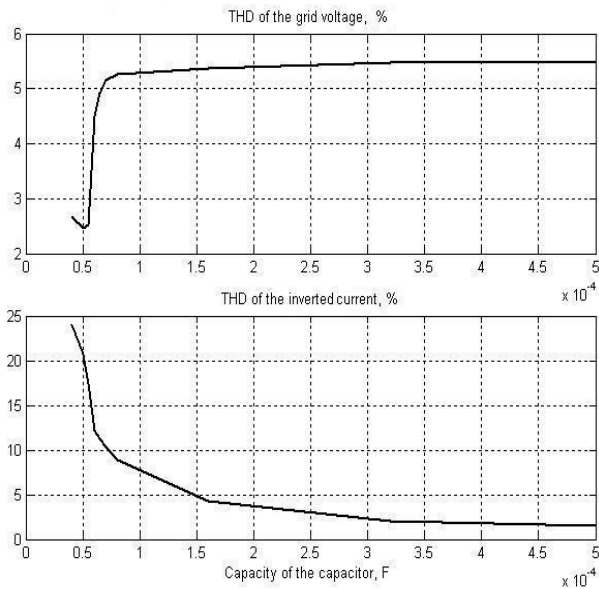


Fig. 5. THD of the grid voltage and inverted current versus the capacity of capacitor when inductor's inductance $L_d = \text{const.} = 0.015 \text{ Hn}$

Figure 7 shows that adjusting of the angle of the inverter modulation voltage can give some positive results. The DC voltage on the input terminals of the inverter can be significantly decreased at the proper values of the angle of the inverter modulation voltage (> 18 degrees). It allows making more favourable operation conditions for the converter. Meanwhile impact of the inverter modulation voltage angle to the DC power and active power supplied to the grid is less significant because the operation of MPPT in the model.

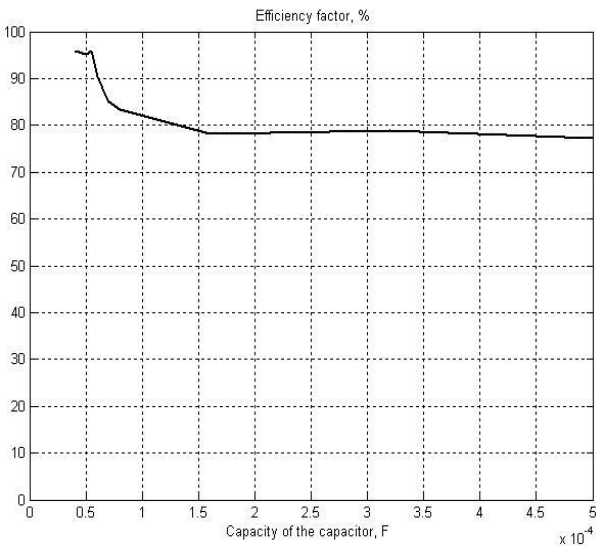


Fig. 6. Efficiency of the converter versus the capacity of capacitor when inductor's inductance $L_d = \text{const.} = 0.015 \text{ Hn}$

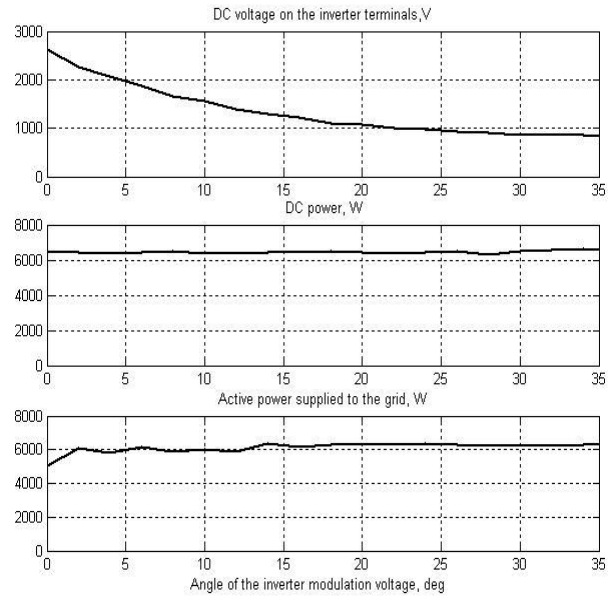


Fig. 7. DC voltage and power on the inverter terminals, active power supplied to the grid versus the angle of the inverter modulation voltage when inductor's inductance $L_d = \text{const.} = 0.015 \text{ Hn}$ and capacity of capacitor $C_k = \text{const.} = 0.0002 \text{ F}$

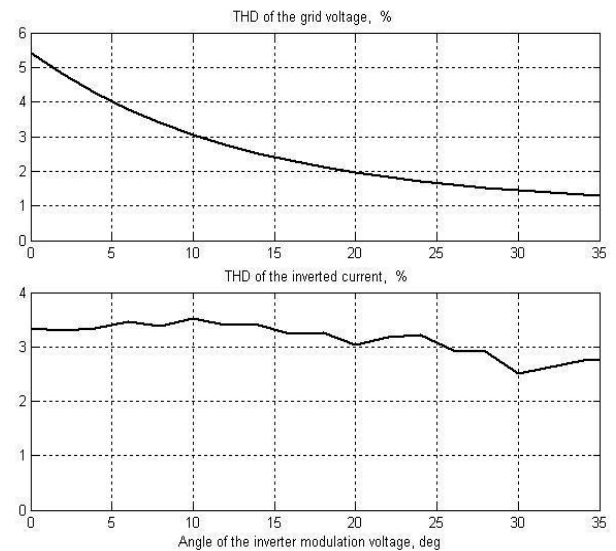


Fig. 8. THD of the grid voltage and inverted current versus the angle of the inverter modulation voltage when inductor's inductance $L_d = \text{const.} = 0.015 \text{ Hn}$ and capacity of capacitor $C_k = \text{const.} = 0.0002 \text{ F}$

Figure 8 shows impact of the angle of the inverter modulation voltage to the THD of the grid voltage and inverted current. Curve of the grid voltage THD allows finding that distortion of the grid voltage can be significantly reduced by choosing proper values of the inverter modulation voltage angle. THD of the inverted voltage is less dependent on the inverter modulation voltage angle.

Figure 9 confirms that the efficiency of the power converter depends on the inverter modulation voltage angle and this dependency can be used for the correction of the converter efficiency.

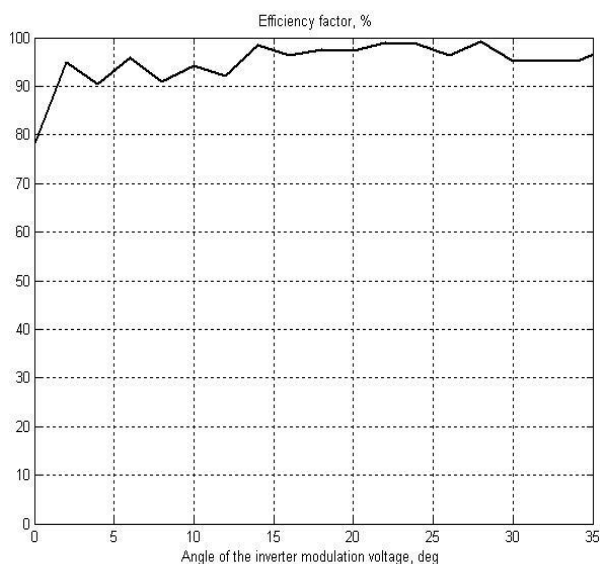


Fig. 9. Efficiency of the power converter versus the angle of the inverter modulation voltage when inductor's inductance $L_d = \text{const.} = 0.015 \text{ Hn}$ and capacity of capacitor $C_k = \text{const.} = 0.0002 \text{ F}$

The performed simulations confirmed that quality of the power conversion system operation depends on the DC chopper inductor's inductance and capacity of the power storage capacitor. Proper choice of these parameters paves the way to the qualitative operation of the power conversion system. The quality parameters of the power conversion system operation also can be improved by the proper adjusting of the angle of inverter modulation voltage.

6. Conclusions

1. The methodology is proposed for determination of the minimal and recommended values for the DC chopper's inductor inductance and capacity of the power storage capacitor.
2. Mathematical analysis of the grid-tied PV power system's equivalent scheme (third contour) disclosed that periodic and exponential modes of operation of the grid-tied inverter are possible. Further researches by means of simulation revealed that more qualitative operation of the converter is received in case of the periodic mode.
3. As it was disclosed by the simulation (Fig. 4), when the capacity of power storage capacitor increases, the DC voltage on terminals of the grid inverter increases very considerably; however this shortage can be effectively removed by means of adjusting the angle of the inverter modulation voltage in respect of the grid voltage phase angle what is shown in Fig. 7.
4. Results of researched PV power conversion system confirmed the possibility of achieving proper

parameters of the system operation quality by means of adjusting the angle of the inverter modulation voltage in respect of the grid voltage phase angle (Fig. 8, Fig. 9.).

7. References

1. F. Blaabjerg, R. Teodorescu, M. Liserre, and A. V. Timbus, "Overview of Control and Grid Synchronization for Distributed Power Generation Systems", *IEEE Trans. Industrial Electr.*, vol.53, no. 5, p.p. 1398–1409, Oct. 2006.
2. M. Lisere, T. Sauter and J. Y. Hung, "Future Energy Systems. Integrating Renewable Energy Sources into the Smart Power Grid Through Industrial Electronics", *IEEE Industrial Electronics Magazine*, p.p. 18–37, March 2010.
3. J. M. Carrasco, L. G. Franquelo, J. T. Bialasiewicz et. al., "Power-Electronic Systems for the Grid Integration of Renewable Energy Sources: A Survey", *IEEE Trans. Industrial Electr.*, vol.53, no. 4, p.p. 1002–1016, August 2006.
4. Адомавичюс, В.Б.; Харченко, В.В. Особенности и проблемы построения микросетей. // Труды 8-ой Международной научно-технической конференции *Энергоснабжение и энергосбережение в сельском хозяйстве*, 16-17 мая 2012, М. Часть 5, Нанотехнологии и инфокоммуникационные технологии. М: ГНУ ВИЭСХ, 2012 С. 50-56.
5. Guozhen Hu, Shanxu Duan, Tao Cai, Changsong Chen. Sizing Analysis of PV System with VRB Storage // *Electronics and Electrical Engineering*. – Kaunas: Technologija, 2012. – No. 2(118). – P. 43–48.
6. Ramonas Č., Adomavičius V. Grid-tied converter with intermediate storage chain for multipurpose applications, *Elektronika ir Elektrotechnika (Electronics and Electrical Engineering)*, no. 7, p.p. 15–20, 2011.
7. Ramonas Č., Adomavičius V. Impact of DC/DC converter parameters on operation of solar power conversion system, in *Proc. of the 6th international conference on Electrical and Control Technologies (ECT 2011)*, Technologija, p.p. 321-324, 2011.
8. Ramonas Č., Adomavičius V. Research of the Reactive Power Control Possibilities in the Grid-tied PV Power Plant, *Elektronika ir Elektrotechnika (Electronics and Electrical Engineering)*, vol. 19, no. 1, pp. 31–34, 2013.
9. Ramonas Č., Adomavičius V. Research of the Converter Control Possibilities in the Grid-tied PV Power Plant, *Elektronika ir Elektrotechnika (Electronics and Electrical Engineering)*, submitted in February 2013.

COMPUTER MODELING OF THE FIELD IN MULTI-ELECTRODE CORONA SYSTEM WITH IONIZED AND NON-IONIZED AREAS

Ričardas BARČIAUSKAS, Stasys ŽEBRAUSKAS
Kaunas University of Technology, Lithuania

Abstract: Multi-electrode corona systems are often used in electric field technologies, such as heat and mass exchange processes and charge transfer procedures. Results of computer modeling of the field in three-electrode corona system represented by two parallel plane electrodes and a wire between them are discussed there. The area of electric flux related to the wire and to the one of plates is occupied by corona field and there is the electrostatic field without the space charge in the rest area. In the first stage of an analysis the solution of the electrostatic field in all the area is determined by the method of complex potential and the equation of separatrix dividing the field into the area with the flux between the wire and the plate and with the flux between plates is derived. In the second stage the first area is simulated as corona field and the second one is represented as electrostatic field. Results of modeling are presented in table and graphical form.

Keywords: separatrix, electrostatic field, corona field.

1. Introduction

Two-electrode systems consisting of ionizing electrode, such as wire, needle or the other one with small radius of surface curvature, and a non-ionizing electrode are often used in many applications of corona field. Multi-electrode systems of more complicated structure are used too, and more complex methods are needed for their analysis.

An original numerical method is proposed for solving the differential equations that describe the corona field with ionized and non-ionized areas [1]. The procedure is based on the use of a special approximation algorithm for non-linear differential operators. It enables the computation of the spatial distribution of the electric field and of the charge density in the electrode system consisting of cylinder, a grounded plate and an emitting wire between them. The assumptions made for the derivation of the mathematical model are similar to those commonly employed for the study of plain corona fields.

A cylindrical triode charger for unipolar diffusion charging of aerosol particles is designed, constructed, and evaluated in [2]. Analytical dependence of discharge current on the voltage and dependence of particle charge on their diameter are derived. This charger has low diffusion and space charge losses due to the short column charging zone, and is a low complexity and inexpensive system.

The field of corona triode consisting of a set of parallel wires, a grounded plane electrode and parallel rods between them is analyzed in [3] using the finite-element and boundary element method combined with the method of characteristics. The distribution of field strength, space-charge density and current density, also the discharge current can be controlled by changing the grid voltage and configuration of electrode system.

Publications [4] and [5] are the further development of ideas given in [1]. The boundary-element method is employed for analyzing the electrostatic field distribution generated by a typical arrangement, consisting of a wire-type corona electrode and an ellipse-profile non-ionizing electrode [4]. The computed results pointed out the effect of various parameters on the uniformity of the electric field near the ionizing element and at the surface of the grounded rotating roll electrode. Results of field computation are represented by field-line plot consisting of two areas: the area with the space charge around the corona wire, and the area without the space charge in the rest part of computation area. These areas are separated by separatrix, i.e. by the line of zero field strength. Our main idea is the following: if we have two areas (one with electric flux related to the wire and another with the flux between two other electrodes) and if the separatrix between these areas is determined we use this information to compute corona field in the first area and electrostatic field in the second one. This idea is based on the assumption that the space charge of corona field does not change the position of separatrix. Assumption employed there isn't so strict as the Deutsch's assumption used by numerous researches [6].

2. Procedure of numerical analysis

An object of our analysis is electrostatic and corona field in the electrode system "the wire between two parallel plane electrodes with different potentials" (Fig. 1).

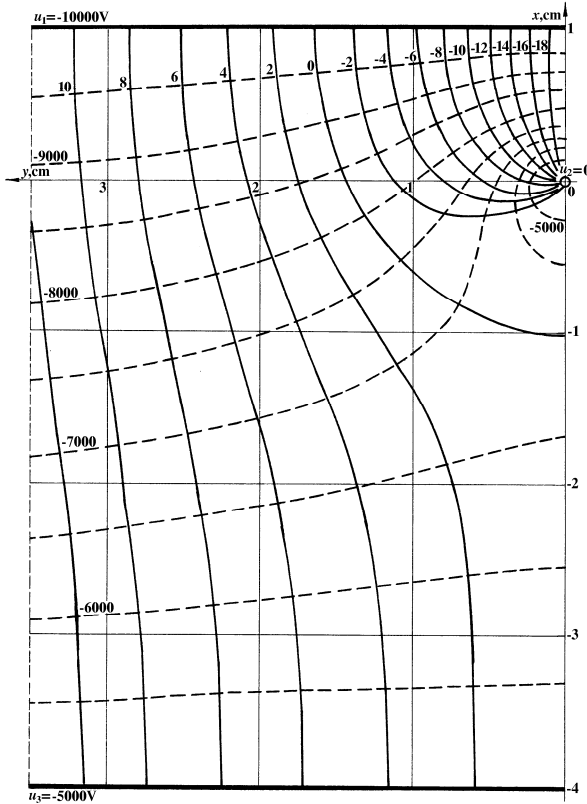


Fig. 1. Configuration of the electrode system under study. Distances are given in cm

Analysis of electrostatic field in the system is performed using the method of complex potential [7]. Equipotential and field lines shown in Fig. 1 correspond to the following values of parameters: distances from the centre of wire to the upper and the lower planes are 10 mm and 40 mm, radius of the wire is 0,025 mm, values of electrode potentials are $u_1 = -10000$ V, $u_2 = 0$, $u_3 = -5000$ V. There are two areas in the field: area occupied by electric flux related to the wire and the area with the flux between plane electrodes. An equation of separatrix which is a boundary line between these two areas is derived there.

An algorithm of the field computation is described in [8]. Finite-difference method is proposed to solve the system of equations in the first area and Laplace's equation in the second one. Polar system of coordinates is used to compute the corona field in the first area because the field is strongly inhomogeneous, and Cartesian system of coordinates is employed to compute the Laplacian field. Equality of potentials of the polar and rectangular grids in the nodes of separatrix is established by solving the system of equations consisting of the equation of separatrix and equations of grid lines as it is shown in [9].

System of corona field equations [8]

$$\begin{cases} \operatorname{div} \mathbf{E} = \rho / \varepsilon_0, \\ \mathbf{E} = -\operatorname{grad} u, \\ \operatorname{div} \mathbf{J} = 0, \\ \mathbf{J} = \rho k \mathbf{E}. \end{cases} \quad (1)$$

is solved iteratively by reducing it to the Poisson's equation and the equation of continuity [10]:

$$\operatorname{div} \operatorname{grad} u = -\rho / \varepsilon, \quad (2)$$

$$\operatorname{grad} \rho \cdot \operatorname{grad} u = \rho^2 / \varepsilon. \quad (3)$$

Procedure of iterative numerical solution of corona field equations (2) and (3) and of Laplace's equation is based on the Kaptzov's assumption [5] stating that corona field strength on the surface of the wire electrode is equal to the value determined from the Peek's formula and space charge density on the wire surface is being varied until this requirement is met.

3. Results of analysis

Distribution of the electric field strength on the axis of symmetry ($y = 0$) is given in Fig. 2. The field is an electrostatic one in the interval $-40 \text{ mm} \leq x \leq -10 \text{ mm}$, and it is of corona field mode in the interval $-10 \text{ mm} \leq x \leq +10 \text{ mm}$. It is equal to 0 in the point $x = -10 \text{ mm}$ as shown in Fig. 1. Value $E = 211,32 \text{ kV/cm}$ (modulus) in the point $x = r_0 = 0,025 \text{ mm}$ corresponds to that determined from Peek's formula ($E_0 = 210,9 \text{ kV/cm}$). The strength of corona field in the point $x = r_0 = 0,025 \text{ mm}$, $y = 0$ equals to 211,32 kV/cm. The value of the electrostatic field strength in this point determined by formulas of [7] is 545,61 kV/cm. Corresponding quantities for the point $x = h_1 = 10,0 \text{ mm}$, $y = 0$ are 11,84 kV/cm and 2,45 kV/cm. These results qualitatively prove the conclusions made for wire-to-plane electrode system in [11] where analysis of the field is based on the use of Deutsch's assumption: corona space charge reduces the field at the surface of emitting electrode (the wire), and amplifies the field at the surface of non-emitting electrode (the plate). This corona field property is emphasized by the fourth equation in (1).

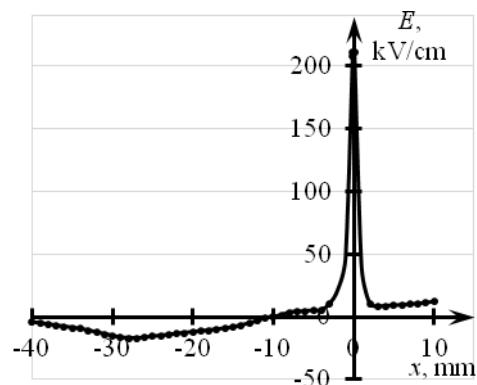


Fig. 2. Distribution of the field strength $E(x)$ on the axis of symmetry

Distribution of the potential function $u(x)$ on the axis of symmetry ($y = 0$) is presented in Fig. 3. Potential function equals to -5000 V at the $x = -h_2 = -40,0$ mm, approaches to 0 at $x = \pm r_0 = \pm 0,025$ mm, and equals to -10000 V at $x = h_1 = 10,0$ mm.

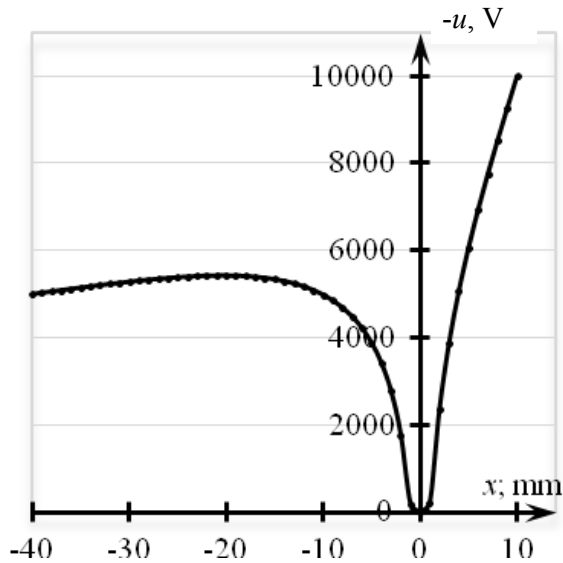


Fig. 3. Distribution of the potential function $u(x)$ on the axis of symmetry

Distribution of the field strength $E(y)$ on the surface of the upper plane electrode ($u_1 = -10000$ V) is given in Fig. 4. Similarly as in Fig. 2 corona field corresponds to the interval $0 \leq y \leq 16,45$ mm (see Fig. 1), and for all values in the interval $16,45 \text{ mm} \leq x \leq 40$ mm the field has no space charge. Coordinate $y = 16,45$ mm denotes the position of separatrix point on the surface of this plane electrode.

Distribution of the field strength $E(\alpha)$ and space charge density $\rho(\alpha)$ on the wire surface is shown in Fig. 5 and 6. Values of the functions $E(\alpha)$ and $\rho(\alpha)$ are presented in Table 1 because of small variation of these functions with the angle. The value of 1,3 % for variation of the field strength on the surface of the emitting electrode corresponds to the mentioned Kaptzov's assumption.

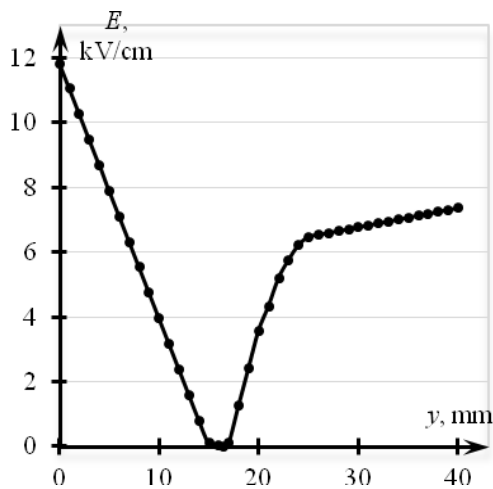


Fig. 4. Distribution of the field strength $E(y)$ on the surface of plane electrode $x = 10 \text{ mm} = \text{const}$

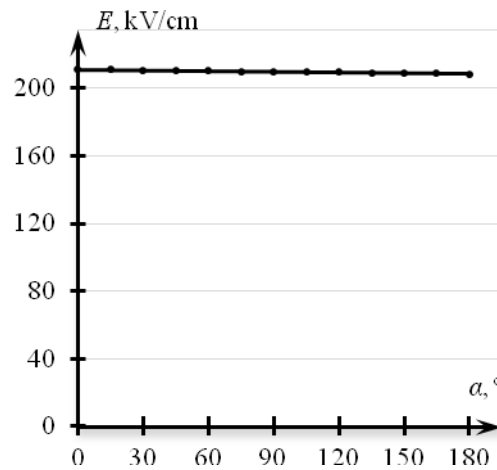


Fig. 5. Distribution of the field strength $E(\alpha)$ on the surface of the wire

Current density J can be determined from the fourth equation of the system (1) by using the values of E and ρ (Table 1). Linear current density I_0 can be determined as an integral

$$I_0 = 2r_0 \cdot \int_0^\pi J(\alpha) d\alpha. \quad (4)$$

Obviously, current between the wire and the lower plane electrode is equal to zero due to zero value of electric flux between these electrodes.

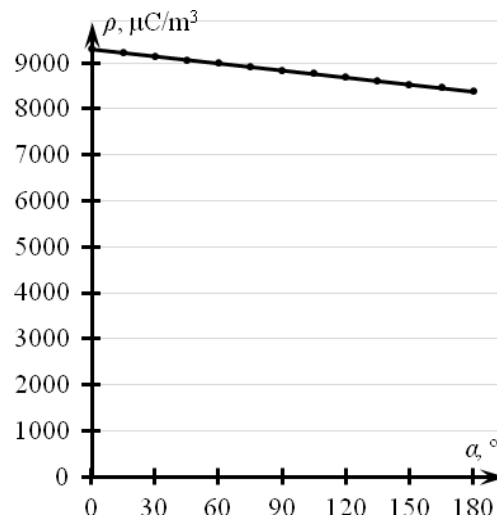


Fig. 6. Distribution of the space charge density $\rho(\alpha)$ on the surface of the wire

4. Conclusions

1. Area of the field occupied by the electric flux related to the electrode with small radius of surface curvature and determined by electrostatic approach corresponds to the area of corona field with distribution of current density vector.
2. Coordinates of points on the upper plane electrode and on the axis of symmetry with zero field (points of separatrix) strength coincide with that determined by an electrostatic approach.

3. There is no current between the wire and the third electrode. This electrode can be used as control electrode managing the discharge current between the wire and the first electrode.

Table 1. Distribution of the field strength and charge density on the surface of the wire

α , deg	E , kV/cm	ρ , $\mu\text{C}/\text{m}^3$
0	211,32	9302,10
15	211,09	9225,99
30	210,86	9149,88
45	210,63	9073,77
60	210,4	8997,66
75	210,17	8921,55
90	209,94	8845,44
105	209,71	8769,33
120	209,48	8693,22
135	209,25	8617,11
150	209,02	8541,00
165	208,79	8464,89
180	208,56	8388,78

5. References

1. Caron A., Dascalescu L. Numerical Modeling of Combined Corona-Electrostatic Fields // *Journal of Electrostatics*, Vol. 61, Iss. 1, May 2004, p. 43–55
2. Intra P. Corona Discharge in a Cylindrical Triode Charger for Unipolar Diffusion Aerosol Charging // *Journal of Electrostatics*, Vol. 70, Iss. 1, Febr. 2012, p. 136–143.
3. Deng X., Adamiak K. The Electric Corona Discharge in the Triode System // *IEEE Transactions on Industry Applications*, Vol. 35, No 4, July/August 1999, p. 767–773.
4. Rafiroiu D., Morar R., Atten P., Dascalescu L. Premises for the Mathematical Modeling of the Combined Corona-Electrostatic Field of Roll-Type Separators // *IEEE Transactions on Industry Applications*, Vol. 36, No 5, Sept./Oct. 2000, p. 1260–1266.
5. Dumitran L. M., Dascalescu L., Atten P., Notingher P. V. , Computational and Experimental Study of Ionic Space Charge Generated by Combined Corona-Electrostatic Electrode Systems // *IEEE Transactions on Industry Applications*, Vol. 42, No 2, March/April 2006, p. 378–384.
6. Amoroso V., Lattarulo F. Deutsch Hypothesis Revisited // *Journal of Electrostatics*, Vol. 63, Iss. 6–10, June 2005, p. 717–721.
7. Mikšta J., Žebrauskas S. Analysis of the Electric Field in Three-Electrode System with Corona Discharge // *Materials science. Proceedings of 4th International Conference on Electrostatics Elstat 90*, Wroclaw, 1990, Vol. 16, No. 1–3, p. 287– 292.
8. Barčiauskas R., Žebrauskas S. Boundary Conditions for Combined Corona and Electrostatic Field Analysis in Multi-Electrode Systems // *The 6th International Conference on Electrical and Control Technologies ECT 2011*, Proceedings, Kaunas, Technologija, 2011, p. 264–267.
9. Barčiauskas R., Virbalis J. A., Žebrauskas S. An Electrostatic Approach to the Numerical Simulation of Combined Corona and Electrostatic Field in Three-Electrode System // *Electronics and Electrical Engineering*, 2012, No 6 (122), p. 105–108.
10. Barčiauskas R., Virbalis J. A., Žebrauskas S. Numerical Analysis of Combined Corona and Electrostatic Field in Multi-Electrode Systems // *The 7th International Conference on Electrical and Control Technologies ECT 2012*, Proceedings, Kaunas, Technologija, 2012, p. 235–238.
11. Vereshchagin I.P., Semenov A.V. *Elektricheskije Polja v Ustanovkach s Koronnym Razrjadom*. Moskva, MEI, 1984, 98 p.

PARAMETER ESTIMATION OF DC MOTOR

Aurelijus PITRĖNAS, Andrius PETROVAS
 Vilnius Gediminas Technical University, Lithuania

Abstract: Currently, manufacturers rarely provide motor parameters, but they are needed for designing electric drive control systems. Thus it is necessary to be able to identify them. This paper presents an approach of DC motor model parameter identification from start and stop transient processes of DC motor.

Keywords: DC motor, identification.

1. Introduction

Various types of electric drives are one of the key elements in mechatronic systems. The main requirement for such drives is a simple control of electric motor. DC motors have many advantages such as high efficiency, linear torque and speed characteristics, low cost. Control of DC motors is also simple and does not require complex hardware [1].

In order to make electric drive control systems, motor parameters are one of the key elements, but nowadays manufacturers rarely provide all the necessary motor parameters, especially when buying cheap or using old motors which are already out of production and the motor data could be no longer obtained.

The aim of this paper is to present the method of motor parameter identification by DC motor speed and current starting transient processes. This method requires simple and ordinary hardware. First of all transient processes of motor start-up speed and current are measured. The data is then transferred to the computer and preprocessed. The main unknown motor parameters are obtained by calculating optimization problem.

2. Mathematical models of DC motor

In this section a linear model of direct current motors with permanent magnets is presented.

The DC motor model can be constructed based on its electrical and mechanical characteristics. The equivalent circuit for a DC motor connected to DC voltage supply is shown in Fig. 1.

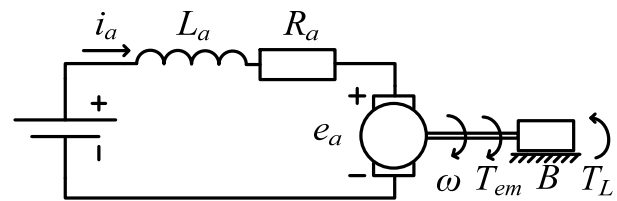


Fig. 1. Equivalent circuit of DC motor

The armature coil can be described with a resistance R_a , inductance L_a series and an induced back electromotive force (EMF) voltage e_a . Back-emf voltage is generated by the rotation of the electrical coil through the flux lines of the permanent magnets inside the motor. [1]

The electrical part of DC motor can be described from Fig. 1. using Kirchhoff's voltage law. These can be written as:

$$U = R_a i_a + L_a \frac{di_a}{dt} + e_a; \quad (1)$$

e_a – back electromotive force and is equal to:

$$e_a = k_e \omega. \quad (2)$$

Assuming there is no viscous friction the mechanical part of motor can be expressed very similar to electric part by [1]:

$$T_{em} = T_L + J \frac{d\omega}{dt}; \quad (3)$$

where:

$$T_{em} = k_m i_a. \quad (4)$$

With influence from viscous friction (3) becomes:

$$T_{em} - T_L = J \frac{d\omega}{dt} + B\omega. \quad (5)$$

The derivatives of current and speed expression have the forms:

$$\frac{di_a}{dt} = -\frac{R_a i_a}{L_a} - \frac{k_e}{L_a} \omega + \frac{U}{L_a}; \quad (6)$$

and:

$$\frac{d\omega}{dt} = \frac{k_m}{J} i_a - \frac{B}{J} \omega. \quad (7)$$

Using (6) and (7) the state space model of DC motor can be obtained [2]:

$$\frac{dx}{dt} = \begin{bmatrix} -\frac{R_a}{L_a} & -\frac{k_e}{L_a} \\ \frac{k_m}{J} & -\frac{B}{J} \end{bmatrix} x + \begin{bmatrix} \frac{1}{L_a} \\ 0 \end{bmatrix} u, \quad (8)$$

In this case the state vector is described as $x=[i, \omega]^T$. According to given motor equations it becomes possible to assemble a DC drive model in *Matlab Simulink* environment. Such model is presented in Fig. 2.

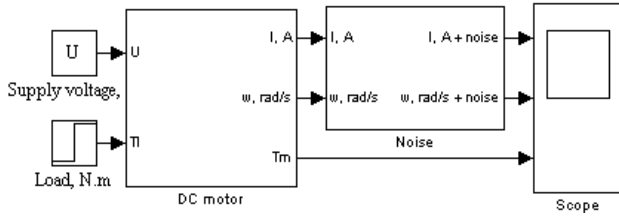


Fig. 2. *Matlab Simulink* model of DC drive

This model consists of DC power supply, DC motor along with motor load and main motor parameter monitoring blocks. Expanded DC drive block provided in Fig. 3.

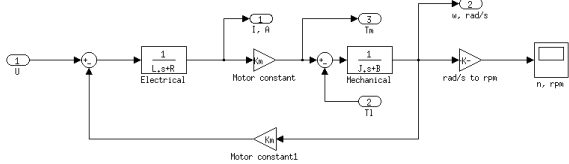


Fig. 3. DC drive block in *Matlab Simulink*

The block is assembled using standard *Matlab Simulink* transference functions. The motor model consists of two transfer functions, one of which describes the motor electrical and other mechanical parts.

3. Parameter identification

There are a lot of techniques for identification of DC motor. Some of them are described in papers [3] – [5]. The object of identification is described by equation (8). When marked:

$$A = \begin{bmatrix} -\frac{R_a}{L_a} & -\frac{k_e}{L_a} \\ \frac{k_m}{J} & -\frac{B}{J} \end{bmatrix}, B = \begin{bmatrix} \frac{1}{L_a} \\ 0 \end{bmatrix}; \quad (9)$$

the equation (8) can be rewritten:

$$\dot{x} = Ax + Bu. \quad (10)$$

After integration expression (10) yields:

$$x = \int_0^T (Ax + Bu) dt = A \int_0^T x dt + B \int_0^T u dt. \quad (11)$$

If none of the motor parameters are known objective function is constructed in the form of:

$$I(R_a, L_a, k_e, k_m, B, J) = \int_0^T \left[x_m - A \int_0^T x dt + B \int_0^T u dt \right]^2 dt; \quad (12)$$

here: x_m – measured value of the state variables. Since the armature resistance R_a and armature moment of inertia J is often known from the manufacturer's catalog and are easily measured values, the number of variable parameters can be reduced by rewriting (12) expression in the form of:

$$I(L_a, k_e, k_m, B) = \int_0^T \left[x_m - A \int_0^T x dt + B \int_0^T u dt \right]^2 dt. \quad (13)$$

Thus, the identification problem comes down to the optimization objective, the purpose of which - varying parameters L_a, k_e, k_m and B to minimize (13) expression of the objective function $I(L_a, k_e, k_m, B)$.

4. Simulation of DC motor

DC motor simulation in *Matlab* was done using parameters shown in Table 1.

Table 1. DC motor parameters [2]

DC motor parameter	Value
Supply voltage, U	10 V
Armature resistance, R_a	0.5 Ω
Armature inductance, L_a	1.5e ⁻³ H
Torque constant, k_m	0.5
Back-emf constant, k_e	0.05
Inertia, J	0.00025 kg·m ²
Friction constant, B	0

Simulation results of DC motor transient process of current is shown in Fig. 4 and motor speed in Fig. 5.

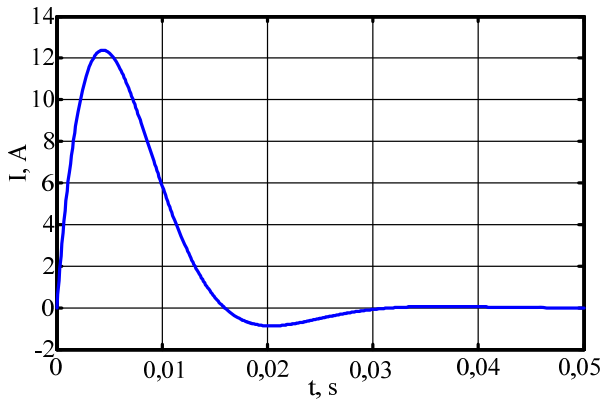


Fig. 4. Transient process of motor current

As seen from the Fig. 4 and Fig. 5 simulated transient processes have no noise thus using this data for motor parameter estimation would give great results, but the results would be incorrect from engineering standpoint. Typically experimental transient processes of DC motor have mid to high noise to signal ratio due to commutation and other factors such as measuring device tolerance. So at first simulated transient processes was disturbed using white noise. Results are shown in Fig. 6 and Fig. 7.

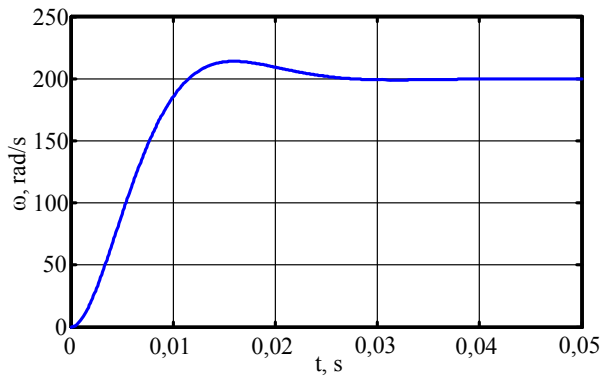


Fig. 5. Transient process of motor speed

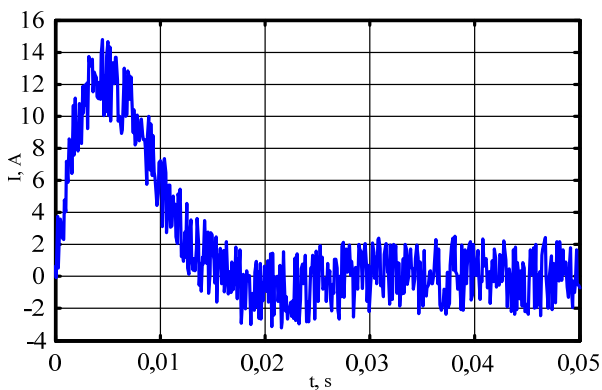


Fig. 6. Disturbed transient process of motor starting current

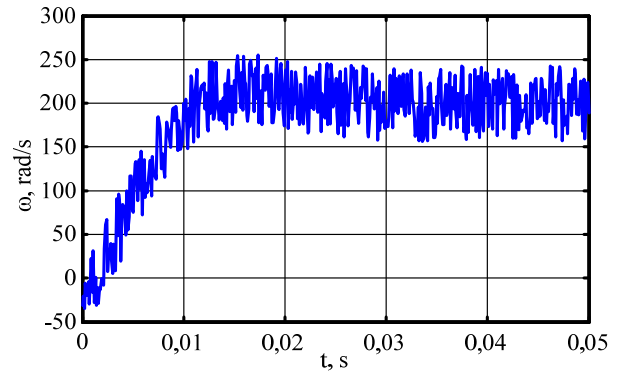


Fig. 7. Disturbed transient process of motor speed

5. Identification of DC motor parameters

In this paper DC motor parameter identification was approached using transient processes which were obtained using simulation with influenced disturbances. The friction coefficient is taken equal to zero in order to simplify the problem and turn it into a three-dimensional optimization problem.

Many nonlinear optimization methods could be applied ranging from classical Newton's method to more sophisticated optimization using neural networks. Main purpose of optimization program is to change L_a , k_e and k_m motor parameters so objective function becomes minimal, according to some algorithm. Minimizing this function means that the error between real transient processes and solution of the systems equations of witch parameters are varied is minimal.

In this paper optimization was done using one of *Matlab's Optimization toolbox's* functions which utilizes Nelder – Mead optimization algorithm which is common choice for zero-order optimization search tasks.

During investigation of the influence of noise level to precision of identification several simulation series with different noise levels were produced. The precision of identification was characterized by relative error which was calculated using expression below:

$$\delta_x = \frac{|x_e - x_i|}{x_e} 100\%; \quad (14)$$

where x_e – exact value of x , x_i – identified of value x , δ_x – relative error of identification.

First of all the identification was made using raw simulation data, i.e. without noises. In this case according to (14) calculated relative error is much less than 1 %.

Relative errors of parameter identification in the case of noisy signals are random variables. To evaluate the maximal value of that error ten cycles of simulation and identification were made. Identification results when the current and the velocity channels are influenced by white noise with amplitude of up to 10% of maximum signal values are shown in Table 2.

Table 2. Estimated parameters with 10 % disturbance

Estimated parameters			Accuracy of estimation, %		
L_a	k_e	k_m	L_a	k_e	k_m
$1.53e^{-3}$	$4.99e^{-2}$	0.495	1.9	0.1	1.1
$1.47e^{-3}$	$4.97e^{-2}$	0.498	2.2	0.5	0.3
$1.57e^{-3}$	$4.99e^{-2}$	0.501	4.7	0.3	0.2
$1.52e^{-3}$	$4.99e^{-2}$	0.495	1.3	0.2	1.0
$1.50e^{-3}$	$4.98e^{-2}$	0.511	0.1	0.4	2.1
$1.40e^{-3}$	$4.97e^{-2}$	0.508	6.4	0.7	1.7
$1.53e^{-3}$	$5.01e^{-2}$	0.493	1.9	0.3	1.3
$1.45e^{-3}$	$4.99e^{-2}$	0.501	3.1	0.2	0.2
$1.62e^{-3}$	$5.01e^{-2}$	0.511	8.1	0.2	2.3
$1.58e^{-3}$	$5.03e^{-2}$	0.496	5.1	0.6	0.8

The first three columns contain the set of L_a , k_e and k_m values acquired during the identification, while the others – identification accuracy. The maximum identification error for variable L_a is about 8%. k_e and k_m were determined more accurately, the maximal errors are approximately 1% and 2%. Since the identification of the maximum error does not exceed the engineering standard of 10 %.

Identification results when the current and the velocity channels are influenced by white noise with amplitude of up to 20% of maximum signal values are shown in Table 2.

Table 3. Estimated parameters with 20 % disturbance

Estimated parameters			Accuracy of estimation, %		
L_a	k_e	k_m	L_a	k_e	k_m
$1.62e^{-3}$	$4.97e^{-2}$	0.498	7.8	0.6	0.4
$1.62e^{-3}$	$4.97e^{-2}$	0.504	7.8	0.6	0.9
$1.50e^{-3}$	$4.97e^{-2}$	0.489	0.0	0.6	2.2
$1.70e^{-3}$	$5.06e^{-2}$	0.513	13.5	1.1	2.5
$1.71e^{-3}$	$5.05e^{-2}$	0.507	14.1	1.0	1.4
$1.40e^{-3}$	$5.00e^{-2}$	0.494	6.6	0.0	1.2
$1.54e^{-3}$	$5.01e^{-2}$	0.495	2.9	0.2	1.0
$1.76e^{-3}$	$4.98e^{-2}$	0.502	17.1	0.3	0.3
$1.51e^{-3}$	$5.09e^{-2}$	0.493	0.9	1.7	1.4
$1.73e^{-3}$	$5.03e^{-2}$	0.498	15.5	0.6	0.4

It was established that k_e and k_m variables are identified more accurately than L_a as the maximum error of L_a identification accuracy was 17%, while identifying k_e error does not exceed 2%, while k_m - 3%. It was also

noted that 200 iterations is too little for such a noise level as the identification error 4 times out of 10 exceeds the engineering standard of 10 %. Table 3. In future this algorithm will be tested using experimental transient processes of real life DC motor.

6. Conclusions

From the test results, it is seen that the application of proposed method for the motor identification is very useful for engineering purposes. Especially good results were obtained when the noise of transient processes is low.

In summary, relative error of armature inductance identification is close to the noise to amplitude ratio in measurement channels.

It was found that, regardless of the noise level, identification error of constants k_e and k_m is about four times smaller than the identification error of armature winding inductance L_a .

7. References

1. Jacek F. Gieras. Permanent Magnet Motor Technology/ Design and Applications. – CRC Press, 2009. p – 608. ISBN 9781420064407
2. Roma Rinkevičienė. Mechatroninių sistemų modeliavimas. – KTU, 2008. p–165.
3. S. Udomsuk, K-L. Areerak, K-N. Areerak, A. Srikaew. Parameters Identification of Separately Excited DC Motor using Adaptive Tabu Search Technique. Advances in Energy Engineering (ICAEE), 2010 International Conference on Latest Trends on Circuits, Systems and Signals 19-20 June 2010 ISBN: 978-960-474-208-0 Page(s): 48 - 51
4. M.Nizam.Kamarudin, Sahazati Md.Rozali. Simulink Implementation of Digital Cascade Control DC Motor Model - A didactic approach. 2nd IEEE International Conference on Power and Energy,December 1-3, 2008, Johor Baharu, Malaysia, pages: 1043-1048
5. Hai-Jiao Guo, Tadashi Ishihara. A Study of Sampled-data Integrator Controller and Its Application in Speed control of DC Motors. 2009 IEEE International Conference on Control and Automation Christchurch, New Zealand, December 9-11, 2009, pages: 2149-2153

THE INVESTIGATION OF SOLAR ENERGY CONVERSION AND STORAGE PROCESSES IN BIOMASS

Povilas Algimantas SIRVYDAS*, Vidmantas KUČINSKAS**

*Aleksandras Stulginskis University, Lithuania; **UAB "ARVI" ir ko, Lithuania

Abstract: The transformation and accumulation of solar energy in a biological form has direct relationships with food, biomass energy and climate change problems, which can be addressed as the processes of the exchange of energies in the plant. The analysis of these processes helps understand the factors affecting the process of the plant's energy exchange. Biomass can only release the amount of energy equal to the radiant energy assimilated by it from the Sun in the process of biomass production. Solar energy accumulation in biomass is highly inefficient as a mere 2 % of the provided energy is used. The remaining share of energy is emitted to the environment. The regulation system of plant leaf temperature may be one of theoretical presumptions for the efficient cooling of microchips.

Keywords: solar energy transformation, temperature, cooling of microchips.

1. Introduction

In the period of state-of-the-art technologies the energy sector relies on the use of concentrated primary energy sources (including biomass) for heat and electricity production. The Sun supplies Earth with one of best forms of energy in the form of rays. Biological process taking place in vegetation predetermining the process of biomass (alternative energy source) creation are directly relating to energy exchange in plants. Irrespective of the intended purpose of use of biomass produced by a plant (for food or energy), biomass cannot emit a larger amount of energy than the amount of the radiant energy taken by it from the Sun during the process of biomass production. Consequently, the development of the use of biomass, as a source of renewable energy, is directly dependent on the possibilities of the assimilation process to satisfy demand for biomass. A global increase in demand for biomass is related not only with a growing demand for food but also with the increasing use of biomass for energy. Currently there are around 0.115 ha of arable land and the same area of forest lands per capita on the Earth. EU states show concerns about a future balance between biomass supply and demand

taking into account the planned development of biomass use. Currently an annual forest increment amounts to around 900, felling – 500 million m³ [1, 2].

Theoretically, the utilisation rate of the solar energy absorbed by plants for the production of organic matter could represent around 20 to 25% [3, 4]. In practice hardly 2% of the absorbed solar energy are utilised for photosynthesis. Visible light absorbed by plants accounts for 80 to 85 %, reflected light – 10% and light conducted through leaves – 5 to 10% [5, 6]. According to the Law of the Minimum (limiting factor) applicable in the world of plants, vital processes, including yield, depend on the factor in the minimum under other conditions being identical. Consequently, evaluation of environmental factors and of the importance of metabolism requires a theoretical evaluation of energy exchange between the plant and the environment.

From another standpoint – a plant is a unique, cheap and particularly complex laboratory. The plant is capable of utilising non-concentrated radiant energy from the Sun and creating the most precious asset on Earth – organic matter, absorbing the major part of pollutants emitted into the atmosphere by a modern technological Man and supplying oxygen to the environment by creating conditions for life on Earth. Over a year the terrestrial globe's vegetation assimilates around 640 billion tonnes of carbon dioxide and releases around 500 billion tonnes of free oxygen, thus reducing environmental pollution [3, 4] and transpires around 65,200 km³ of water.

The share of the absorbed solar energy representing 98 to 96% in the plant leaf is converted into energy in the form of heat.

The solar energy converted into heat in plant leaves either has to be released to the environment or accumulated in plant tissues by raising their temperature. The maximum temperature of live plant tissues is limited. If plant tissues are impetuously heated over a temperature of 58 °C proteins coagulate in cells, cell membranes decompose and the tissues are exposed to the lethal termination [8, 9, 10]. Due to a small mass and biologically limited maximum temperature of plant tissues, thin plant leaves are not always able to

accumulate released heat. Therefore, the solar energy converted into heat in plant leaves has to be released to the environment as a metabolite. Heat released to the environment by a plant is of little value and low temperature.

In terms of energy exchange, the plant and its surroundings form an unbroken and undivided system. An important factor in the analysis of the processes of solar energy transformation and accumulation in biomass is a plant organ's temperature. Developments in the plant leaf temperature may be analysed experimentally or theoretically, as an expression of the dynamic balance of energies [4, 11, 12].

2. The methods of research

The work employed the method of the balance of energies in a plant. The leaf temperature of a plant growing in natural environmental conditions was measured by thermocouple temperature sensors made of Cu-CuNi (copper-constantan) wires with a diameter of 0.05 mm. In order to have the same resistance of the sensors, only wires of equal length were used. The measurements were recorded with an instrument ALMEMO 2590-9 having a microprocessor data processing and accumulation system. Temperatures were recorded by necessity taking a maximum of 100 measurements per second. This enabled us to observe short-term dynamic processes of temperature changes. Temperature sensors for all temperature measurements were laid in observance of the requirements to be met by temperature measurements (in respect of the plant and its environment).

3. Results of investigation

Plant leaf temperature and the difference of temperatures between the plant and the environment are those factors that can generate (or intensify) driving forces for energy exchange between the plant and the environment. The local temperature of a plant leaf depends on the local balance of energies in the plant leaf. In terms of energy, the whole plant, like its every organ or part of the organ, has individual contact with the surrounding environment. Since layers resulting from plant organs' exchange with the environment and the pulsations of plant energy exchange processes emerge, individual organs of the plant or parts thereof can experience a different exchange of energy with the environment. Thus, the balance of energies in each organ of the plant or part thereof may be different at a given moment. The influence of individual members of the balance of energies in the plant is rather diverse. This results not only from biological processes within the plant (organ) but also from the specific energy environment of the habitat.

Measurements of the temperature difference between the plant and the environment show that the difference in temperatures between the plant and the environment during the sunny period of the day in natural environmental conditions reaches up to 6.5 0C. Ambient air temperature at the top and the bottom of the plant leaf is different (Figure 1).

Plant tissues release the solar energy transformed into heat to the environment in the form of heat and water vapours. During the sunny period of the day transpiration is that factor that reduces plant tissue temperature and protects plant tissues from thermal overheating and destruction. Therefore, it is important to know the maximum plant leaf temperature in natural environmental conditions upon transpiration termination. When a plant leaf does not evaporate water transpiration.

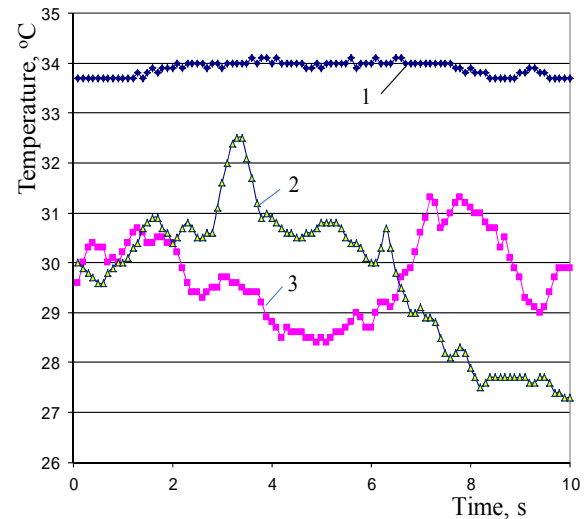


Fig. 1. Temperature change in the plant leaf plate (curve 1) and air (curves 2 and 3) respectively at the top and at the bottom of the leaf during the sunny period of the day under natural conditions. Wind speed $v_{vid} = 0.5\text{m/s}$

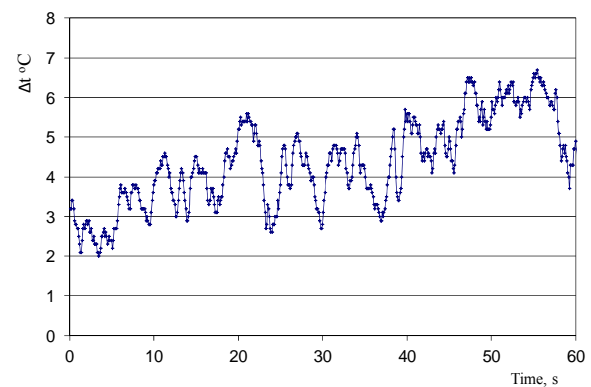


Fig. 2. Fluctuations in the difference between plant leaf and ambient temperature during the sunny period of the day under natural environmental conditions. Wind speed $v_{vid} = 1.1\text{ m/s}$

In that case the total flux of solar energy absorbed by the plant q_1 will be released to the environment by a convective heat transfer. This case is represented by equation (1).

$$aq_1 = 2\alpha(t_1 - t_0) = 2\alpha\Delta t. \quad (1)$$

Equation (1) may be used to identify the difference of temperatures between plant leaf temperature t_1 and the temperature of its environment t_0 :

$$\Delta t = \frac{aq_1}{2\alpha}; \quad (2)$$

where Δt – difference of temperatures between the plant leaf and its environment °C;

t_1 – plant leaf temperature °C;

t_0 – ambient temperature °C;

a – rate evaluating the share of the absorbed solar energy converted into heat in the plant, in % or shares ($a = 0.96-0.98$);

α – heat transfer rate $W/(m^2 \cdot K)$.

These equations (1) and (2) have a theoretical importance and they make it possible to identify the maximum temperature increase Δt in natural environmental conditions when plant leaf transpiration is terminated. Depending of heat transfer rate α and the absorbed integral flux density of solar radiation q_{sp} , the dependencies of an increase in plant leaf temperature are presented in Fig. 2. The Figure shows that in the presence of intensive solar radiation transpiration is the key factor that protects the plant against thermal destruction. As data given in Fig. 2 show, where solar radiation is intensive, on a windless day, i.e. where the values of the heat transfer rate α are low, a plant can be exposed to thermal effects resulting in the lethal process in plant tissues.

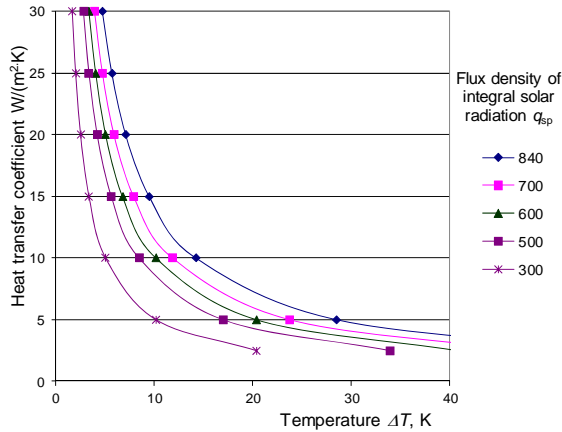


Fig. 3. Theoretically possible increase in plant leaf temperature Δt in the event of transpiration termination depending on heat transfer rate α and the flux density of integral solar radiation q_{sp}

4. Discussion and conclusions

The presented data on temperature measurements suggest that exchange of energies in the plant in a natural environment is continually changing. The dynamics of the balance of energies between the plant and the environment is in particular vivid during the sunny period of the day. Continually changing air parameters in the environment lead to energy changes in the local balances of energies of plant organs. All energy changes are reflected in the local plant leaf temperature, regardless of what causes them.

During a long way of its evolution the plant has adapted to the factors of a physical environment of its habitat

and exists as an open system of the exchange of energies maintaining a continuous dynamic balance of energies. The processes of energy exchange in plants are very diverse. The plant's physiological response to changes in environmental energy exchange is displayed by the distribution of energy fluxes among the main members of the balance of energies: solar energy, transpiration and convective heat exchange [4, 11]. It is convenient to analyse solar energy transformation processes in h - x (enthalpy – air humidity) diagram.

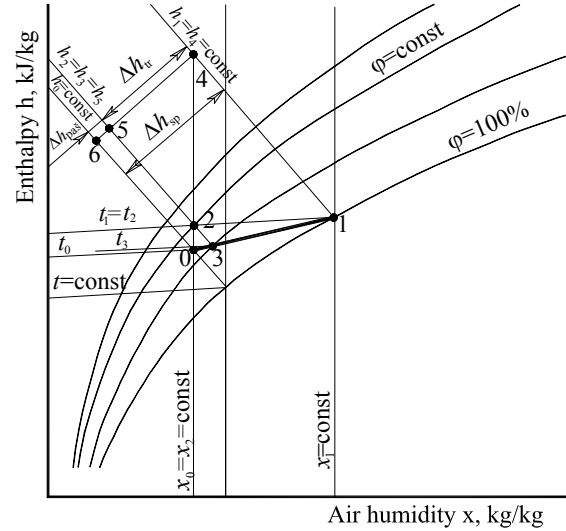


Fig. 4. The chart of energy exchange with the environment by a plant leaf transpiring during the sunny period of the day in diagram h - x . The temperature of a plant leaf is higher than the ambient temperature ($t_1 > t_0$). 0-1 – The process of plant leaf energy exchange

The minimum air amount G_{1min} participating in the process of energy exchange that can absorb 1 kg of moisture evaporated by plants can be determined when knowing the values of air humidity x_1 and x_0 using the equation:

$$G_{1min} = \frac{1}{x_1 - x_0}. \quad (3)$$

The minimum heat amount J , consumed in the process of transpiration for ambient air heating Q_{2min}^{pas} , when the plant evaporates 1 kg of moisture is determined using the equation:

$$Q_{2min}^{pas} = G_{1min} c_p (t_1 - t_0) = c_p \frac{t_1 - t_0}{x_1 - x_0}. \quad (4)$$

The heat amount J used for plant leaf transpiration by evaporating 1 kg of water ($w = 1$) is determined using the equation:

$$Q_3 = wr = r = (h_1 - h_3)G_{1min} = \Delta h_{tr} G_{1min}; \quad (5)$$

where Δh_{tr} increase in air enthalpy due to the increase of air humidity from x_0 to x_1 , resulting from the process of transpiration, kJ/kg.

The analysis of solar energy transformation and its distribution in the plant highlights the lability the energy exchange between the plant and the environment. Biological and energy processes occurring in the plant form the system of the exchange of energies of the plant together with external energy sources participating in the exchange of energies between the plant and the environment. For the performance of vital functions in the plant's tissues a live organism uses temperature difference, potential difference, concentration difference and other gradients describing the direction of movement and the speed of change. This enables plant's adaptation to unfavourable surrounding conditions and creation of the optimum conditions for the process of assimilation. Since the plant is a live organism having formed over a long period of evolution, it has developed a system for the regulation of energy exchange factors. In the course of evolution the plant has created a biological system for leaf temperature regulation-energy exchange with the environment. The plant leaf plate, 0.2 to 0.3 mm thick, has a specific gas exchange and leaf ventilation system. It consists of micro-, macro- and nano-channels in the leaf mesophyll (on the bottom part of the leaf) that interact with the environment via stomata. A plant leaf surface of 1mm² has around 400 stomata. The area of a stomata opening represents 0.5 to 5% of the leaf surface area. Therefore, the actual area of leaves (mini-, macro- and nano-channels) participating in the energy exchange is by 10 to 30 times larger than the external leaf surface [3]. Such anatomic structure of the plant leaf enables the process of accumulation and biological regulation of the exchange of energy between the leaf and the environment to take place.

Observation of the processes of plant energy exchange and their comparison with technological solutions show that following creation of energy transformation devices (channels) in around 1900 the first steam turbines were produced. In the meantime vegetation assimilated analogous energy transformation channels many years ago. An opening in the plate connected with the environment by a channel acts as a thermal engine of nano-quantities when exposed to a changing heat flow. The nano-engines of such basic structure exist in vegetation. The generated mechanical energy is used for the intensification of the processes of exchange with the environment. Recently the utilisation of mini-, micro- and nano-channels has received an increased attention [13-15]. Consequently, the system for the regulation of plant leaf temperature analysed in this work may serve a

theoretical assumption for the development of an efficient system for microchip cooling.

5. References

1. Europos aplinka: Būklė ir perspektyvos. 2010m. apibendrinimas. EEA, Copenhagen, 2011, 222p.
2. Dzenajavičienė E. Pedišius N. Škėma R. Darni bioenergetika. Lietuvos energetikos institutas. Kaunas, 2011. 136p.
3. Šlapakauskas V. Augalų ekofiziologija. Kaunas 2006. Latutė. 413 p.
4. Лыкун, Г.М. Энергетичний баланс рослин. Киев 1967, 234 с.
5. Fitter, A.; Hay, R.. Environmental physiology of Plants. S.D., S.F., N.Y., B., L., S., T., 2002. Academic press, 367s.
6. Šlapakauskas V., Duchovskis P. Augalų produktyvumas. 2008. IDP Solutions, 254p.
7. Brazauskienė, D.M. Agroekologija ir chemija. Kaunas, 2004. 207 p.
8. Stašauskaitė, S. Augalų vystymosi fiziologija. Vilnius, 1995. 226 p
9. Ellwagner, T.; Bingham, Jr.; Chapell, S. We and Tolin SA. Cytological effects of ultra-high temperatures on Corn. Weed Science, 1973, N 21 (4), p. 299-303.
10. Levitt, J. Response of plants on environmental stresses. Academic Press. New York, 1980. Bd 1.
11. Sirvydas, A.; Kerpauskas, P.; Kučinskas, V. Augalų energinė apykaita. Lietuvos Žemės Ūkio Universitetas, 2011. Akademija, 224 p.
12. Sirvydas, A.; Kučinskas, V.; Kerpauskas, P.; Nadzeikienė, J. Theoretical modeling of temperature pulsations in plant leaf which are caused by leaf swing with respect to the sun. Journal of Environmental Engineering and landscape management. 2011. Vol. 19(3). p. 251-259
13. Ide, H.; Kariyasaki, A.; Fukano, T. 2007. Fundamental data on the gas - liquid twophaseflow in mini-channels. Int. J. Therm. Sci. 46 (1): 519-530
14. Sajith, V.; Haridas, D.; Sobhan, C.B. 2011. Reddy Convective heat transfer studies in macro and mini channels. International Journal of Thermal Sciences 50: 239-249
15. Sobhan, C.B.; Garimella, S.V. 2001. Comparative analysis of studies on heat transfer and fluid flow in microchannels. Microscale Thermophys. Eng. 5: 293-311

SYNCHRONOUS INTERCONNECTION OF BALTIC POWER SYSTEM TO THE GRID OF CONTINENTAL EUROPE: REALITIES AND VIEWS

Sigitas KADIŠA, Virginijus RADZIUKYNAS, Arturas KLEMENTAVIČIUS,
Neringa RADZIUKYNIENĖ, Algimantas LEONAVIČIUS
Lithuanian Energy Institute, Lithuania

Abstract: The paper analyses the possibilities and conditions of Baltic Power System for the synchronous connection to Continental European Network (CEN) under asynchronous interconnections with Nordic Grid and IPS/UPS Grid. The real situation is analysed in comparison with the similar practices (CENTREL/UCTE, Burshtynskaia island) and feasibility studies (Turkey/CEN) related to interconnection of other regions. The analysis focuses on the specific challenges for Baltic Power System and presents views on synchronous integration with CEN, including *n-1* incident, sufficiency of load-frequency reserves, operational trials and total transfer capacities of Baltic-CEN cross-border links.

Keywords: power system, synchronous interconnection, Continental European network, generating unit, primary control reserve, cross-border link, secondary control reserve, total transfer capacity, tertiary control reserve.

Abbreviations:

BtB – back-to-back (station)
CEN – Continental European Network
KL – Kaliningrad (region)
NPP – nuclear power plant
PS – power system
TSO – transmission system operator
TTC – total transfer capacity
WPP – wind power plant

1. Introduction. Without hesitations for synchronous interconnection

According to opinion of European Economic and Social Committee, the Baltic States (Lithuania, Latvia and Estonia) are still energy islands vis-à-vis the EU since their networks are still entirely dependent on their former "exclusive" partner, Russia (to a lesser extent, Belarus). Connection of these islands should be a part of European energy integration process. It is indeed a paradox that while the three Baltic States are an integral

part of the political union, they do not reap the benefits of intra-European integration and solidarity in the energy sector. How can we accept that they continue to depend on a third country, moreover a WTO member now, which does not respect European standards regarding access to networks, has not signed the Energy Charter, and does not facilitate the improvement of interconnections between Central and Eastern European countries? [1]

Lithuania, Latvia and Estonia are developing and implementing electricity interconnection projects (*LitPol Link*, *NordBalt* and *Estlink 2*) with other EU countries, in particular Poland. These projects are required, inter alia, by Baltic Energy Market Interconnection Plan (BEMIP) [2] which paves an integration way for Baltic market to NordPool Spot and Continental European markets. At the same time, the three Baltic countries are working towards fully-fledged integration into the European energy system combining electrical power systems with the CEN for synchronous mode (currently undergoing a feasibility) [1].

2. Waiting for technical integration road map

Basing on such a clear political background as referred to Section 1, we can read a new message: the synchronous connection of Baltic systems is *modus vivendi* of integration. It replaces the former view of European Commission/Parliament foreseeing *LitPol Link* as asynchronous project in its TEN programme [3].

On the whole, any synchronous integration is technically complicated and, to certain extent, unique procedure. Technical integration refers to technical requirements, which are meant, firstly, as general rules common for all cases since they reflect physics of system operation. Such rules are laid down in Grid Codes or similar regulations.

On the other hand, technical requirements also are meant as individual rules, i.e. pointing to the specific

needs of interconnection in question. Such rules are compiled into Catalogue of Measures.

As regards the Baltic case, the general rules are currently the former UCTE Operational Handbooks playing a role of ENTSO-E rules. The handbooks stipulate the standards and guidelines for a PS operating in a synchronous area. Despite of being confirmed rather recently they are “at expiry threshold” since the UCTE as organization does not exist and merged with others into ENSTO-E. The latter is drafting a new ENTSO-E grid code, at least 2 years as yet. [4].

The on-going feasibility study as mentioned in Section 1

(carried out by international consortium) and the new ENTSO-E rules will lay down both major principles and tasks for Baltic/CEN interconnection. Further step is most likely the preparation to Catalogue of Measures providing roadmap for the technical integration.

Finding themselves in the area of interests for synchronous Baltic/CEN integration, the authors present below their preliminary views and estimations on technical feasibility of such an integration.

3. Some aspects of Baltic/CEN interconnection

The Baltic PS will enter the CEN synchronous zone as one control area (control block) with one value for each type of load-frequency control reserve (primary, secondary and tertiary).

We suppose the on-going feasibility study should determine the maximum power flow to be transferred over the synchronous cross-border links in both directions with respect to technical considerations and simulations of a large number of probabilistic operational situations.

Dynamic behavior of the Baltic and Poland systems should include analysis of behavior of the load-frequency control, analysis of transient stability due to short circuits and outages) and, if possible, identification of probable local or inter-area oscillations. The study should give reasoned answers to the questions of utmost importance: what are possibilities of Baltic PS to operate in island mode? What incidents could be assumed (in CEN and Baltics) which may lead to the disconnection of Baltic PS from CEN?

Finally, principles of system defence and restoration plans should be outlined.

Agreeing on a lot of uncertainties for the situation development up to 2020, we suggest the following eventual synchronous integration scenario for Baltic PS.

2014-2016 –construction of *LitPol Link*, (2x400 kV, 2x750 MW) and Alytus BtB station (500 MW)

2014-2016 –construction of *Alytus-Kruonis HPP* line (2x330 kV, 2x700 MW)

2014-2016 –1st stage extension of 400 kV network in North-Eastern Poland

2016 –start-up of asynchronous operation of *LitPol Link*

2017-2020 –construction of linking transformers in Alytus substation (2x400/330 kV, 2x1000 MVA)

2018-2020 –2nd stage of extension of 400 kV network in North-Eastern Poland

2017-2019 –construction of Narva BtB station for asynchronous interconnection with Russia

2020 –start-up of synchronous operation of *LitPol Link* (2x400 kV, 1500 MW)

2020 –start-up of *LT-BY* asynchronous operation via Alytus BtB station (500 MW) and *Alytus-Grodno* cross-border link (1x330 kV, 700 MW)

2020 –simultaneous start-up of *EE-RU* asynchronous operation via Narva BtB station (most probable 500 MW) and *Narva-Kingisepp* cross-border link (330 kV).

4. Baltic primary control reserves: too small to be a problem

Baltic primary control reserve will be determined by mandatory contribution of each control area in response to the loss of 3000 MW of generating capacity in the CEN area [5].

$$P_{prim} = (P_{Baltic} / P_{CEN}) \times 3000 \quad (1)$$

The calculation results in accordance with (1) are presented in Table 1, with the breakdown to national reserve contributions.

Table 1. Primary control reserve of Baltic Power System for the time horizon 2025

Area	System peak, MW	Participation in CEN peak	Reserve contribution
Baltic control area	<i>LT</i> : 2370	0.37 %	11 MW
	<i>LV</i> : 1515	0.24 %	7 MW
	<i>EE</i> : 1786	0.28 %	8 MW
	<i>KL</i> : 901	0.14 %	4 MW
	<i>Baltic</i> : 6572	1.02 %	30 MW
CEN	643000	100 %	3000 MW

Being such small in size, the reserve seems to be easy attained.

The insensitivity range of primary controllers should not exceed ±10 mHz. The time for starting the action this control is a few seconds after the incident, the deployment time for 50 % or less of the total P_{prim} is at most 15 seconds and from 50 % to 100 % the maximum deployment time rises linearly to 30 seconds. The minimum duration for the capability of delivery for primary control is 15 minutes. The cycle for measurements of the system frequency for control area observation must be in the range of 1 second (strongly recommended) to at most 10 seconds [5].

5. Baltic secondary and tertiary control reserves: how to cope with $n-1$ problem?

The secondary control reserve is assumed to replace the primary reserve P_{prim} , to compensate load-generation fluctuations and to replace the loss (outage) of area's biggest generating unit. The latter component of reserve is far more bigger than first two ones, and is commonly named ($n-1$) reserve. The ENTSO-E rules stipulate that $n-1$ category covers not only the biggest operating generator, but also generation set (generators connected to one point) and HVDC link [5]. The inventory of potential Baltic ($n-1$) units is presented in Table 2.

Table 2. Potential Baltic ($n-1$) units for the time horizon 2020

($n-1$) category	($n-1$) unit on national scale	Capacity MW	($n-1$) on Baltic scale, MW
Biggest generator, MW	<u>LT</u> : Visaginas NPP	1350	1350, <i>probable</i>
	<u>LV</u> : Riga CHP 2	450	450, <i>existing</i>
	<u>LT</u> : Lithuanian PP	455	455, <i>existing</i>
	<u>EE</u> : Auvere	300	<i>too small</i>
Biggest WPP, MW	<u>LT</u> : Šilutė WPP	250	<i>too small</i>
	<u>EE</u> : Hiiuamaa-Saaremaa WPP, off-shore <u>LV</u> : <i>to small for consideration</i>	2000	600*, <i>the latest vision</i>
Biggest HVDC link, MW	<u>LT</u> : NordBalt;	700	700, <i>projected</i>
	<u>LT-BY</u> : Alytus BtB	500	500, <i>projected</i>
	<u>EE</u> : Estlink 2	650	650, <i>probable</i>
	<u>EE-RU</u> : Narva BtB	500	500, <i>probable</i>
		1000	1000, <i>hardly probable</i>

* 30% of WPP nominal capacity is assumed to be replaced by $P_{sec\ n-1}$ as a forecast error.

Table 2 suggests that Baltic ($n-1$) unit is Visaginas 1350 MW unit followed by Narva BtB station (1000 MW) and NordBalt HDVC link (700 MW). 1350 MW is really a very big capacity on Baltic scale. It was found to be fully compatible with a pre-determined steady-state and dynamic operational modes of Baltic PS [7]. Hence assuming the loss of this capacity, we conducted identification of Baltic secondary and tertiary control reserves for operation in transit mode (Table 3) and export mode (Table 4). Here the tertiary reserve is assumed to be mobilized in 12 h replacing all the secondary ($n-1$)-specific reserve, i.e.

$$P_{tert} = P_{sec\ n-1}, \quad (2)$$

Consequently the total demand of both reserves would be very high

$$P_{tert} + P_{sec\ n-1} = 1350 + 1350 = 2700 \text{ MW}$$

The Tables 3 and 4 give essential information for the discussion. Under normal loading conditions, Baltic power system has sufficient amount of secondary and tertiary reserves provided the export to other system is zero (Table 3). Nevertheless, when export is on a high level (Table 4), the system will be subjected to small deficit of secondary reserve but to sharp deficit of tertiary reserve (as some units are taken from tertiary reserve and run for exports).

Table 3. Own reserve availability of Baltic PS for $n-1$ event (loss of Visaginas NPP) under big transit via the Baltic PS, winter 2020, normal demands

Parameter	Baltic PS (without KL)	LT	LV	EE
Demand, MW	4820	2014	1288	1518
Generation, MW	all: 4820 wind: 630	all: 2710 wind: 250 Visaginas unit: 1350	all: 1045 wind: 170	all: 1065 wind: 210
Transit, MW	1300	<u>LT-SW</u> : 400 <u>LT-KL</u> : -300 <u>LT-BY</u> : 300 <u>LT-PL</u> : -1000		<u>EE-RU</u> : 100 <u>EE-FI</u> : 500
Sec. control reserve, MW	1580	610	900	70
Tert. control reserve, MW	1265	965	225	75

Table 4. Own reserve availability of Baltic PS for $n-1$ event (loss of Visaginas NPP) under big export from Baltic PS, winter 2020, normal demands

Parameter	Baltic PS (without KL)	LT	LV	EE
Demand, MW	4820	2014	1288	1518
Generation, MW	all: 6020 wind: 630	all: 3540 wind: 250 Visaginas unit: 1350	all: 1415 wind: 170	all: 1065 wind: 210
Export, MW	1200	<u>LT-PL</u> : 500 <u>LT-SW</u> : 300 <u>LT-KL</u> : 0 <u>LT-BY</u> : 0		<u>EE-FI</u> : 400 <u>EE-RU</u> : 0
Sec. control reserve, MW	1280	610	600	70
Tert. control reserve, MW	365	135	155	75

The deficit tertiary reserve will amount to as much as 985 MW (1350 MW-365 MW, see Table 4). This deficit could be mitigated by purchasing from CEN tertiary reserve providers (see Section 6).

As a part of system defense and restoration plans, secondary control system will be provided with a new functionality – frequency leader. After a severe disturbance with a frequency deviation higher than the maximum permissible or in case of system split, the frequency leader shall be chosen within each synchronous area. As a default the transmission system operator with the highest K-factor under operation within its control area will be appointed as the frequency leader [6].

6. Is cross-border capacity sufficient for Baltic system?

As physically determined, the candidate area (system) can participate in parallel operation with the accepting synchronous area only through the cross-border links. Their transfer capacity should be sufficient to transmit a load flow to support the deficient area.

The expiring UCTE rules [5,6] do not stipulate anything directly related to the transfer capacities of integration-enabling cross-border links. Thus a minimum threshold of these capacities is no more than a case-specific or even optional parameter.

The following cross-border capacities were identified in the precedents of synchronous integration to (former) UCTE – see Table 5:

Table 5. Cross-border total transfer capacities (TTC) of the implemented synchronous integration projects

	CENTREL [8]	Bursht. island [9]
Peak, MW	42900	1050
Year	1995	2002
Physical cross-border links	<i>PL-DE: 1x380 kV (900 MW); 2x220 kV (600 MW); 2x220 kV (600 MW)</i> <i>CZ-DE: 2x380 kV (1800 MW); 1x380 kV (900 MW); 2x220 kV (600 MW);</i> <i>SK-AT: 1x380 kV (900 MW);</i> <i>HU-AT: 1x380 kV (900 MW)</i>	<i>Bursht-HU: 1x380 kV (900 MW); 1x220 kV (300 MW); 1x220 kV (300 MW); 1x750 kV (1000 MW)*</i> <i>Bursht-SK: 1x380 kV (900 MW) []</i>
TTC of all links, MW	7200	3400
TTC/peak ratio	0.17	3.24

* estimate made assuming that 1 transformer, 750 kV, is connected to the 750 kV link *Zakhidnoukrainska- Albertirsa*

Similarly, Table 6 presents estimates of cross-border capacities for candidate systems.

Table 6. Cross-border total transfer capacities (TTC) of the potential synchronous integration projects

	Turkey [10]	Ukraine, Moldova*
Peak, MW	36120	30525
Year	2011	2012
Physical cross-border links	<i>BL: 1x400 kV (995 MW); 2x400 kV (1510 MW);</i> <i>GR: 2x400 kV (1510 MW)</i>	<i>UA-PL: 1x220 kV (300 MW); 1x750 kV (2000 MW);</i> <i>UA-RO: 1x750 kV (2000 MW);</i> <i>MV-BL: 1x400 kV (900 MW)</i>
TTC of all links, MW	4015	5200
TTC/peak ratio	0.11	0.17

* estimates of Lithuanian Energy Institute (as results of on-going Ukraine, Moldova/CEN study are still unavailable)

Likewise, Baltic capacities are presented in Table 7

Table 7. Cross-border total transfer capacities (TTC) of Baltic PS synchronous integration

Peak, MW	6572 (<i>Baltic PS</i> , including <i>KL</i> region)
Year	2025
Physical cross-border links	<i>LitPol Link: 2x400 kV, 2x750 MW</i>
TTC of all links, MW	1500
TTC/peak ratio	0.23

The *LitPol Link's* ratio 0.23 (Table 7) is really high and overruns those found for CENTREL, Ukraine and Turkey (*Burshtynskaya* case with 3.24 is an extremity and cannot be used for benchmarking).

As for neighbouring power systems, the Rules [5,6] stipulate few legal provisions on cross-border links ("tie lines" in terminology of the Rules).

The TSO of neighbouring systems can agree on transfer margin for reserve exchange. Namely, the secondary control reserve can be exchanged border-crossing provided that 66 % of the needed reserve are kept geographically within the control area. In addition a fixed share of 50 % of the total needed secondary control reserve plus tertiary control reserve must also be kept inside the control area [5].

As regards critical contingencies (overrunning those handled with secondary and tertiary reserves), the TSOs are supposed to provide maximal assistance through tie lines in case of an emergency situation experienced by neighbouring TSO [5]. Nevertheless, this provision does not specify the amount of transfer margin.

If a critical contingency is a severe disturbance with a frequency deviation higher than the maximum permissible one, the Rules [5] lay down only that a transfer margin of tie lines (in export in case of under-frequency situation, in import in case of over-frequency situation) should be considered. Thus, no standard values of safety margin is set.

Accordingly, concerning the safety margin of *LitPol Link* for secondary and tertiary reserves, the total reserve margin is allowed to reach 50 % of total reserve, i.e: $2700 \times 50 \% = 1350$ MW. It would take practically all the TTC ($1350/1500=90\%$). It could be seen as purely theoretical case.

Baltic need for the purchase of tertiary reserve is 985 MW (see Table 4) and would correspond to 66%. It also would be severe case, but, to some extent, realistic. To mitigate the situation, we would suggest to diminish this huge purchase by 300-500 MW calling for imports via four aforementioned HVDC links.

7. What operational trials should be passed?

Operational trial is a "field test" for power system to prove its smooth operation with the accepting synchronous area.

In general, three major types of trials could be distinguished:

1 type. “island” mode;

2 type. autonomous operation;

3 type. synchronous operation.

Rationales of the trials would be to examine the candidate system’s capabilities:

1 type. to cope with load-frequency regulation in “island” mode, i.e. using own resources only. It refers to system which intends to switch from one synchronous area to another;

2 type. to “ride through” the test conditions, e.g. outages of equipment or losses of generating units or loads, working separately, i.e. in autonomous mode. It refers mostly to candidate synchronous areas, to whom the load-frequency regulation was inherent function;

3 type. to comply with requirements for parallel operation with the accepting zone, and, first and foremost, to contribute to the load load-frequency regulation.

The expiring UCTE rules [5] stipulate/does not stipulate the trial of first/both types.

We suggest the following findings of the review of the precedents with respects to the trials:

1) CENTREL/UCTE [8]:

- no 1st type trial (as the CENTREL system was a synchronous area, not a part of it);
- 2nd type trial: two weeks from September 13, 1995; 4 planned outages of generation or load (200-300 MW), one in each system (PL, CZ, SK, HU); satisfactory results for system performance under unplanned outages and normal operation (effectiveness of primary and secondary control in each system; voltage control on-cross-border links, operation of Power System Stabilizers in PL and HU power systems);
- 1st year of 3rd type trial (started on October 18, 1995)
- 2nd year of 3rd type trial (started on October 18, 1996)

2) Burshtynskaya island/UCTE, the smallest candidate system [9]:

- no 1st and 2nd type trial;
- 3rd type trial: 2 weeks of parallel operation (April 6-20, 2002); good preliminary results for response to frequency deviations in UCTE, to deviation of cross-border exchanges; good preliminary estimation of secondary load-frequency regulator in Lviv;
- 3rd type trial: one year of parallel operation (July 1, 2002 – June 30, 2003); the same trial methodology as used for Centrel/UCTE integration; effectiveness of primary and secondary load-frequency regulation; response to sudden changes (both scheduled and unscheduled) of load or generation; voltage control on-cross-border links;

3) Turkey/CEN [10]:

- no 1st type trial (as the Turkish system was not a part of a synchronous area, but actually a separate synchronous area);

- 2nd type trial: two 2-week trials undertaken; first trial (January 11-24, 2010) was to examine operation under high load conditions; second trial (March 22-April 5, 2010) – under low load conditions;
- First Phase (September 18, 2010) of 3rd type trial which can be called *Stabilization Period* (when no scheduled cross-border exchange between Turkey, Bulgaria and Greece was allowed);
- Second Phase (July 2010 - June 2011) of 3rd type trial which can be called *Physical Exchange Period* (non-commercial cross-border exchange was allowed);
- Third Phase (June 2011 - September 2012, prolonged until autumn 2013) of 3rd type trial which can be called *Commercial Exchange Period* (limited commercial cross-border exchange was allowed);

Attempting to summarize this experience for Baltic PS, we suppose that the precedent of Burshtynskaya island cannot be applied to Baltic system and the system should be subjected to operational trial in island mode (1st type trial). Nevertheless, the system should be exempted from challenge to withstand *n-1* incident in island mode as loss of 1350 MW would be too difficult to ride through without cross-border support in the first minute after the incident.

8. Conclusions

1. The European Commission recently declared the sound and technically justified viewpoint on power system control: who controls synchronicity of a power system operation, actually controls such a system in essence. This viewpoint is crucially applicable to Baltic system.
2. Baltic power systems should be considered as one control area or one control block vis-à-vis neighbouring Poland system (i.e. CEN) as regards, at least, frequency regulation, mutual support in emergency cases and use of cross-border transfer capacities.
3. The Baltic PS integration into CEN synchronous area via *LitPol Link* will be tighter in terms of cross-border capacities than that of CENTREL, Ukraine (with Moldova) and Turkey, with the ratio of total transmission capacity and peak demand as high as 23 %.
4. The safety margin of *LitPol Link* seems to be an open question. The huge size of *n-1* unit (1350 MW) may require of significant purchases of tertiary reserves outside the system. To diminish *n-1* unit’s impact on reserve purchase via *LitPol Link*, a part of tertiary reserve could aquired via HVDC links.
5. The Baltic PS has huge secondary control reserve capable to replace *n-1* unit (1350 MW) in zero-export operational mode.
6. Burshtynskaya island precedent cannot be applied to Baltic PS and the system should be subjected to operational trial in island mode (1st type trial).
7. Baltic PS the system should be exempted from challenge to withstand *n-1* incident in island mode as loss of 1350 MW would be too difficult to ride

through without cross-border support in the first minute after the incident.

8. Baltic secondary control system will be provided with a frequency leader to cope with the system defense or restoration. The transmission system operator (*LT*, *LV* or *EE*) with highest *K*-factor has most chances to take such a responsibility.
9. The paper presents preliminary estimate values of Baltic secondary and tertiary control reserves. The comprehensive evaluation of these reserves will be provided by the on-going feasibility study which expectedly will be sufficient for preparation of Catalogue of Measures for Baltic/CEN integration.

9. References

1. Opinion of the European Economic and Social Committee on 'Getting EU energy islands connected: growth, competitiveness, solidarity and sustainability in the EU internal energy market'. Official Journal of the European Union. 2013/C 44, p. 9-15.
2. BEMIP (Baltic Energy Market Interconnection Plan) 3rd Progress Report. June 2011. http://ec.europa.eu/energy/infrastructure/doc/20120726_3rd_bemip_progress_report_final.pdf
3. Decision No 1364/2006/EC of the European Parliament and of the Council of 6 September 2006 laying down guidelines for trans-European energy networks. OJ 2006/L 262, p. 1-23.
4. Network code development process. European Network of Transmission System Operators for Electricity. February 17, 2012. <https://www.entsoe.eu/major-projects/network-code-development/>
5. ENTSO-E. Operation Handbook, Policy 1: Load-Frequency Control and Performance. <https://www.entsoe.eu>.
6. Ibidem, Policy 5: Emergency Operations
7. V. Radziukynas, S. Kadiša, A. Klementavičius, N. Radziukynienė, A. Leonavičius. Technical feasibility of the largest generating unit in the Baltic power system. Proceedings of the 6th International Conference on Electrical and Control Technologies (ECT2011):Kaunas, Lithuania, May 5-6, 2011, pp. 325-329.
8. CENTREL Regional Activities. Report on Review of Available CENTREL Documents, Task 2.1. Prepared by Electrotek Concepts, Inc. January, 1998
9. I. Biernacka, D. Miotke, I. Radzio. Przyłączenie Wyspy Bursztyńskiej do systemu UCTE. Biuletyn Miesięczny. Last available in 2003 at <http://www.pse.pl/>.
10. Turkish Electricity Transmission Corporation. Mevcut enterkonneksiyon hatlarının net transfer kapasiteleri duyurusu. <http://www.teias.gov.tr>.

TRANSFORMER MODEL BASED ON ADMITTANCE INVERTER

Adam ABRAMOWICZ

Warsaw University of Technology, Institute of Electronic Systems, Poland

Abstract: The transformer theory based on impedance inverter with inductances is well known and quite successful in describing electrical properties of power as well as RF transformers. Any circuit theory textbook has at least several pages on transformers modelled with mutual inductances i.e. impedance inverter. In many cases up to 10% of the student book is devoted to transformers and mutual inductances. Thus writing about a new model of transformer is quite surprising and may be annoying. But there are some aspects of the existing theory, which are not consistent with the transformer physical properties. In the paper basic facts on magnetic field distribution and its relation to transformer model are given. And first of all a new model of transformer based on admittance inverter consisting with inductances is presented.

Keywords: transformer, magnetic coupling, impedance inverter, admittance inverter.

1. Introduction

A transformer is a device that transfers energy between its magnetically (inductively) coupled windings. A varying current in the primary winding creates varying magnetic flux in the transformer core and consequently varying magnetic flux through the secondary winding. As a result one can observe varying voltage and current in the secondary winding. A long list of great researchers contributed to the discovery, design and theory of transformers starting from Michael Faraday [1] and Joseph Henry and ending with Karoly Zipernovskiy, Otto Blathy and Miksa Deri (ZBD) [2], William Stanley [3] and Charles Proteus Steinmetz [4]. The discovery of electromagnetic induction and development of transformers as well as development of their theory were done in nineteenth century. Nowadays transformers range in size from thumbnail-sized units hidden in microphones to units weighing hundreds of tons used in the power grid. A wide range of transformer designs are used in electronic and electric power applications. Transformers are essential for the transmission, distribution, and utilization of electric power. The Steinmetz circuit includes an ideal transformer thus a

non-existing element. The ideal transformer is a useful tool in circuit modelling of many structures and systems. It has a very simple chain matrix that corresponds to real transformer properties: isolation between windings, transformation of voltages and currents. The ideal transformer parameters are constant in frequency and time. They do not depend on magnitude thus describe a perfect, linear element. The ideal transformer shown in Fig.1 belongs to the class of abstract models. Its chain matrix is as follows:

$$A = \begin{bmatrix} 1/p & 0 \\ 0 & p \end{bmatrix} \quad (1)$$

where: transformer turns ratio p ($p=N_s/N_p$, number of turns in secondary and primary winding) is defined as:

$$\frac{U_1}{U_2} = 1/p \quad (2)$$

$$\frac{I_1}{I_2} = p \quad (3)$$

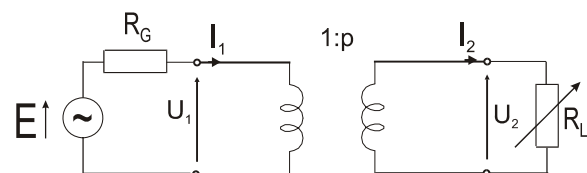


Fig. 1. An ideal transformer

For the ideal transformer the ratio of input voltage to output voltage and ratio of input current to output current are independent from both source resistance R_G and load resistance R . In real transformers such ratios depend on load resistance and source resistance. Moreover the transformer parameters depend on frequency and signal level. Due to non-physical properties the ideal transformer is a reference model used to compare and classify other linear transformer models. In this paper the models of linear transformer based on inverters are considered. The model of

transformer employing impedance inverter with inductances (i.e. mutually coupled inductances) is well known and commonly used. The new transformer model employing admittance inverter with inductances is introduced. The properties of both models are compared and discussed.

2. Mutually coupled inductances

A most popular linear model of the transformer is based on mutually coupled inductances. Mutually coupled inductances are in fact an impedance inverter. The transformer circuit with mutually coupled inductances is shown in Fig.2.

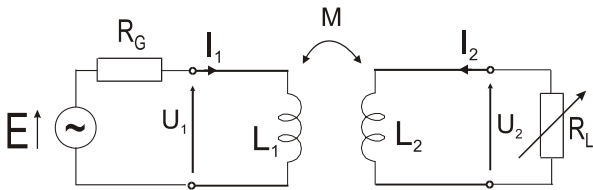


Fig. 2. Model of transformer based on mutually coupled inductances

When inductances are coupled the obvious circuit is assumed with parallel mutual inductance M introduced between inductances L_1 and L_2 resulting in T-type circuit. The same model drawn with impedance inverter is presented in Fig. 3.

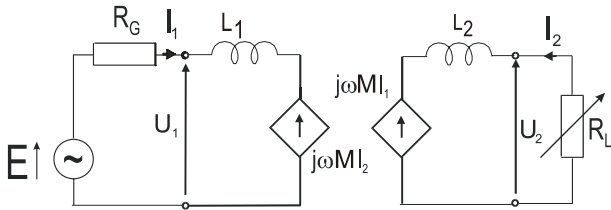


Fig. 3. Model of transformer based on impedance inverter. Diamonds with arrows are current controlled voltage sources

S. B. Cohn introduced immittance inverters in 1957 [5]. He used them for design of microwave direct-coupled filters. Inverters are closely related to the gyrator [6]. Inverters are used to describe couplings between resonators and transmission lines. The circuits with inverters are very convenient in creating their immittance matrices. The circuit in Fig. 3 can be described with the following equations defining the impedance matrix parameters:

$$U_1 = j\omega L_1 I_1 + j\omega M I_2 \quad (4a)$$

$$U_2 = j\omega M I_1 + j\omega L_2 I_2 \quad (4b)$$

It is convenient to define the coupling coefficient k and leakage coefficient σ .

$$k = \frac{M}{\sqrt{L_1 L_2}} \quad (5)$$

$$\sigma = 1 - k^2 \quad (6)$$

Additionally one can remember that turns ratio p is related to inductances of primary and secondary winding as follows:

$$p = \sqrt{\frac{L_1}{L_2}} \quad (7)$$

Let us compare the chain matrix (1) with the chain matrix of the model in Fig.3 given below.

$$A = \frac{1}{j\omega M} \begin{bmatrix} j\omega L_1 & -\sigma \omega^2 M^2 / k^2 \\ 1 & j\omega L_2 \end{bmatrix} \quad (8)$$

The ABCD matrix (8) transformed according to (7) is somehow similar to (1) but its off diagonal elements are not zero.

$$A = k \begin{bmatrix} 1/p & j\sigma \omega M / k^3 \\ 1/j\omega M k & p \end{bmatrix} \quad (9)$$

Even assuming that $k = 1$, it is clear that mutually coupled inductances are not equivalent to ideal transformer because it is impossible to specify first $\sigma = 0$ and then M infinite. These two conditions contradict each other. They are non-physical. Anyway the transformer model based on impedance inverter is used all over the world.

By changing the load resistance R_L between 0 and infinity it is possible to obtain ratio of currents and voltages on primary and secondary windings. For short circuit ($R_L = 0$):

$$I_2 = -\frac{k}{p} I_1 \quad (10)$$

For open circuit ($R_L = \infty$):

$$U_2 = kp U_1 \quad (11)$$

The short circuit condition applied to the secondary winding results in strange behaviour of magnetic flux in the transformer core and disagreement between the model and observations. As can be seen in [7] and in many papers on computations of electromagnetic field distribution in the transformer core [8-9] the magnetic flux tends to zero in the area of short-circuited secondary winding. In [7] measurements show that in the core on primary side the magnetic flux is high, while in the core on the secondary side the magnetic flux is small. Certainly this is different than theory resulting from equations given e.g. (4a). Under short-circuit condition (4a) produces U_1 close to zero ($I_2 = -I_1$, and $M = L_1$ for a transformer with $p = 1$) while it is not observed in reality. The problem of magnetic field (magnetic flux) distribution is known from twenties of the previous century [10-11] but finally neglected and

underestimated [13]. Now when electromagnetic modelling is common one can analyze transformer behaviour completely.

3. New model of transformer

It is possible to create another models of a transformer. Let us consider a transformer as a transducer, which converts input current into output current. In such a way one can use admittance inverter [5,14] to model transformer properties. The admittance inverter should base on inductances because the transformer operates due to magnetic fields. The new transformer model based on admittance inverter is shown in Fig. 4. In the model L_s denotes coupling inductance. Other parameters are the same as in the classical model.

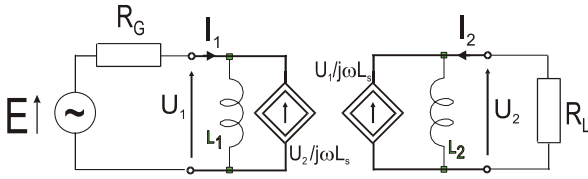


Fig. 4. Model of transformer based on admittance inverter. Double-line diamonds with arrows are voltage controlled current sources

The circuit in Fig. 4 can be described with the following equations defining the admittance matrix parameters:

$$I_1 = \frac{1}{j\omega L_1} U_1 + \frac{1}{j\omega L_s} U_2 \quad (12a)$$

$$I_2 = \frac{1}{j\omega L_s} U_1 + \frac{1}{j\omega L_2} U_2 \quad (12b)$$

It is convenient to define the coupling coefficient k_s .

$$k_s = \frac{\sqrt{L_1 L_2}}{L_s} \quad (13)$$

The leakage coefficient σ is defined according to (6)

$$\sigma = 1 - k_s^2 \quad (14)$$

and transformer ratio p is the same as (7).

The ABCD matrix of the new model is as follows and it has again the off diagonal elements different than zero.

$$A_S = \frac{-1}{k_s} \begin{bmatrix} 1/p & j\omega L_s k_s \\ \sigma / j\omega L_s k_s & p \end{bmatrix} \quad (15)$$

Even assuming that $k_s = 1$, it is clear that admittance inverter is not equivalent to ideal transformer because it is impossible to specify first $\sigma = 0$ and then $L_s = 0$. These two conditions contradict each other. They are non-physical. But this time the model agrees with the magnetic flux distribution in the transformers core. By changing the load resistance R_L between 0 and infinity it is possible to obtain ratio of currents and

voltages on primary and secondary windings. For short circuit ($R_L=0$):

$$I_2 = -\frac{k}{p} I_1 \quad (16)$$

For open circuit ($R_L=\infty$):

$$U_2 = kpU_1 \quad (17)$$

The basic properties of the new transformer are the same as in the ideal transformer and mutually coupled inductances cases. The short circuit condition applied to the secondary winding does not results in a strange behaviour of magnetic flux in the transformer because U_2 is equal to zero and there is no influence of the secondary winding on primary side. Zero voltage means zero of the magnetic flux, which is in agreement with observations and simulations.

4. Comparison of models

A comparison of basic parameters of transformer models presented above is given in **Table 1**. Both models predict the same ratio of currents and voltages. When one assumes ideal coupling i.e. coupling coefficients equal to 1 the ratio of currents and voltages is the same as in ideal transformer. The only, but quite important, difference between impedance inverter and admittance inverter is in input impedances. For short-circuited secondary winding the input impedance of the transformer modelled with impedance inverter is zero ($k=1$). For short-circuited secondary winding the input impedance of the transformer modelled with admittance inverter is equal to impedance of the primary winding. For open-circuited secondary winding the input impedance of the transformer modelled with impedance inverter is equal to impedance of the primary winding. For open-circuited secondary winding the input impedance of the transformer modelled with admittance inverter is infinite ($k_s=1$).

Table 1. Comparison of transformer models

	model with impedance inverter	model with admittance inverter
ratio of voltages	$U_2 = kpU_1$	$U_2 = k_s pU_1$
ratio of currents	$I_2 = -\frac{k}{p} I_1$	$I_2 = -\frac{k_s}{p} I_1$
short circuit at secondary winding	$Z_{we} = j\omega L_1(1 - k^2)$	$Z_{we} = j\omega L_1$
open circuit at secondary winding	$Z_{we} = j\omega L_1$	$Z_{we} = \frac{j\omega L_1 k_s}{(1 - k_s^2)}$

The models are different. They have the same characteristic parameters except input impedances. In some cases especially at radio frequencies the measured impedances are closer to the model with admittance inverter. Both models can be easily appended with losses,

although it is somehow easier to calculate influence of lossy windings in the model with admittance inverters. The circuit model with impedance inverter can be presented in the form of a T-circuit comprising mutually coupled inductances. The circuit model with admittance inverter can be presented in the form of a π -circuit. But it should be stressed that a transformation of the T-circuit corresponding to the impedance inverter into its π -circuit representation employing Star-Triangle transformation produces different π -circuit than that representing the model with the admittance inverter.

5. Conclusions

In the paper a new model of a transformer is presented. The new model is based on admittance inverter. The reason for introducing the new model is to find better agreement between magnetic flux distribution in the transformer core and the circuit description of transformer. Although the circuit and equations are different the obtained model has basic parameters the same as a traditionally used model with mutually coupled inductances. The difference is in the input impedance of the transformer. The new model presented is simple and easy to comprehend it can be advantages over other more complicated transformer models e.g. [15].

6. References

1. Faraday, Michael: "Experimental Researches on Electricity, 7th Series". *Philosophical Transactions of the Royal Society of London* 124, 1834, pp 77–122
2. Zipernovsky C., Deri M., Blathy O.T.: *Improvements in induction apparatus for the purpose of transforming electric currents*, Deutsches Reichspatent 40414, issued March 6, 1885
3. Stanley, W.: *Induction Coil*, U.S. Patent 349 311, issued Sept. 21, 1886
4. Steinmetz, C.P., Berg E.J.: *Theory and Calculation of Alternating Current Phenomena*, McGraw Publishing Company, New York, 1897
5. Cohn S. B.: Direct-coupled resonator filters, *Proc. IRE*, vol. 45, Feb. 1957, pp. 187–196
6. Tellegen D.: The gyrator, a new electric network element, *Philips Research Reports* 3, 1948, pp. 81
7. Alfás S.: Basic electric quantities updated in non-abstract terms, *Proc. PIERS 1991*, Cambridge 1991, pp.470-476
8. Stojkov M., Damir Sljivac D., Jozsa L.: Electric and magnetic field computation of 35 kv voltage level of transformer substation 35/10 kv using the cdegs software, *Acta Electrotechnica et Informatica*, Vol. 10, No. 4, 2010, pp. 64–68
9. Tsili M.A., Kladas A.G., Georgilakis P.S., Souflaris A.T., Paparigas D.G.: Wound Core Power Transformer Design: Classical Methodology and Advanced Magnetic Field Analysis Techniques, *Advanced Research Workshop on Modern Transformers*, ARWtr 2004, 28 -30 October 2004, Vigo – Spain, pp. 23-28
10. McEachron K.B.: Magnetic flux distribution in transformers, *A.I.E.E. Trans.*, vol. 41, 1922, pp. 247-261
11. Dahl O.G.C: Separate leakage reactance of transformer windings, *A.I.E.E. Trans.*, vol. 44, 1925, pp. 787-791
12. Boyajian A.: Resolution of transformer reactance into primary and secondary reactances, *A.I.E.E. Trans.*, vol. 44, 1922, pp. 805-810
13. E.E. Staff of MIT: *Magnetic Circuits and Transformers*, John Wiley & Sons, New York 1943
14. Abramowicz A.: Analysis of coupled dielectric resonators by means of eigenfrequency method, *Proc. 24th European Microwave Conf.*, Cannes 1994, pp. 1197–1202
15. Dixon L.: Deriving the equivalent electrical circuit from the magnetic device physical properties, Unirode Corporation Seminar, Oct. 1994, pp. R3-1-R3-6

DISPATCH TRAINING FOR TSO FROM POWER FLOW CALCULATIONS

T. KUZNECOVS*, A. MAHNITKO*, T. LOMAN*, V. RIMAREVS**, A. DAMBIS**

*Rīgas Tehniskā Universitāte, Latvia; **Augstspieguma tīkls, Latvia

Abstract: Modern power systems are well but not fully automated. Therefore, dispatchers are needed for reliable power system operation in any conditions. Training in emergency management promotes the development of skills that are very important, but do not come with experience. Efficiency of training depends on the level of realism and on the assumptions made in the model. In fact, the most realistic model - a complete copy of the original system. The way from the simplest model to more realistic model has certain feasibility limits in model development. The more realistic model is less available because the more difficult to make it in the right way. "Very realistic model" has another drawback - a time-consuming data preparation for the exercises. In this article we will try to describe how to build a relatively simple system for TSO (Transmission System Operator) dispatcher training based on a power flow calculation program and on a SCADA (Supervisory Control And Data Acquisition) system display emulator.

Keywords: TSO dispatcher training; power flow; cross reference; emulator; calculations.

1. Problem definition

None problem can be solved if it was not defined in proper way. Suppose we are planning to train TSO dispatchers for rare operational conditions. What we need in and there we will go?

TSO dispatchers work with SCADA system in most cases. Therefore, first of all, we need in working place very similar to original SCADA workstation. Of course, dispatcher can study on completely different system. But, in case of very similar operational environment, dispatcher trains not only "What to do?" but also learns "the correct button to push". It will be very useful in our opinion, if TSO dispatchers will train unusual conditions with usual operational environment.

The second, we must have the study system. Study system, of course cannot be the real, except "the field tests". We assume the study system is the model of the real transmission system. What are the prerequisites to the model for TSO training? The model must display all

information necessary for operations, must reproduce all changes in real life close to original and must support the proper response time for loop command-action-result.

The third, the study system must be connected with operational environment in order to reflect time-related changes in power system model and in order to control equipment remotely. This can be done in two ways. The common data base is the first way; the way of data links with conversions is the second.

There are two types of model available: physical model and mathematical model. Physical model is the copy, in most cases scaled copy, of the system studied. Physical model is most accurate, but extremely expensive, therefore only the small system can be modeled at the reasonable cost. Mathematical models can be based on special digital hardware; there each power system element can be modeled, with connection to real control equipment, or can be based on calculation programs. The second way is more acceptable for TSO because simplicity and very low cost, in comparison with digital hardware. Of course, model build on digital hardware is more accurate, but it is very problematic way to create the system dimensioned for TSO based on this approach. Calculation programs perform power system dynamics calculations or power flow calculations. Power system dynamic more applicable if the system subjects to large changes in case of faults. Power flow calculations much more simple and work better if the system is stable with relatively small changes. It is impossible to simulate the power system behavior during the transients with power flow model.

It appears from mentioned above, abilities of training simulator strongly depends on the model of real system. The physical model is needed for equipment studied, if we want to check the relays or PMU (Phasor Measurement Units). The power system dynamic model is needed, if we want to study transients and generator excitation systems [11]. We are very happy in our case, because the human is the slowest active element in electric power system control and cannot find the problem and respond in time less than one second. The several seconds measurement data refresh step is typical for SCADA system. We must obtain response time for

loop command-action-result less than half of data refresh step in order to perform realistic model behavior from the operator point of view according to Nyquist-Shannon-Kotelnikov sampling theorem. Therefore, we can try power flow calculation program in order to create the model for TSO dispatcher training as a good approach if we can sample this model close to the real system state in each step.

Our task is to create automated power flow calculations on power system model with possibility of control equipment remotely by operator via usual operational environment. We need in calculation program with connection to working place of dispatcher. We also need in fast performance.

2. Automated power flow calculations

We use MUSTANG [1], [3] under Windows [developed by V. Ivanov, V. Rimarev] industrial program for power flow calculations in our Operational Planning Department. The program has so called “black box” mode in order to make calculations faster. “Black box” mode means only ASCII (The American Standard Code for Information Interchange) file packet data can be used for data input, output and case control with no other (tabular or graphical) user interface. This allows program be loaded in memory and not perform unnecessary disk operations.

ASCII file packet data are in form KEY; ID; VALUE. Idea of this data representation is clear, if we imagine unlimited rectangular table with rows and columns, there program puts all the data and controls. In our case, KEY – the number of column, ID – the number of row and VALUE – is value to get or to put. Each line in this file corresponds to one value or command in most cases. Program has directory for input data and stencil file for output data. Packet data exchange is not so compact, but simple, powerful and very flexible.

Power flow calculations are “bus oriented”, but dispatch operation is “breaker oriented”. As a rule, programs use special logical commutation elements in order to adjust power flow calculation for dispatcher needs. Program MUSTANG hasn’t “breaker oriented” model, because it can calculate load flow even if some branches have very small reactance (e.g. about 0.00001 Ohm). User can easy connect buses with small reactance branches in closed loops, or chains, or how he wants. Therefore, the full-topology model can be created without “logical” breakers. In fact, program MUSTANG works without numerical instability in case of very small reactance, but not in case of extremely small reactance less than one micro Ohm (such small reactance, seems, has none physical sense in load flow calculation). It is, of course, impossible to control different voltages at buses connected with “zero impedance” line. Algorithm for calculation of “very short wires” (i.e. breakers) in MUSTANG load flow model was written by V. Ivanov about fifteen years ago. Author considered analogous method must-have of each industrial power flow calculation program. We hope this already done in many programs, but no information available for us about it. Therefore, this data may be useful also for load

flow calculation program developers. Advantages of full-topology model of control area creation inside “bus oriented” load flow model are possibility to see the flow via breakers and absence of temporary buses in case after bus split. As disadvantage we can note bus count increase in case, but this is not critical. In whole, we can gain time for calculation based on above mentioned approach.

3. SCADA system display emulation

We have SCADA system from General Electric in our Dispatch Department. This system allows develop customer’s own programs in order to increase SCADA abilities and meet each customer’s requirements. This very positive feature made it possible develop [developed by M. Korshunov] the program in order to get original displays from SCADA system and show the real time data, or historical data, or text formatted data for SCADA users in local network outside the SCADA system. Why we need in this program? This program works on Windows computer in local network and the SCADA system not feel any load in this case. This program works fast and secure and provides more functionality in comparison with genuine SCADA tools. Our program can also read and write ASCII data in form ID; VALUE; TLQ. In this case, ID – the measurement or signal identifier, VALUE – is value to get or to put, TLQ – is the quality code (good, bad, etc.) of information. In fact, our SCADA system display emulator also supports packet data exchange. SCADA system display emulator works also inside the SCADA system, but not installed in real time SCADA in order to avoid the possibility of remote control execution to ASCII file by accident.

4. Automated data exchange and handling

Both our programs are ready for automated data exchange. But we need, additionally, in time going, in values changing and in definition what is what if we want to link power flow calculation data and SCADA data. Decision for third program development was taken in our case. This program has ASCII file packet data exchange (from file to file) with MUSTANG in MUSTANG form and ASCII file packet data exchange (from directory to file/files) with SCADA system display emulator in emulators form.

Initially, the program [developed by V. Rimarev] performs mapping of values according to cross reference (or X-reference) table. This idea is the typical approach to data mapping problem and used, for instance, in SCADA system from General Electric.

Let \mathbf{a} – the n-dimensional column vector from the “Black box” model space and \mathbf{b} – the counterpart n-dimensional column vector from the the SCADA data space. Then the coordinate system transforms can be done according (1a) and (1b):

$$\mathbf{b} = \mathbf{D} \times \mathbf{a} , \quad (1a)$$

$$\mathbf{a} = \mathbf{D}^{-1} \times \mathbf{b} . \quad (1b)$$

There **D** is $n \times n$ diagonal matrix with all d_{ii} elements are predetermined constant rational numbers in our case.

This can be written for instance in ASCII file with n rows, there each row consists of $b_i; d_{ii}; a_i$, there b_i – the SCADA data (measurement or signal) identifier, d_{ii} – the multiplier in order to perform scale adjustments for different measurements, a_i – the power flow model information type with the data identifier. This mapping allows determine the other value adjusted in the “Black box” model or in the SCADA display emulator if only one of the counterpart values was set.

Also, the program has its own internal clock. This clock not only shows the time, but performs the scheduled changes in terms of SCADA values. In case, if the values are mapped, the power flow program performs necessary calculations in order to recreate the scheduled changes on model. Schedules have a 24 hour loop with one minute step. Instructor can start the study system from any time. The program has the time multiplication accelerator in order to simplify the check of schedules on study system during preparation for training.

Then the above mentioned functions of data exchange were developed, it became clear, that the data handling will make the program more powerful. The build-in calculation module RTC (Real Time Calculations) was developed in order to perform instant or time dependent calculations in terms of SCADA system data.

Typically, each y datum calculated in RTC has the own function. This can be expressed as (2).

$$y = F(y_{t=0}, y_{t=\Delta t}, x_1, \dots, x_n, t/\Delta t); \quad (2)$$

where, $y_{t=0}, y_{t=\Delta t}$ - the initial and the target values of y ; x_1, \dots, x_n - the other data values and constants; $t/\Delta t$ – per unit time value based on Δt – calculation lifetime.

Each RTC function has its own lifetime or no lifetime (simple calculation formula). The lifetime starts, if the function is triggered by definite data change and goes synchronous with the internal clock until Δt , in this case the calculation ends, or until next trigger, in this case the lifetime restarts again. The y value gradually changes during RTC function process from initial value to final depending on the time value. Note, the data values not mandatory the real SCADA points and can be also special calculation points.

Then the data comes from and goes to SCADA system display emulator, they pass through calculations. Gradual transitions or relay actions can be modeled in this way. Moreover non-electrical values, for example water inflow and flow rates for hydro power plants or ambient temperature, can be calculated.

Simplified data exchange and handling process is shown in “Fig. 1”. Data exchange stages in terms of power flow program are drawn with filled arrows. Data exchange stages in terms of SCADA values are drawn with blank arrows. Power flow data are mapped. SCADA values can be mapped or used in RTC module. Therefore some SCADA points can be idle and not be used for SCADA display emulators. Than the mapped value goes through cross reference, it changes the data loop. User can participate in data exchange process

even with unmapped values or put the commands in “black box”. Moreover, user can calculate on external module, if he, for instance, is not satisfied with RTC or with power flow model in parallel or instead the process stages. Note, that data for data exchange is, typically, the small part of the data used by programs.

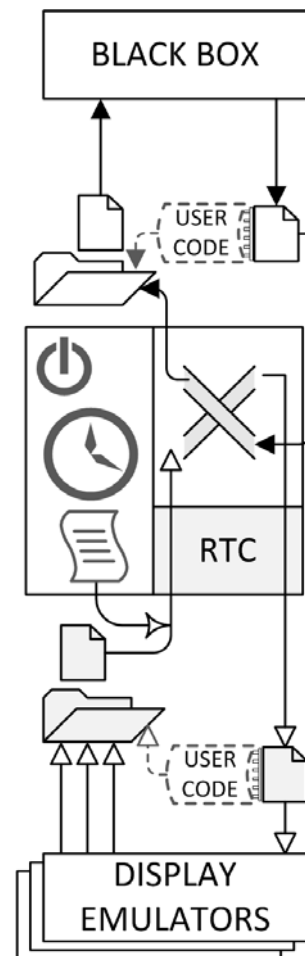


Fig. 1. Simplified data exchange and handling process

5. Conclusions

There are many things to do along the way of development the own system for TSO dispatcher training. However, the way, described above, is practically good and realistic. This is predicated upon our current stage. System works and we see, how to improve it. For instance, it is possible to organize transition via fault by dynamic calculation in case of eventual problems infeasible by means of power flow calculation program.

Question is: “Why we try to develop the system for TSO dispatcher training by ourselves? There are so many systems on the market!” Actually, solving the problem by do-it-yourself development method has only one disadvantage if it based on standard components: problem can be infeasible, i.e. it can be impossible to reach certain quality of solution at reasonable time and money. On the other hand, we have two advantages, especially, if we can solve the problem. First, the experience learned. We will know that we want better

because the better understanding the problem. Second, as a result, our system can be more economical because the right choice and free support and more usable because absence of redundant modules and capabilities. Of course, if you must check the relays, you will need to buy the industrial training simulator like RTDS [7]. You will not find any software alternative in this case. On the other hand, if you plan use mathematic model for simulation and do not need in data refresh more than one time per second, you can start from simple model and develop your system step by step without additional powerful hardware.

6. References

1. V. Ivanov, V. Rimarev, J.Gerhards, A. Mahnitko, Calculations Of Steady And Transient States In The Complex Power Systems According To The Program "Mustang"// CONTROL OF POWER & HEATING SYSTEMS, 5th International Conf. CP&HS'02, Zlin, Czech Republic, May 21-22, 2002, p.116, CD.
2. T.J. Overbye, P.W. Sauer, C.M. Marzinzik, G.Gross A User-Friendly Simulation Programm for Teaching Power System Operator // IEEE Transactions on Power Systems, Vol. 10. No. 4, November 1995.
3. Mahnitko A., Lomane T., Kuznetsov T., Rymarev V. PROGRAM SET MUSTANG USE IN THE DISPATCH CONTROL FOR THE UNITED EPS REGIMES // 9th Intern.Conference CPS'2010 (CONTROL OF POWER SYSTEMS '10) , High Tatras, Slovak Republic, May 18-20, 2010, Štrebské Pleso
4. Моделирование, синтез и оценка режимов межсистемных связей объединенных энергосистем / Махнитко А. Е. [и др.] // Электричество. - 2011. - N 5. - С. 8-16
5. Рабинович М.А., Моржин Ю.И., Потапенко С.П. Комплекс программ технологической обработки и отображения оперативной информации // ОАО «НТЦ электроэнергетики» Москва
6. Nesterenko M. „Multi-Control Center Dispatcher Training” 2011 EMS Users Conference Philadelphia, PA September 18-21, 2011.
7. RTDS Technologies. 100-150 Innovation Drive Winnipeg, Canada. <http://www.rtds.com>
8. OPAL-RT Technologies. 1751 Richardson, Suite 2525 Montreal, Quebec, Canada. <http://www.opal-rt.com>
9. Incremental Systems. 3380 146th Pl. SE Ste. 440, Bellevue WA, 98007. <http://www.incsys.com>
10. PowerWorld Corporation. 2001 South First Street, Champaign, IL 61820 <http://www.powerworld.com>
11. Pan European Grid Advanced Simulation And State Estimation (PEGASE). Tractebel Engineering S.A. Avenue Ariane, 7 1200 Brussels BELGIUM <http://fp7-pegase.com>
12. Закрытое акционерное общество «Монитор Электрик». Российская Федерация, Ставропольский край, г. Пятигорск, ул. Подстанционная, 28 357506. <http://www.monitel.ru>

A REVIEW OF THE EFFECTS OF ELECTRIC VEHICLE CHARGING ON DISTRIBUTION NETWORK OPERATION AND POWER QUALITY

Lauri KÜTT*, Eero SAARIJÄRVI*, Matti LEHTONEN*, Heigo MÖLDER**, Jaan NIITSOO***

*Aalto University, Dept. of Electrical Engineering, Finland

**Tallinn University of Technology, Dept. of Electrical Engineering, Estonia

***Tallinn University of Technology, Dept. of Electrical Power Engineering, Estonia

Abstract: Electric vehicles (EVs) are currently one of the active topics being discussed in transportation sector. In everyday use the EV would be staying for the longest in home parking space and it is also rather convenient to use the electric network supplying a household for charging the EV. This means rather high additional load for the residential network. Based on the literature survey, this paper presents an overview on the expected impacts to the residential distribution networks. Expected network loading is described and power quality aspects related to high loading, such as voltage drop in the point of common coupling (PCC), voltage unbalance and harmonics are discussed. This paper aims to summarize research carried out up to date and gives general guidelines for evaluating the EV charging effects in the low-voltage distribution networks.

Keywords: Electric vehicle, distribution network, power quality, voltage drop, voltage unbalance, harmonics.

1. Introduction

A modern vehicle with internal combustion engine uses on the average only 12,5% of primary energy contained within fuel. For an electric vehicle (EV) that is charged using power produced in thermal power plant, the primary energy utilization rate of 23,1% [1] shows significant improvement. This means also that using the EVs the CO₂ emissions of the transportation sector would be significantly lower. EVs could provide further reduction of emissions if charged from power plants utilizing renewable energy sources.

Promoting the EV use and EV market breakthrough, the likely share of EVs on the roads has been discussed in many studies [2]. Optimistic estimates for USA have assumed as much as 1,5 million EVs on the roads by 2016 and 50 million by 2030 [3]. EVs expected market share would be at 10% in 2015 and with rise predicted from 2015 onwards to reach even 50% in 2025 [4]. A more realistic note estimating 300 thousand vehicles to

be sold annually in USA by 2017 [5] seems more achievable. In Europe, Belgium is expected to have 30% of EV penetration by 2030 [6], which could be realistic given the EU priorities in energy efficiency. Similar plan for Germany [7] targets 1 million EVs for 2020 and 5 million EVs for 2030.

In order to provide an efficient and comfortable use of EVs, the EVs would need the batteries charged after every longer trip. For the most of the week the EV would be used for daily commuting, so the end point of the trips is most likely home [8]. Here the EV is most likely to be recharged, presenting also a healthy load increase for the residential distribution network. EV charging is different from other residential loads as the power utilized is significant and it takes rather long to charge the EV. Thus the probability for simultaneous charging is rather high, compared to other everyday appliances [9].

The residential grids are planned keeping in mind that the load has a steadily increasing trend. For developed countries the load growth rate is rather slow, indicated at percent [11] or few percent annually. Some powerful loads like the addition of heat pumps [12] and air conditioning can however make the power demand growth rather fast. The single-phase EV charging presents load comparable to air conditioner [3] or a water heater [13]. Still, in some areas the network can be rather loaded during intense heating or cooling seasons, with only little headroom for added EV charging load.

The electrical utilities are required to provide continuous supply of power that meets the characteristics set in the electric supply standards (e.g in Europe the utilities are following characteristics provided in EN50160 [10]). The added EV charging load can bring excessive voltage drop in the point of common coupling (PCC), increased level of harmonics and voltage unbalance that could lead to violations of the supply standard from the utility side. Increased harmonics and unbalance present more stress to

distribution transformers and network cables, but also to customers' appliances. This would decrease both the utilities and customers devices' life expectancy but could also lead to power outages. These topics are addressed in present paper and have to be considered by the electric utilities prior to making the conclusions on distribution networks' (especially low-voltage networks) capabilities of supporting the EV charging.

2. EV characteristics, usage and charging

In context of present paper the electrical vehicles considered are those with 1) significant on-board energy storage and 2) ability to use the mains power supply for charging the energy storage. Typical such vehicles are battery electric vehicles (BEVs) and plug-in hybrid vehicles (PHEVs). Due to similar characteristics of the charging process and the on-board battery chargers, there would practically be any differences for the distribution networks depending on the particular vehicle type. Therefore, within this paper, all such vehicles are referred to only as electric vehicles (EVs).

In essence, the EVs could be divided into groups as proposed in [14], with 4 classes of EVs by their size, presented in Table 1.

Table 1. EV classification and battery capacities

Classification	Battery size, kWh	Energy usage Wh/km
microcar	8 ... 12	230
economy	10 ... 14	266
mid-size	14 ... 18	356
light truck / SUV	19 ... 23	510
PEV-10	4.85	(Range 16 km / 10 miles)
PEV-40	16.6	(Range 64 km / 40 miles)

Other basis for classification could be the electric range [15], with PEV-10 and PEV-40 (see Table 1) standing for the all-electric range in miles respectively. The battery maximum capacity is not the sole factor determining the charging characteristics. The energy required for a recharge is directly and most strongly dependent on daily actual energy usage, based on driving patterns. Other factors influencing the electric range can be listed as driving habits, terrain type, weather conditions [17] and many more.

From vehicle traffic investigations there is quite much information available on driving patterns. It is expected that the EV will not provide a significant change in drivers' habits. Driving patterns are highly stochastic; however, the average trip of 42 km per day [3] could be indicated. This can vary based on location, for example if observing rural and urban areas [11]. Daily recharge energy required can be found basically using driven range multiplied by energy required per km.

Battery charger of an electric vehicle can be a rather powerful load, reaching typically from 500 W until 100 kW. Quite powerful chargers are required, if the EV battery with high energy capacity should be charged in a time convenient for the owner, that is, in limited

number of hours. Most typical power ratings for chargers have been listed in Table 2 [18] [19]. Standards applicable for chargers have been laid out in [20].

Table 2. EV charger classification and expected costs

Charging level	Power, kW	Approximate cost, USD
Basic / opportunity	1.4 ... 1.9 (Single-phase, onboard)	500 ... 800
Primary	3.5 ... 6 (1-phase); 8 ... 19.2 (3-phase)	1000 ... 3000
Fast	50 ... 100 (DC charging stations)	30 000 ... 160 000
Ultrafast	200+	> 1 000 000

The home-owners' typical capabilities would be mainly using the EV on-board chargers. The single-phase charging would be especially popular as it uses the same power as provided by each common mains socket. Three-phase charging would be the solution appropriate with larger cars or if faster charging is needed. Still, the three-phase charging is expected not to be as popular for the house-owners as the single-phase charging.

When more power or better connection to grid is available, it can be assumed that the EV could be charged also faster. Still the faster DC charging stations are likely to remain out of reach for a typical homeowner as the expected price for establishing such a charging point can be quite high. The most basic charging set-up is expected to cost 500...800 USD [18] and three-phase charging equipment 1000...3000 USD [17]. Considering the price, EV usage and charging patterns, faster DC charging stations capable of half-hour full charging and "ultrafast" stations capable of full charging in less than 10 minutes [19] are likely to remain enclosed with the service stations.

The most common charging method would still be single-phase charging, which will bring additional power electronic load to the distribution grid. As a result, different power quality issues can emerge in the low-voltage residential networks which have had relatively low load up to now. The question arises – how many EVs home charging could the network support in a manner that the other customers are not affected?

3. Expected network load

It is expected that the EV charging load alone will not be significant enough to cause the deficiencies in power production nor shortage of transmission capacities once the initial EV charging load is introduced [13]. For example, additional energy production for supplying 1 million EVs in Germany is estimated roughly at 20 TWh, that is 0.3% of energy annually produced in Germany [22]. The first of the major questions therefore would not be the overall power production for the supply of EVs even at relatively significant penetration levels.

The electrical engineers in charge of power supply management will more likely see the issues arising from

distribution networks. For the network operation planning, it should be first defined where and when the EVs are likely to be charged. An EV behavior model presented in [23] provides the vehicles most likely whereabouts during the daytime. These are driving, parking at home, parking at work, parking at shopping, parking elsewhere. The most convenient of these selections for charging is while parking at home, after arrival in the end of the working day (4 pm – 6 pm). Some of the EVs are likely also to be charged during the working time, there are estimations of charging start during lunchtime [4] [24]. For the distribution network, office charging is not considered as stressful as home charging. Latter poses higher simultaneity and the intense charging is expected to occur during the same time as the evening power peak (between 5 pm and 10 pm). Additional load during this time means more expensive peak power production [21], affecting the price of electric energy.

The amount of load added by the EV charging is also dependent on the charging management level. For the nature and management of the EVs, three control levels could be identified: uncontrolled or dumb charging, controlled or shifted charging and smart(er) charging [25]. The evolution of level of management and flexibility expected for the EV charging in the near future is laid out in [17] and [26].

3.1. Uncontrolled charging

The simplest charging scenario is uncontrolled charging, which can be defined as charging immediately when the EV is plugged in or in another case after a fixed delay set by user [27]. The issue of convenience here is that customers most likely expect that the EV would be charged as fast as possible after connecting the EV. Taking into account the lack of control functions from the grid towards the customer available at this time, it is likely that this charging scenario will be the initial one. Question from the network side would be that how far the EV penetration could reach before some other charging scenario would be needed.

For the elimination of failures due to overload caused by uncontrolled EV charging, the probable worst cases would need to be addressed and there are some studies available describing these situations. Analysis has generally presented tolerable EV penetration up to 20 ... 25% [28] [29] as no-problem range for the simplest charging scenario. Above this level the network components are very likely to suffer from overload.

3.2. Controlled charging

Charging with load shifting, compared to uncontrolled charging provides the EV owners less control of the process. There are two main methods proposed. The first is load shifting by the control of the network operator and price incentives, and the second one is household individual load shedding. Charging control could benefit from the presence of smart meters that are able to communicate with the distribution network

operator. Using this, control commands would be sent to each EV [16] to start charging, when there is a surplus of power delivery capacity.

Price incentives can be rather motivating to customers [31] [32] for load shedding and shifting the EV charging to off-peak periods. Local management with specifying household each load either as controllable or uncontrollable [33] or priority systems could be used. Simple examples of simpler prioritization of local loads are available from Finland [12]. When sauna stoves are turned on, space heaters are turned off to relieve the power usage.

There are several case studies, pointing out the peak power load decrease due to charging control and the gained benefits. Described in [30], the charge shifting for time between 4 pm and 8 am is observed while 3.5 kW charging power is used. In this case uncontrolled charging, peak demand is reported over 3 times higher than in case of diversified (time shifted) EV charging. This means that significantly higher EV penetration could be reached without network overload. It has been presented in [34] that using controlled charging at 46% penetration level could allow reducing peak power to previous daily peaks. In [11], possibilities to reduce the overload by half, presuming 100 % EV penetration, have been presented. It has been also pointed out that if the charging occurred at off-peak, the power grid in USA as it is now could handle 84% EV penetration [35].

3.3. Smart charging

To further improve the network operation intelligent charging control could be implemented. For realizing the smart charging control, more complex aspects of network operation are observed and two-way communication is a prerequisite [33]. Furthermore, there should also be a charging agent present, this is a computer system responsible for giving priorities, providing the charging commands and using a scenario-based management algorithm to reach the goals of the smart charging process. Although in theory the smart charging applicability and success could be proven, the consumers may want or need to charge their EVs as fast as possible [14], therefore it might not be acceptable when the user has only littlest control on the charging schedule. Charging could be controlled from the network operator side, but also local agent options have been proposed. One of such is presented as a concept of local energy hub, described in [36], which would bring the control of the charging closer to the customer.

Smart charging algorithms could target load leveling for avoiding highest power peaks and for leveraging the effect to the networks, by limiting usage of power that the chargers can provide [32] [37]. Another target could be highest utilization of renewable resources for charging the vehicles [21]. A proposal to use smart charging algorithms to avoid charging with highest transformer temperatures has been presented in [38].

The smart charging management has been shown to provide better results than for example, the tariff-based charging control incentives [32]. It is yet difficult to

estimate the most likely scenarios adopted, as the wider deployment of smart meters and devices capable of smart control in the grid is yet in the future.

4. Voltage drop and voltage in PCC

Charging load is expected to provide higher currents and additional voltage drop is expected on the transformers and cables. By EN50160 [10] voltage deviations of 10% are tolerated up to 95% of the total time. This will be problematic for the customers furthest from the supplying substation, who would also like to use the network for the EV charging. This means that attention should be on the weakest node and worst case scenario [39]. The closer the customer is to the substation, the higher would the allowed power for the charger be.

Analysis considering limit line length and expected voltage drop has been presented in [22] observing both urban and rural networks. An estimate is provided on how long section of distribution line would accommodate specific number 2 ... 8 of charging EVs. The lengths have been identified as 700 m down to 300 m respectively, correlating with the suggestions of the previous analysis.

The winter and summer load in Central European conditions and added EV charging load effects have been presented in [16]. Analysis is focusing on the different power demand time-frames and power peaks associated with them. It is presented that the maximum voltage deviation is likely to remain well under 10% in case of EV penetration levels of 10 and 20%. The simulations present that the voltage deviation is likely to reach 10% for EV penetration level of 30% or slightly above. Similar conclusions have been drawn in [30] where several different scenarios are presented for the voltage drop analysis. Results of 16 A charging in a 230 V network (3.5 kW) are indicating that EV penetration level around 28% would provide 10% voltage drop in the end of the line.

In some cases the voltage drop can be observed with stricter levels. Results of analysis using 5% voltage level tolerance have been presented in [27]. It is concluded that the tolerable range for EVs would be less than 15%, as this penetration level would provide voltage drop of 6%. This assumption is using the chargers with lowest power rating, however for more powerful chargers the voltage drop is expected to be even more significant.

The voltage drop and voltage deviation analysis discussed above was observed in scope of uncontrolled EV charging load. These studies are presenting similar results to network overall loading discussed with the uncoordinated charging case. It could be concluded that EV penetration up to 30% would probably not cause significant violations in voltage level limits.

5. Voltage unbalance

Most likely type of EV chargers to be deployed would be the single-phase chargers found onboard the EV. In general, it can be expected for a larger number of

customers and three-phase system, the current of single-phase loads would be distributed evenly among the three phases. However, the EV charging differs from other single-phase loads due to longer charging times and higher coincidence [9]. Given the stochastic characteristics of the EV owners, there is a good possibility that at some time instances the charging current in one phase is significantly higher. The current imbalance will in turn cause voltage unbalance on the distribution transformer, leading to high currents in the neutral conductor.

The unbalanced voltage in three-phase network can be observed as a sum of positive, negative and zero sequence voltage components. The voltage unbalance is commonly observed as negative sequence unbalance, a relation of negative sequence voltage to positive sequence voltage

$$u_2\% = \frac{U_2}{U_1} \cdot 100\%; \quad (1)$$

where U_1 is the positive sequence voltage and U_2 is the negative sequence voltage of frequency 50 or 60 Hz. The compatibility levels in LV networks have been set by standard at 2% [40]. However some authors have also been using stricter numbers as 1.3% [41]. A common residential area expected unbalance, without EV charging, is likely at 1% or even over this limit [9]. The unbalance that could occur in the network when EV charging is added is dependent on the charging current. A comprehensive analysis has been presented in [9], observing network with 200 customers supplied by 400 kVA transformer. Using random single-phase load placement with 1000 different variations introduced, it is presented that while the expected unbalance for the equipment with 5 A load currents is quite low, multiple single-phase loads having 20 A load current are likely to cause unbalance over 2%.

Voltage unbalance sensitivity definition has been used in analysis in [8]. With the sample load configuration used, it is reported that there is almost 0.9% voltage unbalance in the beginning and over 1.8% unbalance in the end of the feeder, without charging load. For similar stochastic scenario with Monte Carlo method used, a likely distribution of voltage unbalance in the furthest feeder is presented. The EV penetration of 30% is assumed in the network utilizing chargers with 20 A load current during the simulation. Average voltage unbalance is presented as 1.89%, however it is presented that for 34% of occasions the 2% voltage unbalance would be exceeded in the end of the longest feeder.

It is rather difficult to estimate what is the resulting voltage imbalance for a defined EV penetration rates. From the results of the studies it is likely that the EV charging would cause exceeding the standard limits.

6. Harmonic currents and voltages

Every non-linear load in the network produces non-sinusoidal current waveform. Such current can be represented using a sum of different sinusoidal voltage

and current components having different harmonic frequencies. The amount of harmonic voltage and current components, compared to the mains frequency sinusoidal component, is presented with the total current harmonic distortion THDi, calculated as

$$THDi, \% = \frac{\sqrt{\sum_{h=2}^H I_h^2}}{I_1} \cdot 100\%; \quad (2)$$

where h is the harmonic order number, H is the highest number of harmonic observed, I_h is the RMS-value of the current h -th harmonic component and I_1 is the mains frequency current component RMS value. Similarly, the total voltage harmonic distortion THDv is calculated, but with the current values in (2) replaced with respective voltage values.

The harmonics associated with the EV charging are directly related to charger topology. EV battery requires DC for charging and the simplest approach is to use a single-phase full-bridge rectifier, for higher power ratings three-phase diode rectifiers could be implemented. Shortcoming of all the uncontrolled rectifiers is the high current harmonics provided to the AC power networks. Measurements of different first-generation chargers have been presented in [42], revealing uncontrolled or low-control rectifiers with average THDi of 50%. Modern EV chargers, based on controlled fast power electronics, could provide THDi well below 5% at load range 50...100% of rated power [43]. Measurements of modern commercial EVs [44] [45] present charging THDi of 11.6, while also lower THDi has been indicated in [46] at around 4.5%.

The harmonic currents can cause presence of significant harmonic voltages. The standard [10] limits the permissible THDv to 8%, however in many cases lower limits could be set. Worst-case study of residential network harmonic voltages has been presented in [47] where a smaller LV network with 15 kVA supply transformer is observed. Using highest permissible limits for a commercial charger set by standard [48], worst-case current waveforms were constructed, resulting in charger THDi of 17.3%. The network was also loaded with typical household appliances for balance, with background THDv of 1.5%. It is reported that with all households having EV (penetration 100%) the THDv is expected in range from 2.6% to 5.2%. However, a case is also presented for lower penetration of 50% where THDv is not increasing due to addition of EV charging, but remaining at 1.5% level. This kind of variation in harmonics levels can be expected, as different loads can provide the harmonic cancellation [49] effects. This effect occurs when harmonics with different phase angles provide a sum in the magnitude that is smaller than the individual harmonics magnitudes together. Though mentioned in several papers, there is actually quite little practical research on the rate of the harmonics cancellation associated with EV charging and normal household loads.

A worst-case simulation presented in [50] observes the network not as a lumped model but the effects of cables

have been included. This way, the THDv, dependent also on the harmonic voltage drop on the cables, due to the harmonic current present in the cable, can be analyzed for the consumer furthest away from the supplying transformer.

Prediction of voltage distortion levels has been analyzed in [51], taking into account the probabilistic nature of the EV charging currents. The worst case scenario is observed as the time with least residential linear load available during nighttime. EV penetration of 50% is assumed and voltage distortion is calculated for individual buses. The method presented gives a probabilistic output, revealing the expected probability of a voltage distortion above allowed value. This method has its virtue in the fact, that the modern power supply standards [10] state the requirements fulfillment for a specified portion of time. The probabilistic method could be used to determine the probability of each bus to exceed or meet the requirements.

7. Conclusions and discussion

Observing the results provided in the studies discussed, it could be assumed that the EV penetration rate of 20...25% would be tolerable to present distribution networks. This figure seems to apply for both overload as well as power quality issues. It should be kept in mind that expected lifetime of the network components is such that the new networks planned today might have to face substantially high EV penetrations. Therefore, some new approach on network planning would be beneficial considering the future.

Especially the expected voltage unbalance and harmonic levels are rather unpredictable and depend on several stochastic factors. In essence high levels of voltage harmonics and unbalance are possible even with low EV penetration. It would need more research to determine the likely levels associated with everyday EV charging to ensure that even present networks would be capable of providing support for the first breakthrough of EVs.

8. Acknowledgement

This paper is supported by project "Electrical Vehicle Charging Infrastructure for Urban Environments (eSINI)" and ERA NET Smart Grid project "Power Quality and Safety Requirements for People and Electrical Equipment in Smart Grid Customer Domain".

9. References

1. Roe, C., Meisel, J., Meliopoulos, A.P., Evangelos, F., Overbye, T., Power System Level Impacts of PHEVs, 42nd Hawaii International Conference on System Sciences, 2009, pp. 1 - 10.
2. Foley, A.M., Winning, I.J., Ó Gallachóir, B.P., State-of-the-Art in Electric Vehicle Charging Infrastructure, IEEE Vehicle Power and Propulsion Conference (VPPC), 2010, pp. 1 - 6.
3. Alternate route: electrifying the transportation sector. Technical report. New York ISO, Jun 2009.
4. Environmental Assessment of Plug-In Hybrid Electric Vehicles, Electric Power Research Institute, 2007.
5. Assessment of plug-in electric vehicle integration with ISO/RTO systems, KEMA Inc. and ISO/RTO Council, 2010, 121 p.
6. Emissions of road traffic in Belgium, Transport & Mobility Leuven, Jan 2006, 131 p.

7. Nationaler Entwicklungsplan Elektromobilität der Bundesregierung, Die Bundesregierung, Aug 2009, 53 p.
8. Shahnia, F.; Ghosh, A.; Ledwich, G.; Zare, F., Voltage Unbalance Sensitivity Analysis of Plug-in Electric Vehicles in Distribution Networks, Australasian Universities Power Engineering Conference (AUPEC), 2011 21st, pp. 1 - 6.
9. Meyer, J.; Hahle, S.; Schegner, P.; Wald, C., Impact of electrical car charging on unbalance in public low voltage grids, Electrical Power Quality and Utilisation (EPQU), 2011, pp. 1 - 6.
10. EN 50160:2010, Voltage Characteristics in Public Distribution Systems. European standard.
11. Verzijlbergh, R.A., Lukszo, Z., Slootweg, J.G.H., Llic, M.D., The Impact of Controlled Electric Vehicle Charging on Residential Low Voltage Networks, IEEE Networking, Sensing and Control Conference ICNSC 2011, pp. 14 - 19.
12. Rautiainen, A., Repo, S., Järventausta, P., Intelligent charging of plug-in vehicles, The 9th Nordic Electricity Distribution and Asset Management Conference 2010, NORDAC 2010, 11 p.
13. Schneider, K., Gerkensmeyer, C., Kintner-Meyer, M., Fletcher, R., Impact Assessment of Plug-In Hybrid Vehicles on Pacific Northwest Distribution Systems, IEEE Power and Energy Society General Meeting, 2008, 6 p.
14. Gan Li, Xiao-Ping Zhang, Modeling of Plug-in Hybrid Electric Vehicle Charging Demand in Probabilistic Power Flow Calculations, IEEE Transactions On Smart Grid, Vol. 3, No. 1, Mar 2012, pp. 492 - 499.
15. Kelly L., Rowe A., Wild P., Analyzing the Impacts of Plug-in Electric Vehicles on Distribution Networks in British Columbia, IEEE Electrical Power & Energy Conference (EPEC), 2009, 6 p.
16. Clement-Nyons, K., Haesen, E., Driesen, J.L.J., The Impact of Charging Plug-In Hybrid Electric Vehicles on a Residential Distribution Grid, IEEE Transactions on Power Systems, Vol. 25, No. 1, Feb 2010, pp. 371 - 380.
17. Tuttle, D.P., Baldick, R., The Evolution of Plug-In Electric Vehicle-Grid Interactions, IEEE Transactions On Smart Grid, Vol. 3, No. 1, Mar 2012, pp. 500 - 505.
18. Yilmaz, M., Krein, P.T., Review of Charging Power Levels and Infrastructure for Plug-In Electric and Hybrid Vehicles, IEEE Electric Vehicle Conference (IEVC), 2012, 8 p.
19. Hõimoja, H., Vasiladiotis, M., Grioni, S., Capezzali, M., Rufer, A., Püttgen, H.B., Toward Ultrafast Charging Solutions of Electric Vehicles, CIGRE 2012, paper C6-207, 8 p.
20. Moschakis, M.N., Karpopoulos, E.L., Zountouridou, E.I., Papathanassiou, S.A., On Adaptation of Electric Vehicle and Microgrid Issues to EMC-Power Quality Standards, Electrical and Electronic Engineering 2012, Vol. 2, No. 5, pp. 249 - 257
21. Sourkounis, C., Einwächter, F., Smart charge management of electric vehicles in decentralized power supply systems, Electrical Power Quality and Utilisation (EPQU), 2011, 6 p.
22. Teuscher J., Götz, A., Schufft, W., Electric vehicles and their effects in low-voltage grids, International Conference on Renewable Energies and Power Quality (ICREPQ), 2011, 4 p.
23. Zhao, L., Prousch, S., Hübner, M., Moser, A., Simulation methods for assessing electric vehicle impact on distribution grids, IEEE PES Transmission and Distribution Conference and Exposition 2010, 7 p.
24. Koyanagi, F., Inuzuka, T., Uriu, Y., Yokoyama, R., Monte Carlo Simulation on the Demand Impact by Quick Chargers for Electric Vehicles, IEEE Power Engineering Society Summer Meeting, 1999, Vol. 2, pp. 1031 - 1036.
25. Farkas, C., Szabo, K.I., Prikler, L., Impact Assessment of Electric Vehicle Charging on a LV Distribution System, Youth Conference on Energetics (IYCE), 2011, 8 p.
26. Rautiainen, A., Evens, C., Repo, S., Jarventausta, P., Requirements for an interface between a plug-in vehicle and an energy system, IEEE PowerTech 2011, 8 p.
27. Akhavan-Rezai, E., Shaaban, M. F., El-Saadany, E. F., Zidan, A., Uncoordinated Charging Impacts of Electric Vehicles on Electric Distribution Grids: Normal and Fast Charging Comparison, IEEE PES General Meeting, 2012, 7 p.
28. Marra, F., Jensen, M.M., Garcia-Valle, R., Traholt, C., Larsen, E., Power Quality Issues into a Danish Low-Voltage Grid with Electric Vehicles, Electrical Power Quality and Utilisation (EPQU) 2011, 6 p.
29. Masoum, M.A.S., Moses, P.S., Smedley, K.M., Distribution transformer losses and performance in smart grids with residential Plug-In Electric Vehicles, Innovative Smart Grid Technologies (ISGT), 2011, 7 p.
30. Richardson, P., Flynn, D., Keane, A., Impact Assessment of Varying Penetrations of Electric Vehicles on Low Voltage Distribution Systems, IEEE PES General Meeting, 2010, 6 p.
31. Shao, S., Pipattanasomporn, M., Rahman, S., Challenges of PHEV Penetration to the Residential Distribution Network, IEEE Power & Energy Society General Meeting, 2009, 8 p.
32. Trovao, L., Jorge, H.M., Power Demand Impacts of the Charging of Electric Vehicles on the Power Distribution Network in a Residential Area, Youth Conference on Energetics, 2011, 6 p.
33. Shao, S., Pipattanasomporn, M., Rahman, S., Demand Response as a Load Shaping Tool in Intelligent Grid With Electric Vehicles, IEEE Transactions on Smart Grid, Vol. 2, No. 4, Dec 2011, pp. 624-631.
34. Masoum, M.A.S., Moses, P.S., Hajforoosh, S., Distribution Transformer Stress in Smart Grid with Coordinated Charging of Plug-In Electric Vehicles, IEEE Innovative Smart Grid Technologies (ISGT), 2012, 8 p.
35. Kintner-Meyer, M., Schneider, K., Pratt, R., Impact assessment of plug-in hybrid vehicles on electric utilities and regional US power grids. Part I: Technical analysis, Pacific Northwest National Laboratory, 2007, 39 p.
36. Galus, M.D., Andersson, G.O., Integration of PlugIn Hybrid Electric Vehicles into Energy Networks, IEEE PowerTech 2009, 8 p.
37. Deilami, S., Masoum, A.S., Moses, P.S., Masoum, M.A.S., Real-Time Coordination of Plug-In Electric Vehicle Charging in Smart Grids to Minimize Power Losses and Improve Voltage Profile, IEEE Transactions on Smart Grid, Vol. 2, No. 3, Sep 2011, pp. 456 - 467.
38. Hilshey, A. D., Hines, P.D.H., Rezaei, P., Dowds, J.R., Estimating the Impact of Electric Vehicle Smart Charging on Distribution Transformer Aging, IEEE Transactions on Smart Grid, early access 2013, 9 p.
39. Broy, A., Sourkounis, C., Influence of charging electric vehicles and on the quality of the distribution grids, Electrical Power Quality and Utilisation (EPQU), 2011, 4 p.
40. IEC 61000-2-2 ed2.0:2002 Electromagnetic compatibility (EMC) - Part 2-2: Environment - Compatibility levels for low-frequency conducted disturbances and signalling in public low-voltage power supply systems.
41. Putrus, G.A.; Suwanapingkarl, P.; Johnston, D.; Bentley, E.C.; Narayana, M., Impact of Electric Vehicles on Power Distribution Networks, IEEE Vehicle Power and Propulsion Conference, VPPC 2009, pp. 827 - 831.
42. Berisha, S.H.; Karady, G.G.; Ahmad, R.; Hobbs, R.; Karner, D., Current Harmonics Generated By Electric Vehicle Battery Chargers, Conference on Power Electronics, Drives and Energy Systems for Industrial Growth, 1996, Vol. 1, pp. 584 - 589.
43. Musavi, F.; Edington, M.; Eberle, W.; Dunford, W.G., Evaluation and Efficiency Comparison of Front End AC-DC Plug-in Hybrid Charger Topologies, IEEE Transactions on Smart Grid, Vol. 3, No. 1, Mar 2012, pp. 413-421.
44. Zamri, M., Wanik, C., Fadzil, M., Siam, M., Ayob, A., Yanto, S., Azah, M., Azit A.H., Sulaiman, S., Azrin, M., Ali, M., Hussein, Z.F., Kamil, A., Hussin, M., Harmonic Measurement and Analysis during Electric Vehicle Charging, Engineering, 2013, No. 5, pp. 215-220.
45. Melo, N.; Mira, F.; de Almeida, A.; Delgado, J., Integration of PEV in Portuguese Distribution Grid. Analysis of harmonic current emissions in charging points. Electrical Power Quality and Utilisation (EPQU), 2011, pp. 1 - 6.
46. Wenge, C.; Stotzer, M.; Winkler, T.; Komarnicki, P., Power quality measurements of electric vehicles in the low voltage power grid, Electrical Power Quality and Utilisation (EPQU), 2011, pp. 1 - 5.
47. Bass, R.; Harley, R.; Lambert, F.; Rajasekaran, V.; Pierce, J., Residential Harmonic Loads and EV Charging, IEEE Power Engineering Society Winter Meeting, 2001, Vol.2, pp. 803 - 808.
48. IEC/TS 61000-3-4 ed1.0 : 1998, Electromagnetic compatibility (EMC) - Part 3-4: Limits - Limitation of emission of harmonic currents in low-voltage power supply systems for equipment with rated current greater than 16 A.
49. Monteiro, V.; Goncalves, H.; Afonso, J.L., Impact of Electric Vehicles on Power Quality in a Smart Grid Context, Electrical Power Quality and Utilisation (EPQU), 2011, pp. 1 - 6.
50. Gomez, J.C., Morcos, M.M., Impact of EV Battery Chargers on the Power Quality of Distribution Systems, IEEE Transactions on Power Delivery, Vol. 18, No. 3, Jul 2003, pp. 975 - 981.
51. Staats, P.T., Grady, W.M., Arapostathis, A., Thallam, R.S., A Statistical Analysis of the Effect of Electric Vehicle Battery Charging on Distribution System Harmonic Voltages, IEEE Transactions on Power Delivery, Vol. 13, No. 2, Apr 1998, pp. 640 - 646.

INFLUENCE OF ELECTRIC RAILWAY SYSTEM ON VOLTAGE UNBALANCE DISTRIBUTION BETWEEN HIGH VOLTAGE AND LOW VOLTAGE ELECTRICAL NETWORKS

Tanel SARNET, Jako KILTER, Ivo PALU

Department of Electrical Power Engineering, Tallinn University of Technology, Estonia

Abstract: This paper presents the results of the research performed to assess the distribution of voltage unbalance between different voltage levels due to the connection of 25kV AC electric railway system. Typically this type of AC railway system is connected to the high voltage electrical network between two phases and therefore can be considered as a significant source of voltage unbalance. In the paper a discussion on the influence of the voltage unbalance distribution between high voltage and low voltage networks is given. Moreover, the results of the research provide indication that there is a straightforward relation between the electric railway system and low voltage residential electricity network. The paper covers the electrical network and traction system modeling aspects and presents the results of the case study.

Keywords: Power quality, power system analysis, PSCAD, traction power supplies.

1. Introduction

AC electrified railway systems are common around the world and there are substantial amount of research results available about the problems concerning interactions between electrified railway systems and power grids [1]-[5]. These studies and existing practice show that adding AC fed railway system to the grid has negative impact on power system due to the relatively high proportion of unbalanced load.

The development of electrified railway systems in Europe has been parallel with the overall development of the power systems and therefore most of the problems were solved or taken into account during the design phase of the new transmission networks [1]. However, in different counties there are different technical solutions to mitigate problems which rose with connection of AC fed railway and also different traction system design principles are implemented [1].

In the Rail Baltica project, the most probable approach to consider, regarding the possible connection, in the

future is the 50Hz AC powered electrified railway system [6]. Based on the available information it is important to assess the influence of the planned railway system because the current system configuration and design principles used have not considered this type of loads peculiarities. Due to this possible negative impact on the Estonian power system operation is uncertain.

With this study, the authors are continuing the research of the voltage unbalance caused by the AC fed electric railway system on the basis of Estonian power grid example. Similar study is also performed in Finland where existing electric railroad traction system impact on transmission network is analyzed [2].

Studies [2]-[5] describe voltage unbalance and affected power quality issues caused by traction system spreading to the distribution network and it can be assumed that as a result the consumers connected to the low voltage distribution network are influenced.

In this paper, electric railway systems influence to the residential electrical installations is analyzed. The study is performed using models created in PSCAD software. The results of the analysis are applicable to be used as an input for study scenarios and to provide input for the Estonian power system development plans.

2. Overview of the transmission system model

Authors' previous studies have concentrated on the influence of electrified railroad traction systems load to the transmission system. The interest has been to determine the disturbance level and its accordance with the transmission system operator (TSO) power quality standards [7].

In [3], the transmission system model was compiled to determine the voltage unbalance level caused by electric railway system and its distribution between the transmission network substations. In the second paper [4] the combined heat power plant model was incorporated to the transmission network model in order to determine its influence on voltage unbalance in transmission system level.

Transmission network PSCAD model used in this study is further developed version of the model in [4]. Compared to the previous studies the power supply conditions outside of the selected transmission system fragment have changed. Because of that the model dynamics and overall electrical strength has changed compared to models in [3] and [4].

Additional model tuning has been made in order to obtain appropriate voltage unbalance factors. The influence of the PSCAD model calculation time step was analysed and it was determined that corresponding value should be less than $4.5 \mu\text{s}$. The specified voltage unbalance factors in transmission network level are presented in section 4.

The short-circuit power values which describe the transmission network strength are provided in Table 1.

Table 1. Transmission network substation short -circuit power

Substation	Short – circuit power (MVA)
SS1 (110kV)	920
SS2 (110kV)	450
DS1 (110kV)	655
DS2 (110kV)	190
DS3 (110kV)	705

Simplified scheme of the modeled transmission network with combined heat power plant, distribution network and consumer residential electrical installation is presented in Fig. 1. The transmission network fragment loads are at the same level in distribution substations as in [4].

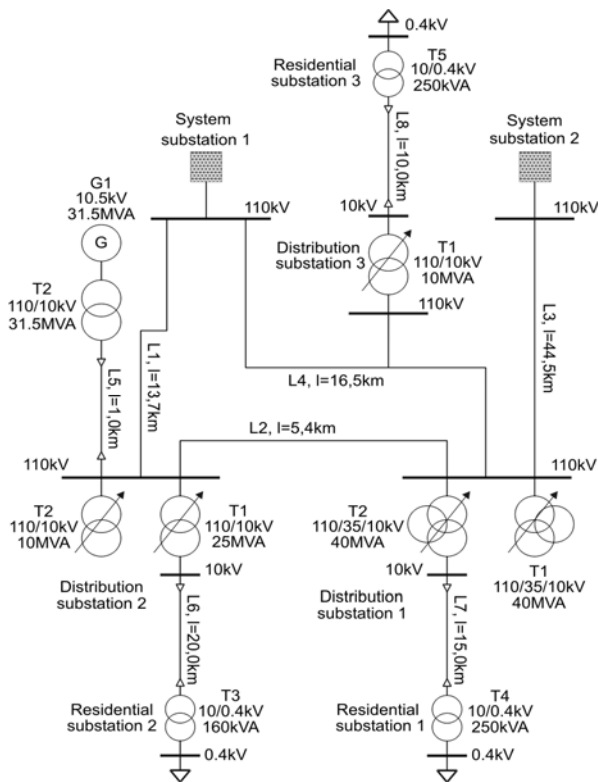


Fig. 1. Principal diagram of the modeled power system

2.1. Combined heat power plant model (CHP)

The combined heat and power plant model used in this study corresponds to those plants which have been built in Estonia. The modeled maximum electrical power of the CHP is 25 MW and thermal power is 50 MW. More detailed description of the CHP is provided in previous study [4].

Model of the combined heat and power plant is connected to the distribution substation 2 as seen from Fig. 1.

2.2. Electric railway traction system model

The approach for traction system model is the same as in [3], [4]. The up and down contact lines are fed from separate transformers which allowed to use simplified representation of traction system model in the PSCAD. The general scheme of the modeled system is presented in Fig. 2. In order to represent two rail track system the traction system is modeled consisting of two parallel center fed contact feeder lines.

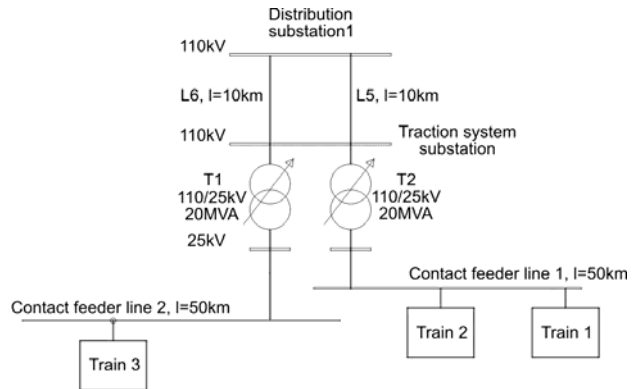


Fig. 2. Principal diagram of the traction system

The contact feeder line system is modeled in PSCAD as PI segments with longitudinal impedance $(0.169+j0.432) \Omega/\text{km}$ and with a shunt capacitance of $0.011 \mu\text{F}/\text{km}$ at 50 Hz. These PI section values are very approximate representation of electric railway contact line system.

The traction system load was modeled consisting of three trains each with rated power 5.5 MW and power factor of 0.8. The trains are modeled as fixed lumped loads to represent their movement with stable speed and while using maximum rated power. The modeled traction system load parameters are similar to the ones used in [2].

3. Distribution network model

In the study the voltage unbalance and power quality issues caused by traction system connections are analyzed on the consumer level. Accordance with the aim of this study the simplified theoretical distribution network model is incorporated to the transmission network model.

The model does not cover full distribution network, it only covers selected radial feeder lines as seen on Fig. 1.

For this study the lines are selected to represent the consumers which are electrically farthest from transmission system.

The parameters used for modeling these feeder lines are presented in Table 2.

Table 2. Distribution system line parameters

Line	R (Ω)	L (mH)
L6	5.06	6.00
L7	2.53	3.00
L8	3.795	4.5

The Distribution substations lumped loads were redistributed so that introduced residential network load did not change the overall distribution substation load.

The low voltage simplified network model consists of lumped load and longest low voltage feeder line model.

The line supplies private consumer electrical installation with maximum current load of 3x10A. The low voltage network consists of small cross-section aluminum wires with TN-C voltage system. This system is representing the installations which were built many decades ago using GOST standards. These electrical installations are considered to be more sensitive to disturbances and voltage unbalance than modern electrical installations.

The small distribution transformers in Fig. 1 were modeled using typical parameters corresponding to common values of these type of transformers.

The total load value on the low voltage side was selected to be equal to distribution transformer rated power. The loads were modeled with PSCAD standard library load models with fixed dP/dV and dQ/dV characteristics to exclude any effects caused by the load models.

4. Simulation results

The analysis of voltage unbalance distribution in transmission system and between different voltage levels was carried out according to TSO requirements for power quality [8]. The requirements limit maximum allowable voltage unbalance factor for single connected load to 1% and overall voltage unbalance in transmission network to 2%. Equation (1) is most commonly used for calculating voltage unbalance factor (VUF) [8]:

$$k_a = \frac{U_2}{U_1} 100\%; \quad (1)$$

where k_a is unbalance factor, U_2 is voltage negative sequence component and U_1 is voltage positive sequence component.

Alternatively equations (2) and (3) can be used to assess VUF [2; 5]:

$$k_a = \sqrt{\frac{(1 - \sqrt{3 - 6 \cdot \beta})}{(1 + \sqrt{3 - 6 \cdot \beta})}}, \quad (2)$$

$$\beta = \frac{(U_{AB}^4 + U_{BC}^4 + U_{CA}^4)}{(U_{AB}^2 + U_{BC}^2 + U_{CA}^2)}; \quad (3)$$

where U_{AB} , U_{BC} , U_{CA} are measured line to line voltage values.

In this study Equation (1) is used due to the possibility to compose this in PSCAD using only standard library components. Detailed description of the measuring tool used in this study is provided in [3].

Due to further development and optimization of model new baseline results are established for the transmission network level. To provide comparable results with [3] and [4] the simulation was carried out in two stages, with and without CHP connected to the grid.

The results of the baseline simulation to determine the voltage unbalance caused by introducing AC electric railway system to existing transmission network are provided in Table 3.

Table 3. Transmission network VUF by substations

Substation	Unbalance factor without CHP (%)	Unbalance factor with CHP (%)
SS1 (110kV)	1.54	1.34
SS2 (110kV)	1.20	1.00
DS1 (110kV)	2.13	1.93
DS1 (35kV)	2.13	1.93
DS1 (10kV)	2.13	1.93
DS2 (110kV)	1.95	1.75
DS2 (10kV)	1.95	1.75
DS3 (110kV)	1.91	1.71
DS3 (10kV)	1.91	1.71

In the Table 3 the indexes SS1, SS2, DS1-DS3 correspond to system substation 1 - 2, distribution substation 1-3 according to Fig. 1.

The results presented in Table 3 outline that traction system causes unacceptable level of voltage unbalance in transmission network according to TSO established power quality requirements for 110V networks [8]. CHP capability to mitigate VUF is 0.2% as seen from results in Table 2.

Compared to the previous studies [3]-[4] the results of VUF's in the current study are higher. This is due to the improvements made with model optimization and tuning. Results of model tuning outline that compiled models sensitivity to calculation time step which may cause inaccuracy in VUF measurement. Compared to the similar study conducted in Finland [2] the results for Kainuu transmission network are in the similar range. The Finnish results range from 2.1% to 1.1% for the Kainuu 110kV network and in the current study the VUF results range from 2.3% to 1.2%.

From the established baseline the transmission system the VUF in the residential electrical installation is determined. The simulation results with distribution network model are presented in Table 4.

In the Table 4 the indexes DS1-DS3, RS1-RS3 correspond to distribution substation 1-3 and residential area substation accordingly as seen on Fig. 1. The REI 1-3 symbolizes residential electrical installation 1-3.

Simulation results presented in Table 4 indicate that voltage unbalance from transmission system level distributes directly to the distribution network and from there to residential electrical installations.

Table 4. Distribution network VUF by substations

Measurement point	Unbalance factor (%)
DS1 (10kV)	2.13
RS1 (10kV)	2.26
RS1 (0.4kV)	2.26
REI1 (0.4kV)	2.30
DS2 (10kV)	1.95
RS2 (10kV)	2.02
RS2 (0.4kV)	2.02
REI2 0.4kV)	2.06
DS3 (10kV)	1.91
RS3 (10kV)	1.98
RS3 (0.4kV)	1.98
REI3 (0.4kV)	2.01

The voltage unbalance from higher level of power system causes lower levels to operate under unbalanced condition. Because of that the VUF increases in distribution network and in REI. By comparing voltage unbalance in DS, RS and in REI measurement points it can be easily observed that most of the VUF increase takes place in the distribution network. Comparing results presented in Table 3 and Table 4 indicates that transformers with different vector groups do not affect the VUF as the results in primary and secondary side are the same.

On the basis of these results it can be concluded that voltage unbalance caused by 25kV AC electric railway system affects all other consumers connected to this transmission network.

The unbalanced voltage in REI causes current in the neutral wires. The traction system caused neutral currents in consumer electrical installations are presented in Table 5.

Table 5. Measured REI neutral currents

Measurement Point	In (A)
REI1 (0.4kV)	2.10
REI2 (0.4kV)	1.90
REI3 (0.4kV)	1.77

Measured neutral currents from the model are noticeable for the old Soviet era electrical installations where TN-C voltage system is applied. Assuming that residential electrical installation was built with small cross-section aluminum wires with maximum rated current of 10 amperes, the neutral currents would cover range from 17.7% to 21% of the maximum allowable current. Due to continuous nature of the voltage unbalance this may lower the electrical installation capability to handle additional disturbances. Also the neutral currents would contribute additional heat to the cables and create safety risks in the electrical installation.

The neutral current assessed in this case should not pose direct electrical safety issues if the electrical installation is maintained and has a good grounding system. With weak or unreliable grounding system or lack of maintenance it can be contributing factor to other disturbances in the low voltage network. The neutral current in combination with other factors could cause electrical safety

problems and financial losses through damages to the electrical installation and devices.

5. Conclusions and future work

This paper presents analysis results which show that voltage unbalance caused by electric railway system distributes from transmission network level to residential electrical installations. The voltage unbalance rises mainly in distribution network due to supply voltage unbalance which affects the distribution system loads and power losses. The results give basis to the assumption that all consumers connected to the transmission system are directly affected by the voltage unbalance.

The analysis of neutral currents in low voltage networks indicate that voltage unbalance causes neutral currents in the residential electrical installations. The neutral current level in this scenario may cause indirect electrical safety issues and possible financial losses to consumers through damaged devices and electrical installation.

The simulation results in this paper indicate that in the future works has to incorporate more detailed distribution system model.

6. Acknowledgments

Authors thank Estonian transmission system operator Elering AS for financial support of this study.

7. References

1. Steimel A. Power-Electronic Grid Supply of AC Railway Systems. 13th International Conference on Optimization of Electrical and Electronic Equipment (OPTIM), 2012, pp. 16-25.
2. Heine P., Hyvärinen M., Niskanen J., Oikarinen A., Renner H., Lehtonen M. The Impact of 50 Hz Railroad Systems on Utility System Power Quality. Electric Power Quality and Supply Reliability Conference (PQ), 2010, pp. 61-66.
3. Sarnet T., Kilter J. Modeling and Analysis of Voltage Unbalance and its Influence on Transmission Network and Power Quality. The 7th International Conference on Electrical and Control Technologies, 2012, pp. 179-182.
4. Sarnet T., Kilter J. Assessment of Synchronous Generator's Influence on Transmission Network with Significant Level of Voltage Unbalance. Electronics and Electrical Engineering, Vol. 18, No. 9, 2012, pp. 11-14.
5. Golovanov N., Lazaroiu C. G., Roscia M., Zaninelli D. Voltage Unbalance Vulnerability Areas in Power Systems Supplying High Speed Railway. Power Engineering Society General Meeting, IEEE, 2005, Vol. 3, pp. 2509-2514.
6. AECOM Rail Baltica Final Report, 2011. [Online].
7. Elering AS, "Power quality requirements in 110 kV network," Tallinn, 2010 (in Estonian).

MODELLING POSSIBILITIES FOR THE ASSESSMENT OF WIND ROTOR BLADES' AEROELASTICITY AND STRENGTH

Tomas NARBUTAS, Jonas VALICKAS

Faculty of Technologies of Panevėžys Institute at Kaunas University of Technology, Lithuania

Abstract: efficient small-scale wind turbines in windy localities can be applied for power and heat supplying into the buildings and therefore demand of such wind turbines is high. Development of new advanced small-scale wind turbines often involves modelling in the initiate stages of designing. Modelling was applied for the assessment of aeroelasticity and strength of wind rotor blades of small-scale vertical axis wind turbine and described in this paper. A picture of wind turbine blades profile deformation was made for the assessment of the applied modelling method reliability. The same deformations were determined from the wind turbine blades photos taken during the natural experiments. It was confirmed that results received by means of modelling are reliable enough.

Keywords: wind turbines, blades, modelling of loads, deflection, strength, finite element analysis.

1. Introduction

Installation of small-scale wind turbines is steadily increasing as well as installation of the large-scale wind turbines. Development of small-scale wind turbines employment could be even more impressive in case of reduction of the expenses of their production and installation. Technical and economic efficiencies of small-scale wind turbines (WTs) are very different. Identification of small-scale WTs sometimes is problematic. Some of them have low technical efficiency and are very expensive. This is true for both varieties of WT – for the horizontal axis wind turbines (HAWT) and vertical axis wind turbines (VAWT). Therefore a criterion was suggested for preliminary assessment of technical and economic efficiency of a small WT in reference [1]. Advantages and disadvantages of HAWT and VAWT are analysed in references [1, 2]. Efficient, reliable and not expensive small-scale WTs can be successfully applied in the distributed energy systems for power and heat supplying into the buildings [3, 4, 5] and for power generation in

the microgrids [6]. This is why interest in efficient small-scale WTs is very high.

Experts from the International Science Panel on Renewable Energies (ISPRES) highlighted the main targets for improving of the WT and reduction of their prices during the coming years. The main problems to be solved include investigation of intelligent materials for WTs, reliability issues, advanced blades, investigation and application of new nano-materials for blades, incorporation of recyclable materials in the WTs, integral structural intelligence and other [7]. Solving of the mentioned above problems will pave the way for development of less expensive WTs produced from less expensive materials and components while maintaining high efficiency and reliability of the turbines. It will allow elaborating of updated small-scale WTs designed for the open and windy localities for high and medium wind energy resources, urban and periurban areas. The target to be achieved for the price index of small-scale WTs is considered about 1000 €/kW.

Modelling of the WT's wind rotor is often used in the initial stages of design for the evaluation of aeroelastic stability and strength of blades and other elements [8]. It allows significant reduction of the designing duration and expenses as well. It also provides possibility to change in a short time the materials and other initial data required for the designing.

2. Object of investigation

In this paper impact of the wind-caused acting forces to the blades of the wind rotor of the experimental VAWT, which rated capacity is 5 kW, was investigated by means of modelling.

Laminar and turbulent air fluxes make various actions to the turbine blades during the wind turbine rotation in natural conditions.

Wind rotor of vertical axis is rather effective for the generator's shaft rotation torque development but, from other hand, it is very sensitive to the actions of strong wind-created air flow fluctuations.

It is practically known that small-scale vertical axis wind turbines exploitation show big rate damages caused by the strong wind because of the insufficiently correct wind rotor design and wrong choice of materials for its construction elements and fastening system. Damages of the wind rotor are not only the losses of materials, but also they can be harmful for the surrounding objects and people.

A small scale wind turbine with synchronous generator capacity of 5 kW was designed for the simulation and investigation of the wind impacts to the main parts of wind rotor. Picture of the investigation object is presented in Figure 1. The main parameters of wind rotor and the maximal supposed outside load data are presented in Table 1.

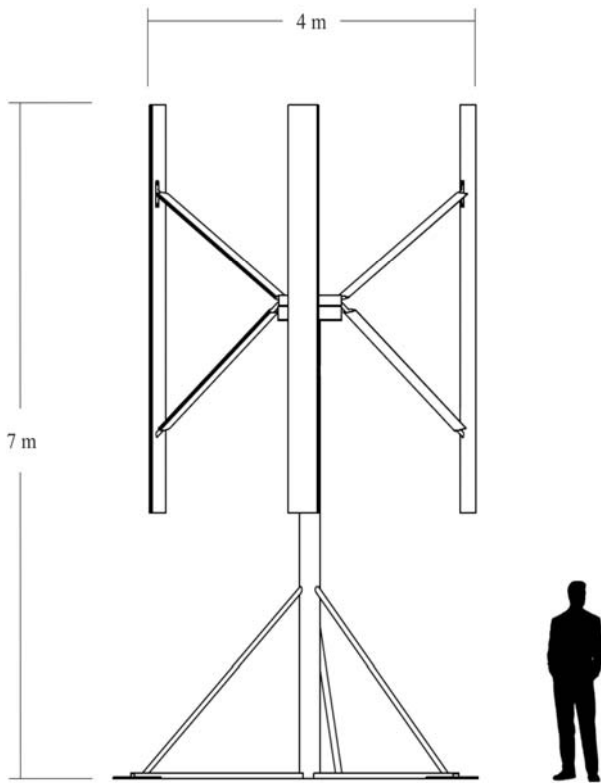


Fig. 1. Picture of the investigation object

Calculation of maximal loads for wind turbine's construction elements at the maximal wind speed was performed (see Table 1).

If the wind speed exceeds the set maximal value, the automatic switch to the not hazardous state of wind turbine operation necessarily must be performed. The maximal rotational velocity of the vertical axis wind rotor is 145 rev./min. It can be got at the permanent wind speed 20 m/s. It is a typical storm wind speed in Lithuania.

The variations of air parameters are not critical point for the modelling and investigations because of not important deviations in the dedicated area. Sometimes blades icing phenomena exists depending on the environmental conditions and this is included into the calculations and designed in the experimental wind turbine model.

Table 1. Main parameters of the designed wind turbine and supposed maximal wind-caused loads

Parameters	Notation	Parameter's value	Units
Supposed max environmental conditions			
Wind turbine angular velocity	ω_v	15.177	rad/s
Max supposed wind speed	v	20	m/s
Average air density	q	1.23	kg/m ³
Average air viscosity	γ	$1.45 \cdot 10^{-5}$	m ² /s
Air temperature	T	15	⁰ C
Main parameters of the designed wind rotor			
Length of blade	l	4	m
Chord	c_y	0.33	m
Surface area	S_m	1.32	m ²
Weight of one blade	m	11.5	kg
Number of blades	n	3	–
Wind turbine loads			
Aerodynamic load	F_n	2362.41	N
Centrifugal force	F_i	5297.85	N
Calculated load	q_{sk}	13141.75	N
Blade torque	M_s	203.48	Nm

Wind turbine's rotor has 3 blades. Each of them has 4 m length, 0.33 m width and weight 11.5 kg.

3. The main acting forces

Blades of the wind rotor and turbine's design must withstand wind-caused forces with large enough reserve and ensure effective rotation of power generator. Simulation methods allow saving of time for designing, well understanding of different wind forces impacts for designer and help to choose right shapes of the wind rotor design, fastening system and materials.

Autodesk Simulation Multiphysics software was used for determination of the wind created forces actions to wind rotor construction parts. Main forces acting to the vertical blade are described below.

Aerodynamic force (creates the rotational motion of the turbine) distributed by the blade surface can be expressed as follows [9]:

$$F_n = C_y \cdot \rho \cdot \frac{(\omega \cdot R + V_{max})^2}{2 \cdot S}, \quad (1)$$

where C_y – the resistance coefficient; ρ – the air density = 1.225 kg/m³; ω – the turbine rotation speed, rad/s; R – the turbine radius, m; V_{max} – the rated wind velocity, m/s; S – the blade area, m².

Centrifugal force

$$F_i = m \cdot \omega^2 \cdot R, \quad (2)$$

where m – the blade's mass, kg; ω – the turbine's rotation speed, rad/s; R – the turbine radius, m.

Wind rotor's steady state wind acting force [9]

$$F_{st} = C_x \cdot \rho \cdot v_{st}^2 \cdot \frac{S}{2}, \quad (3)$$

where C_x – the resistance coefficient; v_{st} – the storm wind speed, m/s.

Wind rotor's blade gravity force

$$q_{sk} = \frac{F_{sm} \cdot n_{eks} \cdot f}{S_m} \cdot c_y, \quad (4)$$

where F_{sm} – the blade gravity force, N; $n_{eks} = 1.5$ – the overload factor; $f = 1.2$ – the safety factor; S_m – the blade area, m^2 ; c_y – the blade chord, m.

Vectors of the above mentioned forces are presented in Fig. 2 [10].

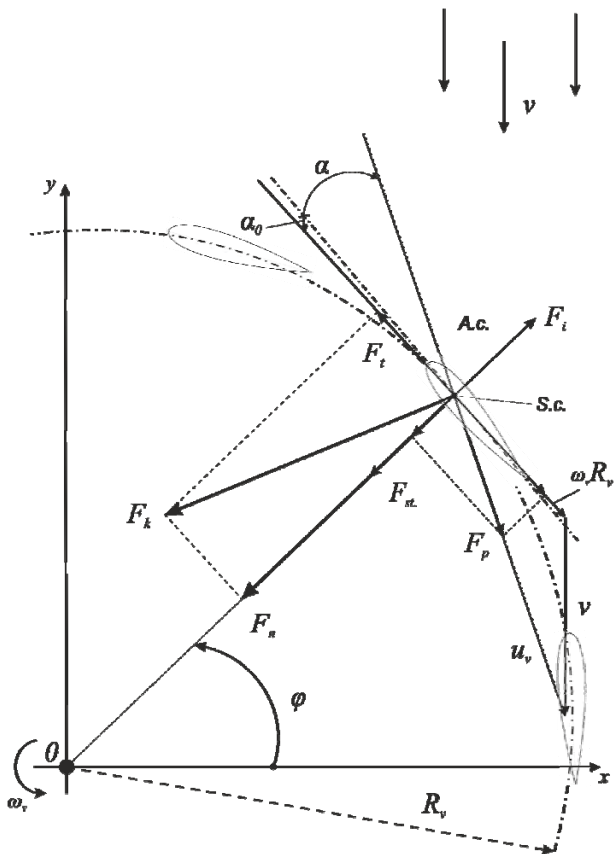


Fig. 2. Scheme of the one blade's track and acting forces vectors of the vertical axis small scale wind turbine:

F_k – the lift force (perpendicular to the rotational velocity vector u_v); F_p – the resistance force (acts in parallel to rotational velocity vector u_v); F_t – the blades pull force, F_n – the normal force acting to the wind turbine axis; A. c. – the aerodynamic center

All these actions make impact to the wind rotor construction. Authors have a target to analyse weak points of the vertical axis wind rotor design and to define its strength limit values by using the simulation method in order to suggest to wind rotor makers how to improve construction strength using the best suitable shapes and materials for the wind rotor parts and to avoid of possible particular wind rotor construction damage. Aerodynamic and centrifugal forces make impact to the wind turbine during the operation time. The steady state wind acting force acts when the turbine do not rotates (see Table 1).

The main wind rotor's parts laying under strongest impact of the wind forces are:

- ✓ wind turbine blades;
- ✓ blades fastening part;
- ✓ fastening screws.

4. Modeling of the mechanical wind turbine blades strength

Design of the wind turbine's blades was done using Autodesk Inventor Professional Suite 2012¹ software. Model for the blades strength investigation was created using Autodesk Simulation Multiphysics 2012² software. Before blades strength model simulation design drawings data were corrected:

- Auxiliary design planes, axes, lines, marking points were removed from the drawings;
- Parameters and constants of materials of the main wind rotor construction elements, which were used for fabrication of the investigation object, were described;
- Contacts between the wind turbine structural elements (walls spar components, used blade coating and fasteners design) were inserted into the simulation model;
- Reasons of the finite element program choice for the wind rotor components are presented below.

Maximal wind exposed load (see Table 1) was used for the investigation of parts of the wind turbine's rotor construction. The main reaction forces to the wind rotor construction elements are presented in Figure 3.

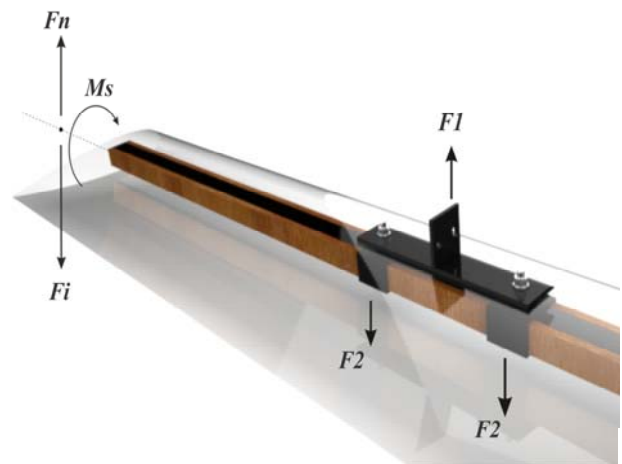


Fig. 3. Reaction forces to the wind turbine construction: F_n – the normal force acting to wind turbine axis; F_i – the centrifugal force, acting from the mass of the element (reaction forces F1); Q_x – the barred force and M_s – the rotational torque acting to the blade fastening elements (reaction forces F2).

¹<http://usa.autodesk.com/autodesk-inventor/>

²<http://usa.autodesk.com/adsk/servlet/pc/index?siteID=123112&id=13773836>

FEA elements items menu explanation. Autodesk Simulation Multiphysics finite elements program was used for modeling of the wind turbine construction parts. First of all, various wind turbine construction parts have a different material structure and different physical shape as well. The different finite elements from the programme were selected in order to evaluate more strictly the wind action to all of them and approach maximally the model to reality.

3D BRICK type element was selected for modelling of inner and outside fastening parts (see Figure 4). Properties of the mentioned above element allow adapting it to each wind rotor part specifics. Isotropic, plasticity, creep, viscoelastic, electrical and piezoelectric properties of the part structure may be evaluated [11].

As it was ascertained by investigation of strength of the wind rotor elements, the most reliable and least expensive parts of the construction can be made from the multilayer tubular materials.

SHELL type finite element was selected for blade spar modelling. It is 3D finite element which allows including the thickness of the element to the model nodes and material properties used for investigated part of wind rotor construction. So, every node of the selected model may include isotropic, anisotropic, plasticity, hyper plasticity, creep, increasing stiffness, thermoplastic, viscoelastic, composite, large displacement and large deformation properties of the element and all deformation types can be evaluated [11].

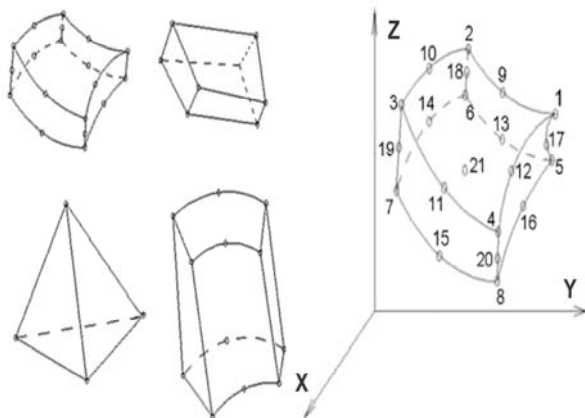


Fig. 4. BRICK type finite element. It includes 21 nodes

THICK COMPOSITE type finite element was used for the layered blade modeling. Every finite element of the blade model is composed from the multilayer elements interacting interdependently.

The mentioned above structure of the element was chosen in order to include in the model strict design of the investigated wind rotor. Composite materials of the blades layers were included to the model accordingly with the recommendations of the simulation programme [11].

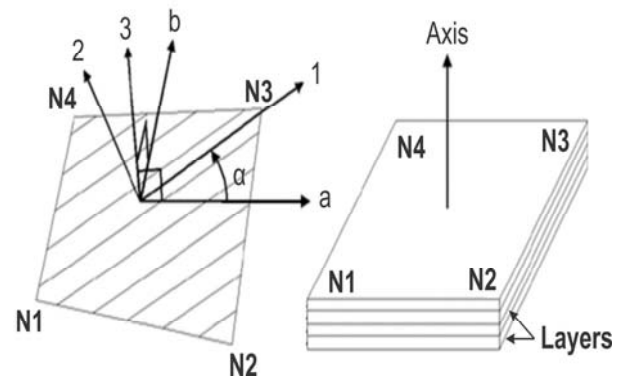


Fig. 5. Four layers THICK COMPOSITE finite element

FEA meshing. Selected algorithms give possibility to create optimal enough finite element mesh of wind turbine's rotor component. Wind turbine blade was made from multilayer composite material.

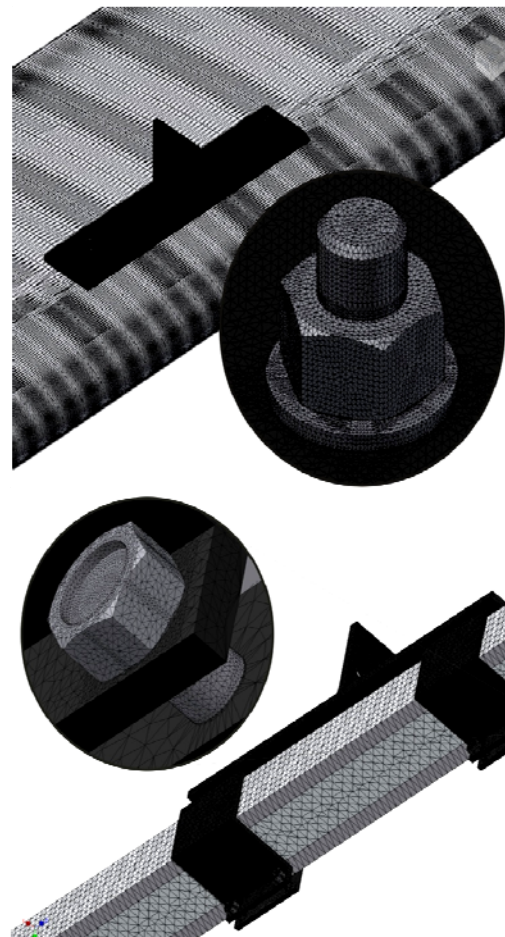


Fig. 6. Picture of the samples: finite element mesh for wind turbine blade and fasteners, 3349031 units and 2214177 totally in the model

Structure of composite material hypothetical periodically repeated layers was done using thick composite element for the modeling of blade.

The thickness of the one composite layer is 0.27 mm. The filament orientation angle α of each material layer is included into the model as well.

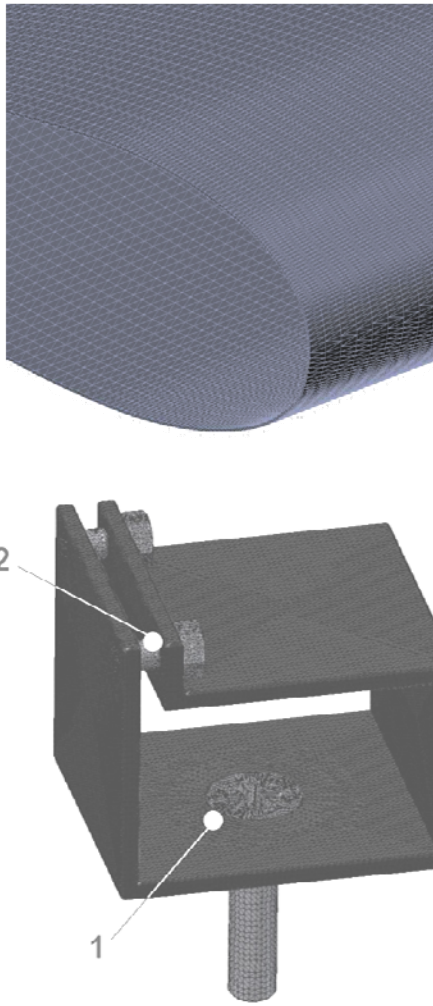


Fig. 7. Picture of the composite material finite element mesh for blade and fasteners. Blade mesh composition: 695473 nodes and 570312 elements Size of the blade element – 7.50642 mm

5. Results of investigation

Analysis of the finite element models allowed accurate assessment of stress in the parts and construction. Figure 8 submits the stress distribution of various elements of the blade attachment which shows the strength requirement to the design and construction of the blade components.

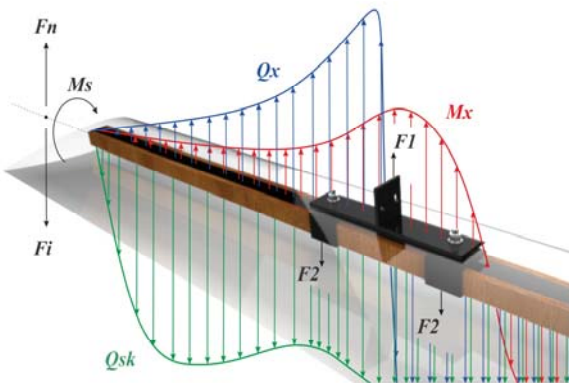


Fig. 8. Modeling result of the wind turbine blade and fastening element

The knowledge of stress distribution allows right selection of suitable materials and manufacturing technology that guarantee strength of the components. Indirect investigation methods were applied as well. The investigation was done by taking pictures of the wind rotor parts deformation in natural conditions under the wind-caused forces. It was found that the simulation results well correlate with the natural deformations estimated from the pictures, which were taken during the natural experiments.

The elaborated finite element model for the design of given wind turbine parts allow evaluate the strength in not destructive way and in short time. Maximum wind power load creates in the blade $343 \cdot 10^6$ Pa strain for the investigated model (see Table 1). Strain distribution of wind rotor different samples is shown in Figure 9.

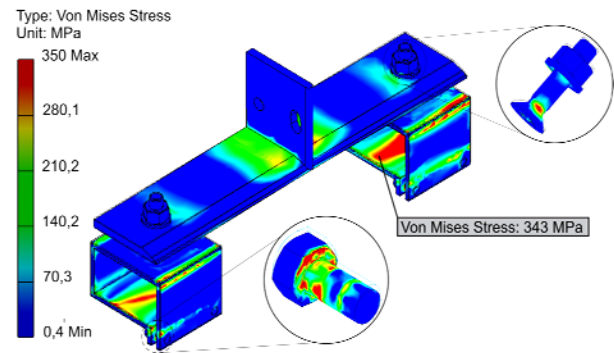


Fig. 9. Strain distribution in the fastening parts of blades at maximally loaded wind turbine (see Table 1)

Picture of wind turbine blades profile deformation was made (see Fig. 10) for the reliability assessment of the applied modelling method. The results of modelling were compared with deformations determined from the photos of wind turbine blades taken during the natural experiments. Coincidence of the results received by means of modelling and natural experiments is about 90 %.

Modelling results show that all strains of the wind turbine blade adopt one of the key elements of the blade construction – spar. A special attention have to be paid to the walls of spar and interconnection characteristics of the spar elements in the analysis of wind turbine blade's spar construction in approach of fatigue.

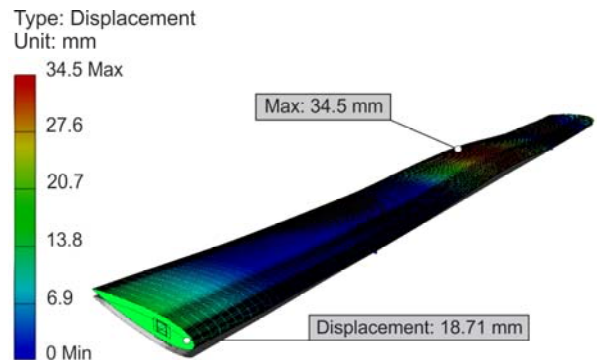


Fig. 10. Result of the symmetric airfoil blade spar resistance test (the outer side of blade)

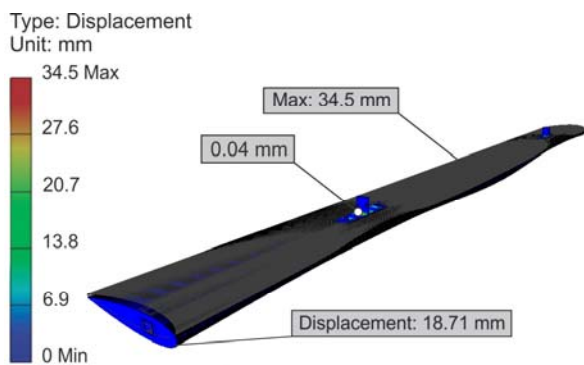


Fig. 11. Result of the symmetric airfoil blade spar resistance test (the inner side of blade)

6. Conclusions

1. The worked out finite element model for design of experimental wind turbine's wind rotor parts allows inexpensive evaluating of the blade strength in not destructive way during a short time.
2. The designing of longeron of the experimental wind rotor blade was carried out using the approach method and seeking to reduce the price of the blade while maintaining the necessary strength reserve.
3. The strength reserve of the designed longeron of the experimental wind rotor blade final specimen makes up 1.5.
4. The elaborated model of small-scale wind turbine rotor allows designing of rotor elements which have low price and well enough strength to withstand storms and hurricanes.
5. The elaborated model and modelling can be used only as a preliminary method for designing of wind rotor and it can not substitute the certified tests of new wind turbines and their parts according to the effectual standards.

7. References

1. Mittal R., Sandhu K. S. and Jain D. K. . An Overview of Some Important Issues Related to Wind Energy Conversion System (WECS). *International Journal of Environmental Science*

- and Development, vol. 1, no. 4, ISSN 2010-0264, p.p. 351-363, Oct. 2010.
2. Adomavičius V., Watkowski T., Žilinskas E., Adomavičius A. Comparison of small wind turbines properties. Proceedings of International Conference *Electrical and Control Technologies – 2009*, KTU, Kaunas, p.p. 374-379, May 2009.
3. Adomavičius V., Watkowski T. Hybrid water heating systems based on solar and wind energy. Proceedings of International Conference *Electrical and Control Technologies – 2008*, KTU, Kaunas, p.p. 349-354, May 2008.
4. Ramonas Č., Adomavičius V., Kepalas V. Research of the grid-tied power system consisting of wind turbines and boiler Galan. *Electronics and Electrical Engineering = Elektronika ir elektrotechnika*, no. 10 (106), p.p. 27-32, 2010.
5. Adomavičius V.; Ramonas Č. Small scale wind energy systems for farmsteads. *Research papers of Aleksandras Stulginskis University*, vol. 43, no. 4, p.p. 5-16, 2011.
6. Адомавичюс В. Б. , Харченко В. В. Особенности и проблемы построения микросетей. Труды 8-ой Международной научно-технической конференции *Энергоснабжение и энергосбережение в сельском хозяйстве*, часть 5, Нанотехнологии и инфокоммуникационные технологии, ГНУ ВИЭСХ, Москва, с. 50-56, 16-17 мая 2012.
7. International Science Panel on Renewable Energies (ISPRE). Research and Development on Renewable Energiesю *A Global Report on Photovoltaic and Wind Energy*, 32 p., Dec. 2009.
8. Zhang P., Huang S. Review of aeroelasticity for wind turbine: Current status, research focus and future perspectives *Front. Energy*, vol. 5, no.4, p.p. 419-434, 2011.
9. Kundu P. K.,. Cohen I. M. Fluid Mechanics. Fourth Edition, p.p. 679-709, 2008.
10. Gulbinas A. Power regulation of the wind turbines. *Research papers of IAg Eng LUA & LU of Ag*, vol. 39, no. 3, p.p. 81-94. 2007.
11. Autodesk, Inc. Finite Element Analysis in Practice. Autodesk, p.p. 56-61, 2010.

STATIC ELECTRICITY AS DISBURBANCE IN HIGH VOLTAGE SUBSTATIONS

Nerijus BARŠIUKAITIS*, Vitalijus GVOZDAS**

* Kaunas University of Applied Engineering Sciences, Lithuania

** Kaunas University of Technology, Lithuania

Abstract: Fast growing quantity of electronic and microprocessor equipment in HV substations more often rises problems with static electricity. Staff static electricity discharge can rise up to a few kV and that can cause serious problem for equipment. That is why we need to research humidity variation limits and other circumstances.

Keywords: Static electricity, electrostatic charge, electromagnetic compatibility, spark discharge.

1. Introduction

HV substations are high-level and complex objects, because fail of power equipment can cause serious subsequences. To ensure steady work of HV substation we need to appreciate various factors and one of them is technical equipment electromagnetic compatibility (TEEC). TEEC is described by two components: interference resistance and electromagnetic environment in object. Usually in HV substations electromagnetic environment is characterized as hard and described as entire electromagnetic appearance and process. One component of electrostatic environment is electrostatic load which negatively affects work of electronic technical devices [1]. Problem of static electricity is actual in manufacturing where electrostatic loads can cause fire or explosion and detune technological processes.

2. Electrostatic human environment

Often high speed digital components and digital interface elements fails during static discharge. Such load influence is especially danger for unprotected equipment nodes. That is why we need to take care of TAAC during any maintenance or tuning works. Electrostatic load in HV substation originates from friction or during direct human body contact with various stuff: chair, table, floor or clothing.

Human body load q and energy W_h depends from capacity C and voltage U between body and earth:

$$q = CU \quad (1)$$

$$W_h = 0,5CU^2 \quad (2)$$

Human's body electric capacity assesses by vertical conductor formula:

$$C_1 = \frac{3\varepsilon\varepsilon_0 l}{lg l/D}; \quad (3)$$

where l – human height, m; D – waist diameter, m
Without capacitance C_1 is also rated feet capacitance:

$$C_2 = \frac{\varepsilon_0 \cdot S_2}{\sum_{i=1}^n d_i/\varepsilon_i}; \quad (4)$$

where S_2 – foot area, m²; i – footwear layer number; d_i – „i“ layer thickness; ε_i – „i“ layer dielectrical permittivity.

If human stands, then his capacitance is $C_1 + 2C_2$; runs – $C_1 + C_2$; walks $C_1 + 2C_2$.

Capacitance also changes if human sits on chair, puts on warm reflecting clothes:

$$C_3 = \frac{\varepsilon_0 \cdot S_3}{\sum_i d_i/\varepsilon_i}; \quad (5)$$

where S_3 – sitting place area, m².

Practical measurements show those human body capacitances can various from 40 pF till 8000 pF. Voltage level which human body can charge depends upon grounding resistance. In this case load will be equal $Q = \tau I = RC I$ and recharge time $\tau = RC$. If human walks on floor with synthetic carpet body can charge up to 15 kV and accumulate energy from 10 till 35 mJ. When human approach to the grounded case spark discharge will rise, because almost every time condition $R > 2\sqrt{L/C_k}$ is realized. Discharge process will be aperiodic and current steepness which describes disturbance level can reach till 100 A/ns.

Human body is the main static load generator in working area, that's why individual ESD tools are the main subsection of any antistatic program. It is considered that about 70% of electronic component fails by static electricity rises from unreliable grounding of

working staff. To ensure reliable ESD in working area it is essential to use antistatic materials and to use device to secure reliable grounding of all grounded elements. To remove dielectrics (materials which surface resistance is bigger than 1000 GΩ) from working area, because grounding through conductor to discharge the load it is inexpedient.

Table 1. Parameters of objects in antistatic zone

Parameters of objects in antistatic zone	Transitional resistance till ground or antistatic zone grounding point	Load discharge time when object resistance is greater than 10 GΩ
Floor material	1 GΩ using working shoes as first or secondary grounding device, resistance from 750 kΩ till 35 MΩ	-
Working shoes as first or secondary grounding device	From 50 kΩ till 100 MΩ (pair of shoes)	-
Clothing	-	From 100 V till 1000V not more than 2 seconds
Tools	1000 GΩ	From 100 V till 1000V not more than 2 seconds

Grounding of working staff like static load source and carrier can be realized: by help of wrist bracelet through 1 MΩ resistor with grounding bus; like additional grounding network antistatic materials (chair, floor material) can help.

3. Factors influencing electrostatic discharge magnitude

Electrostatic discharges are short processes with minor energy level. The current of such short time discharge can make from 100 pA till a few μA and load size from 3 nC till 5 μC. Not looking that these loads are short time and minor energy presumable that their influence can cause various problems for electronic devices [2]. Influence for electro technical devices can cause both current and discharge voltage. Every static electricity discharge conducts electric and magnetic fields. In distance till 10 cm electric field strength can reach 4 kV/m and in distance till 20cm – up to 1 kV/m. Analogical magnetic field strength will be 15 A/m and 4 A/m.

Sometimes discharge current is made from very short impulses which compounds on basic long time current part. Picture 1 shows diagram of discharging current from human body, which carriers 8 kV potential.

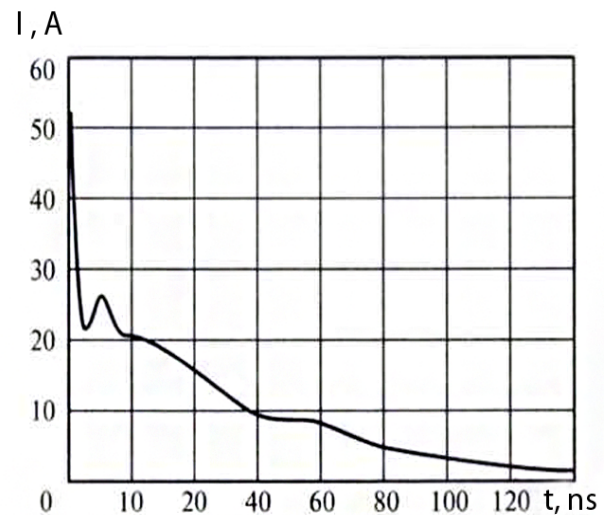


Fig. 1. Typical discharge current diagram from human body with metal tool in hands

Preconceived short time current impulses usually originate from minor charge voltage. During discharge influence as disturbance source it is essential to know if there are preconceived current spikes. Picture 2 shows full spectrum discharge current composition.

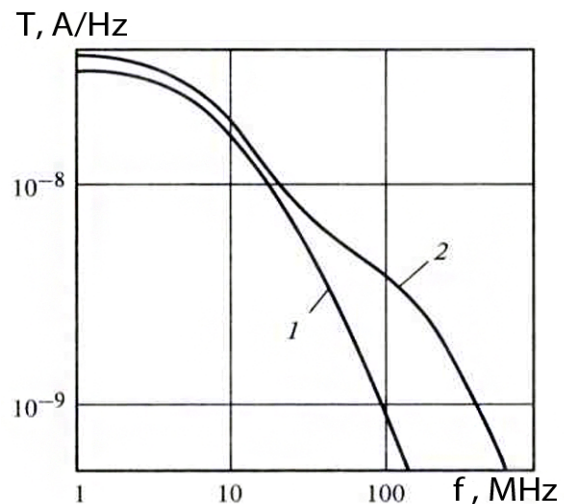


Fig. 2. Static electricity discharge diagram full spectrum composition; T – amplitude spread density; 1 – long time component; 2 – full impulse

Short time component being is raising spectral density in high frequency range. Consecution from here these current components are very important, because mostly disturbance transmission is in high frequency range. If human body charge potential reaches coronal discharge coming voltage, then discharge impulse steepness outlined by object moving speed to discharge object [3]. If approach happens very fast then impulse current front has great steepness. Mostly static electricity discharge effect is reached when human hand holds metal tool (screwdriver, key, conductive wristband). In this case current steepness which outlines inducted disturbance origin can reach up to 100 A/ns.

Current influence in semiconductors can make local melt zone and in oxides 1 micron diameter spot hole can occur. Voltage influence could destroy semiconductor's crystal surface or make dielectric blowhole [4]. Value of electrostatic load depends upon several factors; we will analyze analytic dependence, [5] which let us determine potentials of electrostatic load by indirect measuring:

$$U = \frac{16j_0h}{\gamma_v\pi^2} \sum_{m=0}^{\infty} \sum_{n=0}^{\infty} \frac{(-1)^{m+n}}{(2m+1)(2n+1)} \cdot \frac{1}{\left[1 + \frac{\gamma_s h}{\gamma_v} \left(\frac{\pi^2}{4} \left(\left(\frac{2m+1}{l_1} \right)^2 + \left(\frac{2n+1}{l_2} \right)^2 \right) \right) \right]} ; \quad (6)$$

where j_0 – electrification current density, $\mu\text{A}/\text{m}^2$; $\gamma_s = 1/\rho_s$ ir $\gamma_v = 1/\rho_v$ s/m – comparative surface and volumetric material conductance; l_1, l_2, h - cover measurements and its thickness, m.

We can see from formula that potential of the load depends from: friction surfaces properties (j_0, γ_s, γ_v), friction surfaces area, cover dimensions and thickness, solid parameters and contact method (j_0).

We should mention humidity between changing parameters. Resistivity (table 2) and electrostatic discharge potential (table 3) depends from humidity also.

Table 2. Material resistivity dependence from humidity

Medziaga	Surface resistivity, Ω	
	Humidity 0%	Humidity 100%
Politetraforethylene	$5 \cdot 10^{17}$	$3,6 \cdot 10^{12}$
Polystyrene	$5 \cdot 10^{17}$	$8,4 \cdot 10^{11}$
Polythene	$5 \cdot 10^{13}$	$1,3 \cdot 10^9$
Nylon	10^{12}	$3,8 \cdot 10^9$
Drawn silica	10^{17}	$6,5 \cdot 10^{10}$
Aminoplast	$6 \cdot 10^{14}$	10^{13}

Table 3. Electrostatic discharge potential dependence from humidity

Operation	Potential kV, when humidity is		
	10%	40%	55%
Walking on carpet	35	15	7,5
Walking on vinyl carpet	12	5	3
Movements on bench	6	0,8	0,4

Static discharge voltage dependence from relative humidity is shown in Picture 3

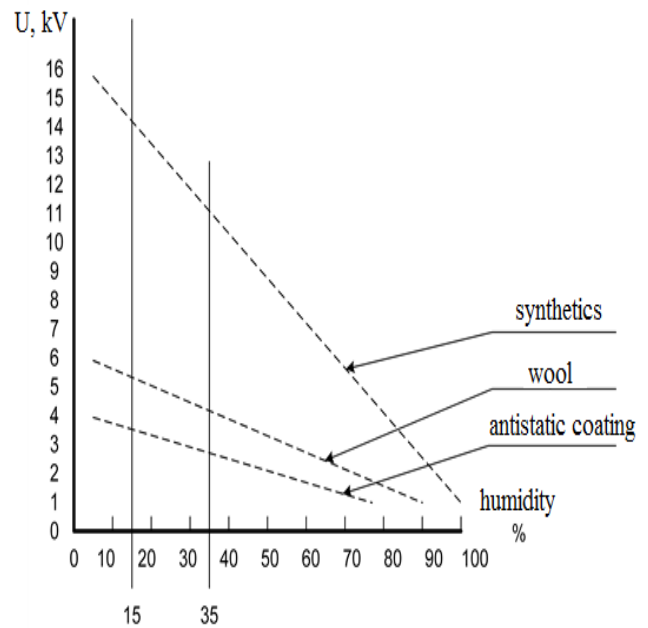


Fig. 3. Static discharge voltage dependence from relative humidity

Dependence of electrostatic discharge potential when walking on polyvinylchloride or rubber carpeted floor is shown in Picture 4.

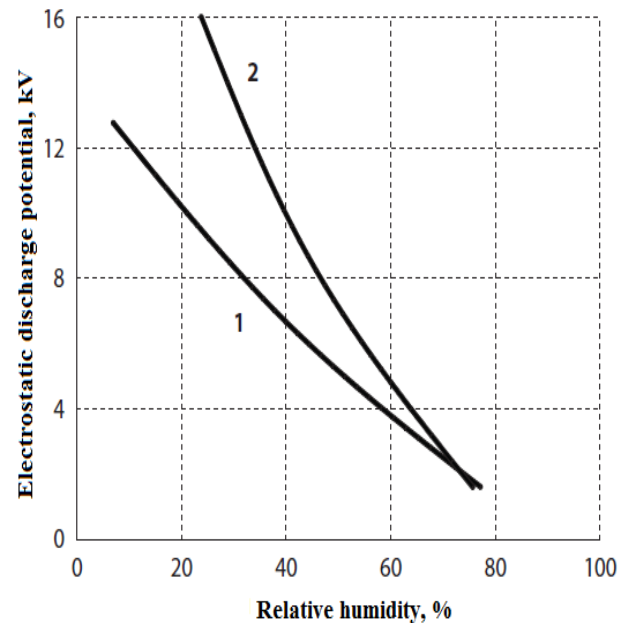


Fig. 4. Dependence of electrostatic discharge potential when walking on polyvinylchloride (1) or rubber (2) carpeted floor

Dependence of electrostatic discharge potential from humidity in closed type substation is shown in Picture 5.

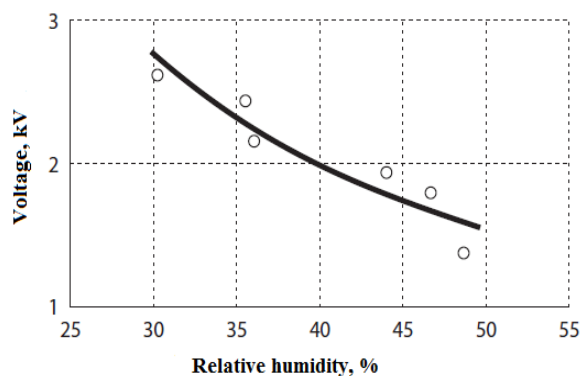


Fig. 5. Dependence of electrostatic discharge potential from humidity in closed type substation

Dependence of electrostatic discharge potential from humidity in room with linoleum floor is shown in Picture 6.

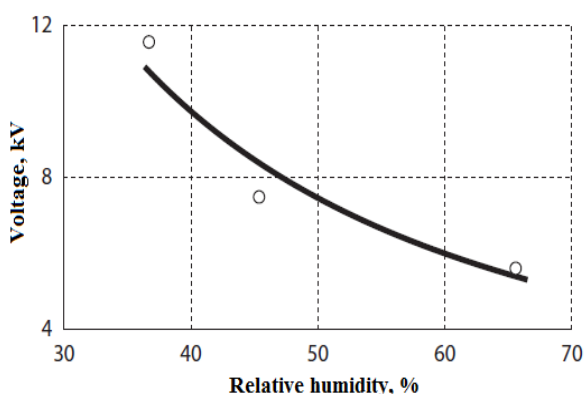


Fig. 6. Dependence of electrostatic discharge potential from humidity in room with linoleum floor

Dependence of electrostatic discharge potential from humidity in room with parquet floor is shown in Picture 7.

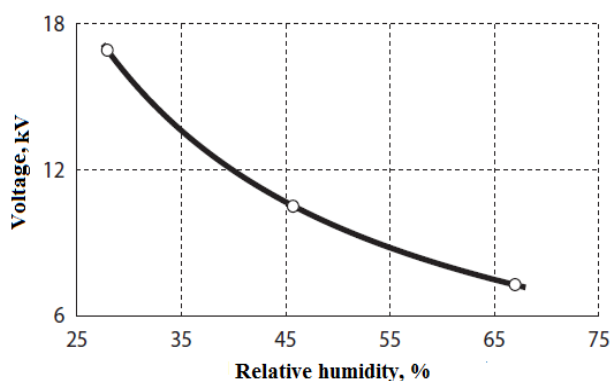


Fig. 7. Dependence of electrostatic discharge potential from humidity in room with parquet floor

Research outcomes show us essence of electrostatic discharge potential dependence from humidity and friction surfaces. During experiment in working substation were measured maximum potentials which can occur in substation and can influence requirements for electromagnetically compatibility: false floor 2.7 kV, concrete floor 3.1 kV, linoleum 11.3 kV, varnished parquet 18.9 kV.

Measured potentials are equated with disturbances of electrostatic discharge and that let us define if electronic equipment will work with no fail, or we need extra security implement. For power-stations and high and medium voltage substations it is defined such levels of electrostatic discharge: 6 kV – in contact discharge; 8 kV – discharge through air.

4. Conclusions

Discharges of static electricity during maintenance of technical devices regarding to staff can reach up to several kV. During discharge current flow can easy reach device case that is why sensitive elements disturbance can occur.

Potential of static electricity discharge is variable value and it depends from various parameters, if humidity will rise from 10% to 55% potential will change about 15 times.

In every case we need to define size of potential separately, during researches, analyzing humidity changing range, it also depends from staff shoes, clothing and other conditions.

5. References

1. А. Ф. Дьяков, И. П. Кужекин, Б. К. Максимов, А. Г. Темников. Электромагнитная совместимость и молниезащита в электроэнергетике. 2011, p. 45-50.
2. Горлов М. И. Статическое электричество и полупроводниковая электроника. Природа, No 12, 2006, p. 27–36.
3. Максимов Б. К., Обух А. А. Статическое электричество в промышленности и защита от него. М.: Энергоатомиздат, 2000.
4. Кечнев Л. Н., Пожидаев Е. Д. Защита электронных средств от воздействия статического электричества. М.: ИД «Технологии», 2005. 352 p.
5. John B. Beaver, Don Powers. Electricity and Magnetism, Grades 6–12: Static Electricity, Current Electricity, and Magnets, 2004. 65 p.
6. J. J. Lowke (1992). Theory of electrical breakdown in air. Journal of Physics D: Applied Physics 25 (2). p. 202–210.

THE ASYMMETRY EVALUATION IN THE DISTRIBUTION NETWORK

Gintvilė MASLAUSKAITĖ, Ugnė ILIOITIENĖ
Kaunas University of Technology, Lithuania

Abstract: This paper analyzes the asymmetry voltage in distribution network. Voltage asymmetry is costly, potentially damaging and it is a serious power quality problem. Asymmetry affects and distribution network operators and customers. At the same time, the customers that are supplied with asymmetrical voltage are billed not only for the useful energy but also for the energy which may cause harmful effects on their equipment. In this paper, a new methodology is presented which part of distribution network has impact the emergence of asymmetry. The developed methodology is novel and it shown that overhead lines layout configurations on the pole has big evaluation the emergence of asymmetry in distribution network. In the same time the main mitigation techniques for this specific problem are briefly summarized.

Keywords: Asymmetry, distribution network, overhead lines.

1. Introduction

In nowadays, reliability is and will be a very important in electric distribution network to supply electric energy with a competitive price, good quality, and sufficient quantity, secure and reliable. Reliability has a direct effect on the outage costs and even power outage is for several moments, may cause huge damage.

The biggest parts in Lithuania medium voltage (MV) networks are built using overhead lines. The statistics shows that MV has the highest impact on reliability, because more than 90% of the customers experienced outages are due to faults in the MV networks. Most of the outages are unexpected disturbances or other interruptions in the MV (35kV) Lithuanian's distribution network.

Overvoltages, damages, lightning, not correct projecting overhead lines configurations, cable laying on the poles can be the main cause to emerge of asymmetry.

From the fault resulting asymmetry effect MV distribution network reliability, security and efficiency of the power system equipment and consequently, on the supply quality and loading quality. Asymmetry can cause damages for customer's equipments, line connected equipment.

This part provides a comprehensive compilation of a lot of published information about voltage asymmetry in the distribution network and who has the biggest impact of it has is origin. Asymmetry mainly caused by the structural asymmetry of parameters of generators, transformers transmission and distribution lines, also is caused by the voltage drop on the system impedance by asymmetrical currents.

Voltage asymmetry effects the economic benefits, strongly depend on the supply reliability, security, supply and loading qualities, energy losses. For sure it has to be mitigating, because the negative sequence voltage causes temperature increase, negative effects in power system. Furthermore, asymmetry reduction of life expectancy and so reduce efficiency. The main interest in this paper is to show that overhead lines layout on the pole has influence to occur of asymmetry. The main interest in this paper is asymmetry in MV distribution network.

2. The asymmetry in distribution network

Distribution systems are defined by an unbalanced loading or by an asymmetrical construction, frequently, both these features are present, more about this describing [1].

A three-phase power system is called balanced or symmetrical if the three-phase voltages and currents have the same amplitude and are phase shifted by 120° with respect to each other. If either or both of these conditions are not met, the system is called unbalanced or asymmetrical [2].

The 3-phase system is decomposed into a so-called direct or positive-sequence, inverse or negative-sequence and homopolar or zero-sequence system, indicated by subscripts A, B, C. They are calculated using matrix transformations of the three-phase voltage or current phasors. The superscripts +, -, 0 indicate the different phases. The expressions here are formulated for the voltage U. Negative phase and sequence set of phasors given respectively by the two equations:

$$\begin{aligned}\underline{U}_p &= \frac{1}{3}(\underline{U}_1 + a\underline{U}_2 + a^2\underline{U}_3) \\ \underline{U}_n &= \frac{1}{3}(\underline{U}_1 + a^2\underline{U}_2 + a\underline{U}_3)\end{aligned}\quad (1)$$

where a is vectorial operator $\exp(j2\pi/3)$.

The phasor \underline{U}_p and \underline{U}_n are each balanced, but the system imbalance is given by the ratio:

$$\underline{\tau} = \frac{\underline{U}_n}{\underline{U}_p} = \tau \exp(j\theta);$$

where: τ is imbalance factor has two dimensions and is quoted above in a polar coordinate system.

$$\begin{bmatrix} \underline{U}_A \\ \underline{U}_B \\ \underline{U}_C \end{bmatrix} = \begin{bmatrix} 1 & 1 & 1 \\ 1 & a^2 & a \\ 1 & a & a^2 \end{bmatrix} \cdot \begin{bmatrix} \underline{U}^+ \\ \underline{U}^- \\ \underline{U}^0 \end{bmatrix}; \quad (2)$$

where: \underline{U}_A , \underline{U}_B and \underline{U}_C are the voltage phasors; \underline{U}^+ , \underline{U}^- and \underline{U}^0 are the positive, negative and zero symmetrical systems sequence voltages. The inverse transformation is:

$$\begin{bmatrix} \underline{U}^+ \\ \underline{U}^- \\ \underline{U}^0 \end{bmatrix} = \frac{1}{3} \begin{bmatrix} 1 & a & a^2 \\ 1 & a^2 & a \\ 1 & 1 & 1 \end{bmatrix} \cdot \begin{bmatrix} \underline{U}_A \\ \underline{U}_B \\ \underline{U}_C \end{bmatrix}; \quad (3)$$

where: a – rotation operator which is given by: $a = 1\angle 120^\circ$.

The typical factor range is between 60% and 80%, compensating 100% network can be overcompensated. In the case of zero sequence components, there is no rotation between phasors [2]. The voltage unbalance can be quantified using the following definition:

$$\text{Unbalance factor: } k_U^- = \frac{U^-}{U^+}; \quad (4)$$

$$\text{Asymmetry factor: } k_U^0 = \frac{U^0}{U^+}; \quad (5)$$

$$\text{Total unbalance factor: } k_U = k_U^0 + k_U^-; \quad (6)$$

$$\text{Complex unbalance factor: } \underline{k}_U^- = \frac{\underline{U}^-}{\underline{U}^+}; \quad (7)$$

$$\text{Complex asymmetry factor: } \underline{k}_U^0 = \frac{\underline{U}^0}{\underline{U}^+}; \quad (8)$$

Where U^+ , U^- and U^0 are the magnitude of positive, negative and zero-sequence voltage, respectively.

The ratio of the negative – to the positive sequence component can be used to specify the percentage unbalance. This definition is used in Engineering recommendation [4]. According to standard IEEE, the percentage voltage unbalance factor (%VUF) /rate is defined as following:

$$\%VUF = \frac{\text{negative seq. } U \text{ component}}{\text{positive seq. } U \text{ component}} * 100$$

EN50160 standards require <2% voltage asymmetry limits when 95% of the sequence of valid 10 minutes values. period is one week

3. Effect of Tower Design

Voltage asymmetric in three-phase distribution systems regards the changing in the three-phase voltage differ in amplitude or displace from their normal 120° phase relationship or both. [4] and [5] papers describes the main causes leading to voltage asymmetry which's are:

- Asymmetrical or unstable utility supply.
- Open delta or wye transformers.
- Asymmetrical distribution systems, that are equipment and phase conductors, present different impedance values.
- Different voltage drops due to differences in mutual impedances between phase conductors and between phase conductors and ground. This depends on the special configuration of conductors.

In this part of paper we are comparing four overhead lines constructions of distribution network: flat, vertical, delta and inverted delta.

The asymmetry of a line may be caused by the kind of laying the cables. [6] Article research about the feeder configuration which was modeled using the Alternative Transients Program and checked the impact of line geometry on voltage unbalance. It is not enough, the emergency of asymmetry depends and of tower high, feeder's configuration on the pole. Fig. 1 shows the spacing distance between cables for overhead lines:

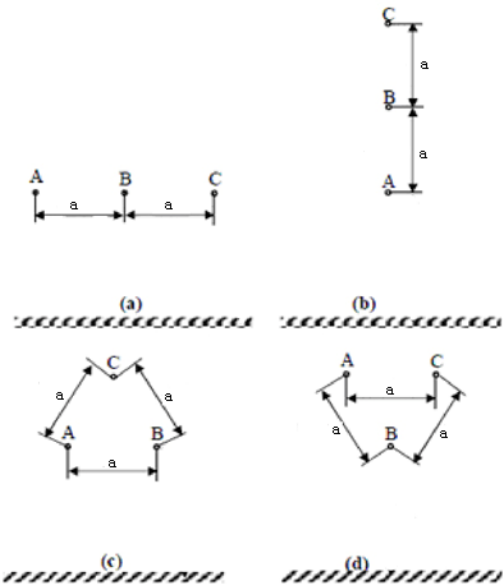


Fig. 1. Overhead lines configuration: a) flat (b) vertical tower configuration, (c) delta tower configuration, (d) inverted delta

The most common effect of voltage asymmetry is to degrade the performance and shorten the life of distribution network equipment.

4. Analysis of asymmetry mitigation in distribution network

In this part of paper, the principle for a calculation of an asymmetrical network compensation degree show how much network should be compensated.

Several methodologies have been proposed how to locate an asymmetrical fault [3].

Using Stokvis – Fortescue theorem [2] was created experiment with MV distribution network overhead lines. Model was built using Matlab package. The supply system was modelled as an ideal 3-phase voltage source which produces symmetric waveforms of constant amplitude.

First of all, this method shows stress of projecting overhead lines of distribution network. Second, if network we be compensated right, the network can avoid big damages, otherwise the end user can suffer and network can be overcompensated.

Assuming that the 35kV network consist of overhead line with the configuration as shown in Fig. 2.

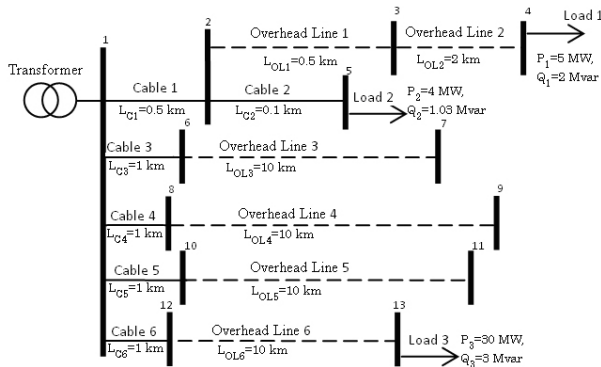


Fig. 2. Model of distribution system

The numerical experiment of asymmetry evaluation in distribution network was performed assuming that the distance a between wires is 3 m and the vertical distance between the upper wire and ground is 15 m. Different configurations of overhead lines towers were analysed. For the uncompensated network, the asymmetry of voltages is very small. Phasor diagrams of voltages at bus 3 for flat, vertical and inverted delta configurations when the network is compensated are presented in Fig. 2, Fig. 3 and Fig. 4. The diagrams show all the three asymmetrical phasors U_A , U_B , U_C . It is obvious that asymmetries exist not only in the magnitude of the voltages, but also in the phase angles, as the 3 phasors are no longer separated by exactly 120° , as with the symmetrical case.

Results show what a big influence has the overhead line's layout on the poles for spring up bigger or smaller asymmetry in the network. Asymmetry exists not only in the magnitude of the voltages, but also in the phase angles, as the 3 phasors are no longer separated by exactly 120° , as with symmetric case.

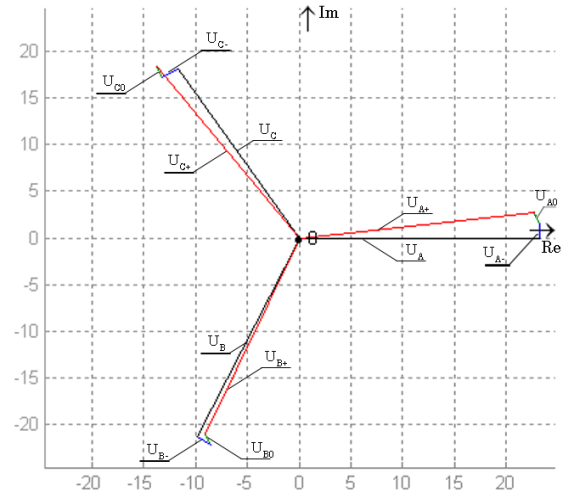


Fig. 3. Phasor diagram of voltages at bus 3 (flat configuration of overhead lines towers)

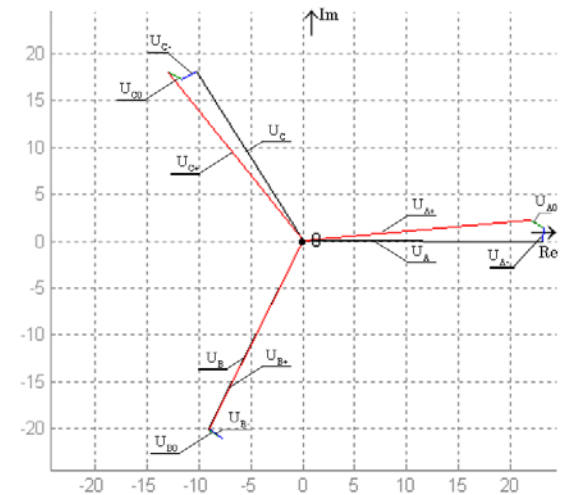


Fig. 4. Phasor diagram of voltages at bus 3 (vertical configuration of overhead lines towers)

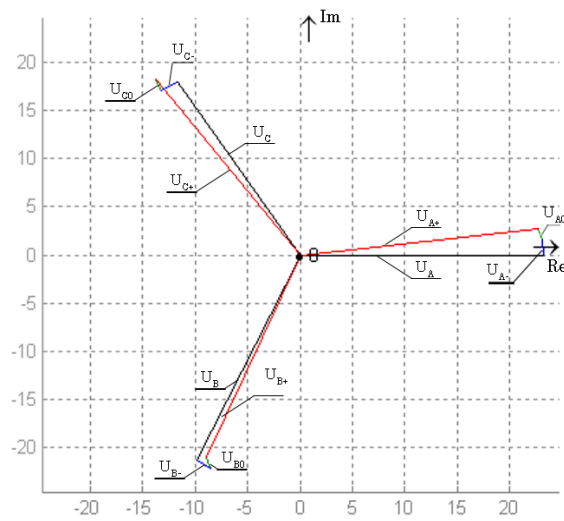


Fig. 5. Phasor diagram of voltages at bus 3 (inverted delta configuration of overhead lines towers)

When network is not compensated, the data of voltages is presented in Table 1. Bus voltages for different

configurations of the compensated network with compatibility factor $k=0.9$ are presented in Table 2, Table 3 and Table 4.

Table 1. Bus voltages in p.u. (flat configuration of overhead lines towers, uncompensated network)

Bus No	1	3	6	7	12	13
Phase A	1.1500	1.1491	1.1470	1.1501	1.1501	1.1198
Phase B	1.1500	1.1483	1.1462	1.1492	1.1492	1.1154
Phase C	1.1500	1.1492	1.1471	1.1502	1.1502	1.1118

Table 2. Bus voltages (flat configuration of overhead lines towers, compensated network)

Bus No	1	3	6	7	12	13
Phase A	1.1500	1.1492	1.1470	1.1501	1.1501	1.1236
Phase B	1.1604	1.1595	1.1574	1.1604	1.1604	1.1275
Phase C	1.1501	1.1491	1.1471	1.1502	1.1502	1.1084

Table 3. (vertical configuration of overhead lines towers, compensated network)

Bus No	1	3	6	7	12	13
Phase A	1.1500	1.1491	1.1470	1.1501	1.1501	1.1228
Phase B	1.1649	1.1639	1.1619	1.1649	1.1649	1.1307
Phase C	1.1591	1.1581	1.1562	1.1592	1.1592	1.1166

Table 4. (inverted delta configuration of overhead lines towers, compensated network)

Bus No	1	3	6	7	12	13
Phase A	1.1500	1.1491	1.1470	1.1501	1.1501	1.1159
Phase B	1.1500	1.1491	1.1470	1.1501	1.1501	1.1159
Phase C	1.1500	1.1491	1.1470	1.1501	1.1501	1.1159

Results show, that overhead lines layout configuration and diameters between lines, height from the ground has big effect to become of asymmetry. Also, to reduce asymmetry, network should be compensated. Compensate network with compatibility factor also should be regulated, otherwise network will be not enough compensated or overcompensated.

5. Conclusion

To strain after an effect electricity grid of good quality, economic and reliable work requires to monitoring the network, its operation, life time at the same time to evaluation of potential failures in order to avoid them.

Electric energy reliability concern with appropriate equipment isolation, rapid response fault removal and reaching avoid all of this. Big influence of reliability has power lines arrangement on power line poles, grounding and properly compensated network given fault or given asymmetry. Voltage asymmetry affects the insulation and its aging process, equipment life time, equipment irretrievable.

The asymmetry of a line may be caused by the kind of not good project laying the cables and the right height of the pole, at the same time paying attention to the amount of lines voltage. In this paper created method with MATLAB shows that asymmetry can reduce compensated network and good design of network.

6. References

1. Dzafic I., Neisius H.-T., Generic Three-Phase Power Flow methods using symmetrical components for symmetrical and unsymmetrical power system networks. Innovative Smart Grid Technologies (ISGT), 2011 IEEE PES, 2011, pp. 1-6.
2. Cziker A., Chindris M., Miron A. Voltage unbalance mitigation using a distributed generator Technical University of Cluj – Napoca, Romania. 2008
3. Du J., Lu Y., Zhu G., and Lin X., An asymmetrical fault location method based on communication system in distribution network with DGs. in Power Systems Conference and Exposition, 2009. PSCE'09. IEEE/PES, 2009, pp. 1-6.
4. Kiahinezhad R., Seifossadat G., Heidari M., Monadk M. Effects of Distribution Network Unbalance Voltage Types in Respect to Identical Unbalance Factor on the Induction Motor. Islamic Azad University, Shushtar, Iran, 2009, pp. 193-196.
5. Santos Valois, P.V., Vieira Tahan, C.M.; Kagan, N.; Arango, H. Voltage unbalance in low voltage distribution networks. Companhia Paranaense de Energia, Brazil. 2001.
6. Browne N., Spoor D., Byrnes J. Voltage Unbalance in an Urban Distribution Network – A Case Study. Syst. Dev. Branch of Integral Energy, Huntingwood, NSW. 2008.pp. 1-5.